VOLUME 79 FEBRUARY 13, 1975 NUMBER 4

JPCHAx

THE JOURNAL OF PHYSICAL CHEMISTRY

PUBLISHED BIWEEKLY BY THE AMERICAN CHEMICAL SOCIETY

THE JOURNAL OF

PHYSICAL CHEMISTRY

AMERICAN CHEMICAL SOCIETY, *1155 Sixteenth St., N.W., Washington, D.C. 20036*

Books and Journals Division

JOHN K CRUM *Director*
RUTH REYNARD and VIRGINIA E. STEWART *Assistants to the Director*

CHARLES R. BERTSCH *Head, Editorial Processing Department*
D. H. MICHAEL BOWEN *Head, Journals Department*
BACIL GUILEY *Head, Graphics and Production Department*
SELDON W. TERRANT *Head, Research and Development Department*

 Published biweekly by the American Chemical Society at 20th and Northampton Sts., Easton, Pa. 18042. Second-class postage paid at Washington, D.C., and at additional mailing offices.

All manuscripts should be sent to *The Journal of Physical Chemistry,* Department of Chemistry, University of Minnesota, Minneapolis, Minn. 55455.

Additions and Corrections are published once yearly in the final issue. See Volume 78, Number 26 for the proper form.

Extensive or unusual alterations in an article after it has been set in type are made at the author's expense, and it is understood that by requesting such alterations the author agrees to defray the cost thereof.

The American Chemical Society and the Editor of *The Journal of Physical Chemistry* assume no responsibility for the statements and opinions advanced by contributors.

Correspondence regarding accepted copy, proofs, and reprints should be directed to Editorial Processing Department, American Chemical Society, 20th and Northampton Sts., Easton, Pa. 18042. Department Head: CHARLES R. BERTSCH. Associate Department Head: MARIANNE C. BROGAN. Assistant Editor: CELIA B. MCFARLAND. Editorial Assistant: JOSEPH E. YURVATI.

Advertising Office: Centcom, Ltd., 50 W. State St., Westport, Conn. 06880.

Business and Subscription Information

Send all new and renewal subscriptions *with payment* to Office of the Controller, 1155 16th Street, N.W., Washington, D.C. 20036. Subscriptions should be renewed promptly to avoid a break in your series. All correspondence and telephone calls regarding changes of address, claims for missing issues, subscription service, the status of records, and accounts should be directed to Manager, Membership and Subscription Services, American Chemical Society, P.O. Box 3337, Columbus, Ohio 43210. Telephone (614) 421-7230. For microfiche service, contact ACS Journals Department, 1155 16th St. N.W., Washington, D.C. 20036. Telephone (202) 872-4444.

On changes of address, include both old and new addresses with ZIP code numbers, accompanied by mailing label from a recent issue. Allow four weeks for change to become effective.

Claims for missing numbers will not be allowed (1) if loss was due to failure of notice of change in address to be received before the date specified, (2) if received more than sixty days from date of issue plus time normally required for postal delivery of journal and claim, or (3) if the reason for the claim is "issue missing from files."

Subscription rates (hard copy or microfiche) in 1975: $20.00 for 1 year to ACS members; $80.00 to nonmembers. Extra postage $4.50 in Canada and PUAS, $5.00 other foreign. Supplementary material (on microfiche only) available on subscription basis, 1975 rates: $15.00 in U.S., $19.00 in Canada and PUAS, $20.00 elsewhere. All microfiche airmailed to non-U.S. addresses; air freight rates for hard-copy subscriptions available on request.

Single copies for current year: $4.00. Rates for back issues from Volume 56 to date are available from the Special Issues Sales Department, 1155 Sixteenth St., N.W., Washington, D.C. 20036.

Subscriptions to this and the other ACS periodical publications are available on microfilm. For information on microfilm write Special Issues Sales Department at the address above.

Notice to Authors last printed in the issue of January 16, 1975

THE JOURNAL OF
PHYSICAL CHEMISTRY

Volume 79, Number 4 February 13, 1975

JPCHAx 79(4) 295–402 (1975)
ISSN 0022-3654

■ Supplementary and/or miniprint material for this paper is available separately, in photocopy or microfiche form. Ordering information is given in the paper.

* In papers with more than one author, the asterisk indicates the name of the author to whom inquiries about the paper should be addressed.

AUTHOR INDEX

ANNOUNCEMENT

On the last two pages of this issue you will find reproduced the table of contents of the January 1975 issue of the Journal of Chemical and Engineering Data.

THE JOURNAL OF
PHYSICAL CHEMISTRY

VOLUME 79, NUMBER 4 FEBRUARY 13, 1975

Temperature Dependence of the Absolute Rate Constants for the Reaction of $O(^3P)$ Atoms with a Series of Aromatic Hydrocarbons over the Range 299–392°K

R. Atkinson and J. N. Pitts, Jr.*

Department of Chemistry and Statewide Air Pollution Research Center, University of California, Riverside, California 92502
(Received August 21, 1974)

Publication costs assisted by the University of California

Rate constants, k_2, for the reaction of $O(^3P)$ atoms with a series of aromatic hydrocarbons have been determined over the temperature range 299–392°K using a modulation technique. The Arrhenius expressions obtained are as follows (l. mol^{-1} sec^{-1}): k_2(benzene) = $11.1 \times 10^9 e^{-(3980\pm400)/RT}$, k_2(toluene) = $8.2 \times 10^9 e^{-(3100\pm300)/RT}$, k_2(o-xylene) = $6.25 \times 10^9 e^{-(2430\pm300)/RT}$, k_2(m-xylene) = $7.7 \times 10^9 e^{-(2150\pm300)/RT}$, k_2(p-xylene) = $7.9 \times 10^9 e^{-(2540\pm300)/RT}$, k_2(1,2,3-trimethylbenzene) = $10.3 \times 10^9 e^{-(1600\pm300)/RT}$, k_2(1,2,4-trimethylbenzene) = $9.35 \times 10^9 e^{-(1650\pm300)/RT}$, k_2(1,3,5-trimethylbenzene) = $6.05 \times 10^9 e^{-(770\pm300)/RT}$.

Introduction

Although there is a considerable body of reliable rate constant data available in the literature for the reactions of $O(^3P)$ atoms with alkenes and alkanes, there have been few rate constant determinations for the reaction of $O(^3P)$ atoms with aromatic hydrocarbons.[1] Thus benzene is the only aromatic compound for which absolute rate constants have been obtained over a range of temperature.[2]

Recently we determined the absolute room-temperature rate constants for the reaction of $O(^3P)$ atoms with a series of aromatic hydrocarbons using a modulation phase-shift technique.[3] In this work we have extended these measurements to elevated temperatures in order to obtain the Arrhenius parameters.

Experimental Section

The apparatus and techniques used have been described previously,[3-5] and hence only a brief summary will be given here. $O(^3P)$ atoms were generated by the sinusoidally modulated mercury photosensitization of N_2O and their concentrations monitored by the NO_2 emission using a cooled EMI 9659A photomultiplier fitted with a cutoff filter transmitting $\lambda \geq 4700$ Å. Phase shifts ϕ between the incident 2537-Å radiation and the NO_2 emission were measured using a PAR HR-8 lock-in amplifier fitted with a Type C preamplifier.[4]

The reaction cell was enclosed by a furnace whose temperature, monitored by a thermocouple probe, could be held constant to ±0.2°K. The reactant gas stream was determined to be within ±0.5°K of the furnace temperature under all conditions used. The gases used, their purities, and their purifications were as described previously.[3]

Results

Under the experimental conditions used, the phase shift, ϕ, is given by[3,4]

$$\tan \phi = 2\pi\nu/(k_1[NO][M] + k_2[\text{aromatic}]) \quad (I)$$

where k_1 and k_2 are the rate constants for the reactions

$$O + NO + M \longrightarrow NO_2 + M \quad (1)$$

$$O + \text{aromatic} \longrightarrow \text{products} \quad (2)$$

and ν is the modulation frequency (1200 ± 1 Hz). Total pressures were in the range 51–75 Torr.

Rate constants k_2 were determined over the temperature range 299–392°K as described previously.[3] Thus, for example, Figure 1 shows plots of $2\pi\nu/\tan\phi$ against [aromatic] for m-xylene at the three temperatures studied. The rate constants k_2 obtained from such plots are given in Table I and are plotted in Arrhenius form ($k_2 = A_2 e^{-E_2/RT}$) in Figure 2. The Arrhenius parameters A_2 and E_2 determined by least-squares analysis of the data are given in Table II.

TABLE I: Rate Constants k_2 for the Reaction of $O(^3P)$ Atoms with Aromatics[a]

Aromatic	Temp, °K	$10^{-8}k_2$, l. mol^{-1} sec^{-1}
Benzene	300.3 ± 0.3	0.144 ± 0.02
	341.2 ± 0.5	0.303 ± 0.035
	392.2 ± 0.5	0.69 ± 0.08
Toluene	300.4 ± 0.2	0.450 ± 0.045
	341.2 ± 0.5	0.85 ± 0.09
	392.2 ± 0.5	1.52 ± 0.15
o-Xylene	299.1 ± 0.3	1.05 ± 0.11
	341.2 ± 0.5	1.72 ± 0.18
	392.2 ± 0.5	2.77 ± 0.3
m-Xylene	299.5 ± 0.5	2.12 ± 0.21
	341.2 ± 0.5	3.09 ± 0.3
	392.2 ± 0.5	5.0 ± 0.5
p-Xylene	300.4 ± 0.5	1.09 ± 0.11
	341.2 ± 0.5	2.01 ± 0.2
	392.2 ± 0.5	2.94 ± 0.3
1,2,3-Trimethylbenzene	299.7 ± 0.4	6.9 ± 0.7
	341.2 ± 0.5	9.9 ± 1.0
	392.2 ± 0.5	13.0 ± 1.5
1,2,4-Trimethylbenzene	300.2 ± 0.3	6.0 ± 0.6
	341.2 ± 0.5	8.1 ± 0.8
	392.2 ± 0.5	11.5 ± 1.2
1,3,5-Trimethylbenzene	299.9 ± 0.5	16.8 ± 2.0
	341.2 ± 0.5	18.9 ± 2.0
	392.2 ± 0.5	22.8 ± 3.0

[a] The errors include precision limits derived from least-squares standard deviations and estimated accuracy of other parameters such as pressure and composition of mixtures.

TABLE II: Arrhenius Parameters for the Reaction of $O(^3P)$ Atoms with Aromatics[a]

Aromatic	$10^{-9}A_2$, l. mol^{-1} sec^{-1}	E_2, kcal mol^{-1}
Benzene	11.1	3.98 ± 0.4
Toluene	8.2	3.10 ± 0.3
o-Xylene	6.25	2.43 ± 0.3
m-Xylene	7.7	2.15 ± 0.3
p-Xylene	7.9	2.54 ± 0.3
1,2,3-Trimethylbenzene	10.3	1.60 ± 0.3
1,2,4-Trimethylbenzene	9.35	1.65 ± 0.3
1,3,5-Trimethylbenzene	6.05	0.77 ± 0.3

[a] The indicated errors in the activation energies E_2 include the least-squares standard deviations and the estimated overall error limits.

Discussion

As discussed previously[3] the reactions of $O(^3P)$ atoms with reactant impurities and secondary products are estimated to cause errors in the measured rate constants of less than 5% at room temperature. At elevated temperatures, such errors should be lower because the $O(^3P)$ atom reaction rate constants for the reactant are expected to approach those for the reaction products.

It can be seen from Table II that, within the likely experimental errors, the preexponential factor A_2 is reasonably constant for all the aromatics studied, while the activation energy E_2 decreases with the degree of methylation. Hence, in a similar manner to the reaction of $O(^3P)$ atoms with olefins,[6-8] the different reactivities shown by the aromatics are primarily due to differences in the activation energies. The preexponential factors for the reactions of $O(^3P)$ atoms with the aromatic hydrocarbons are somewhat higher (by a factor of ~2) than those recently determined for the simple olefins.[5,8-10]

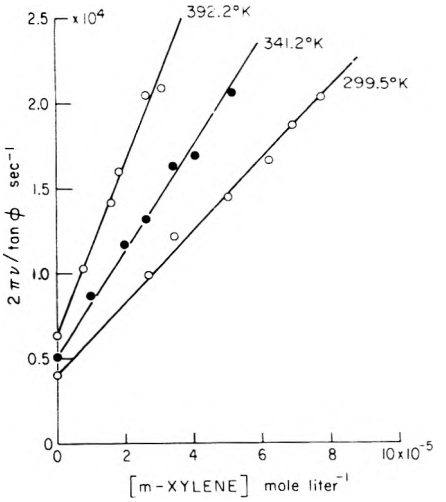

Figure 1. Plots of $2\pi\nu/\tan\phi$ against [*m*-xylene]. (Total pressures and NO pressures are as follows: 299.5°K 53 and 0.66 Torr; 341.2°K, 65 and 1.08 Torr; 392.2°K, 68 and 1.45 Torr. The data points at 392.2°K have been displaced vertically $+0.2 \times 10^4$ sec^{-1} for clarity.)

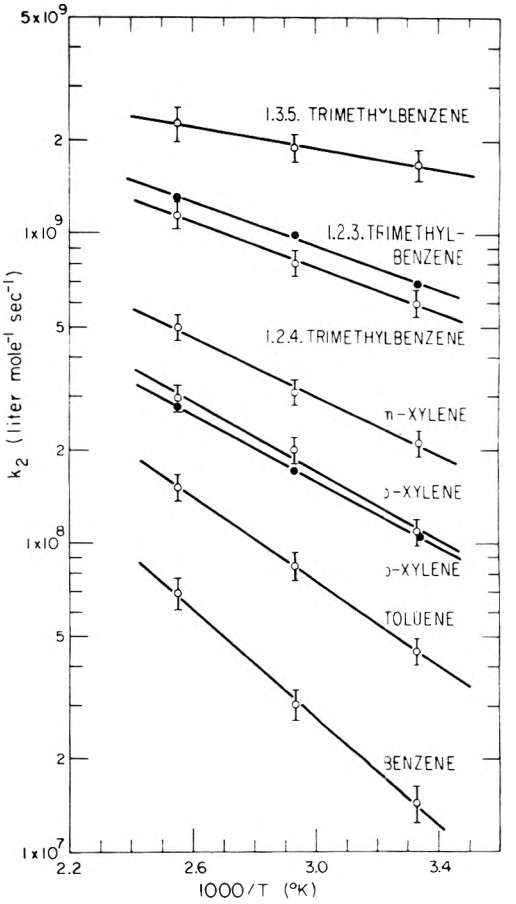

Figure 2. Arrhenius plots of log k_2 against $1/T$ for the aromatic hydrocarbons. (The error bars on the data points for o-xylene and 1,2,3-trimethylbenzene have been omitted for clarity.)

TABLE III: Comparison of the Arrhenius Activation Energies (E_2) and the Room-Temperature Rate Constants (k_2) from the Present Work with Selected Literature Values

	E_2, kcal mol^{-1}			$10^{-8}k_2$, l. mol^{-1} sec^{-1}		
Aromatic	Present work	Lit.	Derived from rel rates[a]	Present work	Lit.	Derived from rel rates[a]
Benzene	3.98 ± 0.4	4.4 ± 0.5[b]	3.27 ± 0.7	0.144 ± 0.02	0.28 ± 0.07[b] 0.36 ± 0.07[c]	0.16
Toluene	3.10 ± 0.3		2.47 ± 0.4	0.45 ± 0.045	1.4 ± 0.3[c]	0.57
o-Xylene	2.43 ± 0.3			1.05 ± 0.11	6.7 ± 1.6[c]	
m-Xylene	2.15 ± 0.3			2.12 ± 0.21	7.7 ± 2.0[c]	
p-Xylene	2.54 ± 0.3			1.09 ± 0.11	4.5 ± 1.4[c]	

[a] References 6, 7, 12, and 13. Placed on an absolute basis using $k_2 = 3.37 \times 10^9 e^{-1270/RT}$ for ethylene.[5] Error limits on E_2 are those associated with [E_2(aromatic) − E_2(cyclopentene)];[12,13] the overall errors may thus be larger. [b] Reference 2. [c] Reference 11.

The activation energies E_2 and the room-temperature rate constants k_2 determined in this work are compared to selected literature values in Table III.

The room-temperature rate constants obtained by Mani and Sauer[11] using a pulsed radiolysis technique are a factor of 3–6 higher than the present values, as discussed previously.[3] Similarly, the room-temperature rate constant k_2 for benzene of Bonanno, *et al.*[2] determined by discharge flow mass spectrometry is a factor of 2 higher than the present value, although their activation energy of 4.4 ± 0.5 kcal mol^{-1}, obtained over the range 255–305°K, is in good agreement with the activation energy E_2 = 3.98 ± 0.4 kcal mol^{-1} determined here.

The relative rate constant data of Cvetanovic and coworkers[6,7,12,13] obtained at 393–493°K have been placed on an absolute basis using $k_2 = 3.37 \times 10^9 e^{-1270/RT}$ l. mol^{-1} sec^{-1} for ethylene.[5] They are seen to be in reasonable agreement with the present work for both benzene and toluene within the overall experimental errors.

Recently the room-temperature relative rate constants for the reaction of OH radicals with *n*-butane and a series of aromatic hydrocarbons have been determined.[14] The aromatic hydrocarbons studied show a similar order of reactivity toward OH radicals as with O(^{3}P) atoms, although with a smaller range of rate constants. These rate constants, placed on an absolute basis[14] using the rate constant for OH + *n*-butane of 1.8×10^9 l. mol^{-1} sec^{-1},[15-18] range from $(2.5 \pm 0.9) \times 10^9$ l. mol^{-1} sec^{-1} for toluene to $(3.1 \pm 0.4) \times 10^{10}$ l. mol^{-1} sec^{-1} for 1,3,5-trimethylbenzene, demonstrating the higher reactivity of the OH radical toward the aromatic hydrocarbons compared to O(^{3}P) atoms.

Acknowledgments. The authors are grateful to Drs. A. C. Lloyd and J. L. Sprung for helpful discussions. The financial support of NSF Grant GP-38053X and Environmental Protection Agency Grant 800649 is gratefully acknowledged. The contents do not necessarily reflect the views and policies of the Environmental Protection Agency, nor does mention of trade names or commercial products constitute endorsement or recommendation for use.

References and Notes

(1) J. T. Herron and R. E. Huie, *J. Phys. Chem. Ref. Data*, **2**, 467 (1973).
(2) R. A. Bonanno, P. Kim, J. H. Lee, and R. B. Timmons, *J. Chem. Phys.*, **57**, 1377 (1972).
(3) R. Atkinson and J. N. Pitts, Jr., *J. Phys. Chem.*, **78**, 1780 (1974).
(4) R. Atkinson and R. J. Cvetanovic, *J. Chem. Phys.*, **55**, 659 (1971).
(5) R. Atkinson and J. N. Pitts, Jr., *Chem. Phys. Lett.*, **27**, 467 (1974).
(6) R. J. Cvetanovic, *J. Chem. Phys.*, **33**, 1063 (1960).
(7) R. J. Cvetanovic, *Advan. Photochem.*, **1**, 115 (1963).
(8) D. D. Davis, R. E. Huie, and J. T. Herron, *J. Chem. Phys.*, **59**, 628 (1973).
(9) D. D. Davis, R. E. Huie, J. T. Herron, M. J. Kurylo, and W. Braun, *J. Chem. Phys.*, **56**, 4868 (1972).
(10) M. J. Kurylo, *Chem. Phys. Lett.*, **14**, 117 (1972).
(11) I. Mani and M. C. Sauer, Jr., *Advan. Chem. Ser.*, **No. 82**, 142 (1968).
(12) G. Boocock and R. J. Cvetanovic, *Can. J. Chem.*, **39**, 2436 (1961).
(13) G. R. H. Jones and R. J. Cvetanovic, *Can. J. Chem.*, **39**, 2444 (1961).
(14) G. J. Doyle, A. C. Lloyd, K. R. Darnall, A. M. Winer, and J. N. Pitts, Jr., *Environ. Sci. Technol.*, in press.
(15) N. R. Greiner, *J. Chem. Phys.*, **53**, 1070 (1970).
(16) E. D. Morris, Jr. and H. Niki, *J. Phys. Chem.*, **75**, 3640 (1971).
(17) F. Stuhl, *Z. Naturforsch. A*, **28**, 1383 (1973).
(18) R. A. Gorse and D. H. Volman, *J. Photochem.*, **3**, 115 (1974).

Reactions of CH_3, CH_3O, and CH_3O_2 Radicals with O_3

R. Simonaitis and Julian Heicklen*

Department of Chemistry and Ionosphere Research Laboratory, The Pennsylvania State University, University Park, Pennsylvania 16802 *(Received July 5, 1974)*

Publication costs assisted by the National Science Foundation, the National Aeronautics and Space Administration, and the Department of Defense

Ozone was photolyzed at 253.7 nm at 25 and −52° in the presence of CH_4 and O_2 to measure the reactions of O_3 with CH_3, CH_3O, and CH_3O_2. The $O(^1D)$ atoms produced in the primary photochemical act react with CH_4 to give CH_3 radicals which in turn can react with O_2 to give CH_3O_2 and CH_3O radicals. At very high values of $[O_2]/[O_3]$, the quantum yield of O_3 disappearance, $-\Phi\{O_3\}$, approached 1.0, indicating that O_3 reactions with CH_3O_2 and CH_3O are slow. Upper limits to the rate coefficients at 25° were computed to be 2.4×10^{-17} and 2×10^{-15} cm^3/sec, respectively. At lower values of $[O_2]/[O_3]$, chain decomposition of O_3 occurred which could be explained by the reaction of O_3 with CH_3 radicals to produce CH_2O, O_2, and H atoms all the time. The two routes to these products are $CH_3 + O_3 \rightarrow O_2 + CH_3O^{\pm} \rightarrow CH_2O + H$ (9a) and $CH_3 + O_3 \rightarrow CH_2O + HO_2^{\pm} \rightarrow H + O_2$ (9b). The competition between O_3 and O_2 for CH_3 was measured: $CH_3 + O_2 \rightarrow CH_3O_2$ (10). It was found that $(k_{9a} + k_{9b})/k_{10} = 2.2$ and 1.2, respectively, at 25 and −52°. When this ratio is combined with the literature value of 4.3×10^{-13} cm^3/sec for k_{10}, the Arrhenius expression becomes $k_{9a} + k_{9b} \approx 5.4 \times 10^{-12} \exp(-1050/RT)$ cm^3/sec. The large preexponential factor suggests a linear transition state, and thus reaction 9a is probably the preferred reaction channel.

Introduction

The reactions of CH_3, CH_3O and CH_3O_2 radicals with O_3 have never been studied, as far as we know. These radicals are produced in the earth's atmosphere by CH_4 oxidation; therefore, their reactions with O_3 are of interest.

In the study reported here, the CH_3 radicals are generated by the photolysis of O_3 in the presence of excess CH_4. The primary photolytic act produces $O(^1D)$ which abstracts an H atom from CH_4 to produce CH_3. If O_2 is also present in the system, it will add to CH_3 to produce CH_3O_2. These radicals can produce CH_3O by mutual interaction. Thus CH_3, CH_3O_2, and CH_3O can all be produced in the same system. From the measurement of the O_3 removal quantum yield, $-\Phi\{O_3\}$, information regarding the reactions of these radicals with O_3 is obtained.

Experimental Section

The experimental procedure is identical with that described in an earlier publication where O_3 was photolyzed at 253.7 nm in the presence of H_2 to study the reactions of HO_2 radicals.[1] In the present study CH_4 was used instead of H_2. The CH_4 was from the Matheson Co., and it was used without further purification. The O_3 removal was monitored photometrically, and initial quantum yields were obtained.

Results

Irradiation of CH_4–O_3–O_2 mixture at 253.7 nm at 25 and −52° leads to the removal of O_3. The initial quantum yields for O_3 removal, $-\Phi\{O_3\}$, are presented in Table I. In these experiments, the absorbed light intensity, I_a, was varied by a factor of 15, the CH_4 and O_3 pressures each were varied by a factor of 5, and the O_2 pressure was varied by a factor of 200. The results show that $-\Phi\{O_3\}$ decreases regularly as the $[O_2]/[O_3]$ ratio increases, but is otherwise relatively insensitive to other variables at a given temperature. In particular $-\Phi\{O_3\}$ is independent of I_a.

Some experiments were also done at 25° in the "absence" of O_2. Actually some O_2 (~20 mTorr) is always present because of O_3 decomposition during the gas handling process. Initially $-\Phi\{O_3\}$ is very large, approaching 100 in some of our experiments. However as the run progresses, O_2 accumulates as a product, and the rate of O_3 removal rapidly diminishes. The initial quantum yields are presented in Table II. The experiments are listed in order of increasing $[O_3]/I_a^{1/2}$ since the chain-propagating steps are expected to be proportional to $[O_3]$; the radical concentrations are expected to be proportional to $I_a^{1/2}$. There may be a trend in the data, possibly $-\Phi\{O_3\}$ tends to rise along with $[O_3]/I_a^{1/2}$. However there is considerable scatter, and this probably reflects the variable amount of background O_2 present at the beginning of the run.

Discussion

The initial act in the photolysis is the decomposition of O_3 by the well-known process

$$O_3 + h\nu\ (253.7\ nm) \longrightarrow O_2(^1\Delta) + O(^1D) \qquad (1)$$

The $O_2(^1\Delta)$ will react predominantly with O_3

$$O_2(^1\Delta) + O_3 \longrightarrow 2O_2 + O(^3P) \qquad (2)$$

The reactions of $O_2(^1\Delta)$ with O_2 and CH_4 are negligible as can be shown by using the rate coefficients in Table III. The $O(^3P)$ atoms produced in reaction 2 can react with O_2, O_3, and CH_4

$$O(^3P) + O_2 + M \longrightarrow O_3 + M \qquad (3)$$

$$O(^3P) + O_3 \longrightarrow 2O_2 \qquad (4)$$

$$O(^3P) + CH_4 \longrightarrow OH + CH_3 \qquad (5)$$

The rate coefficients for reactions 3, 4, and 5 are also given in Table III.

The $O(^1D)$ will react predominantly (>97%) with CH_4 as can be shown by the rate coefficients given in Table III

TABLE I: Photolysis of CH_4-O_2-O_3 Mixtures at 253.7 nm

$[O_3]/[O_2]$	$[O_3]$, mTorr	$[O_2]$, Torr	$[CH_4]$, Torr	I_a, mTorr/min	$-\Phi\{O_3\}$
		T = 25°			
0.00116	81	70	730	11.0	1.3
0.00153	107	70	720	2.1	1.1
0.00247	370	150	600	6.0	1.4
0.0041	370	90	740	6.0	1.3
0.0042	350	83	590	5.3	1.3
0.0057	380	67	720	0.76	1.05
0.0058	390	68	740	0.48	1.25
0.014	313	22	730	4.5	1.30
0.022	380	17	720	6.0	1.55
0.025	82	3.3	650	1.8	0.93
0.043	268	6.3	750	3.9	1.56
0.057	68	1.2	650	1.3	1.70
0.073	390	5.3	135	4.4	2.1
0.083	245	2.95	144	4.0	3.0
0.105	214	2.03	760	3.4	2.2
0.106	180	1.70	680	0.34	2.6
0.114	320	2.80	760	4.6	2.3
0.117	203	1.74	175	1.09	3.3
0.147	200	1.36	166	5.4	3.9
0.165	340	2.06	660	8.9	3.4
0.175	315	1.80	690	1.42	3.2
0.200	340	1.70	700	8.4	3.2
0.235	296	1.26	680	0.71	3.4
0.308	330	1.07	155	8.3	6.9
0.356	320	0.90	720	4.6	5.5
0.41	290	0.71	650	6.7	6.7
		T = -52°			
0.059	202	3.45	650	5.35	1.06
0.066	82	1.24	650	2.65	1.4
0.145	216	1.49	650	5.70	1.75
0.256	230	0.90	650	4.85	2.6
0.259	216	0.834	650	5.75	2.2
0.41	285	0.700	650	6.75	3.3

$$O(^1D) + CH_4 \longrightarrow OH + CH_3 \quad (6a)$$
$$\longrightarrow CH_2O + H_2 \quad (6b)$$

According to Lin and DeMore, channel 6a and 6b account for 88 and 9%, respectively.[7] However, Greenberg and Heicklen[8] report that channel 6a occurs 95 ± 5% of the time. Whether the former or latter result is correct will not significantly affect the results of this study.

The OH radical produced in reactions 5 and 6a will react with CH_4. The reaction with O_3 is negligible for all $[CH_4]/[O_3]$ ratios used in the present study.

$$OH + CH_4 \longrightarrow H_2O + CH_3 \quad (7)$$
$$OH + O_3 \longrightarrow HO_2 + O_2 \quad (8)$$

The CH_3 radical produced in reactions 5 and 6a can react with O_3 as follows:

$$CH_3 + O_3 \longrightarrow CH_3O^{\ddagger} + O_2 \quad (9a)$$
$$CH_3 + O_3 \longrightarrow HO_2^{\ddagger} + CH_2O \quad (9b)$$

where the superscript ± designates excess vibrational energy. The energetic $CH_3O^{\pm}$ and $HO_2^{\pm}$ may be stabilized or they may decompose

TABLE II: Photolysis of CH_4-O_3 Mixtures at 253.7 nm and 25°

$[O_3]/I_a^{1/2}$, (mTorr min)$^{1/2}$	$[O_3]$, mTorr	$[CH_4]$, Torr	I_a, mTorr/min	$-\Phi\{O_3\}$
53	84	700	2.5	30
89	233	680	6.8	43
89	233	680	6.8	48
110	76	680	0.48	30
188	180	184	0.93	91
188	180	680	0.93	63
196	180	680	0.80	60
285	276	700	0.94	48
286	350	680	1.5	65
336	248	147	0.59	100
360	276	680	0.55	68

$$CH_3O^{\ddagger} \longrightarrow H + CH_2O \quad (9a')$$
$$CH_3O^{\ddagger} + M \longrightarrow CH_3O + M \quad (9a'')$$
$$HO_2^{\ddagger} \longrightarrow H + O_2 \quad (9b')$$
$$HO_2^{\ddagger} + M \longrightarrow HO_2 + M \quad (9b'')$$

and in the presence of O_2, reaction 10 will occur

$$CH_3 + O_2 + M \longrightarrow CH_3O_2 + M \quad (10)$$

The HO_2 radicals produced in 9b'' will propagate the chain decomposition of O_3 *via* the reaction

$$HO_2 + O_3 \longrightarrow OH + 2O_2 \quad (11)$$

The H atoms produced in reactions 9a' and 9b' will propagate the chain decomposition of O_3 *via* the known reactions

$$H + O_2 + M \longrightarrow HO_2 + M \quad (12)$$
$$H + O_3 \longrightarrow OH^{\ddagger}(v = 9) + O_2 \quad (13)$$
$$OH^{\ddagger} + O_3 \longrightarrow H + 2O_2 \quad (14)$$
$$OH^{\ddagger} + CH_4 \longrightarrow H_2O + CH_3 \quad (15)$$

Since $-\Phi\{O_3\}$ is independent of I_a under all experimental conditions, chain termination cannot be by radical-radical reactions. Therefore, all radical-radical reactions which involve chain carriers and do not lead to chain carriers are not important.

The CH_3O_2 radicals produced in reaction 10 will be removed *via*

$$2CH_3O_2 \longrightarrow 2CH_3O + O_2 \quad (16a)$$
$$\longrightarrow CH_3OH + CH_2O + O_2 \quad (16b)$$
$$\longrightarrow CH_3O_2CH_3 + O_2 \quad (16c)$$

The most recent measurements give $k_{16a}/k_{16} = 0.43$.[6] The CH_3O radical produced in reactions 9a'' and 16a will be removed by

$$2CH_3O \longrightarrow CH_3OH + CH_2O \quad (17)$$

and by

$$CH_3O + O_2 \longrightarrow CH_2O + HO_2 \quad (18)$$

CH_3O_2 and CH_3O may also react with O_3

$$CH_3O_2 + O_3 \longrightarrow \text{products} \quad (19)$$
$$CH_3O + O_3 \longrightarrow \text{products} \quad (20)$$

To estimate the importance of reactions 19 and 20, consider the results at high values of $[O_2]/[O_3]$. Under these

TABLE III: Summary of Rate Coefficients

	Reaction	Rate coefficient, cm^3/sec	Ref
2.	$O_2(^1\Delta) + O_3 \rightarrow O(^3P) + 2O_2$	$5.0 \times 10^{-11} \exp(-5650/RT)$	3
	$O_2(^1\Delta) + CH_4 \rightarrow O(^3P) + O_2$	Too slow to measure	
3.	$O(^3P) + O_2 + M \rightarrow O_3 + M$	$6.6 \times 10^{-35} \exp(1020/RT)$[a]	3
4.	$O(^3P) + O_3 \rightarrow 2O_2$	$1.4 \times 10^{-11} \exp(-4600/RT)$	3
5.	$O(^3P) + CH_4 \rightarrow OH + CH_3$	$3.5 \times 10^{-11} \exp(-9100/RT)$	3
6a.	$O(^1D) + CH_4 \rightarrow OH + CH_3$	4×10^{-10}	3
6b.	$O(^1D) + CH_4 \rightarrow CH_2O + H_2$	$k_{6a}/k_{6b} \geq 7$	3
	$O(^1D) + O_2 \rightarrow O(^3P) + O_2$	7.5×10^{-11}	3
	$O(^1D) + O_3 \rightarrow O_2 + O_2^*$ (or $2O(^3P)$)	5.0×10^{-10}	3
7.	$OH + CH_4 \rightarrow H_2O + CH_3$	$4.8 \times 10^{-11} \exp(-5000/RT)$	3
8.	$OH + O_3 \rightarrow HO_2 + O_2$	$1.6 \times 10^{-12} \exp(-2000/RT)$	3
10.	$CH_3 + O_2 \rightarrow CH_3O_2$	4.3×10^{-13}[b]	3
11.	$HO_2 + O_3 \rightarrow OH + 2O_2$	$1 \times 10^{-13} \exp(-2400/RT)$	3
12.	$H + O_2 + M \rightarrow HO_2 + M$	$6.7 \times 10^{-33} \exp(660/RT)$	3
13.	$H + O_3 \rightarrow OH(v = 9) + O_2$	2.6×10^{-11}	3
14.	$OH^* + O_3 \rightarrow H + 2O_2$	7.7×10^{-12}	4
15.	$OH^* + CH_4 \rightarrow H_2O + CH_3$	1.4×10^{-14}	4
16a.	$2CH_3O_2 \rightarrow 2CH_3O + O_2$	$k_{16} = 2.4 \times 10^{-13}$	5
16b.	$\rightarrow CH_3OH + CH_2O + O_2$	$k_{16a}/k_{16} = 0.43$	6
16c.	$\rightarrow CH_3O_2CH_3 + O_2$		6
17.	$2CH_3O \rightarrow CH_3OH + CH_2O$	$1\text{–}6 \times 10^{-11}$	3
18.	$CH_3O + O_2 \rightarrow CH_2O + HO_2$	$\sim 3 \times 10^{-18}$[c]	3
21.	$CH_3O_2 + HO_2 \rightarrow CH_3O_2H + O_2$	$\sim 5 \times 10^{-12}$	9

[a] For M = Ar. Efficiency for CH_4 taken as 4 times that for Ar. [b] High-pressure limit at 298°K. Applicable at >100 Torr pressure. [c] At 25°, $E_a \sim 6$ kcal/mol.

conditions, more CH_3O radicals are removed *via* reaction 18 than reaction 17. With the assumption that the rate of reaction 17 is negligible compared to reaction 18, and the realization that reaction 19 is less important than reaction 16, then at high values of $[O_2]/[O_3]$, the steady-state rate law is

$$-\Phi_\infty\{O_3\} \geq 1 + k_{19}\left(\frac{k_{6a}}{k_6 k_{16}}\right)^{1/2}\frac{[O_3]}{I_a^{1/2}} + 2\frac{k_{6a}k_{16a}}{k_6 k_{16}}\frac{k_{20}[O_3]}{(k_{18}[O_2] + k_{20}[O_3])} \quad \text{(I)}$$

where $-\Phi_\infty\{O_3\}$ represents the limiting value of $-\Phi\{O_3\}$ for large $[O_2]/[O_3]$ ratios. The inequality sign in eq I comes from three separate considerations. (1) The $[O_2]/[O_3]$ ratio might not be sufficiently high to completely supress reactions 4 and 9. (2) Reaction 19 or 20 might lead to a chain decomposition of O_3. (3) Reaction 18 leads to HO_2 which can decompose O_3 *via* reaction 11.

At the highest $[O_2]/[O_3]$ ratios used in our studies $-\Phi\{O_3\}$ is reduced to below 1.3. Thus both the pentultimate and ultimate terms in eq I must be <0.3. With these restrictions and the rate coefficients in Table III, upper limits can be estimated for k_{19} and k_{20} to be $k_{19} < 2.4 \times 10^{-17}$ cm^3/sec and $k_{20} < 2 \times 10^{-15}$ cm^3/sec.

Since reactions 19 and 20 are unimportant we are faced with the dilemma of why $-\Phi_\infty\{O_3\}$ is so low, since reaction 18 followed by reaction 11 will remove O_3. However because CH_3O_2 is present there is an alternate path for HO_2 removal

$$CH_3O_2 + HO_2 \longrightarrow CH_3O_2H + O_2 \quad (21)$$

If we accept Heicklen's estimate[9] of 5×10^{-12} cm^3/sec for k_{21}, then even under the most unfavorable conditions (high $[O_3]$, low I_a) >70% of the HO_2 radicals are removed *via* reaction 21 (plus the fact that some are not even formed because CH_3O production is surpressed).

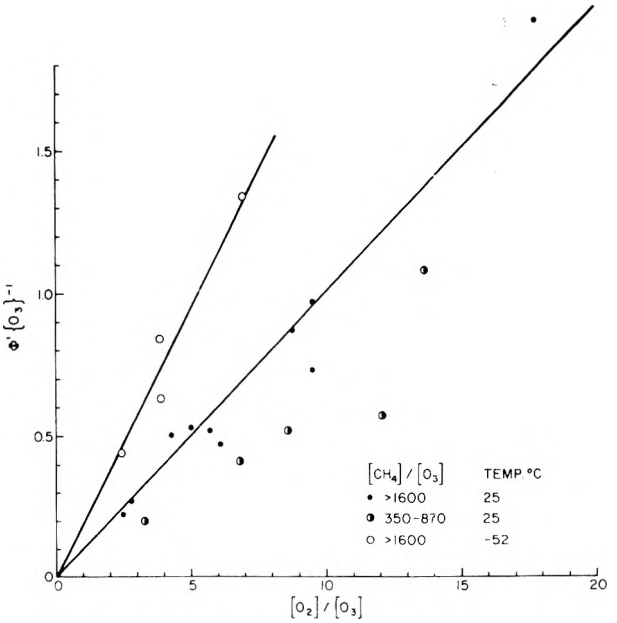

Figure 1. Plot of $\Phi'\{O_3\}^{-1}$ *vs.* $[O_2]/[O_3]$ in the photolysis of O_3–CH_4–O_2 mixtures at 253.7 nm.

At the lower $[O_2]/[O_3]$ ratios, reaction 18 is less important than reaction 17. Also we have just shown that reactions 19 and 20 are negligible. Under these conditions, the mechanism consists of reactions 1–7 and 9–17. The rate law is

$$\Phi'\{O_3\}^{-1} = (1 - f')k_{9a}/k_9' + k_{10}[O_2]/k_9'[O_3] \quad \text{(II)}$$

where

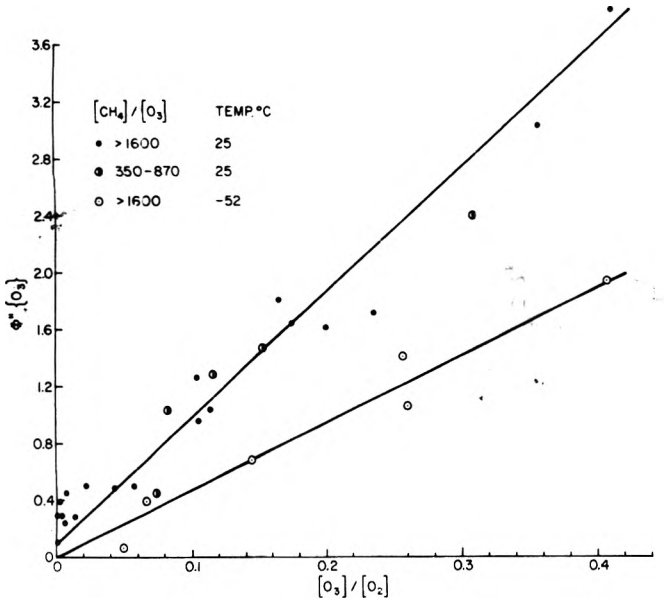

Figure 2. Plot of $\Phi''\{O_3\}$ *vs.* $[O_3]/[O_2]$ in the photolysis of O_3–CH_4–O_2 mixtures at 253.7 nm.

$$\Phi'\{O_3\} \equiv (-\Phi\{O_3\} - \gamma - 2)/\beta$$

$$k_9' \equiv 2\left\{-1 + \left(\frac{1 + \alpha_1\alpha_2}{1 - \alpha_1\alpha_2}\right)f'\right]k_{9a} + \left[2 - f + \left(\frac{1 + \alpha_1\alpha_2}{1 - \alpha_1\alpha_2}\right)f\right]k_{9b}\right\}$$

$$\alpha_1 \equiv k_{14}[O_3]/(k_{14}[O_3] + k_{15}[CH_4])$$

$$\alpha_2 \equiv k_{13}[O_3]/(k_{13}[O_3] + k_{12}[O_2][M])$$

$$f \equiv k_{9b}'/(k_{9b}' + k_{9b}''[M])$$

$$f' \equiv k_{9a}'/(k_{9a}' + k_{9a}''[M])$$

$$\gamma \equiv (k_4[O_3] - k_3[O_2][M])/(k_4[O_3] + k_3[O_2][M] + k_5[CH_4])$$

$$\beta \equiv k_{6a}/k_6 + k_5[CH_4]/(k_4[O_3] + k_3[O_2][M] + k_5[CH_4])$$

In computing β, we have used $k_{6a}/k_6 = 1.0$ since this gives a more consistent fit among the data than using $k_{6a}/k_6 = 0.9$. A plot of $\Phi'\{O_3\}^{-1}$ *vs.* $[O_2]/[O_3]$ will be linear if f' and k_9' are insensitive to changes in reaction conditions. With this hope in mind, $\Phi'\{O_3\}$ was computed from the quantum yields in Table I and the rate coefficients in Table III. $\Phi'\{O_3\}$ is approximately equal to $-\Phi\{O_3\} - 1$ under all conditions since $\gamma \sim -1$ and $\beta \sim 1$; thus $\Phi'\{O_3\}$ is not very sensitive to the values of the rate coefficients used in computing γ and β.

The plot of $\Phi'\{O_3\}^{-1}$ *vs.* $[O_2]/[O_3]$ is shown in Figure 1. It is apparent that the points for which $[CH_4]$ = 600–760 Torr lie reasonably on a straight line with an intercept of 0.0 ± 0.1 at both temperatures. However, the points for which $[CH_4]$ = 135–175 Torr lie well below the line. Thus k_9' is larger at lower [M]. This effect could be due to variations in f, f', α_1, or α_2. The variations in α_1 and α_2 can be computed directly from the known rate coefficients. With the computed values for α_1 and α_2 the only way to account for the discrepancy is if $f = f' = 1$ (see Appendix).

From the intercept of Figure 1, we find $(1 - f')k_{9a}/k_9' = 0.0 \pm 0.2$. Thus the production of CH_3O is not important. This conclusion is further supported by examining the data in the absence of O_2. Here the quantum yields can approach 100. Since $(1 - f')k_{9a}/k_9$ represents the fraction of time that reaction 9 leads to CH_3O production, and since reaction 17 leads to termination, an upper limit of $(1 - f')k_{9a}/k_9 < 0.1$ can be set.

With the assumption that $f = f' = 1.0$, we evaluate the term

$$\Phi''\{O_3\} \equiv \Phi'\{O_3\}(1 - \alpha_1\alpha_2)$$

Equation II can be rearranged to

$$\Phi''\{O_3\} = 4(k_{9a} + k_{9b})[O_3]/k_{10}[O_2] \qquad \text{(III)}$$

Figure 2 shows plots of $\Phi''\{O_3\}$ *vs.* $[O_2]/[O_3]$ at both temperatures. There is some scatter in the data. At −52°, the intercept is zero. However for the data at 25°, the intercept is 0.1 ± 0.1. (We have ignored the inaccurate values at $[O_3]/[O_2] < 0.02$ in drawing the best line.) If the nonzero value of the intercept is real, it indicates that all the assumptions were not exactly fulfilled. However they do not introduce significant errors. The slopes of the two lines give $4(k_{9a} + k_{9b})/k_{10} = 8.7$ and 4.7, respectively, at 25 and −52°. From these two points the Arrhenius expression becomes

$$4(k_{9a} + k_{9b})/k_{10} \simeq 50 \exp(-1050/RT)$$

where the activation energy is given in kcal/mole. Since $k_{10} = 4.3 \times 10^{-13}$ cm³/sec at the high pressure limit with presumably no activation energy

$$k_{9a} + k_{9b} \simeq 5.4 \times 10^{-12} \exp(-1050/RT) \text{ cm}^3/\text{sec}$$

The large preexponential factor favors a linear over a five-membered ring transition state.

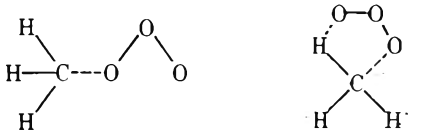

Reaction 9b must proceed through a cyclic transition state. Therefore reaction 9a probably is the major, if not exclusive, pathway by which reaction 9 proceeds. If this is so, then f' must be 1.0 to explain the zero intercept in Figure 1.

Acknowledgment. This work was supported by the Atmospheric Sciences Section of the National Science Foundation through Grant No. GA 12385, by the National Aeronautics Space Administration through Grant No. NGL-009-003, and by the Department of Transportation Climatic Impact Assessment Program through Contract No. DOT-OS-40051 for which we are grateful.

Appendix

We now justify the assertion in the text that $f = f' = 1$. To simplify the analysis we assume that $2 - f = 1.0$ in the expression for k_9', and then test for consistency. Since $(1 - f')k_{9a}/k_9$ was shown to be $\simeq 0$, then eq I can be rearranged to

$$\bar{f} = \frac{(\Phi'\{O_3\}k_{10}[O_2]/2k_9[O_3] - 1)}{(1 + \alpha_1\alpha_2)/(1 - \alpha_1\alpha_2)} \qquad \text{(IV)}$$

where

$$\bar{f} \equiv (f'k_{9a} + fk_{9b})/k_9$$

The values of $\bar{f}$ were calculated where the calculations are meaningful, *i.e.*, for the last 15 entries at 25° in Table I. The average values and mean deviations are 1.15 ± 0.34 for

the five points at $[CH_4]$ = 135–175 Torr and 1.11 ± 0.19 for the ten points at $[CH_4]$ = 650–760 Torr. The fact that the average values slightly exceed 1.0 can be accounted for by a slight change in the ratio k_{10}/k_9. More meaningful is the fact that at both CH_4 pressures, $\bar{f}$ is the same, a result which can only hold if $\bar{f} = 1.0$.

It is interesting to estimate how much $\bar{f}$ could be below 1.0 and still be consistent with the experimental data. Considering the mean deviations, the largest reasonable spread in $\bar{f}$ at the two CH_4 pressures might give an $\bar{f}$ 30% higher at the lower pressure. To be consistent with the definition for $\bar{f}$, the two values for $\bar{f}$ would be 0.915 and 0.705, respectively, at the lower and higher CH_4 pressures.

References and Notes

(1) R. Simonaitis and J. Heicklen, *J. Phys. Chem.*, **78**, 653 (1974).
(2) E. Lissi and J. Heicklen, *J. Photochem.*, **1**, 39 (1972).
(3) D. Garvin, Ed., National Bureau of Standards Interim Report No. NBSIR-203, 1973, "Chemical Kinetics Data Survey IV. Preliminary Tables of Chemical Data for Modelling of the Stratosphere."
(4) S. D. Worley, R. N. Coltharp, and A. E. Potter, Jr., *J. Phys. Chem.*, **76**, 1511 (1972).
(5) D. A. Parkes, D. M. Paul, R. P. Quinn, and R. C. Robison, *Chem. Phys. Lett.*, **23**, 425 (1973).
(6) J. Weaver, R. Shortridge, J. Meagher, and J. Heicklen, Center for Air Environment Studies Report No. 363-74, Penn State University, University Park, Pa., 1974.
(7) C. L. Lin and W. B. De More, *J. Phys. Chem.*, **77**, 863 (1973).
(8) R. I. Greenberg and J. Heicklen, *Int. J. Chem. Kinet.*, **4**, 417 (1973).
(9) J. Heicklen, *Advan. Chem. Ser.*, **No. 76**, Part II, 23 (1968).

Angular Distributions of Molecular Species Effusing from Near-Ideal Orifices

Robert T. Grimley,*[1] L. C. Wagner, and Peter M. Castle

Department of Chemistry, Purdue University, West Lafayette, Indiana 47907

(*Received July 10, 1974*)

A mass spectrometric investigation has been made of the angular number distributions for the NaCl, KCl, CsCl, and Sm vapor systems effusing from a near-ideal cylindrical orifice, L/R = 0.127. The experimental angular distribution curves and transmission probability of Sm are in excellent agreement with the Clausing values. The angular distribution curves and transmission probabilities for the monomeric alkali halide species show positive deviations from the Clausing values whereas the dimeric vapor species exhibit negative deviations. For near-ideal orifices and the monomer–dimer vapor system, the Voronin approximation equations which were based in part on the assumption of monomer–dimer equilibrium at the orifice wall provide a substantially improved representation of the angular distribution curves over the Clausing theory.

Introduction

The Knudsen[2,3] effusion method has been used extensively for the determination of the vaporization thermodynamics of slightly volatile substances. The method involves the measurement of the rate of mass loss of vapor from an equilibrium enclosure through an orifice. An orifice the length of which is vanishingly small is termed an ideal orifice. For the ideal orifice the kinetic theory[4] predicts that the total number of particles which flow through the orifice per unit area per unit time dN/dt is given by

$$dN/dt = n\bar{v}/4 \tag{1}$$

where n is the number of particles per unit volume and $\bar{v}$ is the average molecular speed. Similarly the number of particles $(dN/dt)_\theta$ which pass through an orifice of unit area per unit time at an angle θ from the normal to the orifice plane and which are contained in the solid angle $d\omega$ is given by the equation

$$(dN/dt)_\theta = (n\bar{v}/4\pi) \cos\theta \, d\omega \tag{2}$$

For an ideal orifice, therefore, the ratio of the number of molecules which pass through the orifice at angle θ to those which pass along the normal to the orifice is $\cos\theta$, the so-called cosine law.

For finite or real orifices it is necessary to correct for the effect of nonideality, and it has become standard practice to correct for the nonideality by use of the Clausing transmission factors. The accuracy of the determination of the absolute pressures and related thermodynamic quantities is, therefore, dependent in part on the extent to which flow through an orifice of finite length is described by the Clausing model.[5–7] Clausing has shown that the number of particles which pass through a cylindrical orifice of unit area per unit time at an angle θ from the normal to the orifice plane and which are contained in the solid angle $d\omega$ is given by the equation

$$(dN/dt)_\theta = (n\bar{v}/4\pi)T(\theta, L/R) \cos\theta \, d\omega \tag{3}$$

The functional form of T is dependent on the relationship between $\tan\theta$ and the orifice geometry L/R. At those values of θ for which $\tan\theta < 2R/L$, the molecular flux arises from two sources. There is a contribution from molecules which flow directly through the channel without collision with the walls and a contribution from those molecules which have first undergone wall collisions. For this case

$$p = (L/2R) \tan\theta < 1$$

and

$$T = 1 - (2/\pi)(1 - \alpha)[\arcsin p + p(1 - p^2)^{1/2}] + [4/(3\pi p)](1 - 2\alpha)[1 - (1 - p^2)^{3/2}] \quad (4)$$

where

$$\alpha = [(L^2 + 4R^2)^{1/2} - L]/[2R + 4R^2/(L^2 + 4R^2)^{1/2}]$$

For the condition $p = (L/2R) \tan \theta \geq 1$, only molecules which have struck the walls contribute to the molecular flux. Under these conditions

$$T = \alpha + [4/(3\pi p)](1 - 2\alpha) \quad (5)$$

Integration of eq 3 over the polar and azimuthal angles yields the equation for the total number of particles which flow through the orifice per unit area per unit time

$$dN/dt = Wn\bar{v}/4 \quad (6)$$

where W represents the fraction of particles entering the orifice which pass through. W is called the transmission factor or transmission probability.

The Clausing theory may be tested by direct experimental measurement of the total flow through an orifice of known geometry or by measurement of the angular distribution (AD) of the effusing species. Tests of eq 1 have been made by Knudsen[2,3] and by Carlson, Gilles, and Thorn,[8] who determined the total flow through thin orifices. The latter workers corrected for the orifice nonideality by use of the Clausing factor and found agreement, within a few per cent, between the theoretical and experimental values. Angular distribution measurements of the effusate passing through near-ideal orifices have been reported by Knudsen,[9] Knauer and Stern,[10] Johnson,[11] Mayer,[12] Günther,[13] Naumov,[14] Cook and Richley,[15] Stickney, *et al.*,[16] and Wang and Wahlbeck.[17] Some workers were unable to determine the orifice geometry; and in the earlier work, measurement accuracy was a limiting factor. Except for the results of Wang and Wahlbeck, therefore, no attempt was made to correct for the nonideality of the orifice. In addition, the detection techniques used did not permit the determination of the AD curves of individual vapor species. In each of the studies, agreement with the cosine law was confirmed within the limits of experimental accuracy. The first measurements of the species dependence of the AD curves for a near-ideal orifice were made by Grimley and LaRue.[18]

Two basic assumptions are made in the determination of vapor pressures by the Knudsen cell technique. First the cell is assumed to be at some equilibrium pressure which is undisturbed by the loss of vapor through the orifice. Numerous theoretical papers have been written on this subject and are not properly a part of this discussion. And, as previously mentioned, it is assumed that the mass flow through the orifice may be corrected for any nonideality in the orifice. It is the latter assumption which concerns us in this paper. Accordingly we will consider the accuracy with which the Clausing model describes the angular distribution and transmission probabilities of simple and complex vapor systems effusing through near-ideal orifices.

Experimental Section

A 60° sector field, 30.5-cm radius of curvature, first-order direction-focusing mass spectrometer was used to make the angular distribution measurements. Background pressures of 10^{-8} Torr or better were maintained in the ion source and analyzer sections of the mass spectrometer. At the maximum operating temperatures of this study, pressures of approximately 5×10^{-7} Torr were maintained in the high-temperature chamber. A Knudsen cell capable of angular rotation about an axis which passes through an orifice diameter in the plane of the orifice exit was used as the molecular beam source.[19] The Knudsen cell is precisely located on a movable carriage. Horizontal shafts are attached to the carriage along the axis which passes through the plane of the orifice exit, and a vacuum feedthrough is used to rotate the carriage assembly. The angle of rotation was measured by means of a dial indicator located on the atmospheric side of the rotary feedthrough. The dial indicator was calibrated prior to this study by a procedure which has previously been described.[19,20] In order to ensure the continued accuracy of the data, periodic recalibration checks were made. These checks have shown insignificant variations in the calibration over periods of many months, and the uncertainty in the angular measurements was ±0.1°. A movable, beam-defining slit located between the Knudsen cell and the ion source of the mass spectrometer was used to distinguish between the neutral species which effused directly from the Knudsen cell and scattered or reevaporated species.

Radiant heating was utilized throughout the course of the experiments. Thermal energy was supplied by a bifilarly wound platinum–10% rhodium helical filament surrounding the cell. The dc current to the filament was supplied by a Hyperion Si-10-15 power supply. The temperatures were monitored by means of a calibrated chromel–alumel thermocouple peened into the base of the Knudsen cell. With continuous monitoring of the temperature and manual adjustment of the power level, it was possible to maintain the cell at a constant temperature of ±0.1°.

The Knudsen cell body was 15.87 mm long and 17.85 mm in diameter and was made of tantalum. The cell cavity was 14.7 mm long and 12.5 mm in diameter. Tantalum was used in order to minimize the possibility of reaction with samarium. The lid also of tantalum had a flat outer face and a tapered inner face. The diameter of the orifice as determined microscopically was 1.004 ± 0.002 mm. The length of the orifice was measured by means of a precision height gauge and gauge blocks and was found to be 0.0635 ± 0.0025 mm. The length to radius ratio L/R of the orifice was 0.127 ± 0.005. The cell and lid were carefully cleaned between runs of different substances, and a specially designed jig was used to align the orifice to within the ±0.02 mm in both the xy plane and the z direction thus ensuring mechanical reproducibility between runs.

The distance of the beam-defining detector slit from the effusion orifice is 55.70 mm. The radius vector from the orifice to the center of the detector slit moves in a plane which is perpendicular to the long axis of the slit. The included angle of the detector width is 0.28°, and the half-angle of the length is 6.27°, the long axis of the slit being symmetrically positioned relative to the beam source. The effect of detector geometry on angular distribution measurements has been treated by Grimley and Wagner.[21] In the case of the near-ideal orifice the detector effect is insignificant, and this will be discussed subsequently.

Intensity data were collected using a 16-stage electron multiplier as the detector and a 640 Keithley vibrating capacitor electrometer in series with a 399 Keithley isolating amplifier. The output from the amplifier was simultaneously fed to a strip chart recorder and a Hewlett-Packard Model 2212A voltage to frequency converter whose output was measured with an HP 5202L scaler–timer. The V-

TABLE I: Normalized Samarium Angular Distribution Data for an $L/R = 0.127$ Orifice at 625, 650, and 675°

θ, deg	625°	650°	675°	Av over all temp
0.0	1.000	1.000	1.000	1.000
4.7	0.996	0.996	0.998	0.997
9.4	0.987	0.986	0.987	0.987
14.2	0.968	0.969	0.967	0.968
18.9	0.942	0.942	0.940	0.941
23.8	0.909	0.910	0.906	0.908
28.7	0.869	0.867	0.864	0.866
33.6	0.816	0.817	0.816	0.816
38.5	0.764	0.763	0.762	0.763
43.4	0.703	0.701	0.700	0.701
48.3	0.638	0.637	0.636	0.637
53.2	0.565	0.566	0.564	0.565
58.2	0.495	0.494	0.492	0.494
63.3	0.417	0.415	0.415	0.416
68.3	0.335	0.335	0.335	0.335
73.4	0.253	0.254	0.253	0.253

to-F converter and scaler–timer functioned as a dc integrator with a variable-time base. By varying the integration times it is possible to maintain the same approximate average deviation for a wide range of peak intensities and signal to noise ratios.

Each of the samples was of cylindrical form approximately 12 mm in diameter by 6 mm in length. The NaCl, KCl, and CsCl samples were optical grade crystals from Harshaw. The NaCl and KCl samples were single crystals cleaved along the 100 planes with the 100 faces exposed to the cell cavity; the CsCl sample was polycrystalline. The samarium was machined from a slug of 99.9% pure samarium obtained from Research Chemicals (Nuclear Corp. of America). In order to minimize surface reactions with the atmosphere, the samarium was stored under argon and the vaporizing surface was machined immediately before the sample was placed in the mass spectrometer.

Results

The information required to characterize each angular distribution curve includes the cell θ, the molecular beam intensity $I(\theta)$ as a function of angle, and the temperature of the Knudsen cell. The beam intensities were normalized to the beam intensity at 0° by taking the ratio of the intensity at each angle θ to the intensity at 0°. The relative intensities $I(\theta)/I(0)$ were then plotted as a function of the corrected angle θ. For each of the materials considered, angular distributions of the effusate were obtained at two or more temperatures each separated by 20–25°. The results were obtained for samarium at 625, 650, and 675°; for NaCl at 645 and 665°; for KCl at 585 and 605°; and for CsCl at 525 and 545°. All data were taken at an electron bombardment energy of 18 eV. At each temperature eight separate determinations of the angular distribution were made over a period of 2 or more days. Averages of these eight distributions were computed as well as the deviations of each distribution from the average value. For individual points on each of the experimentally determined curves the largest deviation was of the order of 1%, but the average deviation was 0.5% or less.

The data for monatomic samarium vapor at 625, 650, and 675° are given in Table I. The remaining data for the

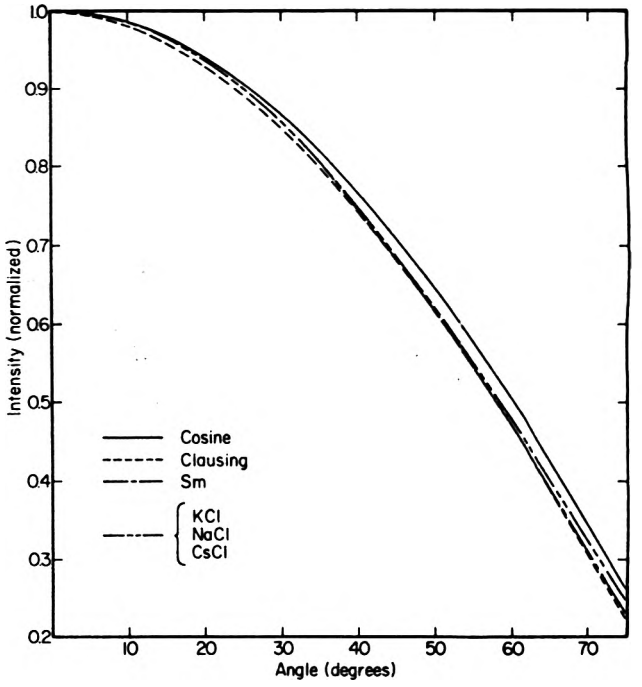

Figure 1. A comparison of the angular distribution curves for an ideal orifice and the monomeric species NaCl, KCl, CsCl, and Sm for an orifice of $L/R = 0.127$ geometry. Note that the Sm curve is identical with that of the halides at the lower angles. At higher angles the Sm and the modified Clausing curves are identical.

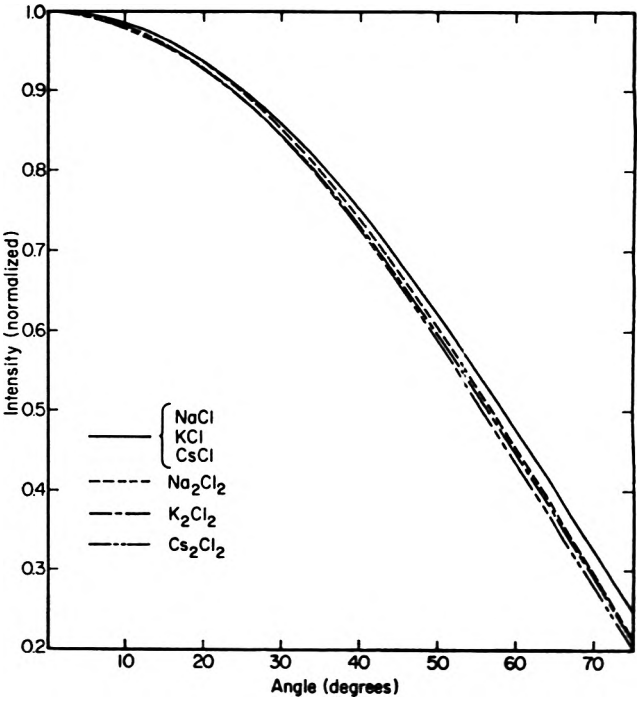

Figure 2. A comparison of the angular distribution curves of the monomeric and dimeric species of the NaCl, KCl, and CsCl systems.

NaCl, KCl, and CsCl systems may be obtained from this journal,[22] and these results are also graphically illustrated in Figures 1 and 2.

Discussion

The theoretical angular distribution data calculated on the basis of the Clausing model represent the ratios of the

TABLE II: Comparison of the Clausing, Clausing-Modified for the Slit Detector, and Normalized Samarium Angular Distribution Data for an $L/R = 0.127$ Orifice

θ, deg	Clausing	Clausing modified	Sm av over all temp
0.0	1.000	1.000	1.000
4.7	0.993	0.995	0.997
9.4	0.980	0.981	0.987
14.2	0.959	0.961	0.968
18.9	0.933	0.935	0.941
23.8	0.899	0.901	0.908
28.7	0.858	0.860	0.866
33.6	0.811	0.813	0.816
38.5	0.758	0.759	0.763
43.4	0.699	0.701	0.701
48.3	0.635	0.637	0.637
53.2	0.566	0.567	0.565
58.2	0.493	0.494	0.494
63.3	0.414	0.415	0.416
68.3	0.332	0.333	0.335
73.4	0.248	0.248	0.253

flux at each angle θ to the flux at the orifice normal ($\theta = 0°$). In order to compare precisely the theoretical distribution with experiment, the experimental measurements must be made with a point detector of infinitesimal solid angle. As the magnitude of the solid angle of the detector increases, a distortion will result in the experimental angular distribution curve. While a point detector is best in principle to maximize resolution, detection of the less intense species demands the use of a detector of finite geometry. Thus the slit detector geometry previously described was used in this study.

A comparison of theory and experiment requires, however, that the effect of the slit geometry on the observed distribution curve be determined. The cases of the arc and planar slit have been treated by Grimley and Wagner.[27] By dividing the slit into a large number of segments and assuming a Clausing distribution, the flux through a planar slit was shown to be

$$F_\theta = (\cos\theta)\left[(1/2)f(\theta) + \sum_{i=1}^{n} f(\theta')\cos^2\theta''_i\right] \quad (7)$$

where, using the Clausing notation

$$f(\theta') = (\nu/\pi)T(\theta'_i, L/R)\mathrm{d}\omega_i$$

The angle θ is the polar angle to the center of the slit, θ' is the polar angle to the center of slit segment i, and θ''_i is the angle from the center of the slit to the center of slit segment i. The minor effect of the slit detector for an orifice of $L/R = 0.127$ geometry is seen in Table II. Column 2 shown the theoretical values of $I(\theta)/I(0)$ as determined from the Clausing equations while column 3 represents the $I(\theta)/I(0)$ values which would be observed for the Clausing distribution as seen by a slit detector of the geometry used in this work. The deviation between the exact and the modified Clausing distribution is less than 0.3% at all angles. For an $L/R = 0.127$ orifice geometry the distortion imparted to the experimental distribution curves by the slit detector is minimal and may be ignored.

The data for samarium (Table I) at 625, 650, and 675° reveal no discernible temperature effect on the angular distribution as a function of temperature. The data averaged over all temperatures are shown in column 5 of Table I. The deviation between the all-temperature average and the measurement at a specific temperature is well within the average deviation of the measurements. In Table II, column 3, the slit-modified Clausing distribution is shown, and this may be compared with the all-temperature average experimental distribution of samarium. Except for the 73.4° value, all data points beyond the 28.7° measurement are in excellent agreement with the slit-modified Clausing distribution, in fact, considerably better than our claimed precision. At the lower angles a slight positive deviation of the experimental data are apparent. Additional measurements[23] with longer orifices lead us to believe that the effect is real, although in the case of the $L/R = 0.127$ orifice the deviation is close to the measurement precision.

For longer orifices, Grimley, Muenow, and LaRue[20] have demonstrated that a substantial difference in the angular distribution curves exists between KCl and K_2Cl_2 and also between these species and the Clausing curves. The AD curves for the NaCl, KCl, and CsCl monomers are nearly identical for an $L/R = 0.127$ orifice geometry, but they differ from the Clausing distribution as is shown in Figure 1 and the supplementary tables. The dimers, on the other hand, show differences in the AD curves among the individual species; and as is observed for longer orifices, the AD curves of the dimers are more focused than those of the monomers. These differences are clearly visible in Figure 2.

As previously mentioned, it is common practice to correct Knudsen cell vaporization measurements for orifice nonideality by the use of the theoretically calculated Clausing transmission factors. Since the transmission factors are obtained by integration of the angular distribution curves, errors in the calculated vapor pressures will result if the experimental AD curve of a vapor species deviates from the Clausing distribution. It is important, therefore, that the magnitude of the error associated with the deviations in the AD curves be determined.

The Clausing transmission factor W is obtained from the equation

$$W_c = \int_0^{\pi/2} 2T(\theta)\cos\theta\sin\theta\,\mathrm{d}\theta \quad (8)$$

Correspondingly the experimentally determined transmission factor is obtained from the equation

$$W_e = \int_0^{\pi/2} 2[I(\theta)/I(0)]\sin\theta\,\mathrm{d}\theta \quad (9)$$

This manner of calculating W_e implies that the beam flux at $\theta = 0°$ is the kinetic theory value. Wang and Wahlbeck,[17] among others, have found that, in the transition region and for near-ideal orifices, the probability of effusion increases at low angles of θ. This effect is manifested in the form of increased focusing in the normalized distribution curves. Since the data points were taken at discrete angular intervals, it was necessary to find a functional relationship which accurately describes the angular dependence of the experimental data. An eighth-degree polynomial was found to be the most satisfactory of a number of trial functions. A least-squares fit of the polynomial was obtained by use of the Purdue University Computer Center program SQUARS. This program also gave the maximum and average error for the least-squares fit. The maximum error of the fit is typically on the order of the experimental error, and the aver-

TABLE III: Experimental W_e and Theoretical W_T Transmission Probabilities for the NaCl, KCl, CsCl, and Sm Systems[a]

	Monomer			Dimer		
	W_e			W_e		
	Uncor	Cor	W_T	Uncor	Cor	W_T
NaCl	0.969	0.960	0.949	0.936	0.928	0.920
KCl	0.967	0.958	0.946	0.925	0.917	0.916
CsCl	0.960	0.951		0.910	0.902	
Sm	0.954	0.945	0.940			

[a] The experimental probabilities W_e represent the average value of the integrals determined from the data at all temperatures and an $L/R = 0.127$ orifice geometry.

age error is considerably lower in magnitude. For the experimental data one obtains

$$[I(\theta)/I(0)](\sin\theta) = \sum_{i=0}^{8} a_i\theta^i \qquad (10)$$

The function W_e may then be obtained by direct analytic integration of the polynomial.

In order to check the magnitude of the errors which might be introduced by the use of the integration technique in the evaluation of the experimental W_e factors, the W factor for the Clausing theoretical distribution of an $L/R = 0.127$ orifice was evaluated assuming a number of variations in the measurement conditions. The value of W calculated using 91 points (1° intervals) generated by the Clausing equations is 0.9405 while W calculated using 19 points (5° intervals) is 0.9402, a negligible difference. Integration of the 91-point distribution modified by the slit detector yields a W value of 0.9424. Thus the observation of this distribution by a slit rather than a point detector results in a 0.2% error. Due to experimental limitations we are unable to make measurements at 80 and 85°. It was therefore necessary to fit the polynomial to the experimental data with 17 rather than 19 points. To obtain an estimate of the error which results from the missing data, the Clausing distribution was fit and W was evaluated using the data at the 17 angles used in the experimental measurements. The W factors were evaluated for both the point and slit detectors and were found to be 0.9471 and 0.9490, respectively. The use of the 17-point fit then results in an additional 0.7% error. If the experimental distribution is close to the Clausing distribution, one may assume the errors to be of the same magnitude and direction for the Clausing and experimental curves. Accordingly, the directly determined experimental factors W_e will be 0.9% higher than the precise values of the transmission probabilities.

The experimental transmission probabilities W_e are shown in Table III for the NaCl, KCl, CsCl, and Sm vapor systems effusing from a near-ideal orifice, $L/R = 0.127$. The first column for both the monomer and the dimer contains experimental values of W_e uncorrected for detector or data-fitting errors. The second column shows the appropriately corrected experimental values. For the monomeric species the deviations from the Clausing W factors range from +2.1% for NaCl to +0.5% for Sm. The W_e value for Sm, within the precision of our measurements for the near-ideal orifice, is equal to the theoretical W obtained from the Clausing model. For the dimeric species the deviations range from −1.4% from the Clausing W value for Na_2Cl_2 to −4.1% for Cs_2Cl_2.

The work of Wang and Wahlbeck[17] (WW) presents an interesting comparison with our results for CsCl. Using a double-oven Knudsen cell and a hot-wire detector, Wang, *et al.*, determined the angular distribution of CsCl. Their results for a near-ideal orifice agreed with the AD predicted by the Clausing theory to within an estimated uncertainty of 2% in $I(\theta)/I(0)$. Unfortunately a direct comparison between the two studies cannot be made for the following reasons. (1) Under the conditions of the double-oven measurements, the ratio of monomer to dimer is increased over the vapor:solid equilibrium ratio. (2) The vapor composition of either measurement as well as the relative efficiencies of surface and electron bombardment ionization are not precisely known. (3) The orifice geometries of the two experiments are not the same. Nevertheless, there are some interesting observations to be made. Because of the failure of the hot-wire detector to distinguish individual species, the AD curve obtained by WW will be intermediate between the AD curves of CsCl and Cs_2Cl_2 with position of the curve depending on the relative monomer–dimer contributions. The CsCl vapor consists of a monomer to dimer ratio of approximately 15:1 in the temperature range of our measurements.[24] Since the vapor will be predominantly monomer, the composite AD curve observed by Wang, *et al.*, will be close to that of the monomer. The deviation of W_e from the Clausing W for CsCl monomer is only +1.2%, a deviation well within the range of measurement precision estimated by Wang, *et al.* Furthermore, since the monomer and dimer AD curve deviations are in opposite directions from the Clausing distribution, contributions of both species to a composite AD curve tend to self-compensate in the direction of the Clausing curve.

Ward, *et al.*,[25,26] have examined a number of metallic systems effusing through knifed-edged orifices and have observed anomalous behavior in the form of AD discontinuities. The experimental behavior observed by these authors was explained in terms of loss probabilities on surfaces relative to the cell and sample geometry under consideration. Effects of this type were not observed under the conditions of our measurements.

Finally, it is worthwhile to examine the modification of the Clausing theory proposed by Voronin[27] in which the effects on the angular distribution of association–dissociation equilibria on the orifice walls are considered. Both exact and approximate equations have been derived. For reasons of simplicity and utility, only the approximate method will be considered here. Both the exact and approximate treatments make the initial assumption that a system consisting of a single monomeric vapor species obeys the Clausing theory. If a monomer–dimer equilibrium is assumed to occur on the walls, it may be shown from the law of conservation of mass that

$$D(\theta) = D_1(\theta) + 2D_2(\theta) \qquad (11)$$

where $D(\theta)$ is the flux at angle θ according to the Clausing theory, $D_1(\theta)$ is the flux of the monomer, and $D_2(\theta)$ is the flux of the dimer. If the exact functions giving the wall bombardment fluxes of the monomer and dimer as a function of position on the wall are replaced by the average bombardment fluxes, equations which describe the approximate angular distributions of a monomer–dimer vapor system may be obtained. The approximate Voronin equations

with appropriate substitutions and simplifications are as follows. For $p = (L/2R)\tan\theta < 1$

$$\phi(\theta) = \frac{D_2(\theta)}{D_1(\theta)} = \phi_0 \frac{\pi + 2[p(1-p^2)^{1/2} + \arcsin p][(\bar{\nu}_2/\nu_2^\circ) - 1]}{\pi + 2[p(1-p^2)^{1/2} + \arcsin p][(\bar{\nu}_1/\nu_1^\circ) - 1]} \quad (12)$$

where

$$\bar{\nu}_2/\nu_2^\circ = (\bar{\nu}_1/\nu_1^\circ)^2 \quad (13)$$

and

$$\bar{\nu}_1/\nu_1^\circ = (1/4\phi_0)\{[1 + 8(\phi_0 + 2\phi_0^2)B(\theta)]^{1/2} - 1\} \quad (14)$$

$$B(\theta) = \frac{\pi[T-1] + 2[p(1-p^2)^{1/2} + \arcsin p]}{2[p(1-p^2)^{1/2} + \arcsin p]} \quad (15)$$

and

$$\phi_0 = \nu_2^\circ/\nu_1^\circ \quad (16)$$

The terms ν_2° and ν_1° are respectively the number of dimers and monomers which enter the orifice per unit area per unit time from the Knudsen cell. The T term is that shown in eq 4. For $p \geq 1$

$$\phi(\theta) = (1/4)\{[1 + 8(\phi_0 + 2\phi_0^2)T]^{1/2} - 1\} \quad (17)$$

where T is as shown in eq 5. The angular distribution data for the monomer $I_1(\theta)/I_1(0)$ and the dimer $I_2(\theta)/I_2(0)$ are obtained from

$$I_1(\theta)/I_1(0) = D_1(\theta)/D_1(0) = T(\cos\theta)[1 + 2\phi_0]/[1 + 2\phi(\theta)] \quad (18)$$

$$I_2(\theta)/I_2(0) = D_2(\theta)/D_2(0) = [\phi(\theta)/\phi_0][D_1(\theta)/D_1(0)] \quad (19)$$

The only experimentally determined parameters required are the orifice geometry L/R and ϕ_0.

In order to calculate the theoretical AD curves, an accurate knowledge of ϕ_0 is seemingly required. For near-ideal orifices, this is fortunately not the case. If a near-ideal orifice is used, an approximate value of ϕ_0 may be obtained from the equilibrium vapor pressures of the monomer and dimer without correction for the orifice nonideality. The approximate ϕ_0 may then be used to calculate theoretical AD curves for the monomer and dimer. Substitution of the AD curves into 9 and 10 will yield approximate values of the transmission probabilities. One may then iterate further to determine more accurate values of the equilibrium vapor pressures and consequently ϕ_0.

In addition to the experimental transmission probabilities W_e, Table III also contains the theoretical transmission probabilities W_T. The third column gives the theoretical probabilities as calculated by the Voronin approximation equations for NaCl and KCl and by the Clausing equations for Sm. The vapor pressure data of Grimley and Joyce[28] for KCl(g) and K_2Cl_2(g) were used to calculate the Voronin transmission probabilities for the $L/R = 0.127$ orifice geometry at 585, 595, and 605°. The theoretical values rounded to three significant figures were found to be temperature independent. These findings are in accord with our experimental observations that, for near-ideal orifices, the AD curves and transmission probabilities are temperature independent over the range of the study. It also means that the calculated W_T values are relatively insensitive to the temperature variation in ϕ_0. The data used to calculate the probabilities for NaCl were obtained from the JANAF tables.[29] The vapor pressure data for the CsCl system obtained from the JANAF tables are substantially different from mass spectrometric intensity data. Because of this discrepancy, the W_T values of the CsCl system were not calculated.

For the worst case the disagreement between the experimental and theoretical transmission probabilities is 1.3%. In addition to the errors associated with the experimental measurements, there are three potential sources of error associated with the theoretical calculations. (1) The assumptions of the model do not adequately describe the behavior of the real systems. (2) The Voronin equations used are the approximations relations rather than the exact equations. (3) A substantial uncertainty exists in our knowledge of the relative ionization cross sections and, therefore, the vapor pressures.

It should be noted that, in addition to the work of Voronin, modifications to the Clausing theory have been proposed by Winterbottom,[30] Liu and Wahlbeck,[31] and Gottwald.[32,33] The resulting equations have been utilized in the treatment of the KCl data for nonideal orifices reported by Grimley, *et al.* However, any attempt to test the validity of a particular model or approach requires, at a minimum, an accurate knowledge of the vapor system with regard to both composition and vapor pressure. This information is presently lacking for complex vapor systems. In addition, the alternate models require either (1) assumptions regarding the magnitudes of the parameters used in the equations, (2) empirical fitting procedures, or (3) a substantial computational effort. And the alternate methods appear to offer no advantage in the accuracy of the calculations. Since angular distribution data are generally lacking, the Voronin approximation equations are recommended for use over the Clausing equations as a means of determining orifice correction factors when the measurements involve near-ideal orifices and monomer–dimer vapor systems.

Supplementary Material Available. Tables IV–VI, showing normalized angular distribution data $I(\theta)/I(0)$ for the NaCl, KCl, and CsCl systems, will appear following these pages in the microfilm edition of this volume of the journal. Photocopies of the supplementary material from this paper only or microfiche (105 × 148 mm, 14× reduction, negatives) containing all of the supplementary material for the papers in this issue may be obtained from the Journals Department, American Chemical Society, 1155 16th Street, N.W., Washington, D.C. 20036. Remit check or money order for $3.00 for photocopy or $2.00 for microfiche, referring to code number JPC-75-302.

References and Notes

(1) To whom correspondence should be addressed.
(2) M. Knudsen, *Ann. Phys.* (*Leipzig*), **28**, 75 (1909).
(3) M. Knudsen, *Ann. Phys.* (*Leipzig*), **28**, 999 (1909).
(4) R. D. Present, "Kinetic Theory of Gases," McGraw-Hill, New York, N.Y., 1958.
(5) P. Clausing, *Physica* (*The Hague*), **9**, 65 (1929).
(6) P. Clausing, *Z. Phys.*, **66**, 471 (1930).
(7) P. Clausing, *Ann. Phys.* (*Leipzig*), **12**, 961 (1932).
(8) K. D. Carlson, P. W. Gilles, and R. J. Thorn, *J. Chem. Phys.*, **38**, 2725 (1973).
(9) M. Knudsen, *Ann. Phys.* (*Leipzig*), **48**, 1113 (1916).
(10) F. Knauer and O. Stern, *Z. Phys.*, **39**, 764 (1926).
(11) T. H. Johnson, *Phys. Rev.*, **31**, 103 (1928).
(12) H. Mayer, *Z. Phys.*, **58**, 373 (1929).
(13) K. G. Günther, *Z. Angew. Phys.*, **9**, 550 (1957).
(14) A. I. Naumov, *Sov. Phys.Tech. Phys.*, **8**, 88 (1963).
(15) H. Cook and E. A. Richley, *NASA Tech. Note*, D-2480 (1964).
(16) R. E. Stickney, R. F. Keating, S. Yamamoto, and W. J. Hastings, *J. Vac. Sci. Technol.*, **4**, 10 (1967).

(17) K. C. Wang and P. G. Wahlbeck, *J. Chem. Phys.*, **47**, 4799 (1967).
(18) R. T. Grimley and J. LaRue, *Rarefied Gas Dyn., Proc. Int. Symp.*, **5**, 1455 (1969).
(19) D. W. Muenow and R. T. Grimley, *Rev. Sci. Instrum.* **42**, 455 (1971).
(20) R. T. Grimley, D. W. Muenow, and J. L. LaRue, *J. Chem. Phys.*, **56**, 490 (1972).
(21) R. T. Grimley and L. C. Wagner, *J. Chem. Phys.*, **58**, 402 (1973).
(22) See paragraph at end of paper regarding supplementary material.
(23) Unpublished work.
(24) T. A. Milne and H. M. Klein, *J. Chem. Phys.*, **33**, 1628 (1960).
(25) J. W. Ward, R. N. R. Mulford, and M. Kahn, *J. Chem. Phys.*, **47**, 1710 (1967).
(26) J. W. Ward, *J. Chem. Phys.*, **47**, 4030 (1967).
(27) G. F. Voronin, *Zh. Fiz. Khim.* **41**, 1663 (1967).
(28) R. T. Grimley and T. E. Joyce, *J. Phys. Chem.*, **73**, 3047 (1969).
(29) *Nat. Stand. Ref. Data Ser., Nat. Bur. Stand.*, **No. 37** (1971).
(30) W. L. Winterbottom, *J. Chem. Phys.*, **51**, 5610 (1969).
(31) M. B. Liu and P. G. Wahlbeck, *J. Chem. Phys.*, **59**, 907 (1973).
(32) B. A. Gottwald, *Vak.-Tech.*, **22**, 106 (1973).
(33) B. A. Gottwald, *Vak.-Tech.*, **22**, 141 (1973).

Photodetachment of Electrons from Alcoholate Ions in Liquid Ammonia

J. Belloni,* E. Saito, and F. Tissier

Laboratoire de Physico-chimie des Rayonnements, Associé au CNRS, 91405 Orsay, France, and DRA, SRIRMA, CEN Saclay, 91190 Gif-sur-Yvette, France *(Received July 16, 1974)*

Publication costs assisted by SRIRMA, DRA, Centre d'Etudes Nucléaires de Saclay

Solvated electrons with a long lifetime (about 1 hr) are produced by photolysis of solutions of potassium ethanolate in ammonia. The quantum yield of e_{am}^- produced by this photodetachment from the ethanolate anion is found equal to the theoretical yield of one electron formed per photon absorbed (for λ 254 or 316 nm), thus indicating the negligible importance of reverse reactions of recombination, particularly in the cage. In the presence of molecular hydrogen, $\Phi_{e_{am}^-} = 2$ for both wavelengths; the formation of the supplementary e_{am}^- being explained by the quantitative reaction of the radical EtO with H_2 under these basic conditions.

Since the early work by Ottolenghi and Linschitz,[1] it has been shown[2] that both radiolysis and photolysis of liquid ammonia solutions of amide ions in the presence of hydrogen lead to the formation of ammoniated electrons whose stability is comparable with that of electrons derived from dissolved alkali metals. Nevertheless, the quantum yields are small, of the same order of magnitude as those obtained for photodetachment processes in other solvents.[3,4] This is due either to a large amount of recombination, possibly favored by a cage effect, between the free radical and the solvated electron or to a rate of deexcitation of the excited anion much greater than that of dissociation.

A solution of potassium ethanolate in liquid ammonia showed anomalies at room temperature which led us to suspect that, even without hydrogen, we should be able to observe the formation of stable solvated electrons by photolysis of this medium and a study of the system is briefly reported here.

The solutions were prepared as described previously[2] taking all precautions concerning the purity of the reagents and the cleanliness of the silica cells, since any impurity increases the rate of disappearance of the solvated electron. The samples were given a preliminary test with a uv lamp; if a short exposure gave a blue color, persisting for more than 10 min, the sample was kept for further experiments.

The photolysis cell which served also for the spectrophotometric measurements (optical path 1.0 cm) was fitted with a side arm to contain the stock solution. The volume of the cell was calibrated before filling. The saturated ethanolate solutions were $(3.1 \pm 0.2) \times 10^{-2}$ *M* and the initial solution in the cell could be diluted with known amounts of ammonia distilled from the side arm.

For photolysis, we used a high-pressure mercury lamp (Hanau Q 600) and interference filters (λ 254 nm, $\Delta\lambda$ = 19 nm, transmission T = 0.21; λ 316 nm, $\Delta\lambda$ = 16 nm, T = 0.17; λ 365 nm, $\Delta\lambda$ = 4 nm, T = 0.34). Parker and Hatchard's ferrioxalate method[5] was used for actinometry.

Spectra were recorded between 220 and 3000 nm with a Beckman DK 1A double-beam spectrophotometer. For these, as for the kinetic measurements made at a selected wavelength, both sample and reference cells (containing also ethanolate ions) were kept in the dark to avoid errors due to stray light.

At room temperature, the ethanolate ion has an absorption spectrum which starts around 330 nm and increases gradually until it merges with the absorption band of ammonia near 230 nm. As is the case for other ions, this absorption is probably a charge-transfer to solvent band.[3,4] At 250 nm, the extinction coefficient is $2 \times 10^3\ M^{-1}\ cm^{-1}$.

The ethanolate ion does not absorb at 365 nm and it was found experimentally that no photolysis occurred at this wavelength. Our studies were therefore confined to the wavelengths 254 and 316 nm.

The spectrum of the solvated electron in liquid ammonia is a large band covering the range between 600 nm, and beyond 2000 nm with a maximum at 1750 nm. Depending on the purity of the sample, the decay of the solvated electron was more or less slow, in some cases the half-life being

* To whom correspondence should be addressed at the Laboratoire de Physico-chimie des Rayonnements, Associé au CNRS.

Scheme I

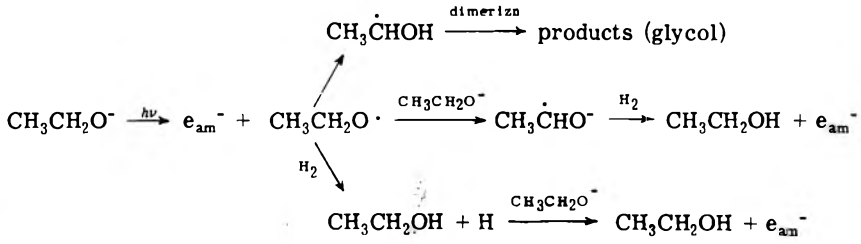

more than 1 hr. After photolysis, this decay was followed for each run, thus allowing an extrapolation to the zero time, *i.e.*, that corresponding to the end of the irradiation. Knowing the extinction coefficients, the concentration of solvated electrons corresponding to the absorption of a known number of photons could be determined and hence the quantum yield.

In the case of the solutions without hydrogen, the quantum yield is $\Phi_{e_{am}^-} = 1$ up to absorbed energies of 3×10^{19} photons $l.^{-1}$, the corresponding concentration in ammoniated electrons being 5×10^{-5} *M* for both wavelengths 254 and 316 nm. For larger doses up to 8×10^{19} photons $l.^{-1}$ the quantum yield decreases to $\Phi_{e_{am}^-} = 0.8$.

In the case of solutions in the presence of hydrogen, the quantum yield is $\Phi_{e_{am}^-} = 2$ for both lines mentioned above. The initial yields remain constant as a function of ethanolate ion concentration in the range 10^{-4}–3×10^{-2} *M*.

Discussion

Applying Stein's scheme of photodetachment of electrons from anions[5] to our case of ethanolate ions in liquid ammonia, we have

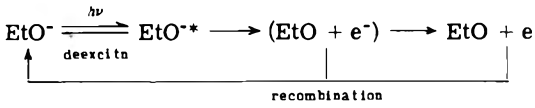

As we obtain a quantum yield equal to the theoretical yield of one electron per photon, we may suppose that the reverse reactions are negligible. In particular the deexcitation of the excited state EtO^{-*} must be very slow compared to the photodetachment. Moreover, the recombination between the radical and the electron, solvated or not, hardly proceeds at all, whether they are still in the cage or separated by diffusion. This recombination should be most probable when the radical and e^- remain close to each other in the cage, but this seems not to hold in the case of photodetachment. In effect, according to the experiments of Rentzepis, *et al.*,[6] on $Fe(CN)_6^{3-}$ in aqueous solution, the electron is ejected to distances of several molecular diameters before the solvation shell of the initial ion is adjusted to the new valency state.

Therefore we are led to conclude that the oxidizing radicals, either the initial ethoxy radical or the α-hydroxyethyl radical which could be formed by rearrangement, react between themselves or with the solvent giving stable compounds at rates much higher than that of recombination with e_{am}^-. At high absorbed doses, when the concentration of e_{am}^- increases markedly, this competition may be reversed and we observed indeed a decrease of $\Phi_{e_{am}^-}$. The most probable product of the reaction of the oxidizing radicals would be glycol or its anion.

The quantum yield $\Phi_{e_{am}^-} = 2$ found in presence of hydrogen can be explained by the hypothesis of a quantitative reaction of the oxidizing radical leading to a second solvated electron. Such reactions are known for OH radicals in water[7] and for NH_2 in liquid ammonia.[2,8] These mechanisms involve either an intermediate formation of a hydrogen atom giving then a solvated electron in the basic solvent or the reaction of the anionic form of the radical with the hydrogen. In the case of the ethanolate solutions, the reaction "f" with the α-hydroxyethyl radical in its neutral form seems improbable as the reverse reaction "r" is known in liquid ammonia, *i.e.*

$$CH_3\dot{C}HOH + H_2 \underset{r}{\overset{f}{\rightleftharpoons}} CH_3CH_2OH + H\cdot$$

We suggest that the hydrogen molecule rather reacts directly with the anionic form of the α-hydroxy ethyl radical $CH_3\dot{C}HO^-$ or with the primary ethoxy radical $CH_3CH_2O\cdot$.

We summarize the whole mechanism proposed by Scheme I.

Thus the solutions of alcoholate ions in liquid ammonia allow us to study the photodetachment of electrons without recourse to scavengers which are normally necessary in media reactive toward the electron. The fact that the quantum yield attains the theoretical values shows that the recombination processes, even in the cage, do not occur.

Acknowledgment. We wish to thank Professor M. Magat and Dr. J. Sutton for their helpful suggestions and discussions.

References and Notes

(1) M. Ottolenghi and H. Linschitz, *Advan. Chem. Ser.*, **No. 56,** 149 (1965).
(2) J. Belloni and E. Saito, "Electrons in Fluids," J. Jortner and N. R. Kestner, Ed., Springer-Verlag, Berlin, 1973, p 461.
(3) G. Stein, *Actions Chim. Biol. Radiat.*, **13,** 119 (1969).
(4) M. J. Blandamer and M. F. Fox, *Chem. Rev.*, **59,** 70, (1970).
(5) C. A. Parker and C. G. Hatchard, *Proc. Roy. Soc., Ser. A,* **235,** 518 (1956).
(6) P. M. Rentzepis, *Chem. Phys. Lett.*, **2,** 117 (1968).
(7) C. J. Hochanadel, *J. Phys. Chem.*, **56,** 587 (1952); J. Jortner and J. Rabani, *J. Amer. Chem. Soc.*, **83,** 4368 (1961).
(8) J. Fradin de la Renaudière and J. Belloni, *Int. J. Radiat. Phys. Chem.*, **5,** 31 (1973).

Rates of Reaction of O^-, OH, and H with Methylated Benzenes in Aqueous Solution. Optical Spectra of Radicals

K. Sehested,* H. Corfitzen,

Danish Atomic Energy Commission, Research Establishment Risø, DK-4000 Roskilde, Denmark

H. C. Christensen,

AB Atomenergi, Studsvik, Fack, S-611 01 Nyköping, Sweden

and E. J. Hart

Argonne National Laboratory, Argonne, Illinois 60439 *(Received April 29, 1974; Revised Manuscript Received October 8, 1974)*

Publication costs assisted by the Danish Atomic Energy Commission

Benzyl type radicals are formed in aqueous alkaline solutions by reaction of O^- with methylated benzenes *via* abstraction of an H atom from a methyl group. The same radicals are formed in acid solutions but in an indirect way. Water elimination from the OH addition complex involving a proton takes place. Besides adding to the benzene ring the OH radicals also react by direct abstraction of an H atom from a methyl group. The amount of abstraction is directly proportional to the number of methyl groups in the hydrocarbon. H atoms add to methylated benzenes to form cyclohexadienyl radicals. The rate constants for O^-, OH, and H reacting with methylbenzenes are of the order of 2×10^9, 7×10^9, and 3×10^9 M^{-1} sec^{-1}, respectively. The rate for the water elimination reaction varies for the different compounds and the values are listed. Recent experiments indicate that this reaction has an intermediate step with a species absorbing above 400 nm. This species is tentatively assigned as a cation radical.

Introduction

Recently we reported[1] that the benzyl radical is formed by pulse radiolysis of aqueous toluene solutions. The formation is a direct abstraction of a methyl H atom by O^- in strongly alkaline solution or an indirect reaction by water elimination from the primarily formed OH addition product in acid solutions.

The objective of the present study is to show that similar reactions take place in aqueous solutions of methylated benzenes and to explore the mechanism of the benzyl formation in acid solutions in more detail.

In aqueous toluene solutions a few per cent of the OH radicals abstract an H atom from the methyl group forming the benzyl radical directly. The ratio of this reaction to the addition reaction was examined as a function of the number of substituted methyl groups.

Some work has been published on the photolysis and radiolysis in pure methylbenzenes and with the benzenes dissolved in organic solvents,[2-5] but very little is published about these compounds in aqueous solutions, probably because of their poor solubility in water.

Experimental Section

Materials. The methylated benzenes were obtained from Merck, BDH, KochLeight, Fluka, K & K, and were of purest available quality and used without further purification. The perchloric acid was reagent grade from G. F. Smith and sodium hydroxide from Merck. The water was triply distilled and all glassware was preheated to 450°.

Irradiation. The pulse radiolysis system on the Risø Linac was described previously.[1,6] The essential features are the Linac delivering 0.2–4-μsec single pulses of 11-MeV electrons with a peak current of 0.25 A as a maximum, an Osram XBO 450-W xenon lamp used in pulsed operation, a Zeiss MM 12 double quartz prism monochromator, an EMI 9558Q photomultiplier tube, and a Tektronix 555 double-beam oscilloscope. In some experiments the set-up on the 2.3-MeV Febetron was used. The pulse is about 20-nsec duration and the detection system is 5–10 times faster than that on the lineac.

Dosimetry. The current induced in a coil surrounding the electron beam was used for relative dosimetry. The absolute dose was measured with the hexacyanoferrate(II) dosimeter[7] using $g(e_{aq}^- + OH) = 5.25$ and ϵ(420 nm) 1000 M^{-1} cm^{-1}.

Preparation of Solutions. Solutions of liquid methylated benzenes were deaerated and saturated with a gas by bubbling the gas through the solution with excess benzene in a 100-ml syringe. Solutions of solid compounds were prepared in a 1-l. flask by repeated evacuation and saturation with the appropriate gas. The pH of the solutions was adjusted with perchloric acid or sodium hydroxide and was measured on a Radiometer digital pH meter, PHM52.

Solubility. Determination of the solubilities of the methylated benzenes was carried out by gas chromatography on a Perkin-Elmer, Model F 11, equipped with a Carbowax 1500 column for the lower methylated compounds and a SE 30 column for the higher ones. The samples were taken from the saturated solution, which also contained 10^{-2} M *tert*-butyl alcohol as a reference, and injected into the gas chromatograph. The calibration was done with the pure compounds. The solubilities in neutral and alkaline solution are shown in Table I.

Corrections. The absorption spectra were corrected for depletion of solute (S) in the wavelength range where the solute absorbs light ($\lambda \leq 270$ nm). $G(-S)$ was assumed to be 5.9 $[= g(e_{aq}^-) + g(H) + g(OH)]$ in N_2O-saturated unbuffered solutions. In 0.5 M NaOH a $G(-S)$ of 6.5 was used.[8]

TABLE I: Solubilities of Methylated Benzenes in Unbuffered and Alkaline Solutions[a]

	Solubility neutral/ alkaline, $M \times 10^3$	Methylbenzyl radical		OH adduct		H adduct	
		λ_{max}	ϵ, M^{-1} cm^{-1}	λ_{max}	ϵ, M^{-1} cm^{-1}	λ_{max}	ϵ, M^{-1} cm^{-1}
Toluene[b] (methylbenzene)	5.9/4.7	258	14,000	320	4,300	319	4,800
		307	3,300				
		317.5	5,500				
o-Xylene (1,2-dimethylbenzene)	2.1/1.4	261	16,100	326	4,700	328	4,500
		312	3,100				
		323	5,900				
m-Xylene (1,3-dimethylbenzene)	1.7/0.95	262	15,600	328	6,000	326	5,900
		311	2,800				
		323	4,700				
p-Xylene (1,4-dimethylbenzene)	2.0/1.4	268	15,500	312	4,300	338	4,300
		298	2,500				
		311	3,200				
		322	4,000				
Mesitylene (1,3,5-trimethylbenzene)	0.53/0.37	265	16,000	333	6,500	328	5,700
		315	2,800				
		328	4,200				
Hemimillitene (1,2,3-trimethylbenzene)	0.75/0.62	263	16,000	328	5,000	330	4,000
		317	3,500				
		329	6,000				
Pseudocumene (1,2,4-trimethylbenzene)	0.70/0.67	266	15,500	328	5,200	337	4,300
		315	2,500				
		328	6,000				
Durene (1,2,4,5-tetramethylbenzene)	0.04/0.03	271	12,000	333	3,500	338	3,500
		318	2,700				
		331	3,500				
Isodurene (1,2,3,5-tetramethylbenzene)	0.40/0.16	267	16,800	332	5,600	326	5,200
		321	3,200				
		331	4,400				
Prehnitene (1,2,3,4-tetramethylbenzene)	0.60/0.28	267	14,600	333	4,800	333	5,200
		317	4,300				
		332	4,600				
Pentamethylbenzene	0.05/0.02	269	16,000	332	4,300		
		320	3,000				
		335	3,700				
Hexamethylbenzene	0.01	270	11,500	333	3,500		
		330	3,000				

[a] Wavelengths of absorption maxima and corresponding extinction coefficients of substituted benzyl radicals, OH, and H adducts in aqueous solutions. [b] Reference 1.

Results and Discussion

Alkaline Solution. Methylbenzyl radicals were produced and studied in aqueous solutions by pulse radiolysis of alkaline N_2O-saturated solutions (0.5 M NaOH). In this solution e_{aq}^-, H, and OH are converted into O^- within 0.1 μsec after the pulse and as shown previously[1,9,10] O^- reacts preferentially with the side group by abstraction of an H atom. The methylbenzyl radicals are thus formed in a direct process, and the resulting spectra are similar and resemble the spectrum of the unsubstituted benzyl radical.[1] As an example the spectrum of the 3,5-dimethylbenzyl radical is shown in Figure 1. The three main absorption peaks are shifted slightly (10–20 nm) to longer wavelength with increasing number of methyl groups (Table I). The extinction coefficients at the absorption maxima are calculated assuming $G(O^-) = 6.5$,[8] and the extinction of the peaks at 260–270 nm are very similar, about 15,000 M^{-1} cm^{-1}, for all compounds. As for the benzyl radical there is an absorption at longer wavelength (450–550 nm) from the methylbenzyl radicals with low extinction coefficients of 100–300 M^{-1} cm^{-1}. The rate constants for the reaction of O^- with methylbenzenes were determined by the increase at the absorption maxima with two–three different concentrations and a dose of about 200 rads. The rate constants for all compounds are of the order of 2×10^9 M^{-1} sec^{-1} (Table III) independent of the number of methyl groups, which indicate that the rate is diffusion controlled. The methylbenzyl radicals disappear in bimolecular reactions with $2k \simeq (1.5 \pm 0.5) \times 10^9$ M^{-1} sec^{-1} (Table III).

Neutral Solution. In unbuffered N_2O-saturated solutions the OH radical preferentially adds to the benzene ring forming a hydroxymethylcyclohexadienyl radical. A small part of the OH radicals react, however, with the methylated benzenes by abstraction of an H atom from a methyl group forming a methylbenzyl radical. The spectrum in neutral N_2O-saturated solution is therefore composed of the spectrum of the OH adduct, the methylbenzyl radical, and a small part of the H adduct. The H and OH adducts have their maximum absorptions at 320–340 nm and a minimum at 260–270 nm where the methylbenzyl radicals have their main absorptions. Using the extinctions for these radicals found in alkaline solution and subtracting a certain percentage of this spectrum from that in neutral solution so that the resulting absorption curves become smooth around 260–270 nm, we compute the proportion of the abstraction reaction relative to the addition reaction. The amount of this abstraction reaction is directly proportional to the number of methyl groups. Figure 2 shows the uncorrected spectra obtained in neutral solutions for one, two, three, and four methyl groups substituted into the

TABLE II: Rate Constants for Benzyl Formation from OH Reacting with Methylated Benzenes by Direct Abstraction of a Methyl H Atom

	H abstrn % OH	k_{abstrn}, M^{-1} sec^{-1}	k, M^{-1} sec^{-1}, per methyl group[b]
Toluene[a]	6.0	4.0×10^8	4.0×10^8
o-Xylene	12.0	8.0×10^8	4.0×10^8
m-Xylene		9.0×10^8	4.5×10^8
p-Xylene		8.4×10^8	4.2×10^8
Mesitylene	18.5	1.18×10^9	3.9×10^8
Hemimillitene		1.30×10^9	4.3×10^8
Pseudocumene		1.15×10^9	3.8×10^8
Durene	26.0	1.81×10^9	4.5×10^8
Isodurene		1.84×10^9	4.6×10^8
Prehnitene		1.87×10^9	4.7×10^8
Pentamethylbenzene	34.0	2.38×10^9	4.7×10^8
Hexamethylbenzene	<50		

[a] Reference 1. [b] Average $(4.2 \pm 0.5) \times 10^8$ M^{-1} sec^{-1}.

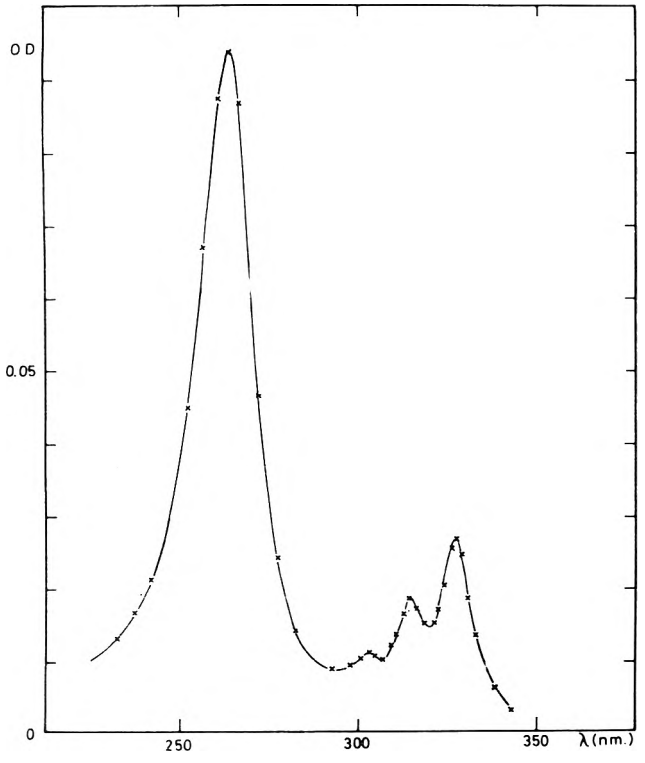

Figure 1. The absorption spectrum of the 3,5-dimethylbenzyl radical in 0.5 *M* NaOH solution saturated with N_2O: dose 175 rads.

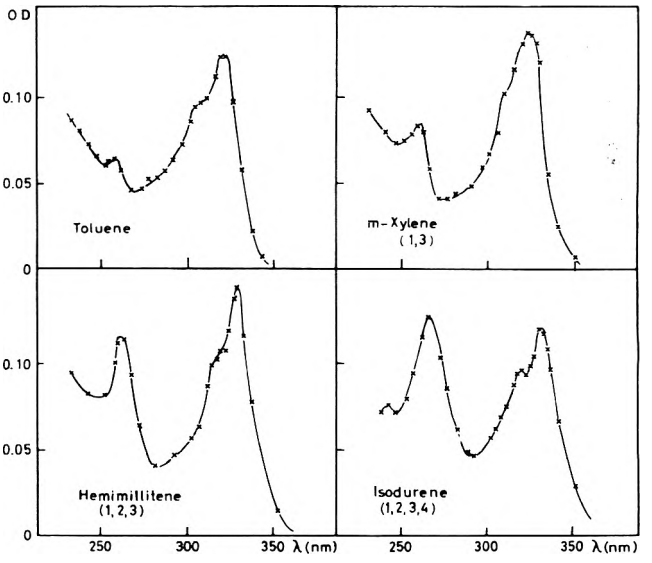

Figure 2. Transient absorption spectra in N_2O-saturated unbuffered solutions of benzene substituted with one, two, three, and four methyl groups. The absorption peaks at 260–270 nm are used as a measure for the direct abstraction of an H atom by the OH radicals forming the methylbenzyl radicals: dose 700–900 rads.

benzene ring. From the peaks at 260–270 nm and the respective extinction coefficients for the corresponding methylbenzyl radicals the amount of these radicals formed in neutral solution can be estimated. The abstraction reaction varies from 6% for toluene (previously reported as 3.3%)[1] up to 34% for pentamethylbenzene (Table II). Because of the high rate for the indirect formation of methylbenzyl radicals in hexamethylbenzene (see later) and the low solubility it is only possible to state that the direct formation of pentamethylbenzyl radicals is less than 50%.

From the overall rate constant for OH reacting with methylbenzene and the percentage of the direct formation of the methylbenzyl radicals, the rate constant for the abstraction of an H atom from a methyl group is determined to be $(4.2 \pm 0.5) \times 10^8$ M^{-1} sec^{-1} (Table II).

The absorption spectra of the OH adducts, the hydroxycyclohexadienyl radicals, are obtained in unbuffered N_2O-saturated solutions after correction for the simultaneously formed methylbenzyl radicals and H adducts. As an example the corrected spectrum of the 1,3,5-trimethylbenzene adduct is shown in Figure 3. In all the corrected spectra we observe a two component structure of the 300–350-nm band, which is similar to that of the hydroxycyclohexadienyl spectrum reported by Mantaka, Marketos, and Stein[11] and the hydroxymethylcyclohexadienyl spectrum reported by us.[1]

The shoulder is always placed at the shorter wavelength except for the adduct of *p*-xylene. The extinction coefficients are of the order of 5000 M^{-1} cm^{-1} (Table I). The OH adducts also have a weak absorption band (100–200 M^{-1} cm^{-1}) in the visible region (500–550 nm). The rate constant of the reaction of OH with methylated benzenes is determined by the increase in absorption at the maximum at different concentrations and is of the order of 7×10^9 M^{-1} sec^{-1} for all the compounds (Table III). For toluene we find a value of 6.8×10^9 M^{-1} sec^{-1}, about twice the reported value.[12,13] The disappearance of the adducts is bimolecular with the rate $2k \simeq (1.5 \pm 0.5) \times 10^9$ M^{-1} sec^{-1}.

Acid Solution. The absorption spectra of the hydrogen adducts, the cyclohexadienyl radicals, are obtained in

TABLE III: Rate Constants of OH, H, and O^- Reacting with Methylated Benzenes and the Bimolecular Rate Constants for the Decay of the Corresponding Radicals

	$10^{-9}k_{OH+MB}$, M^{-1} sec^{-1}	$10^{-9}k_{H+MB}$, M^{-1} sec^{-1}	$10^{-9}k_{O^-+MB}$, M^{-1} sec^{-1}	$10^{-9}2k_{OH\ adduct}$, M^{-1} sec^{-1}	$10^{-9}2k_{H\ adduct}$, M^{-1} sec^{-1}	$10^{-9}2k_{Me\ benzyl\ radical}$, M^{-1} sec^{-1}
Toluene[a]	6.8	2.6	2.2	1.6	2.7	2.4
o-Xylene	6.7	2.0	1.8	1.4	4.1	1.5
m-Xylene	7.5	2.6	2.2	1.3	3.9	1.5
p-Xylene	7.0	2.2	1.8	1.2	3.6	1.9
Mesitylene	6.4	3.6	2.4	1.8	3.8	1.7
Hemimillitene	7.0	2.6	2.1	1.4	3.9	1.3
Pseudocumene	6.2	3.3	2.1	1.4	4.1	1.5
Durene	7.0	2.8	2.3	1.6	3.6	1.7
Isodurene	7.1	3.5	2.6	1.7	4.0	1.3
Prehnitene	7.2	2.8	2.4	1.5	4.0	1.3
Pentamethylbenzene	7.5	2.9	2.6	1.7		1.5
Hexamethylbenzene	7.2		~2.5			~2

[a] Reference 1.

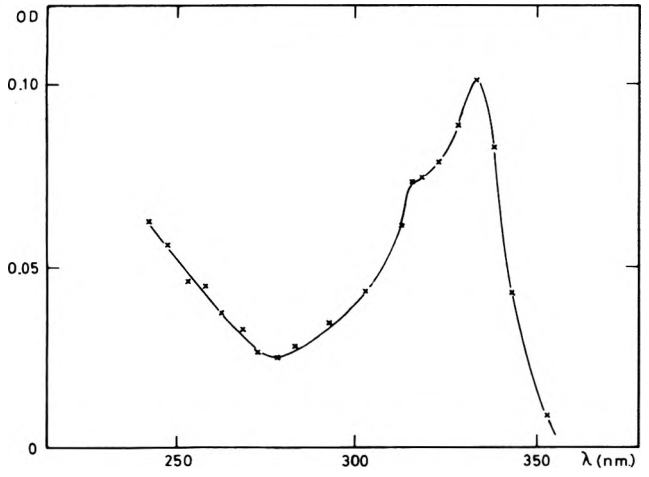

Figure 3. The absorption spectrum of the OH adduct of 1,3,5-trimethylbenzene in N_2O-saturated unbuffered solution corrected for contributions from the H adduct and the methylbenzyl radicals: dose 660 rads.

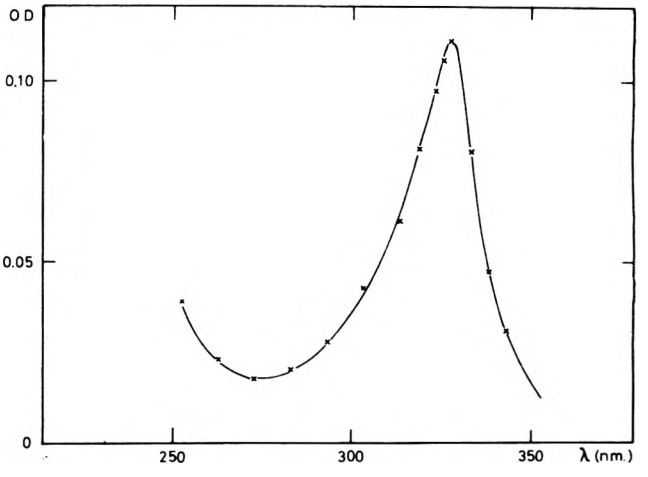

Figure 4. The absorption spectrum of the H adduct of 1,3,5-trimethylbenzene in Ar-saturated 0.1 *M* perchloric acid solution containing 0.2 *M tert*-butyl alcohol: dose 1000 rads.

deaerated 0.1 *M* perchloric acid solutions containing methylated benzenes in a suitable concentration (saturated or 20% saturated) and 0.1–0.5 *M tert*-butyl alcohol, depending on the concentration of methylated benzenes. The OH concentration is reduced to a few per cent without significantly decreasing the H atom concentration. The spectrum shown in Figure 4 is the H adduct of 1,3,5-trimethylbenzene. The adducts are all broad bands with maxima between 320 and 340 nm and with extinction coefficients between 3500 and 6000 M^{-1} cm^{-1} (Table I). Similar spectra and extinction coefficients (within 10%) are also found by subtracting the contribution of the corresponding methylbenzyl radical spectra from the spectra obtained in strong acid without *tert*-butyl alcohol. This proves that the OH adduct is converted into the benzyl radical in strong acid solutions (see later). The rate constants for the reaction of the H atom with methylated benzenes fall in the range 2.0–3.6 $\times 10^9$ M^{-1} sec^{-1} (Table III). These adducts disappear by a second-order reaction only when the concentration of *tert*-butyl alcohol is relatively low, *i.e.*, when not more than 70–80% of the OH is scavenged. The bimolecular rate constants of the H adducts of Table III may therefore be too high.

In acid solution the methylbenzyl radicals are formed in an indirect reaction by water elimination from the OH adducts. The reaction mechanism is similar to that reported for aqueous toluene solutions.[1] The rate of formation of the methylbenzyl radicals is determined as a function of pH in N_2O- or Ar-saturated solutions by the build up of the absorption at 260–270 nm. For aqueous toluene solutions we reported a linear relationship between the rate constant for the formation and the $[H^+]$ concentration in the range 0.48–10^{-2} *M* acid,[1] see Figure 5a. Within a limited pH range similar linear relationships are found for methylated benzenes. However, for these compounds nonlinear ranges are also found.

Figure 5 gives the methylbenzyl radical formation as function of $[H^+]$ concentration for the various methylated benzenes. As a general pattern there are ranges where the rate is pH independent both at high and low pH corresponding to low and high rates, respectively. At an intermediate pH the rate is proportional to the $[H^+]$ concentration. This part of the pH range is different for the various methyl benzenes as are the values of the pH independent rates.

The shape of the curves suggests a protonation of the radicals followed by water elimination from both the protonated and unprotonated radicals each with different rates. This is consistent with the following mechanism

TABLE IV: Equilibrium Constants, K_0, and Rate Constants k_1 and k_2 for the Formation of Methylbenzyl Radicals from Water Elimination from the OH Adducts in Aqueous Acid Solutions

	K_0, M^{-1}	k_1, sec^{-1}	k_2, sec^{-1}
Toluene[a]	≤ 0.2	$<10^3$	$\geq 5 \times 10^5$
o-Xylene	6	$<2 \times 10^3$	2×10^6
m-Xylene	2.5	5×10^3	2×10^6
p-Xylene	30	5×10^3	1.2×10^6
Mesitylene	22	$<2 \times 10^3$	1.7×10^6
Hemimillitene	75	1.1×10^4	1.8×10^6
Pseudocumene	1×10^3	$<2 \times 10^3$	2.5×10^5
Durene	3×10^3	1.0×10^4	$\sim 1 \times 10^5$
Isodurene	1×10^3	1.3×10^4	3×10^5
Prehnitene	2×10^3	5×10^3	3×10^5
Pentamethylbenzene	4×10^3	4×10^4	$\geq 1.8 \times 10^5$
Hexamethylbenzene	$\sim 10^5$		

[a] Reference 1.

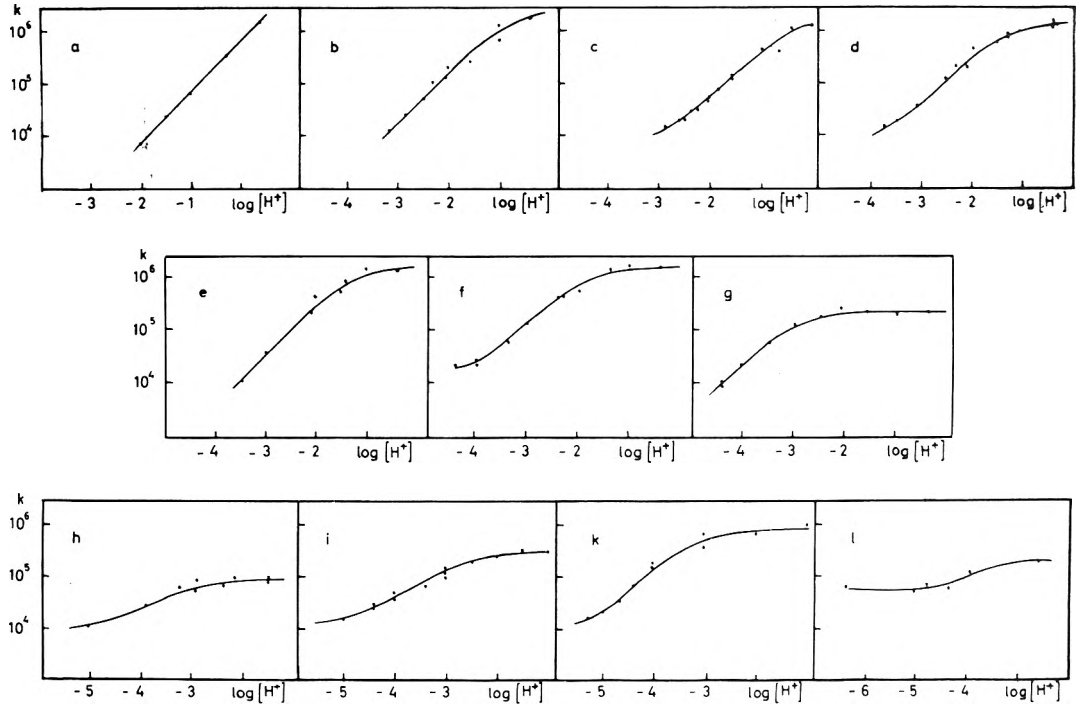

Figure 5. The rate of benzyl formation by water elimination in acid solution as a function of log $[H^+]$ for the various methylated benzenes: (a) toluene, (b) *o*-xylene, (c) *m*-xylene, (d) *p*-xylene, (e) mesitylene, (f) hemimillitene, (g) pseudocumene, (h) durene, (i) isodurene, (k) prehnitene, (l) pentamethylbenzene.

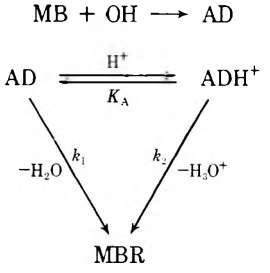

where MB is the methylated benzene, AD the OH addition complex, MBR the corresponding methyl-substituted benzyl radical, and K_A the acid dissociation constant of the acid ADH^+. The rate constant for the formation of MBR according to this mechanism is

$$k = \frac{k_1 K_A + k_2[H^+]}{K_A + [H^+]}$$

or by substituting $1/K_A$ with K_0 the following equation is obtained

$$k = k_1 + \frac{K_0[H^+]}{1 + K_0[H^+]}(k_2 - k_1)$$

The solid lines on Figure 5 are drawn as the best fit to the experimental points by taking $k = k_1$ at high pH ($[H^+] < 10^{-5}$) and $k = k_2$ at low pH ($K_0[H^+] \gg 1$). K_0 is determined at an intermediate $[H^+]$ ($0.01 \leq K_0[H^+] \leq 0.1$) where $k \simeq k_2 K_0[H^+]$ if $k_2 \gg k_1$. The mechanism is independent of the real identity of AD, which is generally believed to be a hydroxycyclohexadienyl radical. AD may also disappear in a second-order reaction but the influence from this reaction is minimized by using a very small pulse (<200 rads). A consequence is, however, that it is difficult to study benzyl formation with rate constants less than 10^4 sec^{-1}. This means that the lower limit for the rate constant can not be obtained experimentally in all cases, but from

the shape of the curves approximate values can be calculated. The higher rate constant, k_2, may also be difficult to determine experimentally in some cases. One limitation is the rise time on our pulse radiolysis set-up. If we use our 2.3-MeV Febetron set-up with $\tau \simeq 0.2$ μsec values of k up to 5×10^6 sec^{-1} can be determined. The other limitation is the acid concentration where we considered 1 M perchloric acid to be the strongest acid we could reasonably use without complicating the system with a direct absorption of radiation energy in the acid.

The values of the rate and equilibrium constants k_1, k_2, and K_0 are given in Table IV. For toluene only the value k_2K_0 (1.1×10^6 M^{-1} sec^{-1})[1] can be determined which means $k_2 \geq 5 \times 10^6$ sec^{-1}, $K_0 \leq 0.2$ M^{-1}, and $k_1 \leq 10^3$ sec^{-1}.

There is a pronounced increase in the value of K_0 and consequently in the pK_A of the acid ADH^+ with increasing number of methyl groups in the hydrocarbon. k_1 varies in a less systematic way, whereas k_2 generally decreases with the number of methyl groups.

Experiments in strong acid solutions reveal data which help to explain the mechanism of the water elimination reaction and the indirect formation of the benzyl radicals. As the upper limit for the rate constant, k_2, is approached at low pHs a new transient absorption appears near 430–470 nm with a second peak at 290–300 nm. This absorption decays very fast in a first-order reaction independent of dose and solute concentration, but slightly dependent on $[H^+]$ concentration. The decay rate corresponds to k_2 for the different methylbenzenes although somewhat lower. The optical density increases with increasing $[H^+]$ concentration and the formation rate of the transient is nearly proportional to the $[H^+]$ concentration. This new band, tentatively assigned to a cation radical, is produced by abstracting OH^- from the OH adduct by the high $[H^+]$ concentration. This may be possible if the OH adduct (hexadienyl radical) is in equilibrium with a charge transfer complex as shown in reaction 1.

The new transient with absorptions at 430–470 and 290–300 nm is assigned to the cation radical.[14-17] New experiments and a closer study of this tentative assignment are in progress and will be published later.

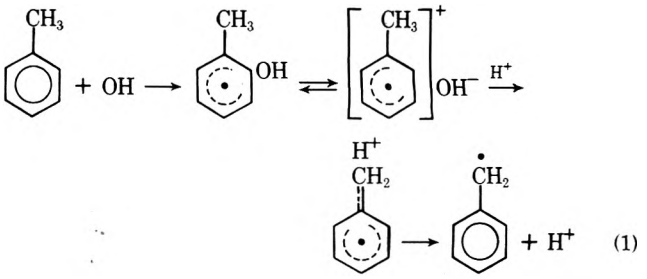

(1)

Acknowledgment. We thank the operator staff of the accelerator at Risø for their assistance and H. Egsgaard Pedersen for measuring the solubilities of the methylbenzenes. We are indebted to B. Skytte Jensen and E. Bjergbakke for many valuable discussions during the work.

References and Notes

(1) H. C. Christensen, K. Sehested, and E. J. Hart, *J. Phys. Chem.*, **77**, 983 (1973).
(2) P. M. Johnson and A. C. Albrecht, *J. Chem. Phys.*, **48**, 851 (1968).
(3) J.-L. Monge and M. Schott, *J. Chim. Phys.*, **69**, 324 (1972).
(4) R. V. Bensasson, J. T. Richards, T. Gangwer, and J. K. Thomas, *Chem. Phys. Lett.*, **14**, 430 (1972).
(5) C. Branciard-Larcher, E. Migirdicyan, and J. Bandet, *Chem. Phys.*, **2**, 95 (1973).
(6) H. C. Christensen, G. Nilsson, P. Pagsberg, and S. O. Nielsen, *Rev. Sci. Instrum.*, **40**, 786 (1969).
(7) R. Rabani and M. S. Matheson, *J. Phys. Chem.*, **70**, 761 (1966).
(8) E. M. Fielden and E. J. Hart, *Radiat. Res.*, **32**, 564 (1967).
(9) P. Neta, M. Z. Hoffmann, and M. Simic, *J. Phys. Chem.*, **76**, 847 (1972).
(10) P. Neta and R. H. Schuler, *J. Phys. Chem.*, **77**, 1368 (1973).
(11) A. Mantaka, D. G. Marketos, and G. Stein, *J. Phys. Chem.*, **75**, 3886 (1971).
(12) L. M. Dorfman, I. A. Taub, and D. A. Harler, *J. Chem. Phys.*, **41**, 2954 (1964).
(13) M. C. Sauer, Jr., and B. Ward, *J. Phys. Chem.*, **71**, 3971 (1967).
(14) D. Bethell and V. Gold, "Carbonium Ions," Academic Press, London, 1967.
(15) R. Hulme and M. C. R. Symons, *J. Chem. Soc.*, 1120 (1965).
(16) R. Hulme and M. C. R. Symons, *J. Chem. Soc. A*, 446 (1966).
(17) W. I. Aalbersberg, G. J. Hoijtink, E. L. Mackor, and W. P. Weiland, *J. Chem. Soc.*, 3055 (1959).

Flash and Steady-State Photolysis of Aqueous Solutions of *p*-Nitrosodimethylaniline. Evidence for Oxygen-Enhanced Water Photolysis above 200 nm[1]

T. Godfrey, R. J. Kobrin, J. E. Fanning, A. El Samahy, and C. N. Trumbore*

Department of Chemistry, University of Delaware, Newark, Delaware 19711 *(Received June 24, 1974)*

Publication costs assisted by the University of Delaware

Evidence is presented of similarities of transient spectra and kinetics in flash photolyzed and pulse radiolyzed aqueous solutions of *p*-nitrosodimethylaniline (RNO). This is unexpected since the energy in radiolysis is absorbed predominantly by H_2O whereas the bulk of the photons in flash photolysis experiments are absorbed by RNO molecules. Detectable transient absorption after the flash photolysis is found only when irradiating with wavelengths of light shorter than 230 nm. Transients with maximum absorbance at 350, 540, and 580 nm have been studied as a function of pH, oxygen and RNO concentration, flash intensity, and wavelength of irradiating light. The 540-nm transient has been characterized as being quite insensitive to experimental conditions with a first-order decay constant of 5.7×10^2 sec^{-1} and is apparently the same transient as that found in the RNO pulse radiolysis system. A study of RNO bleaching under continuous irradiation demonstrated that the wavelength of light used has to be below a threshold value of 230 nm for RNO bleaching (at 440 nm) to occur. This bleaching is essentially zero order in RNO concentration and is enhanced by oxygen in a reaction which is first order in oxygen concentration. This, together with other evidence, strongly implicates water, rather than direct RNO, photolysis as the primary photolysis event. This primary process is probably direct water photolysis or photolysis of a water–oxygen charge transfer complex. It is also necessary to postulate that in flash photolysis, as well as in pulse radiolysis of oxygenated RNO solutions, there are two reactive intermediates, in addition to the hydrated electron (or O_2^- in the case of photolysis and radiolysis of oxygenated solutions), which react with RNO at relatively early times, giving rise independently to the 350- and 540-nm transients. One of these is probably the OH radical. The identity of the other is unknown, but appears to be related to the OH radical rather than the reducing species e_{aq}^- or H.

Introduction

Previous studies[2-8] of the aqueous radiation chemistry and photochemistry of *p*-nitrosodimethylaniline (RNO) have demonstrated the usefulness of this compound because of its apparently specific reactions with OH radicals when oxygen is present in the system. Anomalous behavior has been noted[5] when experimental conditions deviate from "standard" values (pH ~7, 20–50 μM RNO, air saturated).

A recent investigation of the radiolysis and photolysis of oxygenated, H_2O_2-containing solutions of RNO demonstrates similar competition kinetics for OH radicals, but gives a calculated primary quantum yield for H_2O_2 destruction which is in disagreement by a factor of 2 with the commonly accepted yields. In that study,[6] it was found that when an aqueous solution of RNO alone was photolyzed with 254-nm light, negligible bleaching of the 440-nm RNO absorption band occurred compared with that observed when a solution which also contained H_2O_2 was irradiated with light of the same wavelength.

In the work reported below, we find that, in addition to measureable yields for photolytic bleaching of RNO in the presence and absence of oxygen, there are transient absorptions produced in flash photolyzed RNO solutions as long as the photolyzing flash consists of wavelengths less than 230 nm. Spectra of these transients as well as the kinetics of their growth and decay are qualitatively and, in some cases, quantitatively the same as in the pulse radiolysis of the similar solutions.

We report below the effects of wavelength cutoff filters, variation of pH, O_2 and RNO concentration, and flash intensity on transient spectra produced by the flash photolysis of RNO. Correlation of these flash photolysis data with steady-state photolysis data on net overall RNO bleaching rates leads us to propose that a large portion of the primary, reactive transient species responsible for RNO damage originates from water, rather than RNO photolysis. We also observe that oxygen appears to enhance the yield of these reactive species when the irradiating light contains wavelengths between 200 and 230 nm.

Experimental Section

RNO, Eastman White Label Grade, was recrystallized twice from a mixture of ether and petroleum ether and its extinction coefficient was in good agreement with the reported value of 3.2×10^4 at 440 nm. H_2O_2 was a 30% solution, Fisher certified ACS reagent grade. Water was triply distilled. Oxygen (99.9%), argon (99.99%), and N_2O were used without further purification.

A conventional, custom-built, kinetic flash photolysis apparatus[9] was used for the majority of the experiments. (Cells were usually 15 cm long, 0.5 cm in diameter, and constructed from Spectrosil quartz.) The photolysis flash was produced by a discharge of 10 μF usually at 13 kV through an FPA-6 Xenon Corp. flash lamp. The photolysis flash decayed to $1/e$ of its maximum intensity in 30–50 μsec. However, because of the length of tail of the flash, completely reliable *quantitative* data could only be collected about 200 μsec or more after the initiation of the flash. In most experiments, a filter solution was placed between the flash lamp

and the reaction cell. To follow changes in flashed solutions, either a continuous 500-W Xe discharge lamp or a 150-W quartz-iodine tungsten lamp was used together with a Bausch and Lomb monochromator, a 1P28 photomultiplier tube, and a 545A Tektronix oscilloscope from which photographic recordings of kinetic data were taken.

Before flashing, argon, oxygen, or N_2O was bubbled through the RNO solution through a fine glass frit. A few solutions were air saturated. Each sample was flashed only once.

Preliminary flash spectroscopic work for the kinetic studies reported here was carried out in the laboratory of Professor J. W. Boag in the Physics Department of the Institute of Cancer Research, Sutton, Surrey, England.

The illumination source for steady-state photolysis studies was a short-arc, high-pressure, 125-W Xe lamp. Relative actinometry was carried out during the illumination of each sample in order to correct for possible arc wandering and lamp fluctuations. The actinometer used was an air-saturated, 50 μM aqueous RNO solution containing 10^{-3} M H_2O_2. Solutions were photolyzed at room temperature (23 ± 1°). Filter solutions were placed directly in front of the sample cells to be photolyzed and consisted of either 0.1 M NaCl (absorption = 1.99 at 199 nm) or 1 M sodium acetate (absorption = 2.25 at 230 nm). Solutions were saturated with Ar or O_2 using the syringe technique[10] which was also used to prepare 600 μM O_2 solutions.

Results

Continuous Photolysis of RNO Solutions. The rate of net bleaching of the RNO absorbance at 440 nm was followed as a function of illuminating dose, wavelength, and oxygen (0, 600, and 1200 μM) and RNO (10, 20, 35, and 50 μM) concentrations.

Using the acetate filter with its 230-nm cutoff, small amounts of RNO bleaching were measured at 440 nm. This bleaching was directly proportional to photon dose, appeared to be approximately proportional to RNO concentration, and was a more complex function of oxygen concentration (approximately the same bleaching rate was observed with 600 and 1200 μM O_2, with a lower rate in Ar-saturated solutions). When the NaCl filter (200-nm cutoff) was used at the same photon dose rate, the bleaching rate not only increased markedly, but now took on a completely different concentration dependence with respect to RNO and O_2: approximately zero order in RNO and approximately first order in O_2 (using the Ar-saturated solution bleaching rate as a zero O_2 concentration baseline for the two concentrations studied). Correction of the NaCl filter data by subtraction from it of the bleaching of the 440-nm RNO peak when the acetate filter was present brought the data even closer to the orders stated above. For example, with the corrected data, a fivefold increase in RNO concentration (10–50 μM RNO) caused, for oxygen-saturated solutions, only an 18% increase in bleaching rate. For both oxygen-free and 600 μM O_2 RNO solutions, the bleaching rate was, within experimental error, independent of RNO concentration. Conversely, at all RNO concentrations studied, the rate of bleaching in the presence of 1200 μM O_2 minus the rate in deoxygenated (Ar saturated) solution was approximately double the bleaching rate with 600 μM O_2 minus the rate in the absence of oxygen. These data are summarized in Figure 1.

Flash Photolysis Studies. Transient absorptions were observed in most of the ultraviolet and visible portion of the spectrum not obscured by the RNO ground state absorption when the irradiating wavelength was below 225 nm. No transients were observable when using irradiating wavelengths above 300 nm and only very poorly characterized transients could be detected when the photolysis wavelengths were between 225 and 300 nm. For much of the work, an aqueous sodium chloride filter which had an optical density of 1.85 at 200 nm was interposed between the flash lamp and the sample cell.

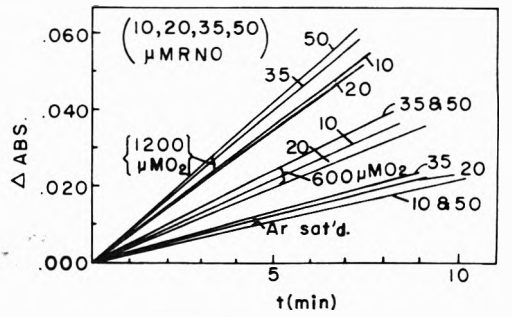

Figure 1. Steady-state photolysis of aqueous RNO solutions. Change in absorbance as a function of photolysis time. Lines are least-squares fits through experimental points. Data have been corrected by subtracting small amount of bleaching detected with sodium acetate filter (see text.)

The absorption spectrum of RNO is shown in Figure 2 (solid line). A tentative assignment of the peaks of the ground-state RNO spectrum has been made[11] as follows: 550 nm, n–π^* ($\epsilon_{550} \approx 100$ M^{-1} cm^{-1}); 440 nm, π–π^* with considerable charge transfer character, probably from the ring toward the nitroso group (ϵ_{440} 3.4×10^4); 275 nm, π–π^* with some charge transfer character but less than the 440 nm band ($\epsilon_{275} \sim 4 \times 10^3$). The dotted line in Figure 2 represents the spectrum of the protonated form of RNO (pK = 3.7), with the proton probably situated on the nitroso oxygen (ϵ_{350} 2.2×10^4 M^{-1} cm^{-1}). Also shown in Figure 2 is the absorption curve for oxygen-saturated water first observed by Heidt and Ekstrom.[12] It should be noted, at this point, that the onset of this water absorption curve corresponds to the minimum energy of irradiating light needed to produce strong transient absorptions during flash photolysis.

Qualitatively, in the presence of oxygen, the kinetic behavior of transient absorptions seen in the flash photolyzed system is quite similar to that of the pulse radiolyzed RNO system.[7,8] A transient with a spectral maximum at 350–355 nm is the first to appear during the flash. This is followed by the slower appearance of a transient with an absorption maximum at 540 nm which does not appear to be related in any simple kinetic manner to the decay of the 350-nm transient. In the absence of oxygen (Ar saturated solutions), the 350-nm transient is still present, again appearing during the flash, but under these conditions is followed by growth of a transient with a peak maximum now shifted to 580 nm. Both the 540 and 580 nm transients have lifetimes of the order of milliseconds, in agreement with similar transients observed in RNO pulse radiolysis studies.[7,8] The kinetics and spectra of these flash photolysis transients were investigated under various experimental conditions and results are reported below and in Table I.

350-nm Transient Absorption. The shape of this flash photolysis transient absorption band is qualitatively the same (see Figure 2) as that observed during the pulse radiolysis of RNO.[7,8] In pulse radiolysis studies, the peak maximum measured at its maximum height following the build-

TABLE I: Flash Photolysis of *p*-Nitrosodimethylaniline Solutions

RNO, *M*	pH	Gas	Flash filter	Flash voltage, kV	540-nm transient: Maximum optical density	540-nm transient: Build-up half-life, μsec	540-nm transient: Decay half-life, msec
5×10^{-5}	6.8	O_2	NaCl	13	0.065	85	1.15
5×10^{-5}	6.2	air	NaCl	13	0.045		1.3
5×10^{-5}	6.9	Ar	NaCl	13	0.03		1.3
5×10^{-5}	6.8	O_2	None	13	0.40		1.35
5×10^{-5}	6.2	air	None	13	0.32		1.1
5×10^{-5}	6.5	Ar	None	13	0.19		Complex
1×10^{-5}	6.4	air	None	13	0.14		1.1
1×10^{-5}	6.2	Ar	None	13	0.15		Complex
1×10^{-5}	6.2	air	NaCl	13	Very small		
5×10^{-4}	6.8	O_2	NaCl	13	0.26	26	1.05
5×10^{-4}	6.8	Ar	NaCl	13	0.10		Probably second order
5×10^{-5}	9.9	O_2	NaCl	13	0.055	106	1.25
5×10^{-5}	4.8	O_2	NaCl	13	~0.01		
5×10^{-5}	6.6	N_2O	NaCl	13	<0.02		
5×10^{-5}	6.8	O_2	NaCl	10	0.035		1.5
5×10^{-5} + 1×10^{-2} *M* H_2O_2	6.7	O_2	NaCl	13	0.64 (0.03 permanent)	Within flash	1.25

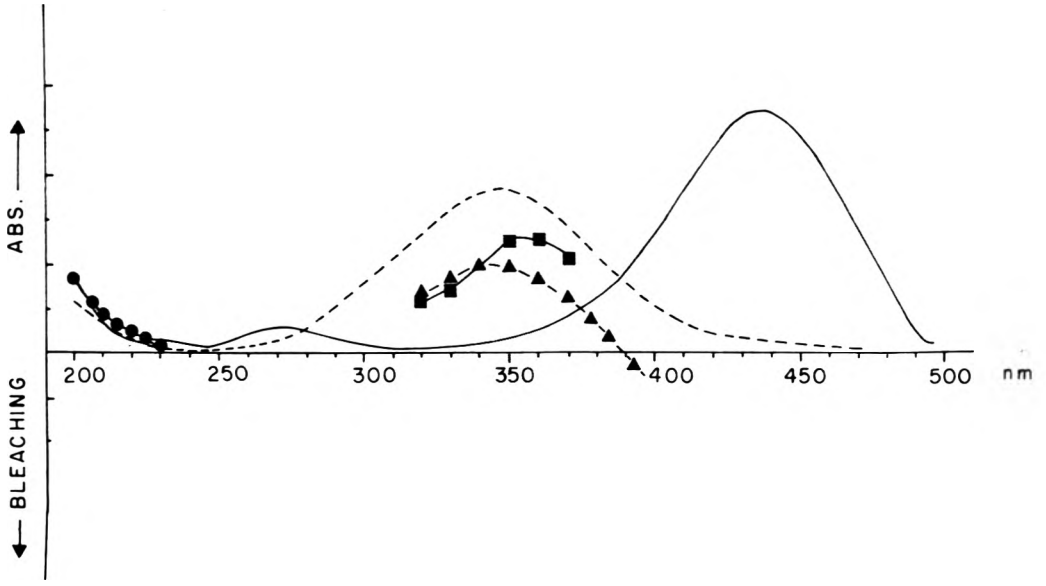

Figure 2. Spectra of aqueous *p*-nitrosodimethylaniline (RNO) and transients found in flash photolysis and pulse radiolysis of these solutions: solid line, spectrum of neutral, air saturated 20 μ*M* RNO; dotted line, spectrum of same concentration RNO solution at pH 1; (●) enhancement of the absorbance of pure liquid water when changing from argon to oxygen saturation (*i.e.*, difference spectrum between oxygen and argon saturated water); (■) spectrum of a flash photolyzed, oxygen-saturated (pH 7), 50 μ*M* RNO solution 150 μsec after initiation of the flash, uncorrected for scattered light and for RNO spectral overlap; (▲) spectrum of pulse radiolyzed, oxygen saturated 20 μ*M* RNO (pH 7) approximately 50 μsec following the electron pulse (taken from ref 7 and normalized, with slight offset, to flash spectrum), also uncorrected for RNO overlap, showing isosbestic point at about 390 nm (bleaching takes place at longer wavelengths).

up in intensity was at ~350 nm in oxygen[13] and N_2O-saturated[8] solutions. However, it was difficult to prove whether or not the pulse radiolysis spectrum was the same as the flash photolysis transient absorption observed within the flash period, since the maximum intensity of the latter was reached during the lifetime of the photolysis flash and kinetic measurements were therefore difficult.

The species responsible for this 350-nm absorption is, therefore, an early, if not primary, product of the photochemical reaction. Decay kinetics for this peak were complex and changed when experimental conditions were changed, although the decay rate was unaffected by decreasing the flash voltage from 13 to 10 kV. No direct correlation was observed under any conditions between the observed transient decay at 350 nm and transient buildup at 540 nm.

An increase in permanent absorption at 350 nm was seen only when the flash was unfiltered, the solution was saturated with nitrous oxide, or when the hydrogen peroxide was added to an oxygenated solution. With added hydrogen peroxide, absorption at 350 nm due to a permanent product was particularly large (approximately half the initial absorbance remained permanently).

540-nm Transient Absorption. The 540-nm absorption increased in intensity after the flash had been fully discharged. Its rate of appearance was approximately pseudo-

first order, increased (nonlinearly) with an increase in RNO concentration and was insensitive to pH changes between 6.8 and 9.9. Buildup half-lives quoted in Table I, although only approximate due to the length of the tail of the photolysis flash, are useful for comparison with one another. The amount of 540-nm absorbance decreased when the gas saturating the solution was changed through the series oxygen, air, argon, and nitrous oxide, and when the pH was dropped to 4.8. However, when H_2O_2 was present (typically 10^{-2} M H_2O_2, 50 μM RNO, O_2 saturated, with NaCl filter), the amount of 540-nm absorption increased greatly (see Table I), and a small amount of a permanent product absorbing at 540 nm remained.

The decay of the 540-nm transient was quite insensitive to changes in experimental conditions, being basically first order with a half-life of $1.2 \pm 0.1_5$ msec over a range of at least several half-lives (Table I). This half-life was independent of RNO concentration, pH (between 6.2 and 9.9), the gas saturating the solution (except Ar + no filter), the presence or absence of a flash filter, or of hydrogen peroxide. The 540-nm spectrum and its decay half-life correspond within experimental error with the spectrum and half-life of the 540-nm transient (1.40 ± 0.2 msec) of oxygen saturated solutions studied with the pulse radiolysis technique.[13]

580-nm Transient. Only in solutions saturated with argon was the 580-nm absorption anything other than part of the 540-nm absorption band. In the presence of argon, its decay kinetics were complex and its maximum intensity greater than that at 540 nm, indicating the presence of another transient species.

Under some conditions, there were other weak absorptions, both transient and permanent, under the main absorption bands described above, but these have not been examined in detail.

Discussion

The similarities between the absorption spectra and kinetics of the transients observed in flash photolysis and pulse radiolysis of aqueous solutions of RNO are many. The first-order lifetime for the spectral transient created by flash photolysis with a maximum absorbance at 540 nm noted in Table I is in excellent agreement with that observed for a similar 540-nm transient in pulse radiolyzed oxygenated solutions of RNO. The 540-nm transient lifetimes are also independent of pH (between 7 and 10) in both systems.[13] In both systems, there is a shift in absorbance maximum from 540 to 580 nm when oxygen is removed from the dilute RNO solutions.[13] Equipment limitations in our flash photolysis studies prevent direct kinetic and spectral comparisons of the 350-nm transient absorptions observed in flash photolysis and pulse radiolysis. However, for oxygenated RNO solutions, the unexpected lack of interdependence between the decay of the 350-nm absorption and the buildup of the 540-nm transient noted during flash photolysis is markedly similar to behavior observed during pulse radiolysis.[7]

When dilute solutions of RNO are radiolyzed, the energy is absorbed almost exclusively in the water, producing the reactive transients H·, ·OH, and e_{aq}^-. When oxygen is present in excess of the RNO (*e.g.*, in 1250 μM O_2, 50 μM RNO solutions), both e_{aq}^- and H react preferentially with the dissolved oxygen forming O_2^- and HO_2, neither of which have been found to react directly with RNO.[2,7,8] Thus, in pulse radiolyzed oxygen-saturated, 20–50 μM RNO solutions, the only species which is able to react with RNO at early times to any great extent is apparently the OH radical. These kinetic arguments are the basis for the frequent use of RNO as a competitive OH radical scavenger in radiation chemistry studies.[3,14,15] Thus, the 350-nm transient observed in pulse radiolysis of RNO has been ascribed to the OH radical adduct of RNO[7,8] since it is formed with a rate constant close to that anticipated for OH radicals reacting with aromatic compounds (of the order of 10^{10} M^{-1} sec^{-1}).[14]

The origin of the 540-nm transient is probably associated directly or indirectly with the OH radical since, in flash photolysis, its intensity (and also that of the 350-nm transient absorption) is enhanced to a large degree by the addition of hydrogen peroxide to photolyzed solutions. Hydrogen peroxide has been shown to be photolyzed at these wavelengths to produce OH radicals by a number of studies,[16] including one with RNO.[6] Addition of ethanol eliminates the growth, following the flash, of the 540-nm transient in these peroxide-containing solutions. Preliminary studies[17] involving the separation and the kinetics of formation of the permanent products of radiolysis and photolysis (in the presence and absence of added hydrogen peroxide) of aqueous RNO solutions indicate quite similar relative yields and kinetics of formation of at least two products in all three systems. These experimental observations reinforce speculation that there are common reactive intermediate(s) producing these products during the photolysis and radiolysis of aqueous RNO.

If the main transients observed in pulse radiolysis and flash photolysis are identical, as appears to be the case with the 540-nm transient, then, as indicated above, the possibility exists that the precursors of these transients are also identical. This is, at first glance, unexpected since, in RNO photolysis, the majority of the photons are absorbed by RNO. However, it has been demonstrated both in this work and elsewhere[2,4,6] that, at wavelengths above 230 nm, the RNO molecule is relatively resistant to photochemical decompositon despite its rather large extinction coefficients in the visible and ultraviolet region of the spectrum. No fluorescence or phosphorescence was detected in oxygen- or argon-containing solutions when these were excited by light of wavelenths between 230 and 500 nm.[18] RNO is also the only reported nitroso compound which does not trap its own excited state to form a nitroxide radical.[19] Since the $n-\pi^*$ band strongly overlaps the 440-nm charge transfer band, which, in turn, overlaps the higher energy bands, there may be present in the RNO molecule an efficient channel for conversion of electronic energy into thermal energy, thus making RNO a very photoresistant molecule, possibly even to wavelengths as low as 200 nm, as will be postulated in the later discussion.

While we cannot completely rule out an electronically excited state as the identity of the 350-nm transient or of its precursor, it is difficult to see how this would lead to the appearance of a transient absorption which as stated earlier, resembles and might well be the same as that of the postulated RNO–OH adduct observed after pulse radiolysis.[7,8] Instead, the evidence would appear to be in favor of the primary photolytic reaction being either direct photoionization of RNO (by wavelengths below 230 nm):

$$RNO \xrightarrow{h\nu} RNO^+ + e_{aq}^- \qquad (1)$$

or photolysis of water

$$H_2O \xrightarrow{h\nu} H_2O^+ + e_{aq}^- \quad (2)$$

$$H_2O \xrightarrow{h\nu} H\cdot + \cdot OH \quad (3)$$

followed by reaction of the resulting reactive intermediates with RNO and/or O_2.

Direct RNO photoionization may have been responsible for the very small, but finite, amount of RNO bleaching noted during its steady-state photolysis by wavelengths above 230 nm when using an acetate filter. However, the much more significant amount of photodecomposition of RNO seen when irradiating continuously with wavelengths *below* 230 nm which was shown to be essentially first order in (O_2) and zero order in (RNO) tends to rule out reaction 1 as the predominant primary process for this bleaching unless, of course, a number of secondary or tertiary reactions combine to yield such a simple concentration dependence. We observed essentially the same oxygen concentration dependence for both the yield of steady-state RNO photobleaching at 440 nm and the maximum yields of the 350- and 540-nm transient absorptions following the photolysis flash. We are, therefore, inclined to believe that the observed oxygen effect arises from the same primary process. No such oxygen concentration dependence is noted in pulse radiolysis studies;[13] *i.e.*, there is no change in the "yield" of the maximum absorbance at 540 or 350 nm following the electron pulse when changing from air-saturated to oxygen-saturated solutions of RNO.

We have observed a long wavelength cutoff of approximately 230 nm for three different photolytic phenomena: (1) the approximately zero order in (RNO) and first order in (O_2) reaction kinetics of bleaching at 440 nm of aqueous RNO solutions during steady-state photolysis; (2) the appearance of transient absorption spectra at 350, 540, and 580 nm in flash photolyzed aqueous RNO solutions; and (3) the enhancement of the ultraviolet absorption spectrum of pure water by oxygen (see Figure 2) first observed by Heidt and Ekstrom[12] and confirmed to be approximately first order in oxygen concentration in our laboratory. These three observations, taken together with the similarities noted regarding the spectra and kinetics of RNO transients in flash photolysis and pulse radiolysis, lead us tentatively to conclude that the predominant primary photolytic process in the photolysis of aqueous RNO solutions with wavelengths between 200 and 230 nm is the direct photolysis of water, *i.e.*, reaction 2 and/or reaction 3, and not the direct photolysis of RNO.

Anbar and coworkers[20,21] have demonstrated that, in the presence of electron scavengers, oxygen-free water is photolyzed to produce measurable hydrated electrons with a quantum yield of 0.08 at ~182 nm. This yield is much higher than that reported by Boyle, *et al.*[22] (ϕ = 0.004), at 184 nm for the yield of hydrated electrons in flash photolyzed, pure water. These differences in quantum yield have been attributed by Anbar, *et al.*,[20,21] to scavenging of hydrated electrons which would have otherwise undergone geminate recombination with H_2O^+ or OH radicals in the absence of the relatively high concentrations of hydrated electron scavengers used in their studies.

As seen in Figure 3, the wavelength dependence of oxygen-free water absorption and of hydrated electron quantum yield, measured up to 204 nm by Anbar, *et al.*[20,21] correlate well with each other and also with the wavelength dependence of the *enhancement* of absorbance caused by dissolved oxygen. From their results, Anbar, *et al.*, have extrapolated the cutoff for pure water photolysis to 205 nm. From our results with oxygen effects, especially the similarity between the first-order dependence on oxygen of the enhancement of the spectral absorbance of water and of the yields of steady-state RNO photobleaching, it would appear that the primary processes 2 and 3 in all probability extend to wavelengths as high as 230 nm, at least when oxygen is present.

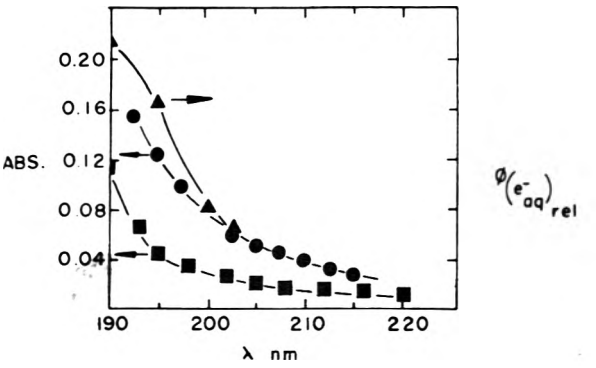

Figure 3. Wavelength dependence of various photochemical processes in liquid water: (■) absorbance of pure oxygen-free water in 1-cm path cell (from ref 25); (●) *increase* induced by oxygen in the absorbance of water, found from difference spectra (1-cm path) between Ar-saturated and oxygen-saturated water; (▲) yields (relative to that for water at 190 nm) of hydrated electrons scavenged by SF_6 dissolved in photolyzed water (taken from ref 21).

As seen in Figure 3, the enhancement of the spectral absorption of water by oxygen has essentially the same wavelength dependence as the absorption spectrum of oxygen-free water itself. Therefore, it would appear that oxygen enhances rather than changes the electronic energy transitions which occur in the absence of oxygen and/or shifts them to a slightly lower energy. Anbar and coworkers[20,21] have postulated that both reactions 2 and 3 arise from a single common excited state water precursor. This leads us to suggest that only *one* electronic transition of water is responsible for the water absorbance in the region between 190 and 230 nm and that the tail of this absorption band belongs to the same electronic transition observed by Anbar and coworkers. We believe the excitation process responsible for the spectral tail and its enhancement by oxygen is being monitored by the reaction of the products of reactions 2 and 3 with RNO. If this is true, it would appear that RNO itself is remarkably resistant to photons of all wavelengths above 200 nm with only a very small amount of direct photolysis of RNO occurring. Below 200 nm the kinetics of the photolytic system are much more complex and direct photolysis of the RNO may, indeed, occur at these higher photon energies.

The chemical identity of the 350-, 540-, and 580-nm transients observed in pulse radiolysis and flash photolysis is still in doubt because of the lack of identification of products and because of the complex kinetic behavior observed. The mechanisms reported for the pulse radiolysis of other aromatic nitroso and nitro compounds[23,24] are not very helpful since with these compounds the type of kinetic complexities encountered with RNO do not arise.

The apparently independent decay of the 350-nm transient and growth of the 540 nm one (in oxygenated RNO solutions) is particularly puzzling. This is because the OH radical would appear to be the only species capable of reacting with RNO at early times after pulse radiolysis and, presumably, after flash photolysis if reactions 2 and/or reaction 3 represent the primary photolytic processes.

Dainton and Wiseall[7] gave no explanation for the 540-nm species observed in pulse radiolysis, and Baxendale and Kahn[8] did not report its existence. While our flash photolysis work has not revealed the identity of this species, we have shown that it is probably the same species as observed in pulse radiolysis, its decay kinetics being very similar in both systems. It has also been observed that in both photolysis and radiolysis systems when the 350-nm transient has *nearly* reached its maximum absorbance, the 540-nm transient has only reached approximately 30% of its maximum absorbance.

Bearing in mind that our evidence is scant for assuming that the flash photolysis and pulse radiolysis transients absorbing at 350 nm are the same, it has been noticed that this absorption has some similarity with the absorption spectrum of RNO in acid solution, that is of $RNOH^+$ (see Figure 2). The isosbestic point at 390 nm which appears in the protonated *vs.* neutral RNO spectrum and in the spectra recorded during pulse radiolysis experiments also correspond. With a pK of 3.7, $RNOH^+$ would have too short a lifetime at the pH of our solutions to be detectable with the flash photolysis apparatus used. However, RNO^+ could have an absorption spectrum resembling that of $RNOH^+$ and we would like to suggest that the species responsible for the 350-nm transient absorption might be RNO^+, although this differs from the conclusion reached after earlier pulse radiolysis studies[7,8] that the 350-nm transient absorption then observed was due to an RNO–OH adduct.

We have considered a reaction mechanism of the following general form:

$$H_2O \xrightarrow{h\nu} X \quad (4)$$

$$X + RNO \longrightarrow Y + \text{350-nm transient} \quad (5)$$

$$Y + RNO \longrightarrow \text{540-nm transient} \quad (6)$$

If the rate constants for reactions 5 and 6 are of the same order of magnitude, this would result in the observed delayed appearance of the 540-nm transient at a rate that was apparently unrelated to the decay of the 350-nm absorption. However, there are some inconsistencies, and this mechanism has not been rigorously tested nor have X and Y been identified. Nonetheless, it is tempting to speculate that X might be H_2O^+, Y an OH radical, and the 540-nm transient an RNO–OH adduct, although there is strong sentiment against the lifetime of H_2O^+ being long enough for significant reaction to occur with the low concentration of RNO used.

A reviewer has pointed out to us the report of Boyle, Ghormley, and Hochanadel[26] on the flash photolysis of oxygenated aqueous solutions in approximately the same wavelength region as our studies. They report observing the spectrum of H atoms in flash photolyzed water and the production of ozone in the flash photolysis of oxygenated water. The latter observation is unexpected if one considers the primary photolytic products to be only e_{eq}^-, H·, and ·OH. It is possible that H_2O^+ may react in some manner in their solutions to form a precursor to ozone.

Further studies are needed on the identification and kinetics of formation of the photolysis and radiolysis products of aqueous RNO solutions. It would appear that RNO is a remarkably photoresistant molecule and that it may be used to probe the primary processes occurring during the photolysis of water in the region above 200 nm. Quantum yields for water photolysis are uncertain in this spectral region, but even though they are probably relatively low at the longer wavelengths, they may well be significant enough to be important in processes occurring in natural waters and to be relevant to theories concerning the origin of life.[20,21] It is possible that the hydrated electron and the OH radical are produced at wavelengths even above 230 nm since the tail of the absorption band of water appears to be exponential.

Acknowledgments. This research was supported in part by the U.S. Atomic Energy Commission and by Public Health Service Grant No. CA-08888 from the National Cancer Institute held by C.N.T. while at the Institute of Cancer Research, Sutton, Surrey, England. Special thanks are due to Professor J.W. Boag and Dr. Martin Fielden and members of the Institute for Cancer Research for their kind hospitality, the use of their facilities and equipment, and for discussions and encouragement. We are indebted to Professor George Porter and Dr. Paul Suppan for first suggesting that water, rather than RNO, might be the species being photolyzed.

References and Notes

(1) Supported in part by the U.S. Atomic Energy Commission.
(2) I. Kraljic and C. N. Trumbore, *J. Amer. Chem. Soc.*, **87**, 2547 (1965).
(3) M. Anbar, D. Meyerstein, and P. Neta, *J. Chem. Soc. B*, 742 (1966).
(4) I. Kraljic in "The Chemistry of Ionization and Excitation," G. Johnson and G. Scholes, Ed., Taylor and Francis, London, 1967, p 303.
(5) S. Shah, C. N. Trumbore, B. Geissner, and W. Park, *Advan. Chem. Ser.*, **No. 81**, 321 (1968).
(6) M. Hatada, I. Kraljic, A. El Samahy, and C. N. Trumbore, *J. Phys. Chem.*, **78**, 888 (1974).
(7) F. S. Dainton and B. Wiseall, *Trans. Faraday Soc.*, **64**, 694 (1968).
(8) J. H. Baxendale and A. A. Kahn, *Int. J. Radiat. Phys. Chem.*, **1**, 11 (1969).
(9) R. J. Kobrin, Ph.D. Thesis, University of Delaware, Newark, Delaware, 1969.
(10) (a) E. J. Hart and J. K. Thomas, Report No. ANL-7856, Argonne, Ill., Sept 1971; (b) E. J. Hart and M. Anbar, "The Hydrated Electron," Wiley-Interscience, New York, N.Y., 1970, Chapters IX and X; (c) E. J. Hart, S. Gordon, and J. K. Thomas, *J. Phys. Chem.*, **68**, 1271 (1964).
(11) P. Suppan and A. Kelly, private communication.
(12) L. J. Heidt and L. Ekstrom, *J. Amer. Chem. Soc.*, **79**, 1260, 5588 (1957).
(13) C. N. Trumbore, unpublished results.
(14) M. Anbar and P. Neta, *Int. J. Appl. Radiat. Isotopes*, **18**, 493 (1967).
(15) L. M. Dorfman and G. E. Adams, *Nat. Stand. Ref. Data Ser., Nat. Bur. Stand.*, **No. 46** (S D Catalog No. C13.48:46).
(16) (a) J. H. Baxendale and J. A. Wilson, *Trans. Faraday Soc.*, **53**, 344 (1957); (b) J. L. Weeks and M. S. Matheson, *J. Amer. Chem. Soc.*, **78**, 1273 (1956); (c) D. H. Volman and J. C. Chen, *ibid.*, **81**, 4141 (1959); (d) J. P. Hunt and H. Taube, *ibid.*, **74**, 5999 (1952); (e) M. Daniels, *J. Phys. Chem.*, **66**, 1473 (1962).
(17) A. Lindemanis and A. El Samahy, unpublished results.
(18) W. Youngblade, M.S. Thesis, University of Delaware, 1972.
(19) Th. A. Wajer, A. Machor, T. J. deBoer, and J. D. vanVoorst, *Tetrahedron*, **23**, 4021 (1967).
(20) M. Anbar, G. A. St. John, H. R. Gloria, and R. F. Reinisch in "Water Structure at the Water-Polymer Interface," H. H. G. Jellinek, Ed., Plenum Press, New York, N.Y., 1972, p 85.
(21) M. Anbar and G. A. St. John, NASA Report NASA-CR-1935, Oct 1971.
(22) J. W. Boyle, J. A. Ghormley, C. J. Hochanadel, and J. F. Reilly, *J. Phys. Chem.*, **73**, 2886 (1969).
(23) K. D. Asmus, G. Beck, A. Henglein, and A. Wigger, *Ber. Bunsenges. Phys. Chem.*, **70**, 869 (1966).
(24) K. D. Asmus, B. Cercek, M. Ebert, and A. Henglein, *Trans. Faraday Soc.*, **63**, 2435 (1967).
(25) F. Williams, S. Hellinius, and S. P. Varma, submitted for publication.
(26) J. W. Boyle, J. A. Ghormley, and C. J. Hochanadel, Progress Report, Chemistry Division, Oak Ridge National Laboratory, ORNL-4437, May 20, 1969.

Spectroscopic and Kinetic Investigations on the Interaction of Tertiary Amines with Chloranil

Satish B. Shah and A. S. N. Murthy*

Department of Chemistry, Birla Institute of Technology and Science, Pilani, Rajasthan 333031, India
(Received April 1, 1974; Revised Manuscript Received November 11, 1974)

The interaction between triethylamine and chloranil has been studied in different solvents by electronic absorption spectroscopy. The kinetics and energetics of the electron transfer reaction in chloroform and acetonitrile leading to the formation of chloranil anion radical and subsequently the product, *N,N*-diethylaminovinyltrichloro-*p*-benzoquinone, have been estimated. The products in methanol and ethanol are different. The interaction of chloranil with triisopropylamine and tri-*n*-butylamine leads only to the formation of chloranil anion radical.

Introduction

Although molecular interactions between electron donors and acceptors have been the subject of exhaustive study,[1] considerable attention has recently been directed toward finding the possible role of electron donor–acceptor (EDA) complexes or charge-transfer (CT) complexes in chemical reactions.[2-4] The chemical reaction between electron donor (D) and electron acceptor (A) may occur through the formation of outer (π) and inner (σ) complexes as reaction intermediates, which are represented as (D,A) and (D^+,A^-), respectively. Nagakura and coworkers[5] studied the reaction between aniline and substituted anilines with chloranil and suggested that substitution reactions occur through outer and inner complexes. No spectral evidence was, however, presented for the inner complex. It is, however, possible that a chemical reaction may also proceed by an electron transfer from the donor to the acceptor and subsequent formation of the ionized species, D^+ and A^- (radical ions), as reaction intermediates in solvents of high ionizing power. The importance of such an ionization process in a chemical reaction was emphasized by Kosower.[3] The ionized species have characteristic absorption spectra in the visible region. For example, in the reaction between tetramethyl-*p*-phenylenediamine (TMPD) and chloranil in methanol,[2] the bands at 426 and 452 nm have been assigned to the chloranil anion radical (semiquinone ion I) and those at 568 and 616 nm to the cation radical,

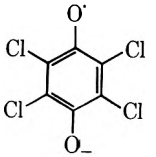

I

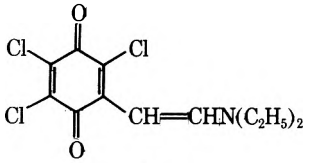

II

$TMPD^+$. Calvin and coworkers[6] found spectroscopic evidence for the formation of radical ions in the reaction between *N,N*-dimethylaniline and chloranil. Certain biomolecules were also found to form the semiquinone ion with chloranil.[7]

Buckley and coworkers[8] studied the reaction between triethylamine and chloranil in benzene solution and presented a mechanism for the formation of the product, *N,N*-diethylaminovinyltrichloro-*p*-benzoquinone (II). They suggested the possible role of the charge transfer complex formed between triethylamine and chloranil in the reaction, although the spectral evidence was not presented. Their absorption spectral curves do not show any evidence for the formation of radical ions. Yamaoka and Nagakura[9] studied the interaction of *n*-butylamine and tri-*n*-butylamine with chloranil in ethanol by a rapid scan-spectrophotometric method and obtained evidence for the formation of chloranil radical anion. The rates of ionization and activation energy for only one amine were determined by a conductometric method. Dwivedi and Rao[10] determined the kinetics and energetics of electron transfer reactions in a few electron donor–acceptor systems and found them to be solvent sensitive.

Although the mechanism for the reaction between triethylamine and chloranil was presented[2,8] in sufficient detail, the lack of experimental evidence either for the charge-transfer complex or for the ionized species besets the validity of such a mechanism. A detailed understanding of the nature of the reaction seems to be necessary in order to correlate with the results obtained with other amines.[9] The present study was undertaken with that view. The studies were carried out in various solvents, such as chloroform, acetonitrile, methanol and ethanol, in order to examine the influence of the solvent. The kinetics and energetics for a few electron transfer reactions were determined from spectral data.

Experimental Section

Chloranil was recrystallized either from benzene or acetone and dried under vacuum (mp 289°). Triethylamine (Riedel) was refluxed with acetic anhydride and distilled under reduced pressure. The fraction ranging in boiling point from 88.5 to 89.5° was collected. Triisopropylamine (Fluka) was used without further purification. Tri-*n*-butylamine (Riedel) was purified in the same manner as triethylamine. The fraction ranging in boiling point from 217 to 218° was used. The solvents benzene, chloroform, acetonitrile, methanol, ethanol, and acetone were purified by standard methods.[11]

Electronic absorption spectra were recorded employing a Perkin-Elmer-Hitachi 139 spectrophotometer equipped with a temperature-regulated cell holder. The temperature was kept constant to within ±0.5° by circulating water from a thermostat through the cell holder. The stock solutions were freshly prepared on the day of measurement and

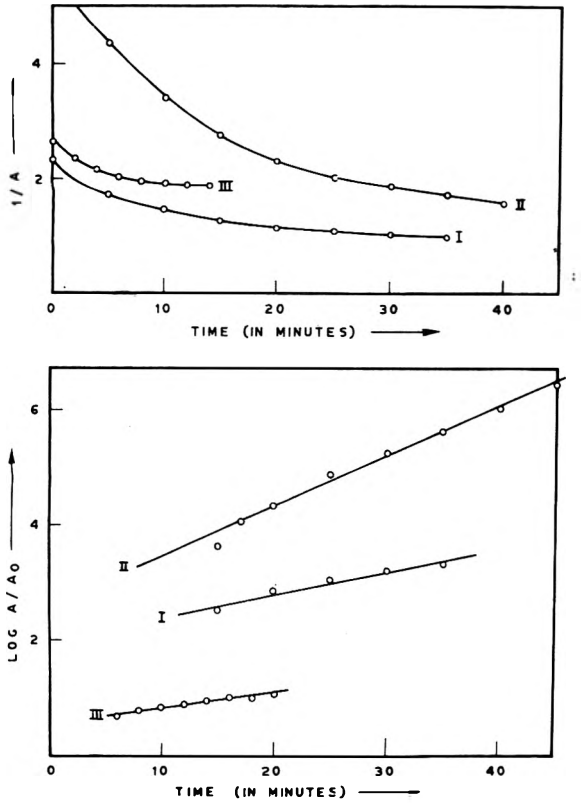

Figure 1. Typical first-order rate plots for the reaction of chloranil with triethylamine (I and II) and triisopropylamine (III) in chloroform at 20°.

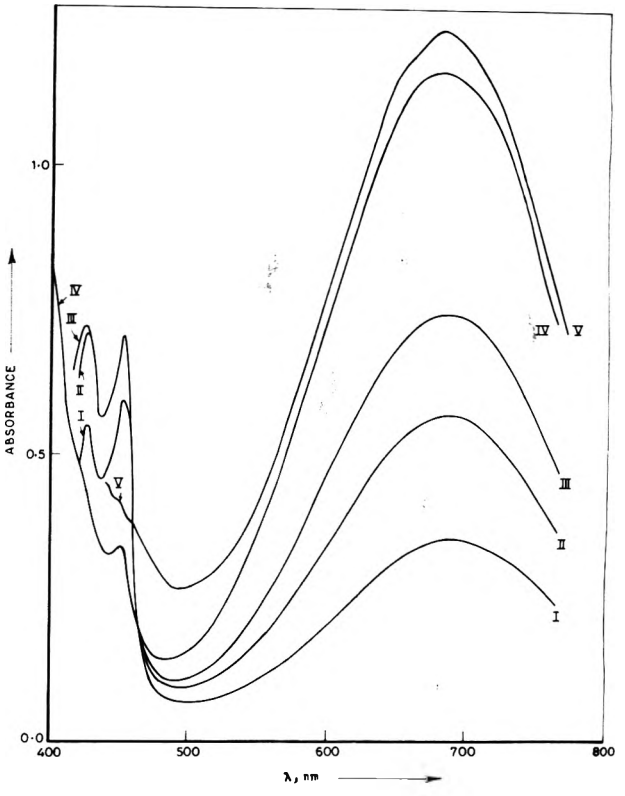

Figure 2. Absorption spectra of chloranil–triethylamine system in chloroform (chloranil 5.0 × 10^{-4} *M* and triethylamine 5.0 × 10^{-2} *M*): (I) immediately after mixing; (II) after 30 min; (III) after 1 hr; (IV) after 3.5 hr; and (V) after 24 hr.

were kept in the dark except during sampling. Matched quartz cells (stoppered) of 1-cm path length were used. The kinetics for the formation of chloranil anion radical (I) and product (II) have been determined by following the variation of the absorbance of the 426- and 680-nm bands, respectively. The absorbance of various species was taken as directly proportional to their respective concentrations. The absorbance data fit very well for a first-order reaction. Typical plots are shown in Figure 1. The specific rate constants were evaluated from the following first-order equation

$$K = \frac{2.303}{t} \log \frac{A_\infty - A_0}{A_\infty - A_t}$$

where A_0, A_t, and A_∞ are absorbances at zero time, at time t, and at the end of the reaction. The energy of activation was obtained by determining the rate constants at two different temperatures. The entropy of activation, ΔS^*, was evaluated from the relation $\Delta G = \Delta H - T\Delta S^*$.

Infrared spectra in chloroform solution were recorded with a Perkin-Elmer 237B infrared spectrometer using sodium chloride cells.

Results and Discussion

Absorption Spectral Changes in the Reaction of Triethylamine with Chloranil. The reaction between triethylamine and chloranil was investigated spectroscopically in chloroform and acetonitrile. When triethylamine is mixed with chloranil either in chloroform or acetonitrile (triethylamine 5 × 10^{-2} *M* and chloranil 5 × 10^{-4} *M*), the color of the solution was yellow and the spectrum taken immediately after mixing showed bands at 426, 452, and 680 nm. The bands at 426 and 452 nm can be assigned to chloranil anion radical.[2] The spectra of Buckley and coworkers[8] do not show the characteristic bands due to anion radical in benzene. Foster[12] and Pott and Kommandeur[13] isolated a green solid from the binary mixture of the two components and found the infrared spectrum identical with that of the sodium salt of chloranil. The intense 680-nm absorption band, in accordance with Buckley and coworkers,[8] was assigned to product II.

The same solutions turned light green in 30 min, green in 1 hr, and dark green in 3.5 hr. The intensity (in terms of molecular extinction coefficient, ϵ) of the 426- and 452-nm bands increased as the color changed from yellow to green. The intensity of the 680-nm band also increased with time. After 24 hr, the absorption due to chloranil radical anion considerably decreased accompanied by an increase in the intensity of 680-nm absorption. After more than 24 hr, although the characteristic bands around 426- and 452-nm disappeared, there is still considerable absorption in that range. No solid was, however, formed in the course of the reaction. The results in chloroform as solvent are shown in Figure 2. It can be seen from the spectral curves of Figure 2 that an approximately constant concentration of chloranil anion radical is reached in 1 hr and completely disappears by 3.5 hr. After 3.5 hr, although the absorption due to the chloranil anion radical has disappeared, the spectral curves (curves IV and V) show an increased absorbance. This is indeed surprising and we cannot currently offer any reasonable explanation for this behavior. We may, however, attribute it to the tail portion of a highly intense ($\epsilon \approx 1.15 \times 10^5$) absorption band that appears around 320 nm, as shown in Figure 3. This band was found to increase in intensity with time along with the 680-nm band. The origin of the 320-nm band is not immediately clear. It was conclu-

TABLE I: Kinetic Data on the Reactions of Chloranil with Trialkylamines in Chloroform

Electron donor	Specific rate constant, 10^4K (293°K), sec^{-1}		Energy of activation, E_a, kJ mol^{-1}		Entropy of activation, ΔS^*, J K^{-1} mol^{-1}	
	Chloranil anion radical	Product	Chloranil anion radical	Product	Chloranil anion radical	Product
Triethylamine	8.2	3.1	12.3	27.9	−101.0	−162.5
Triisopropylamine	26.5		30.0		−152.0	
Tri-*n*-butylamine	12.8		22.8		−133.0	

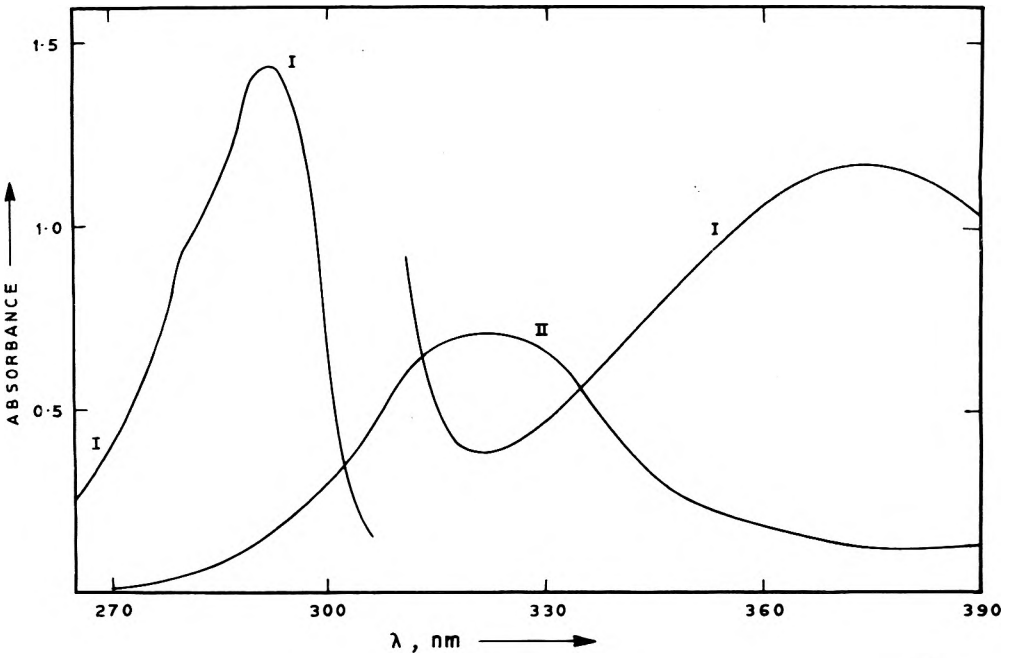

Figure 3. Absorption spectra of (I) chloranil (6.3×10^{-6} *M*) and (II) chloranil (6.3×10^{-6} *M*) + triethylamine (6.3×10^{-4} *M*) *vs.* chloranil (6.3×10^{-6} *M*). For the 375-nm band of chloranil, the concentration employed is 1×10^{-3} *M*. The absorbance scale for this is not shown (the solvent was chloroform).

sively shown that it is not a charge transfer band.[7] A similar band was observed in the interaction of chloranil with amino acids and proteins in water or 50% ethanol.[7,14] Purines and pyrimidines also behaved in a similar way in dimethyl sulfoxide solution.[15]

These spectral changes clearly indicate that electron transfer occurs from triethylamine to chloranil even in a relatively nonpolar solvent such as chloroform prior to the formation of the reaction product. A donor–acceptor complex is presumably formed, for which experimental evidence is lacking. In benzene the absorption due to chloranil radical anion was not observed.

The kinetics of the triethylamine–chloranil reaction in chloroform have been determined from the spectroscopic data. The data are presented in Table I. The energies of activation, E_a, are relatively small and entropies of activation, ΔS^*, are large negative numbers. Many electron transfer reactions show such a behavior.[16] The large negative entropy of activation is probably due to a transition state which is more polar than the initial state (donor–acceptor complex). A similar trend was noticed by Dwivedi and Rao.[10] It is interesting to note that the difference in rate constants and activation energies for the electron transfer reaction and for the formation of the product is quite large. This difference is probably due to the difference in the polarities of the transition states of the two processes.[10]

The interactions of triisopropylamine and tri-*n*-butylamine with chloranil has also been investigated in chloroform. The spectra (Figures 4 and 5) show the characteristic bands due to the chloranil anion radical. No characteristic absorption for the formation of final product (around 680 nm) was observed even after a long time. In fact, there was no marked absorption beyond 500 nm. Thus, triisopropylamine and tri-*n*-butylamine react with chloranil to give only the chloranil anion radical. The kinetic data are shown in Table I. The large rate constant and activation energy for the formation of anion radical with triisopropylamine is possibly because of its low ionization potential as compared to that of triethylamine. The relatively low rate constant in case of tri-*n*-butylamine is probably due to steric factors. A high rate constant was found for the chloranil–triisopropylamine system in acetonitrile. This, as one would expect, is possible due to the high polarity of the solvent.

Chloranil and triethylamine seem to interact differently in hydroxylic solvents. The absorption spectra of triethylamine–chloranil system in ethyl alcohol (Figure 6) shows bands at 425 and 452 nm due to the chloranil anion radical. The spectra also show a broad band centered around 550 nm. This band is not due to the expected product, *N,N*-diethylaminovinyltrichloro-*p*-benzoquinone (II). Slifkin and coworkers[7,15] have found that mixture of chloranil with thymine or adenine in dimethyl sulfoxide gave a band at 520 nm. This was attributed to the formation of trichlo-

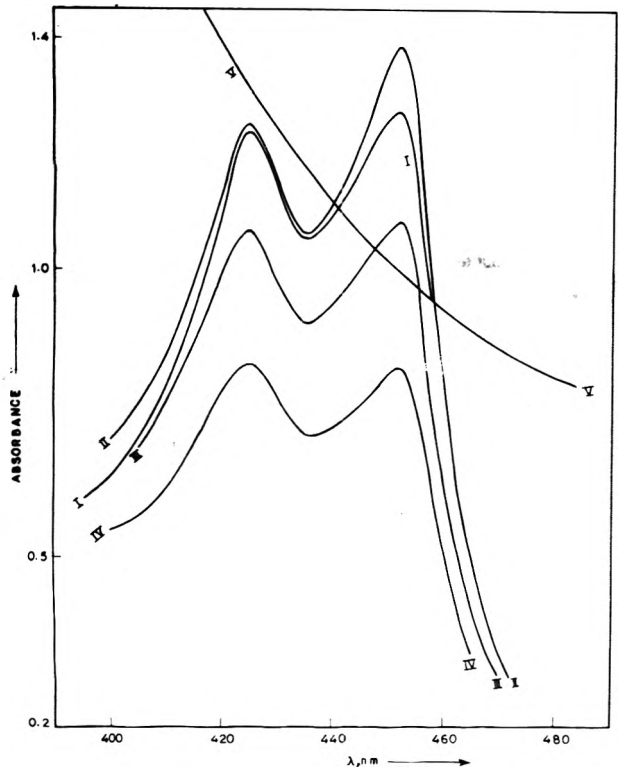

Figure 4. Absorption spectra of chloranil–triisopropylamine system in chloroform (chloranil 5.08 × 10^{-4} *M* and triisopropylamine 4.97 × 10^{-2} *M*): (I) immediately after mixing; (II) after 10 min; (III) after 20 min; (IV) after 30 min; and (V) after 24 hr.

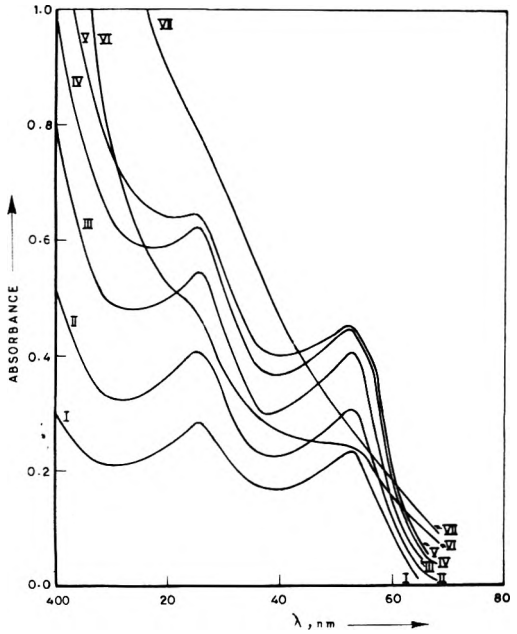

Figure 5. Absorption spectra of chloranil–tri-*n*-butylamine system in chloroform (chloranil 3.42 × 10^{-4} *M* and tri-*n*-butylamine 4.02 × 10^{-2} *M*): (I) immediately after mixing; (II) after 10 min; (III) after 20 min; (IV) after 30 min; (V) after 50 min; (VI) after 4.5 hr; and (VII) after 24 hr.

rohydroxyquinone. So we expect that a different reaction is taking place between chloranil and triethylamine in ethyl alcohol giving trichlorohydroxyquinone, whose spectral absorption was shifted to 550 nm. Similar behavior was also noticed in methanol.

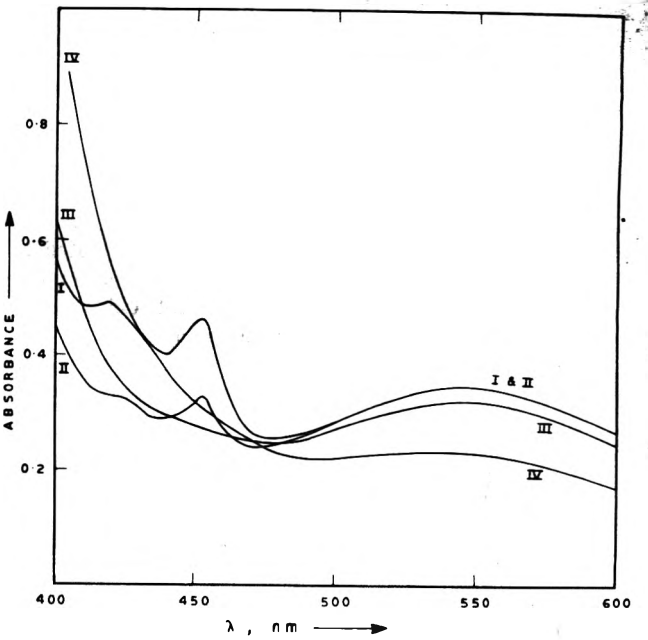

Figure 6. Absorption spectra of chloranil–triethylamine system in ethyl alcohol (chloranil 5.1 × 10^{-4} *M* and triethylamine 5.1 × 10^{-2} *M*): (I) immediately after mixing; (II) after 30 min; (III) after 5.5 hr; and (IV) after 24 hr.

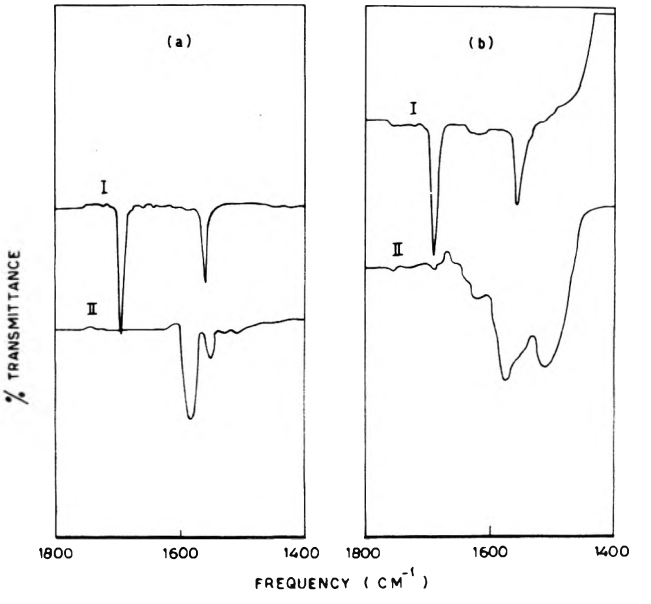

Figure 7. Infrared spectra of chloranil–triethylamine system in (A) chloroform and (B) acetonitrile. Curve 1 refers to the spectra of chloranil alone and curve 2 refers to the spectra of chloranil–triethylamine mixture after 1 hr of reaction.

The infrared spectra of triethylamine–chloranil and triisopropylamine–chloranil mixtures were recorded in chloroform and acetonitrile in the 1800–1400-cm^{-1} region. The infrared spectra for the triethylamine–chloranil system in chloroform and acetonitrile are shown in Figure 7. It can be seen that the C=O stretching vibration of chloranil at 1690 cm^{-1} disappears and a new band around 1560 cm^{-1} appears. A similar behavior is noticed in acetonitrile also. The 1560-cm^{-1} band is due to the chloranil anion radical, as confirmed from the infrared spectrum of the lithium salt of chloranil by Matsunaga.[17] Recently Iida[18] recorded the infrared spectrum of chloranil and its potassium salt and car-

ried out normal vibration analysis. He has also observed the disappearance of the C=O stretching vibration.

Among the many electron transfer reactions that have been reported so far in the literature, only the reaction between tertiary amines and chloranil shows evidence for the formation of a radical ion in a relatively nonpolar solvent such as chloroform. This is probably due to the fact that tertiary amines are the strongest donors toward many electron acceptor.[19] A similar observation has been noted for phenothiazine complexes with the acceptors tetracyanoquinodimethane, tetracyanoethylene, bromanil, chloranil, *p*-benzoquinone, and *m*-dinitrobenzene in chloroform.[20]

References and Notes

(1) R. S. Mulliken and W. B. Person, "Molecular Complexes," Wiley-Interscience, New York, N.Y., 1969.
(2) R. Foster, "Organic Charge Transfer Complexes," Academic Press, New York, N.Y., 1969.
(3) E. M. Kosower, "Progress in Physical Organic Chemistry," S. Cohen, A. Streitweiser, and R. W. Taft, Ed., Interscience, New York, N.Y., 1965.
(4) C. N. R. Rao and A. S. N. Murthy, "Spectroscopy in Inorganic Chemistry," Vol. I, C. N. R. Rao and J. R. Ferraro, Ed., Academic Press, New York, N.Y., 1970, p 107.
(5) T. Nogami, K. Yoshihara, H. Hosoya, and S. Nagakura, *J. Phys. Chem.*, **73**, 2670 (1969).
(6) J. W. Estman, G. Engelsma, and M. Calvin, *J. Amer. Chem. Soc.*, **84**, 1339 (1962).
(7) M. A. Slifkin, "Charge Transfer Interactions in Biomolecules," Academic Press, New York, N.Y., 1971.
(8) D. Buckley, S. Dunston, and H. B. Henbest, *J. Chem. Soc.*, 4880 (1957).
(9) T. Yamaoka and S. Nagakura, *Bull. Chem. Soc. Jap.*, **44**, 1780 (1971).
(10) P. C. Dwivedi and C. N. R. Rao, *J. Chem. Soc., Perkin Trans. 2*, 238 (1972).
(11) "Techniques of Organic Chemistry," Vol. VII, "Organic Solvents," A. Weissberger, Ed., Interscience, New York, N.Y., 1955.
(12) R. Foster, *Recl. Trav. Chim. Pays. Bas*, **83**, 711 (1964).
(13) G. T. Pott and J. Kommandeur, *Mol. Phys.*, **13**, 343 (1967).
(14) J. B. Birks and M. A. Slifkin, *Nature (London)*, **197**, 42 (1963).
(15) M. A. Slifkin, *Biochim. Biophys. Acta*, **103**, 365 (1965).
(16) A. A. Frost and R. G. Pearson, "Kinetics and Mechanism," 2nd ed, Wiley, New York, N.Y., 1961.
(17) Y. Matsunaga, *J. Chem. Phys.*, **41**, 1609 (1964).
(18) Y. Iida, *Bull. Chem. Soc Jap.*, **43**, 345 (1970).
(19) C. N. R. Rao, S. N. Bhatt, and P. C. Dwivedi, *Appl. Spectrosc. Rev.*, **5**, 1 (1971).
(20) A. Fulton and L. E. Lyons, *Aust. J. Chem.*, **21**, 873 (1968).

Photochemistry of Copper Complexes. The Copper(II) Malonate System

J. Y. Morimoto and B. A. DeGraff*[1]

Department of Chemistry, University of Virginia, Charlottesville, Virginia 22903 and
Department of Chemistry, Madison College, Harrisonburg, Virginia 22801

(Received July 5, 1974)

Publication costs assisted by Madison College

The photochemistry of the aqueous copper(II) malonate system in the charge-transfer spectral region has been investigated using continuous and flash illumination techniques. Photolysis of either copper(II) malonate or bismalonatocuprate(II) results in photoredox yielding acetate and carbon dioxide without permanent reduction of the copper(II). Both complexes yielded detectable transients on flashing with λ_{max} 375 ± 5 nm and 390 ± 5 nm for the copper(II) malonate and bismalonatocuprate(II), respectively. Both transients decayed rapidly *via* pseudo-first-order kinetics under the prevailing experimental conditions. Resolution of the data gave $k_{CuMal} = 7.8 \pm 1.2 \times 10^6[HMal^-] + 2.16 \pm 0.11 \times 10^8[H_2Mal]$ and $k_{CuMal_2^{2-}} = 1.76 \pm 0.15 \times 10^7[HMal^-] + 890 \pm 320$ as the appropriate form of k_{obsd} for the decay of the transient formed by flashing mono and bis complexes, respectively. Mechanisms consistent with the stoichiometric and kinetic data are presented and discussed.

Introduction

The photochemical decomposition of monocarboxylate complexes of several transition metal ions has been reported.[2] The photochemistry is characteristically an electron transfer to metal which results in reduction of the metal ion center and formation of a carboxylatoxy radical, RCOO·. From previous studies it appears that this radical loses CO_2 rapidly[3] and the overall process may be represented as

$$RCO_2M^{n+} + h\nu \longrightarrow RCO_2\cdot + M^{(n-1)+} \quad (1)$$

$$RCO_2\cdot \longrightarrow R\cdot + CO_2 \quad (2)$$

* Address correspondence to this author at Madison College, Harrisonburg, Va.

In the case of oxalate complexes a similar mechanism is applicable, although it is not known whether the oxalatoxy radical, $C_2O_4\cdot^-$, loses CO_2.[4]

Recently, studies on the photochemistry of malonato complexes of cobalt(III),[5] manganese(III),[6] and iron(III)[7] have been reported. Based on product studies, the photochemistry of these complexes is that predicted from studies on monocarboxylate complexes. The photochemistry of uranyl malonate has also been reported[8] and unlike that of the first row transition metals is a "sensitized" decomposition of the ligand giving carbon dioxide and acetate as final products.

The photochemistry of copper carboxylates has received little attention and the available literature is limited to copper(II) oxalate.[9] For this system, the photochemical products are reported to be copper(I) oxide and carbon

dioxide and the system appears at least to be similar to other transition metal oxalates. Photochemical studies on malonic acid[10] indicate that the products include oxalic, acetic, and succinic acids, carbon dioxide, and small amounts of carbon monoxide and ethylene.

As part of an investigation of free radical–metal ion reactions we undertook an investigation of the photochemistry of the copper(II) malonate (Mal = malonate) system. Our specific aims were to better understand the photochemistry of copper(II) complexes, and, because of the large number of substituted malonates available, to develop a general means of generating a variety of free radicals in solution.

Experimental Section

Chemicals. Reagent grade copper(II) sulfate, sodium malonate, and malonic acid were used as received. Deuterated reagents, malonic-d_4 acid (99%) and deuterium oxide (99%), were obtained from Diaprep, Inc., and used as received. All other materials were reagent grade.

Equipment. The flash-spectroscopic apparatus has been described earlier.[11] The apparatus for the steady illumination experiments consisted of a cylindrical low-pressure mercury lamp mounted parallel to a cylindrical quartz reaction vessel (*ca.* 60-ml capacity) which was immersed in a water jacket. The entire unit was enclosed in a cylindrical polished aluminum reflector. Quantum yields were determined using a collimated beam from a General Electric G8T5 low-pressure mercury lamp, the output from which was calibrated using the ferrioxalate actinometer.[12] A 2 cm × 5 cm diameter quartz cell was used for the quantum yield experiments.

Procedures. The argon purge and cell filling techniques used for the flash experiments have been described previously.[13] Solutions for the continuous irradiation experiments were degassed by the conventional freeze–thaw method. The products from the continuous irradiation experiments were analyzed as follows. After the solution was acidified with H_2SO_4, the CO_2 was collected and measured with a calibrated gas buret. Mass spectral analysis confirmed that carbon dioxide was the only condensable gaseous product. Carboxylic acids were determined by nmr spectroscopy using succinic acid (which is not a product of the photolysis) as an internal standard. After the carbon dioxide had been removed from the photolyzed solution, it was passed through an ion-exchange (Dowex 50W-X8) column to remove the Cu(II). The effluent was made basic with NaOH, evaporated to dryness on a rotary evaporator, and the salts were redissolved in CF_3COOH or D_2O for nmr analysis.

Equilibrium Constants. The equilibrium constants used in our calculations were for malonic acid: those of Dutt and Bose;[14] $K_{a,1} = 1.6 \times 10^{-3}$ and $K_{a,2} = 2.5 \times 10^{-6}$; for copper malonate, those of Davies,[15] $K_{i,1} = 2.8 \times 10^{-3}$ and $K_{i,2} = 2.5 \times 10^{-6}$. Where necessary, ionic strength corrections were made using the Davies's[16] form of the extended Debye–Hückel equation: $-\log \gamma^{\pm} = 0.509 z_1 z_2 (\sqrt{I}/(1 + \sqrt{I}) - 0.20I)$ at 25°.

Results

Copper(II) forms two labile complexes with malonate, the second of which is formed only with a large excess of the ligand[15] (~3×10^{-2} *M* excess $CH_2(COO)_2^{2-}$, for $[CuMal_2^{2-}]/[CuMal] = 10$). The complexes have d ← d absorption bands in the red (λ_{max} ~700 nm, $\epsilon \simeq 40$ M^{-1} cm^{-1})[17] and charge-transfer (CT) bands in the ultraviolet

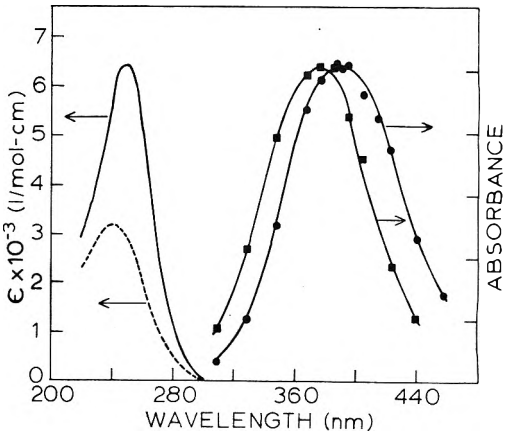

Figure 1. Spectra of bismalonatocuprate(II), copper(II) malonate, and their photochemical intermediates: (——) bismalonatocuprate(II), 1.0×10^{-4} *M* Cu^{2+}, 0.1 *M* Mal^{2-}; (– – –) copper(II) malonate, 2.13×10^{-4} *M* Cu^{2+}, 5×10^{-2} *M* H_2Mal, 5×10^{-2} *M* $HMal^-$; (●) intermediate formed by flashing bismalonatocuprate(II); (■) intermediate formed by flashing copper(II) malonate.

(CuMal, $\lambda_{max} \simeq 240$ nm, $\epsilon \simeq 3200$ M^{-1} cm^{-1}; $CuMal_2^{2-}$, $\lambda_{max} \simeq 250$ nm, $\epsilon \simeq 6400$ M^{-1} cm^{-1}); the ultraviolet portion of the spectra is given in Figure 1. The steady and flash illumination photochemistry of both complexes and their mixtures was investigated in the CT ultraviolet region.

Steady Illumination Photolysis. Experiments done at λ 253.7 nm on degassed copper(II) malonate solutions, the experimental conditions and some results for which appear in Table I, showed that the products of photolysis were acetate ion and carbon dioxide in equimolar amounts over a wide range of solution composition; $\Phi(OAc^-)/\Phi(CO_2) \simeq 0.94 \pm 0.05$. It is difficult to remove small amounts of CO_2 quantitatively from aqueous solutions even though the pH is quite low. Thus, our observed CO_2 yields were corrected using blanks in which a known quantity of $NaHCO_3$ was dissolved in a volume equal to the photolyte and then treated in the same manner as the irradiated solution.

The geometry of the photolysis system was such that most of the light ultimately was absorbed by the sample, however, the configuration was not completely efficient. Thus, our path length is undefined and comparisons should only be made between groups of experiments for which the sample absorbance at λ 253.7 nm is approximately equal. Hence experiments 1–3 and 4–9 form two separate groups. As shown in Table I, neither the $[CuMal_2^{2-}]/[CuMal]$ ratio nor the photolysis time have a strong influence on the rate of photolysis.

A search for succinate in the products by nmr indicated that Φ(acetate) > 20Φ(succinate). Further, integration of the malonate and acetate signals showed that within experimental error the malonate destroyed equalled the acetate formed. No Tyndall effect due to metallic copper was observed nor was cuprous ion, analyzed by adding 1,10-phenanthroline,[18] detected. Experiments with malonic acid alone showed that direct photolysis of the excess ligand was unimportant.

Isotope experiments with malonate-d_2 resulted in the formation of only acetate-d_2. Photoylsis of degassed solutions of copper(II) malonate ($[Cu^{2+}]_{total} = 2.5 \times 10^{-4}$ *M*, $[malonate]_{total} = 3.0 \times 10^{-4}$ *M*, [CuMal] = 2.06×10^{-4} *M*, pH 4.8[9]) and the bismalonatocuprate(II) ion ($[CuMal_2^{2-}] = 9.9 \times 10^{-5}$ *M*, $[Mal^{2-}]_{total} = 0.20$ *M*, pH 8.5[4]) with a lamp whose flux at 253.7 nm had been determined by ferrioxalate actinometry indicated $\Phi(CO_2)$ at 22–23° as 0.08 ±

TABLE I: Experimental Conditions and Results for Steady Illumination Experiments, (λ 253.7 nm, T = 20-22°)

Expt no.	$[Cu^{2+}]$, $M \times 10^2$	[Ligand salt], $M \times 10^2$	Photolysis time, min	CO_2/time, μmol/min	[Acetate yield]/[CO_2 yield]
1	1.0	1.00 Na_2Mal	10	1.80	0.91
2		1.00 NaHMal	10	2.03	0.90
3		1.00 Na_2Mal	240	2.07	0.96
4	0.10	1.00 Na_2Mal	60	1.40	0.94
5		1.00 NaHMal	60	1.42	0.89
6		1.02 Na_2Mal	180	1.47,1.47,1.56	0.97,0.95,0.92
7		1.53 Na_2Mal	180	1.48	1.02
8		1.03 Na_2Mal-d_2	180	1.56,1.64	1.00,0.91
9		0.91 NaHMal-d_2	180	1.38	0.92
10	None	0.09 H_2Mal-d_2 1.00 NaHMal	180	< 0.1	

0.005 for the mono complex and 0.07 ± 0.005 for the bis ion.

Flash Photolysis of Copper(II) Malonate. Solutions of copper(II) malonate were prepared in such a manner that $[CuMal_2^{2-}]/[CuMal] < 1 \times 10^{-2}$; when required, the pH was adjusted with small amounts of NaOH or H_2SO_4. The solution compositions are listed in Table II.

Flash photolysis of solutions of copper(II) malonate revealed a transient which absorbs between 300 and 440 nm with the maximum absorption occurring at 375 ± 5 nm; the spectrum of the transient is shown in Figure 1. The decay of this transient is pseudo-first order with observed rate constants (-d[intermediate]/dt = k_{obsd} [intermediate]) of 800–5000 sec^{-1} under our experimental conditions (Table II). Various treatments of the data indicated that the decay is dependent on $[HMal^-]$ and $[H_2Mal]$; any contribution to k_{obsd} by $[H^+]$ or $[Mal^{2-}]$ is less than the range of experimental scatter or zero. Since $[H_2Mal] = [H^+][HMal^-]/K_{a,1}$ and $k_{obsd} = k_{HMal^-}[HMal^-] + k_{H_2Mal}[H_2Mal]$, then $k_{obsd}/[HMal^-] = k_{HMal^-} + k_{H_2Mal}[H^+]/K_{a,1}$. Our data plotted as $k_{obsd}/[HMal^-]$ *vs.* $[H^+]/K_{a,1}$ (see Figure 2) are linear with a slope = 2.16 ± 0.11 × 10^8 M^{-1} sec^{-1} = k_{H_2Mal} and a y intercept = 7.8 ± 1.2 × 10^6 M^{-1} sec^{-1} = k_{HMal^-}.

Flash Photolysis of the Bismalonatocuprate(II) Ion. Solutions of the bismalonatocuprate(II) ion for these experiments were 1.00 × 10^{-4} M Cu^{2+} and 0.20 M Mal^{2-}, with small amounts of malonic acid added to adjust the pH in some experiments; in all experiments [CuMal]/$[CuMal_2^{2-}] \simeq 0.014$ (Table III).

Upon flashing solutions of $CuMal_2^{2-}$, a transient was observed which absorbs between 320 and 460 nm with the absorption maximum occurring at 390 ± 5 nm; the spectrum of the transient is shown in Figure 1. The transient decays in a pseudo-first-order fashion with observed rate constants which varied linearly with acidity, *i.e.*, $[H^+]$ and/or $[HMal^-]$. Under the experimental conditions used it was not possible to distinguish between $[H^+]$ and $[HMal^-]$ as $[H^+] = (K_{a,2}/[Mal^{2-}])[HMal^-]$ = (constant)$[HMal^-]$. Furthermore, a plot of k_{obsd} *vs.* either $[H^+]$ or $[HMal^-]$ resulted in a nonzero intercept. Hence, $k_{obsd} = k_{HMal^-}[HMal^-] + k_{H^+}[H^+] + k_0$. Since $K_{a,2} = [H^+][Mal^{2-}]/[HMal^-] = 1.12 \times 10^{-5}$, $k_{obsd} = (k_{HMal^-} + K_{a,2}k_{H^+}/[Mal_2^{-}])[HMal^-] + k_0$. Our data plotted as k_{obsd} *vs.* $[HMal^-]$ are linear (see Figure 3) yielding a y intercept = 890 ± 320 sec^{-1} = k_0 and a slope = 1.76 ± 0.15 × 10^7 M^{-1} sec^{-1} = $k_{HMal^-} + K_{a,2}k_{H^+}/[Mal^{2-}]$. Since it is probable that $0 \leq k_{H^+} \leq 10^{10}$ M^{-1} sec^{-1}, then 1.70 × $10^7 \leq k_{HMal^-} \leq$ 1.76 × 10^7 M^{-1} sec^{-1}. Also, if $k_0 = k_{H_2O}[H_2O]$, k_{H_2O} = 16 M^{-1} sec^{-1}.

TABLE II: Experimental Conditions and Transient Decay Rate Constants for Flash Illuminated Copper(II) Malonate Solutions[a]

[total Cu(II)], $M \times 10^4$	[Cu-Mal], $M \times 10^4$	pH	$[HMal^-]$, $M \times 10^5$	$[H_2Mal]$, $M \times 10^6$	I,[d] $M \times 10^3$	k_{obsd}, sec^{-1}
2.50	2.06	4.8_9[b]	7.46	0.580	0.92	795
4.00	1.73	3.9_2	11.5	8.28	1.55	2535
4.00	2.22	4.3_4	7.10	1.94	1.46	970
12.00	2.37	3.8_0	5.66	5.20	4.62	1470
12.00	1.85	3.4_5[c]	9.44	19.4	4.71	5020

[a] Total malonate = 3.00 × 10^{-4} M; $[CuMal_2^{2-}] < 1.2 \times 10^{-6}$ M. [b] NaOH added. [c] H_2SO_4 added. [d] Ionic strength.

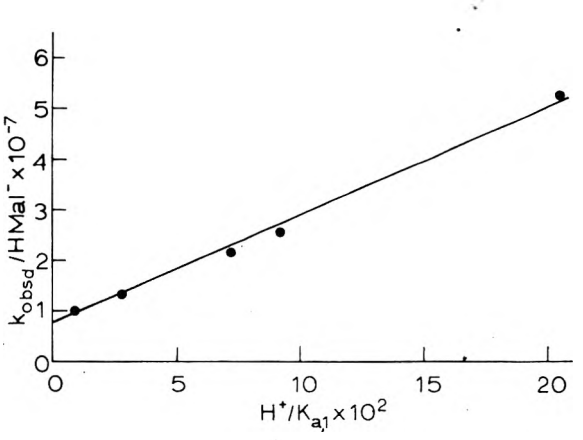

Figure 2. Determination of the concentration dependence of the CuMal transient decay: $k_{obsd}/[HMal^-]$ *vs.* $[H^+]/K_{a,1}$; see Table II.

Flash Photolysis of Mixtures (CuMal-$CuMal_2^{2-}$). Solutions containing various ratios of [CuMal] to $[CuMal_2^{2-}]$ were prepared (see Table IV) and as expected the first-order plots of the sample absorbance decay are curved (Figure 4, solid lines), but can be fitted by the sum of two straight lines (Figure 4, dashed lines), the slopes of which were calculated from the rate constants for the individual intermediates. As required, the intersection of the calculated slopes is 0.69 ln units from the observed absorbance value. This fit at pH's and malonate concentrations intermediate between the two previous extreme cases confirms the sufficiency, though not necessarily the uniqueness, of the k_{obsd} expressions.

TABLE III: Experimental Conditions and Transient Decay Rate Constants for Flash Illuminated Bimalonatocuprate(II) Solutions[a]

pH[b]	$[HMal^-]$, $M \times 10^5$	$k_{obsd} \times 10^{-3}$, sec^{-1}
8.60	6.50	2.11
8.67	5.53	1.60
7.80	40.9	7.66
7.96	28.3	6.58
8.20	16.3	3.62
8.33	12.1	3.07

[a] [Total Cu(II)] = 1.00×10^{-4} *M*, [total Mal^{2-}] = 0.20 *M*, *I* = 0.60 *M*, $[CuMal_2^{2-}] = 9.86 \times 10^{-5}$ *M*, [CuMal] = 1.38×10^{-6} *M*. [b] Small amounts of H_2Mal added to change the pH.

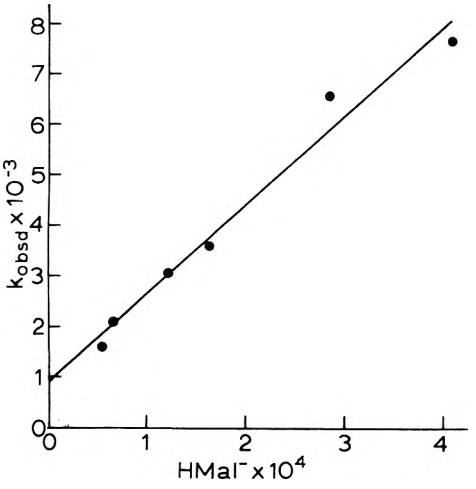

Figure 3. Determination of the concentration dependence of the $CuMal_2^{2-}$ transient decay: k_{obsd} *vs.* $[HMal^-]$; see Table III.

Flash Intensity Studies. The flash energy was varied to determine whether an intensity-dependent step was operative. Variation of the energy supplied to the flash lamps from 170 to 750 J was without effect on the observed rate constants for either complex. At higher intensities (840–1000 J), however, the first-order plots for both complexes showed curvature. Further, the k_{obsd} values obtained late in the decay, presumably after all second-order processes have become unimportant, were greater than the values obtained at lower flash energies. At the highest flash energies, a fine green precipitate was formed by irradiation from the analyzing lamp; the precipitate did not form when a Pyrex filter was placed between the analyzing lamp and the reaction cell.

Scavenger Studies. Oxygen (1 atm) had no effect on the observed rate constant for either complex. At high flash energies (*e.g.*, ~1000 J), oxygen prevented the formation of the fine green precipitate observed for argon-purged solutions under similar conditions. Also, 0.1 *M* 2-propanol had no effect on the observed rate constant for a solution containing both complexes and with a $HMal^-/H_2Mal$ ratio such that both transients should have the about same k_{obsd} in the absence of 2-propanol. The observed rate constant for this same solution but 1 *M* in 2-propanol was 9000 sec^{-1} as compared to 13,800 sec^{-1} for a solution without the alcohol scavenger.

Discussion

The observed charge-transfer photochemistry of the Cu(II) malonate system represents a departure from other typical transition metal carboxylates in that while the ligand is oxidized, ligand radical dimers and related products formed by hydrogen atom abstraction are not observed and the metal ion is not permanently reduced. The photochemistry observed in our experiments cannot be the result of "sensitization" *via* energy transfer from uncomplexed $Cu(H_2O)_6^{2+}$ as

$$Cu(H_2O)_6^{2+} \xrightarrow{h\nu} [Cu(H_2O)_6^{2+}]^* + HMal^- \longrightarrow [HMal^-]^* + Cu(H_2O)_6^{2+} \quad (3)$$

with subsequent decomposition of $[HMal^-]^*$, excited malonate. Three observations argue against a scheme such as (3). First, $Cu(H_2O)_6^{2+}$ does not absorb significantly above 240 nm, yet irradiation at 253.7 nm was quite effective in producing the observed products. Second, experiments at 253.7 nm in which all the Cu(II) was complexed (*cf.* Table I, experiments 4–9) produced carbon dioxide and acetate ion in equimolar amounts without loss of Cu(II). Finally, in the flash experiments (*cf.* Table II) the maximum absorbance of the intermediate observed was related to the concentration of copper(II) complex present and not to the aquo copper(II) concentration. Also, as shown in Table I, direct photolysis of the ligand cannot account for our observations. Thus, we must conclude that the malonato complexes are responsible for the observed photochemistry.

The absorption of simple copper(II) complexes in the ultraviolet region has been assigned as due to a charge transfer transition.[19] The results of this study strongly suggest that for copper(II) malonate and bismalonatocuprate(II) the transition is a charge-transfer-to-metal transition (CTTM). However, the relatively low quantum yield of photoredox indicates that several paths for energy dissipation are available and that the path leading to oxidation of the ligand is a relatively minor one. Since emission is not observed from simple Cu(II) complexes,[20] presumably internal conversion and/or photoaquation are the major dissipative processes.

The question arises as to whether, after excitation and subsequent electron redistribution, the product Cu(I) species and ligand radical remain bound or separate. If separation occurs we might expect to detect spectrally the ligand radical and follow the kinetics of its decay. Since two oxidation sites are possible, the following processes must be considered:

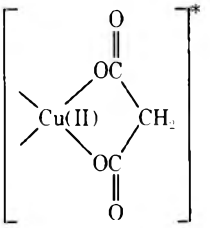

$$\rightarrow >|Cu(I)|< + CO_2 + \dot{C}H_2COO^- \quad (4a)$$
$$\rightarrow >|Cu(I)|< + {}^-OOCCH_2\dot{C}O_2 \quad (4b)$$
$$\rightarrow >|Cu(I)|< + \dot{C}H(COO^-)_2 + H^+ \quad (4c)$$

where (4a) and (4b) differ in the rapidity of CO_2 loss.

Several pieces of evidence mitigate against any of the alternatives shown in (4). Spectra of $\cdot CO_2^-$,[21] $\dot{C}H_2COO^-$,[21] $\dot{C}H_2COOH$,[21] $\cdot CH(COO^-)_2$, and $\cdot CH(COOH)_2$[22] have been reported as well as the rate constants for their second-order decay. The reported spectra do not match the intermediates observed in our flash experiments nor was any evidence found in our experiments for the radical dimers to be expected on the basis of the reported bimolecular rate con-

TABLE IV: Experimental Conditions and Calculated and Observed Rate Constants for Flash Photolysis of Complex Mixtures[a]

[total malonate], M	$[CuMal_2^{2-}]$,[b] $M \times 10^5$	pH	$[HMal^-]$, $M \times 10^5$	$[H_2Mal]$, $M \times 10^{10}$	k_{obsd},[d] sec^{-1}	k_{CuMal},[c] sec^{-1}	$k_{CuMal_2^{2-}}$,[c] sec^{-1}
0.0010	2.34	7.2_2	1.73	6.12	690 ± 94	134	976
0.0030	5.02	7.5_0	2.64	4.72	819 ± 77	205	1044
0.0100	7.77	7.7_8	3.92	3.44	818 ± 97	305	1191
0.030	9.14	8.0_4	5.09	2.25	1219 ± 27	395	1437
0.10	9.73	8.2_7	7.52	1.78	1775 ± 210	584	2078

[a] [Total copper(II)] = 1.00×10^{-4} M. [b] [CuMal] = 1.00×10^{-4} M − $[CuMal_2^{2-}]$. [c] Calculated rate constants; see text. [d] Calculated from the initial slope.

stants. Further, the observed invariance of the CO_2/acetate ratio demands that the ligand radical produced is essentially always transformed into acetate. Such a condition is not readily obtained using any of the possibilities suggested in (4) as a point of departure. Unless the radicals shown in (4a,b,c) react exclusively with the Cu(I), one would expect to observe Cu(I) as Cu_2O or perhaps copper metal *via* disproportionation. The fact that oxygen had no effect on the rate of intermediate decay and that the known free-radical scavenger 2-propanol was without significant effect also suggests that bulk free radicals are not involved. The results of experiments with malonic-d_2 acid rule out mechanisms such as (4c) or other steps in which loss of hydrogen from the central malonate carbon occurs. Finally, the observed 10-nm shift in λ_{max} for the transient on going from copper(II) malonate to the bismalonatocuprate(II) ion strongly suggests that the copper moiety is part of the transient.

We are thus led to the conclusion that after photoredox the oxidized ligand remains bound to or at least proximate to the Cu(I) species. This is followed by rapid (relative to the decay of the Cu(I) intermediate) loss of CO_2 and may be visualized as

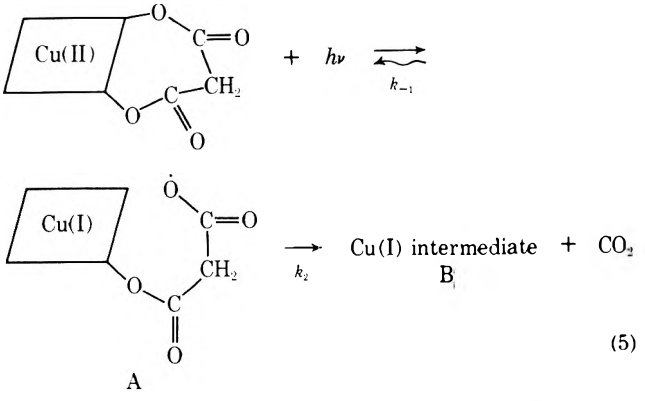

(5)

In keeping with the low product quantum yields, it is likely that $k_{-1} > k_2$, though the operation of other modes of dissipation would remove that requirement. However, loss of CO_2 from A seals its fate and renders the back reaction impossible.

The decay of the Cu(I) intermediate must involve further redox and a proton transfer. That Cu(I) will reduce alkyl and related free radicals is known.[23] The observed decay kinetics suggest that the proton transfer is rate limiting. The dependence of the decay of the copper malonate intermediate on $[H_2Mal]$ and $[HMal^-]$ is somewhat surprising and several, not totally satisfying, explanations can

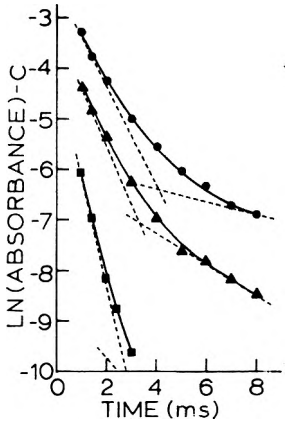

Figure 4. First-order decay plots of CuMal–$CuMal_2^{2-}$ transients: experimental decay (●) 1×10^{-3} M total malonate, $c \simeq 0$; (▲) 1×10^{-2} M total malonate, $c = 0.6$; (■) 1×10^{-1} M total malonate, $c = 2$; calculated slopes using rate constants derived from Figures 2 and 3 (– – –); see Table IV.

be suggested. One of these is:

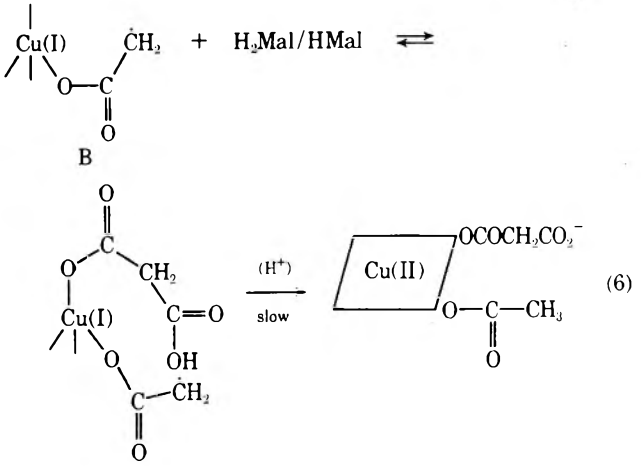

(6)

The Cu(I) species, B, is arbitrarily shown in a tetrahedral configuration in analogy with other simple stable Cu(I) species[24] though the exact geometry is not too important here. According to the proposed scheme, B would be the intermediate observed in the flash experiments and its subsequent decay gives rise to the observed kinetics. Unfortunately, the available spectra of copper(I) complexes with which to compare our transient spectra are limited. Recently the spectra of copper(I) fumarate and maleate in aqueous media were reported with λ_{max} at 358 and 340 nm, respectively.[25] Thus, the observed λ_{max} values for the flash

transients are consistent with but not unique to a Cu(I) species.

Also possible is a mechanism such as:

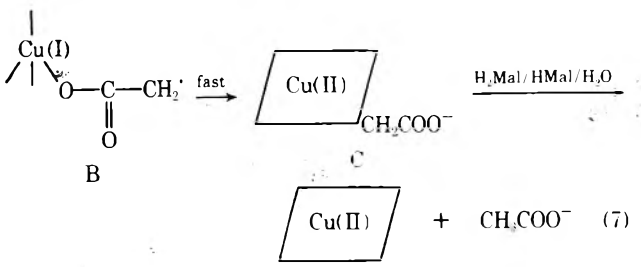

(7)

In the scheme depicted by (6) the $HMal^-$ or H_2Mal coordinates with the Cu(I) species to alter the redox potential and provide for the proton transfer as well. The mechanism shown in (7) involves a rapid isomerization to achieve redox followed by the protonation and release of acetate. In this scheme the intermediate seen in the flash experiments would be C rather than B. While a similar mechanism has been reported in the cases of formato- and oxolatoamine complexes of Co(III),[26] the step following linkage isomerization was electron transfer from the ligand fragment to the Co(III).

Unfortunately the kinetic and spectral data are compatible with either (6) or (7) and possibly other, more adventuresome, schemes. The conditions for the decay of the transients appear to require the presence of (1) malonate and (2) a proton source, though whether malonate serves any function other than a proton donor is not clear. We can not rule out an H_2Mal dependent decay of the transient derived from the bis ion since under our conditions the pH was so high that the concentration of malonic acid is miniscule. Further, we note that k_{HMal^-} for $CuMal_2^{2-}$ is a factor of 2 greater than the k_{HMal^-} for CuMal, even though the former is a reaction between two negatively charged ions. This may imply that the role of $HMal^-$ is not quite the same in both cases. The failure to detect a malonate independent decay mode for the transient derived from CuMal under conditions which, if the rate was of a magnitude similar to that found for the bis ion would have been readily observable, adds credence to the suggestion of somewhat different decay paths for the two transients.

The results of the high-intensity flash experiments suggest that an alternate fate is available to the transient when present in sufficiently high concentration. The spectra of the transients produced by strong flashes were essentially the same as those observed at the lower energies. A likely candidate for the alternate transient decay path is some form of dimerization. Presumably photolysis of the dimer by the analysis lamp results in formation of an insoluble Cu(I) compound. However, oxygen appears to suppress the formation of the precipitate; a result consistent with the presence of Cu(I). Since the composition of the precipitate is not known nor has the product of the alternate transient reaction been characterized, detailed mechanistic speculations seem unwarranted at this time.

Portions of the results presented in this paper have been reported previously.[27]

Acknowledgments. One of us, J.Y.M., wishes to thank the Department of Chemistry, The University of Virginia, for stipend support during the completion of this project.

References and Notes

(1) Note address for correspondence.
(2) See V. Balzani and V. Carassiti, "Photochemistry of Coordination Compounds," Academic Press, London, 1970.
(3) L. Herk, M. Feld, and M. Seward, *J. Amer. Chem. Soc.*, **83**, 2998 (1961); E. R. Kantrowitz, M. Z. Hoffman, and J. F. Endicott, *J. Phys. Chem.*, 75, 1914 (1971).
(4) P. Neta, M. Simic, and E. Hayon, *J. Phys. Chem.*, **73**, 4207 (1969); N. Getoff, F. Schworer, V. M. Markovic, K. Sehested, and S. O. Nielson, *ibid.*, **75**, 749 (1971); A. C. Sarma, A. Fenerty, and S. T. Spees, *ibid.*, **74**, 4598 (1970).
(5) R. Van Eldik and J. A. Van den Berg, *J. S. Afr. Chem. Inst.*, **22**, 175 (1969); *Chem. Abstr.*, **72**, 125452*s* (1970).
(6) R. Van Eldik and J. A. Van den Berg, *J. S. Afr. Chem. Inst.*, **23**, 85 (1970); *Chem. Abstr.*, **73**, 102419*t* (1970).
(7) R. Van Eldik and J. A. Van den Berg, *J. S. Afr. Chem. Inst.*, **23**, 96 (1970); *Chem. Abstr.*, **73**, 104257*n* (1970).
(8) G. E. Heckler, A. E. Taylor, C. Jenson, D. Percival, R. Jensen, and P. Fung, *J. Phys. Chem.*, **67**, 1 (1963).
(9) J. M. Eder, *Monatsh Chem.*, **6**, 495 (1885); N. R. Dhar, *J. Chem. Soc.*, **111**, 690 (1917); B. K. Mukerji and N. R. Dhar, *Quart. J. Indian Chem. Soc.*, **2**, 277 (1925); H. L. Dube and N. R. Dhar, *J. Phys. Chem.*, **36**, 626 (1932); W. V. Bhagwat, *Z. Anorg. Allg. Chem.*, **218**, 365 (1934); N. A. Biskalova, *Ukr. Khim. Zh.*, **17**, 807 (1951).
(10) J. D. Rao, *J. Univ. Bombay*, **9**, 94 (1940); A. Miolati and G. Seonerano, *Atti Ist. Veneto Sci., Part 2*, **100**, 187 (1941).
(11) B. A. DeGraff and K. J. Lang, *J. Phys. Chem.*, **74**, 4181 (1970).
(12) C. G. Hatchard and C. A. Parker, *Proc. Roy. Soc., Ser. A*, **235**, 158 (1956).
(13) G. D. Copper and B. A. DeGraff, *J. Phys. Chem.*, **75**, 2897 (1971).
(14) N. K. Dutt and P. Bose, *Z. Anorg. Chem.*, **295**, 131 (1958).
(15) C. W. Davies, *J. Chem. Soc.*, 910 (1935).
(16) C. W. Davies, *J. Chem. Soc.*, 2093 (1938).
(17) D. P. Graddon, *J. Inorg. Nucl. Chem.*, **7**, 73 (1958).
(18) D. H. Wilkins and G. F. Smith, *Anal. Chim. Acta*, **9**, 538 (1953).
(19) H. Yokoi and T. Isobe, *Bull. Chem. Soc. Jap.*, **42**, 2187 (1969); B. P. Kennedy and A. B. P. Lever, *J. Amer. Chem. Soc.*, **95**, 6907 (1973).
(20) V. Balzani and V. Carassiti, "Photochemistry of Coordination Compounds," Academic Press, New York, N.Y., 1970, Chapter 13; P. D. Fleischauer and P. Fleischauer, *Chem. Rev.*, **70**, 199 (1970).
(21) P. Neta, M. Simic, and E. Hayon, *J. Phys. Chem.*, **73**, 4207 (1969).
(22) M. Simic, P. Neta, and E. Hayon, *J. Phys. Chem.*, **73**, 4214 (1969).
(23) See, for example, J. H. Fitzpatrick, Jr. and D. Hopgood, *Inorg. Chem.*, **13**, 568 (1974); J. Kochi in "Free Radicals," Vol. 1, J. Kochi, Ed., Wiley, New York, N.Y., 1973, Chapter 11.
(24) A. H. Lewin, R. J. Michl, P. Ganis, U. Lepore, and G. Avitable, *Chem. Commun.*, 1400 (1971).
(25) J. K. Hurst and R. H. Lane, *J. Amer. Chem. Soc.*, **95**, 1703 (1973).
(26) A. F. Vaudo, E. R. Kantrowitz, M. Z. Hoffman, E. Papaconstantinou, and J. F. Endicott, *J. Amer. Chem. Soc.*, **94**, 6655 (1972).
(27) J. Y. Morimoto and B. A. DeGraff, *J. Phys. Chem.*, **76**, 1387 (1972).

Hydrogen Bonding of Resorcinol to Ethers and Thioethers

J. N. Spencer,* R. S. Harner, L. I. Freed, and C. D. Penturelli

Department of Chemistry, Lebanon Valley College, Annville, Pennsylvania 17003 *(Received August 23, 1974)*

The hydrogen bonding of resorcinol to the proton acceptors diethyl ether, tetrahydrofuran, di-*n*-butyl sulfide, and tetrahydrothiophene in CCl_4 solvent was studied as a function of temperature by monitoring the hydroxyl stretching frequency at about 3 μ. Thermodynamic functions for the bis-ether complexes with resorcinol were determined. The stepwise enthalpy changes for the addition of two proton acceptors are approximately the same and indicate that hydrogen bonding to one resorcinol hydroxyl does not substantially alter the enthalpy of interaction of the second hydroxyl with a second proton acceptor. Comparison of the resorcinol data to other hydroxybenzene systems is made. The thermodynamics of the hydrogen bonding of phenol with tetrahydrothiophene in CCl_4 solvent is also reported.

Introduction

Few studies of those systems capable of hydrogen bonding through more than one proton have been reported. Other than previous studies[1,2] from this laboratory, the great bulk of literature reports for systems containing 1:1 and 1:2 hydrogen bonded complexes list water as the proton donor. This work describes the hydrogen bonding of resorcinol (1,3-dihydroxybenzene) with ethers and thioethers in CCl_4 solvent and is the third[1,2] report in a series concerned with the hydrogen bonding of the hydroxybenzenes.

Apparently the work of Holmes, *et al.*,[3] on the polymerization of water in various solvents was the first directed toward finding the equilibrium constants for proton donors capable of donating more than one proton. However, no temperature study was carried out so that the enthalpy of hydrogen bond formation could not be determined. Takahashi and Li[4] determined the equilibrium constants and enthalpy for the 1:2 complexes of water with *N*,*N*-dimethylacetamide, acetone, and tetrahydrofuran in cyclohexane solvent. The formation constants of the 1:1 complexes were not obtained. Muller and Simon[5] obtained equilibrium constants and enthalpies for the formation of 1:1 and 1:2 complexes of water with dioxane in CCl_4 solvent. They found K_1 to be 12.1 and K_2 to be 0.82 mf^{-1} at 30°, ΔH_1 to lie between −3.3 and −3.7 kcal mol^{-1}, and ΔH_2 to lie between −1.6 and −2.8 kcal mol^{-1}. Nishimura, Ke, and Li[6] studied the hydrogen bonding of water to tributyl phosphate in CCl_4 solvent. They found that the ratio of K_1 to K_2 was about 10 and decreased with increasing temperature; ΔH_1 was reported as −4.1 kcal mol^{-1} and ΔH_2 as −2.0 kcal mol^{-1}. Bundschuh, Takahashi, and Li[7] studied the hydrogen bonding of hydroquinone and THF in cyclohexane medium. Their data allowed only the determination of the equilibrium properties for the 1:2 complex. The enthalpy and entropy changes were reported to be −3.6 kcal mol^{-1} and −11.0 eu, respectively. Reuben[8] has estimated K_1 and K_2 as 9 and 0.15 mf^{-1} respectively for solutions of water in acetone. All of the above results were obtained through nmr studies.

Experimental Section

Baker analyzed reagent grade resorcinol was purified by sublimation under reduced pressure. Melting point was used as a purity criterion. Aldrich analyzed tetrahydrothiophene was fractionally distilled under nitrogen atmosphere. Index of refraction was used as a purity criterion. Purifications of the other reagents used have been previously described.[1,2] For all studies the resorcinol concentration was about 1×10^{-3} *M*. The molar absorptivities of resorcinol were determined as a function of temperature and were in good agreement with those previously reported.[9] Other experimental details have been given in earlier works.[1,2]

Calculations

The equilibria between resorcinol and proton acceptors were considered in stepwise fashion according to eq 1 and 2.

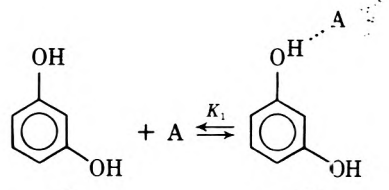

(1)

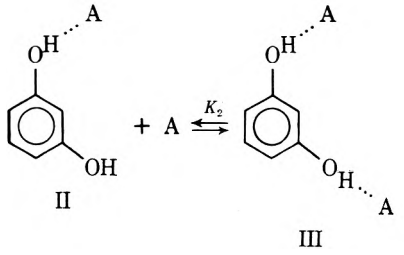

(2)

In studies of stepwise equilibria, it is customary to conduct investigations at sufficiently low A concentrations so as to minimize competition from all but the first step. Because previous studies on dihydroxybenzenes[1,2] gave relative values of K_1 and K_2 different from those obtained from water complexes,[5,6] it was first necessary to obtain initial estimates of K_1 and K_2 so that appropriate concentration ranges could be found. The equilibrium constants for the resorcinol–THF complex were found by using a limiting slope method similar to that employed by Liddel and Becker.[10] An apparent molar absorptivity, ϵ^a, was defined as

$$\epsilon^a = A_f/C \tag{3}$$

where A_f is the absorbance at about 3611 cm^{-1} due to the free hydroxyl groups of resorcinol and C is the initial resorcinol concentration. Under equilibrium conditions

$$C = C_I + C_{II} + C_{III} \quad (4)$$

where the subscripts refer to the species of eq 1 and 2. Further

$$A_f = 2\epsilon_f C_I + \epsilon_f C_{II} \quad (5)$$

where ϵ_f is the molar absorptivity per free hydroxyl at 3611 cm^{-1}. It has been assumed that the molar absorptivity of species II is one-half that of species I.[1]

If K_1 and K_2 are defined as

$$K_1 = C_{II}/C_I A \quad (6)$$

$$K_2 = C_{III}/C_{II} A \quad (7)$$

where A is the equilibrium proton acceptor concentration, and eq 3, 4, 6, and 7 are substituted into eq 5, eq 8 results.

$$\epsilon^a = \epsilon_f[2(C - K_1 C_I A - K_1 K_2 C_I A^2) + K_1 C_I A]/C \quad (8)$$

If eq 8 is differentiated with respect to A while maintaining C constant, followed by taking the limit as A approaches zero, eq 9 is obtained

$$\lim_{A \to 0} \frac{\partial \epsilon^a}{\partial A}\Big)_c = -\epsilon_f K_1 \quad (9)$$

A series of solutions with the same initial resorcinol concentration but with THF concentrations ranging from 0.0025 to 0.04 M was prepared and the spectra were recorded. A plot of ϵ^a *vs.* initial THF concentration was made and the limiting slope found. Substitution of eq 6 into eq 5 gives

$$A_f = 2\epsilon_f C_I + \epsilon_f K_1 C_I A \quad (10)$$

By using K_1 determined from the limiting slope and A_f at a high proton acceptor concentration, C_I may be estimated. For a first estimate, the initial concentration of A is used and from C_I and K_1, C_{II} is found. Then C_I, C_{II}, and C_{III} are refined by successive iteration by recalculating the equilibrium A concentration. Proper application of this method then requires replotting ϵ^a *vs.* [A] using the equilibrium A concentration and repeating the procedure until no further changes are produced in the limiting slope. In practice the slope changes only slightly when the A concentrations are refined in this fashion so that a good estimate of K_1 and K_2 is obtained by using initial A concentrations. The results of the limiting slope procedure showed that a concentration range of A over which species III is neglible could be found. Subsequent determinations of K_1 were made by using eq 5 in the form

$$A_f = 2\epsilon_f C_I + \epsilon_f(C - C_I) \quad (11)$$

for those concentrations of proton acceptor where C_{III} is negligible. Under these conditions eq 11 with eq 6 and 4 gives C_I, C_{II}, and K_1. Then by determinations at higher concentration of A, eq 10 and the procedure given following it may be used to find K_2. K_1 for the THF–resorcinol complex determined over the THF concentration range 0.003 to 0.01 M was constant, showing that at these concentrations of A, C_{III} is negligible. THF concentrations of about 0.1 M were used to determine K_2. Similar calculations were carried out for the diethyl ether–resorcinol system. The ether concentrations used were about 0.015 and 0.15 M. It was found that the limiting slope method and the procedure actually used for analysis gave almost identical results.

Even for proton acceptor concentrations up to 0.3 M, the formation of species III for the thioether systems was negligible. Therefore, thioether concentrations of about 0.1 M were used for analysis and eq 11 was employed to find C_I and C_{II} from which K_1 was calculated. Because of the small values of K_1 and K_2 only an upper limit could be found for K_2 for the thioethers.

Calculations for the phenol–THTP system were the same as previously described.[1]

Results and Discussion

The thermodynamic properties of the complexes with resorcinol are given in Table I. The standard enthalpy change was found from the slope of a plot of log K *vs.* T^{-1} and the standard entropy change was calculated from the intercept. Data previously obtained[1,2] for other hydroxybenzene complexes and that of resorcinol is compiled in Table II (see paragraph at end of text regarding miniprint

TABLE I: Thermodynamic Functions for the Hydrogen Bonding of Resorcinol to Various Proton Acceptors

Proton acceptor	T, °C	K_1	K_2	ΔH_1[a]	ΔH_2	ΔS_1[b]	ΔS_2
THF	20	47	4.9	−5.6 ± 0.1	−5.8 ± 0.5	−12	−17
	30	34	3.4				
	40	25	2.6				
Diethyl ether	10	43	4.3	−6.1 ± 0.4	−5.9 ± 0.2	−14	−18
	20	30	3.0				
	25	25	2.6				
THTP	10	4.9	<0.5	−4.6 ± 0.8		−13	
	20	3.3					
	30	3.1					
	40	2.1					
n-Bu_2S	20	5.0	<0.5	−3.8 ± 0.2		−9.9	
	30	4.2					
	40	3.4					
	50	2.7					
Phenol–THTP	10	1.8		−3.0 ± 0.2		−9.4	
	20	1.6					
	30	1.3					
	40	1.1					

[a] Units are kcal mol^{-1}. The error reported is the error in the least-squares slope of a plot of log k *vs.* T^{-1}. [b] Units are cal mol^{-1} deg^{-1}.

Table II. Comparison of Thermodynamic Data for the Hydrogen Bonding of Hydroxy Benzenes with Various Proton Acceptors[c]

	ΔH_1 (kcal)	ΔH_2 (kcal)	K_1[a]	K_2[a]	ΔS_1[b]	S_2[b]	$\Delta\nu$ (cm^{-1})[e]
Phenol-diethylether	-5.3 ± 0.2	---	9.6	---	-14	---	276
Resorcinol-	-6.1 ± 0.4	-5.9 ± 0.2	30	3.0	-14	-18	285
Catechol-	-8.0 ± 0.3	+4.7 ± 0.2	12.0	7.6	-22	+20	345
Pyrogallol-	-7.1 ± 0.8	+3.1 ± 0.5	27	25	-18	+17	340
Phenol-THF	-4.9 ± 0.2	---	13.5	---	-12	---	287
Resorcinol-	-5.6 ± 0.1	-5.8 ± 0.5	47	4.9	-12	-17	289
Catechol-	-8.6 ± 0.2	+3.6 ± 0.3	16.6	91	-24	+22	363
Phenol-DMSO	-6.3 ± 0.1	---	225[d]	---	-10.8	---	354
Guaiacol-	-3.0 ± 0.1	---	4.1[d]	---	-7.57	---	360
Catechol-	-9.4 ± 0.9	+5.3 ± 1.3	3.26×10^2	7.7×10^2	-21	+31	445
Phenol-n-Bu_2S	-3.3 ± 0.5	---	1.9	---	-9.9	---	266
Resorcinol-	-3.8 ± 0.2	---	5.0	<0.5	-9.9	---	254
Catechol-	-4.0 ± 0.1	+1.1 ± 0.6	1.22	8	-13	+8	321
Phenol-THTP	-3.0 ± 0.2	---	1.6	---	-9.4	---	257
Resorcinol-	-4.6 ± 0.8	---	3.3	<0.5	-13	---	264

[a] Equilibrium constants at 20°C. [b] Units are cal $mol^{-1}deg^{-1}$. [c] Additional data taken from Refs 1 and 2 [d] Extrapolated values [e] The frequency shift is the difference between the free hydroxyl stretching frequency and that of the complex in CCl_4 solution. For guaiacol the complex frequency is compared to 3611 cm^{-1}.

material). For further comparison, the phenol–THTP system was investigated and the results are given in Tables I and II. Frequency shifts for all complexes are given in Table II.

The data of Table I show that the ratio of K_1 to K_2 for the resorcinol complexes with diethyl ether and THF is approximately 10 and that this ratio has little variation with temperature. Nishimura, *et al.*,[6] found that for water–TBP complexes the ratio of K_1 to K_2 was 10 at 10° but decreased to 7 at 45°. This variation is due to a difference of 2 kcal mol^{-1} between ΔH_1 and ΔH_2. Muller and Simon[5] found the ratio of K_1 to K_2 to be about 15:1 at room temperature for the water–dioxane complex and also found a difference of about 1.5 kcal mol^{-1} between ΔH_1 and ΔH_2. The ratio of K_1 to K_2 for resorcinol complexes is in the range of that found for complexes with water, but the enthalpy terms ΔH_1 and ΔH_2 are indistinguishable within experimental error. The difference between ΔH_1 and ΔH_2 for the water–TBP complex has been rationalized by Nishimura, *et al.*,[6] "by considering that when one of the water hydrogens is bonded to TBP, the water oxygen becomes more basic and the other hydrogen (nonbonded) loses is acidity and hence its hydrogen-donor strength." These conclusions appear to be substantiated by recent theoretical studies[11] which show that "all hydrogens attached to the electronegative atom of the proton donor molecule gain electrons upon H-bond formation." Apparently there is little effect due to the hydrogen bonding of the first hydroxyl on the second hydroxyl when resorcinol is the proton donor. The hydrogen bonding of a proton acceptor to one of the resorcinol hydroxyls does not significantly alter the enthalpy of interaction of the second hydroxyl with a second proton acceptor. The hydrogen bonding of the proton of a hydroxyl group has been considered to be analogous to the dissociation of an OH group to the O^- ion.[12] The formation of the hydrogen bond, which involves an increase in the OH bond length, is considered to be a step toward removal of the proton from the OH group. If hydrogen bond formation is but a step in the direction of ionization of the proton, ΔH_2 should be less than ΔH_1 for the resorcinol complexes by analogy with the ionization constants. pK_{a_2} for resorcinol is 11.32 and pK_{a_1} is 9.15.[13] That ΔH_1 and ΔH_2 are approximately the same for the resorcinol complexes with THF and diethyl ether indicates that the ananlogy is not complete.

The data of Table II show that the equilibrium constants, K_1, for resorcinol–THF and resorcinol–diethyl ether complexes are greater than the equilibrium constants for the corresponding phenol complexes. The entropy changes, ΔS_1, for the formation of resorcinol complexes and the entropy changes for the phenol complexes are identical. The large difference in equilibrium constants between phenol and resorcinol complexes results from small differences in ΔH_1. The enthalpy change ΔH_1 for the resorcinol complexes is probably greater than the enthalpy change for the phenol complexes due to the greater acidity of resorcinol (pK_{a_1} for resorcinol is 9.15,[13] that for phenol is 9.9[14]). However, it may be hazardous, as just shown, to apply pK_a values obtained in aqueous environment to results obtained in nonaqueous media.

Despite the similarity between ΔH_1 and ΔH_2 for the resorcinol complexes, K_1 and K_2 differ considerably. The difference between K_1 and K_2 is due to an entropy effect. ΔS_2 is more negative than the entropy change, ΔS_1, for the corresponding phenol complex. Thus the increased steric hindrance for the addition of a second proton acceptor to resorcinol must be responsible for the differences in K_1 and K_2.

There is a difference of about 1.5 between the equilibrium constants for the resorcionl–THF and the resorcinol–diethyl ether complexes. A similar difference is found for the equilibrium constants for phenol complexes with THF and diethyl ether. Bellamy, Eglinton, and Morman[15] have examined the hydrogen bonding for a series of ethers of increasing structural complexity with phenol and conclude that as the complexity of the ether increases the equilibrium constant decreases due to an entropy effect. These workers did not actually determine ΔH for the bonding of the various ethers to phenol but argue on the basis of similar frequency shifts that ΔH does not differ significantly for these complexes so that differences in the equilibrium constant arise from variation in the entropy term. According to these investigators, the shapes of the donor and acceptor molecules determine what proportion of the collisions leads to hydrogen bond formation.

The data of Table II and that of West, *et al.*,[16] show that the difference in equilibrium constants between the phenol–diethyl ether and the phenol–THF complex is accounted for by the small difference in ΔS. Even though the enthalpy term is more favorable for the phenol–diethyl ether complex the entropy term is more favorable for the phenol–THF complex. Similar conclusions apply to the resorcinol complexes with THF and diethyl ether but the trend in equilibrium constant is not observed when *n*-Bu_2S or THTP is the proton acceptor. It would also appear that if the shapes of the molecules were of paramount importance to the determination of the equilibrium constant, the entropy change, ΔS_1, for the formation of resorcinol complexes should be more positive than that for the formation of corresponding phenol complexes. This would be expected because the number of collisions leading to formation of a hydrogen bond should be greater with the two hydroxyls of resorcinol than with the single hydroxyl of phenol. An examination of the data in Table II shows this is not the case.

The data of Table II have been arranged so that a comparison of hydrogen bonded properties of the hydroxybenzenes with a given proton acceptor may be made. For the complexes with diethyl ether, it is seen that the frequency shift and ΔH_1 show an abrupt change when the proton donors are catechol and pyrogallol. The trends in $\Delta\nu$ and ΔH_1 seen in this series are repeated for the other entries of Table II. Bellamy and Pace[12] have previously postulated that the hydrogen atom of an OH group whose oxygen is acting as a proton acceptor should become more acidic. This postulate is in agreement with recent theoretical stud-

ies.[11] Thus the hydrogen of the free hydroxyl group of catechol and pyrogallol is more acidic than the hydrogen of the hydroxyl group(s) of resorcinol, hydroquinone, phloroglucinol, or phenol due to the acceptance of a proton by the free hydroxyl oxygen to form the intramolecular hydrogen bond. The frequency shifts for hydroquinone and phloroglucinol complexes have been previously reported[1,2] and are about the same as those for the corresponding phenol and resorcinol complexes. Due to the limited solubilities of hydroquinone and phloroglucinol in carbon tetrachloride, it was not possible to conduct equilibrium studies for these compounds. The large frequency shifts observed for those complexes formed with proton donors containing intramolecular bonds support Bellamy's[17] specific interaction theory which argues that solvent effects on hydrogen bonded frequencies may be quite significant if the solvent interaction occurs through the hydroxyl oxygen of the solute.

It has previously been shown[1,2] that neither diethyl ether nor THF form complexes with guaiacol with a sufficiently large equilibrium constant to permit spectroscopic observation. However both of these proton acceptors do form complexes with the hydroxyl group involved in the intramolecular bond of catechol. The positive ΔH_2 observed for the second stepwise reaction between catechol and these acceptors has been attributed in part to solvation effects.[2] The results of the present investigation on the corresponding complexes of resorcinol make this assessment dubious. If the solvation effects for catechol complexes are due in part to the disruption of solvent structure by the bulky species containing two proton acceptor molecules, similar ΔH_2 and ΔS_2 values would be expected for resorcinol and catechol systems. Since this is not the case, it appears that steric differences between the *o*- and *m*-dihydroxybenzene complexes containing two proton acceptors must be held accountable for the unusual ΔH_2 of the catechol complexes.

Acknowledgment. Support for this work was provided by the Research Corporation through the Cottrell College Science Grants program.

Miniprint Material Available. Full-sized photocopies of the miniprinted material from this paper only (Table II) or microfiche (105 × 148 mm, 24× reduction, negatives) containing all of the miniprinted and supplementary material for the papers in this issue may be obtained from the Journals Department, American Chemical Society, 1155 16th St., N.W., Washington, D. C. 20036. Remit check or money order for $3.00 for photocopy or $2.00 for microfiche, referring to code number JPC-75-332.

References and Notes

(1) J. N. Spencer, R. A. Heckman, R. S. Harner, S. L. Shoop, and K. S. Robertson, *J. Phys. Chem.*, **77**, 3103 (1973).
(2) J. N. Spencer, K. S. Robertson, and E. E. Quick, *J. Phys. Chem.*, **78**, 2236 (1974).
(3) J. R. Holmes, D. Kivelson, and W. C. Drinkard, *J. Amer. Chem. Soc.*, **84**, 4677 (1962).
(4) F. Takahashi and N. C. Li, *J. Amer. Chem. Soc.*, **88**, 1147 (1966).
(5) N. Muller and P. Simon, *J. Phys. Chem.*, **71**, 568 (1967).
(6) S. Nishimura, C. H. Ke, and N. C. Li, *J. Amer. Chem. Soc.*, **90**, 234 (1968).
(7) J. E. Bundschuh, F. Takahashi, and N. C. Li, *Spectrochim. Acta, Part A*, **24**, 1639 (1968).
(8) J. Reuben, *J. Amer. Chem. Soc.*, **91**, 5725 (1969).
(9) E. A. Robinson, H. D. Schreiber, and J. N. Spencer, *J. Phys. Chem.*, **75**, 2219 (1971).
(10) U. Liddel and E. D. Becker, *Spectrochim. Acta*, **10**, 70 (1957).
(11) P. A. Kollman and L. C. Allen, *Chem. Rev.*, **72**, 283 (1972).
(12) L. J. Bellamy and R. J. Pace, *Spectrochim. Acta*, **22**, 525 (1966).
(13) G. Kortüm, W. Vogel, and K. Andrussow, "Dissociation Constants of Organic Acids in Aqueous Solution," Butterworths, London, 1961.
(14) D. T. Y. Chen and K. J. Laidler, *Trans. Faraday Soc.*, **58**, 480 (1962).
(15) L. J. Bellamy, G. Eglinton, and J. F. Morman, *J. Chem. Soc.*, 4762 (1961).
(16) R. West, D. L. Powell, M. K. T. Lee, and L. S. Whatley, *J. Amer. Chem. Soc.*, **86**, 3227 (1964).
(17) L. J. Bellamy, K. J. Morgan, and R. J. Pace, *Spectrochim. Acta*, **22**, 535 (1966).

Thermoosmosis in Semipermeable Membranes

M. S. Dariel

Chemistry Department, Nuclear Research Center, Negev, Israel

and O. Kedem*

Polymer Department, The Weizmann Institute of Science, Rehovot, Israel *(Received October 2, 1973; Revised Manuscript Received April 29, 1974)*

Publication costs assisted by The Weizmann Institute of Science

Thermoosmotic flow in the presence and absence of an osmotic pressure difference was measured in cellulose acetate and other synthetic membranes. The thermoosmotic pressures in cellulose acetate membranes were found to be a function of temperature, and very high compared to those previously observed in other membranes. Values between 0.94×10^6 and 3.5×10^6 dyn cm^{-2} deg^{-1} were observed. An analysis of the flow equations shows that the heat of transport across a membrane is a sum of two terms: the homogeneous heat of transport in the membrane phase and the enthalpy of dissolution of water in the membrane.

Introduction

The creation of a pressure gradient across a porous wall as a consequence of a temperature gradient has been studied and interpreted in detail for gases.[1] In liquids, thermoosmotic flow across membranes was observed for a number of systems[2-6] and was compared to thermal diffusion in solution.[6]

In this investigation thermoosmotic flow of water was measured in the highly selective cellulose acetate membrane. While thermoosmotic pressures across these membranes are large as compared to those previously observed, a simple analysis shows that much larger effects might in principle be expected in properly chosen systems.

Flow Equations for Thermoosmosis in Solvent Membranes

The general description of thermoosmosis is based on the thermodynamics of irreversible processes.[7]

The usual experimental system consists essentially of two large compartments (subsystems I and II) containing an isotropic, j-component fluid, separated by a capillary, porous wall, or membrane (subsystem III). The compartments exchange only heat with the surroundings but can exchange both heat and matter. Treating this as a discontinuous system, all flows and driving forces refer to compartments I and II, while the membrane (III) appears only as a barrier which sustains the finite differences in pressure, concentration, etc. This membrane is often characterized by the phenomenological coefficients appearing in the flow equations for transport between I and II but in some cases it is possible to analyze the flows in the membrane itself, treating it as a continuous system.

De Groot and Mazur[7] distinguish between two classes of separating subsystems: (a) capillaries of macroscopic dimensions; (b) passages smaller than the free path, *e.g.*, membranes containing small holes, or very thin barriers. In case a, temperature, pressure, and composition are all continuous at the surface of contact between the capillaries and the large compartments and the phenomenological equations describing transport between phases I and II as a discontinuous system can be derived from the corresponding local equations in subsystem III. In case b such relations cannot be given.

The polymer membranes examined here belong to a third class of systems (c) comprising a separate homogeneous phase, with well-defined properties and macroscopic overall dimensions, and a composition differing from that of the large compartments. Unlike an assembly of inert capillaries containing a pure fluid, a homogeneous membrane through which a single substance permeates is a two-component system in which the membrane may be regarded as the solvent. This is not merely a formal device for the thermodynamic description, but was found to be a reasonable model for a number of systems, notably cellulose acetate–water. Assuming that equilibrium is always maintained at the interfaces, it follows that the temperature and the electrochemical potentials of the permeating species must be continuous. However, pressure, concentrations, and electric potentials may be discontinuous. Flow in the membrane can be described by local equations and from these the discontinuous coefficients can be derived, allowing for equilibrium conditions at the surfaces. Hence, in general for systems of type c, the relation between coefficients in the continuous and discontinuous flow equations will contain a thermodynamic magnitude characteristic of the equilibrium between subsystems I and II and the membrane subsystem III.

All gradients in the membrane are in the x direction perpendicular to the membrane surfaces and, at equilibrium, temperatures and chemical potentials at points $x = 0$ and $x = \Delta x$ in the membrane (at opposite surfaces of the membrane) are equal to those in the contiguous solutions. Denoting parameters in the membrane by a bar

$$\bar{T}^{(0)} = \bar{T}' \qquad \bar{T}^{(\Delta x)} = T'' \tag{1}$$

Similarly

$$\bar{\mu}_w^{(0)} = \mu_w' \qquad \bar{\mu}_w^{(\Delta x)} = \mu_w'' \tag{2}$$

where μ_w is the chemical potential of water, dependent on composition, pressure, and temperature. The equilibrium concentration of water in the membrane is determined by the osmotic pressure and the temperature of the adjacent aqueous phases.

Isothermal water flow in a solvent membrane is determined by the mobility of water in the organic phase, $\bar{m}_w$, and the equilibrium water uptake.[8] The linear velocity of water flow in the membrane $\bar{v}$, relative to the membrane matrix is

$$\bar{v} = -\bar{m}_w \frac{d\bar{\mu}_{w,T}}{dx} \quad (3)$$

(The subscript T indicates constant temperature.) The water flow is then

$$J_{w,T} = \bar{c}_w \bar{v} = -\bar{c}_w \bar{m}_w \frac{d\bar{\mu}_{w,T}}{dx} \quad (4)$$

and

$$l_w = \bar{c}_w \bar{m}_w \quad (5)$$

where $\bar{c}_w$ denotes the concentration of water in the membrane. In the stationary state $J_{w,T}$ is constant across the membrane, and eq 4 may be integrated in the isothermal system; using eq 1 and 2

$$J_{w,T}\Delta x = -\int_{\bar{\mu}_{w,T}^{(0)}}^{\bar{\mu}_{w,T}^{(\Delta x)}} \bar{c}_w \bar{m}_w \, d\bar{\mu}_{w,T} = \bar{c}_{wa} \bar{m}_w \Delta\mu_{w,T} \quad (6)$$

In eq 6 and in the following Δ denotes the difference in parameters in compartments I and II: $\Delta\mu_w \equiv \mu_w' - \mu_w''$

$$J_{w,T} = \frac{l_w}{\Delta x} \Delta\mu_{w,T} \quad (7)$$

$\bar{c}_{wa}$ is the average concentration of water in the membrane; in most practical cases $\bar{c}_w$ changes only slightly across the membrane and the mobility is assumed to be constant.

While only water penetrates the membrane, the compartments separated by the membrane may contain solutions of some impermeable solutes, thus creating a difference in osmotic pressure, $\Delta\Pi$, in addition to the hydrostatic pressure difference, Δp.

The overall driving force is then

$$\Delta\mu_{w,T} = V_w(\Delta p - \Delta\Pi) \quad (8)$$

where V_w is the molar volume of water. The isothermal flow of water is, from eq 7 and 8

$$J_{w,T} = \frac{V_w l_w}{\Delta x}(\Delta p - \Delta\Pi) \quad (9)$$

introducing the relation

$$L_p = V_w^2 l_w / \Delta x$$

we finally obtain

$$J_{v,T} = V_w J_{w,T} = L_p(\Delta p - \Delta\Pi)$$

where $J_{v,T}$ is the isothermal volume flow in cm sec^{-1} and L_p is the hydraulic permeability of the membrane.

For a multicomponent system in which gradients of pressure, concentration, and temperature may be maintained, the local dissipation function is of the following form:[7]

$$\phi = T\frac{d_i S}{dt} = -\sum_j J_j \frac{d\mu_{j,T}}{dx} - \frac{J_q}{T}\frac{dT}{dx} \quad (10)$$

where $d_i S$ is the entropy produced in the system by irreversible processes, J_j is the molar flow of component j, and $d\mu_{j,T}/dx$ is the gradient of the chemical potential of j at constant temperature. The reduced heat flow is defined by

$$J_q = J_\phi - \sum_j h_j J_j \quad (11)$$

J_ϕ is the total heat flow and h_j the partial molar enthalpy of component j. With water as the only permeant and choosing the membrane matrix as the frame of reference, the dissipation function is simplified to

$$\phi = -J_w \frac{d\mu_{w,T}}{dx} - \frac{J_q}{T}\frac{dT}{dx} \quad (12)$$

The term for the membrane component disappears because its flow is zero, by definition, but of course that does not mean that the gradient of its chemical potential vanishes.

In general, both J_w and J_q are proportional to both driving forces: water flow may be expected for zero $d\bar{\mu}_{w,T}/dx$ and there may be a, usually small, heat flow even in the absence of an applied temperature gradient. The local phenomenological equations are

$$J_w = -l_w \frac{d\bar{\mu}_{w,T}}{dx} - \frac{l_{wT}}{T}\frac{dT}{dx} \quad (13)$$

$$J_q = -l_{Tw} \frac{d\bar{\mu}_{w,T}}{dx} - \frac{l_T}{T}\frac{dT}{dx} \quad (14)$$

The ratio J_q/J_w at zero dT/dx is the heat flow linked to the flow of 1 mol of water within the membrane phase, the homogeneous heat of transport Q_m. The subscript m indicates that this heat of transport relates to the flow process inside the membrane. From (13) and (14)

$$Q_m = l_{Tw}/l_w \quad (15)$$

According to Onsager's reciprocity law, $l_{wT} = l_{Tw}$, in the linear range of the flow-force relations. With this relation, the dependence of the water flow on the temperature gradient may be expressed in terms of the heat of transport:

$$J_w = -l_w\left(\frac{d\bar{\mu}_{w,T}}{dx} + \frac{Q_m}{T}\frac{dT}{dx}\right) \quad (16)$$

The gradient $d\bar{\mu}_{w,T}/dx$ comprises the contributions of concentration and pressure gradients and possibly also the influence of changes in polymer conformation due to varying degree of swelling. It is neither necessary nor always possible to separate these contributions in order to relate the measured overall transport parameters to the local coefficients. Only in some simple specific systems is such a subdivision of $d\bar{\mu}_w/dx$ justified and useful and, in general, it suffices to assume that the linear velocity, $\bar{v}$, is proportional to the driving force. In the absence of a temperature gradient this leads to the previously given equation for water flow (eq 9).

In the presence of a temperature gradient, however, integration of the flow eq 16 is possible only if the total gradient $d\bar{\mu}_w/dx$ may be separated into the temperature dependent part and the "isothermal" part. This is a good approximation in a narrow enough temperature range, in which no phase transition takes place. The difference of $\bar{\mu}_w$ between two points (inside the membrane) near the surfaces at opposite sides of the membrane may thus be written as a sum of two terms:

$$\bar{\mu}_w^{(0)} - \bar{\mu}_w^{(\Delta x)} = \left(\frac{\partial\bar{\mu}_w}{\partial T}\right)_{c,p}(T^{(0)} - T^{(\Delta x)}) - \int_0^{\Delta x} \frac{d\bar{\mu}_{w,T}}{dx} dx \quad (17)$$

The temperature dependent part is equal to the molar entropy in the membrane, again assumed to be constant in the range $\Delta T = T^{(0)} - T^{(\Delta x)}$

$$(\partial\bar{\mu}_w/\partial T)_{\bar{c},p} = -\bar{s}_w \quad (18)$$

The difference in μ_w between compartments I and II can

also be written as the sum of an isothermal part and a term due to the temperature difference:

$$\Delta\mu_w = \left(\frac{\partial\mu_w}{\partial T}\right)_{c,p}\Delta T + \Delta\mu_{w,T} = -s_w\Delta T + V_w(\Delta p - \Delta\pi) \quad (19)$$

Introduction of eq 1, 2, 17, and 18 into eq 19 gives

$$-\int_0^{\Delta x}\frac{d\bar{\mu}_{w,T}}{dx}dx = V_w(\Delta p - \Delta\pi) - (s_w - \bar{s}_w)\Delta T \quad (20)$$

When water is equilibrated between solution and membrane phase, $\bar{\mu}_w = \mu_w$, and hence

$$s_w - \bar{s}_w = (h_w - \bar{h}_w)/T \quad (21)$$

With (21), eq 20 becomes

$$-\int_0^{\Delta x}\frac{d\bar{\mu}_{w,T}}{dx}dx = V_w(\Delta p - \Delta\pi) + \frac{\Delta H^s}{\bar{T}}\Delta T \quad (22)$$

where ΔH^s is the molar enthalpy change for the dissolution of water in the membrane phase. The driving force for water flow in the membrane, $d\bar{\mu}_{w,T}/dx$, is thus expressed by means of two well-defined, experimentally measurable quantities.

The integrated form of the flow eq 16 is, with the relation given in (22)

$$J_w = \frac{l_w}{\Delta x}\left[V_w(\Delta p - \Delta\pi) + \frac{\Delta H^s + Q_m}{T}\Delta T\right] \quad (23)$$

(According to our sign convention $-\int_0^{\Delta x}dT = \Delta T$)

The volume flow as a function of the overall driving force is, finally

$$J_v = L_v\left[(\Delta p - \Delta\pi) + \frac{Q^*}{V_w T}\Delta T\right] \quad (24)$$

where $Q^* = Q_m + \Delta H^s$.

Q^* is the total heat of transport for the discontinuous system, consisting of two parts: the homogeneous heat of transport for flow in the membrane phase, and the heat effect of transfer between the aqueous and membrane phases.

Equation 24 is a form of the usual description of thermoosmosis in discontinuous systems, where the fluxes and forces can be described by

$$J_w = L_w V_w(\Delta p - \Delta\pi) + L_{wT}\frac{\Delta T}{T} \quad (25)$$

The overall straight coefficient is related to the local one in the usual manner:

$$L_w = l_w/\Delta x \quad (26)$$

However, L_{wT}/L_w is not equal to l_{wT}/l_w. From eq 15, 23, and 25

$$L_{wT}/L_w = l_{wT}/l_w + \Delta H^s \quad (27)$$

As expected from the general discussion of homogeneous membranes (subsystem III belonging to class c), the relation between coefficients in the continuous and discontinuous flow equations contains a magnitude characteristic of the surface equilibrium: in eq 27 the enthalpy of transfer from the aqueous phase to the membrane phase. The well-known relation between thermoosmotic pressure and total heat of transport is, from (24) and (25)

$$\left(\frac{\Delta p - \Delta\pi}{\Delta T}\right)_{J_v} = -\frac{L_{wT}}{L_w V_w T} = -\frac{Q^*}{V_w T} \quad (28)$$

(A subscript on the parentheses indicates a flow or force held at zero.) Hence Q^* can be derived from the total hydrostatic and osmotic pressure in the stationary state, or from separate measurements of volume flow at $\Delta T = 0$ and at $\Delta p - \Delta\pi = 0$

$$\left(\frac{J_v}{\Delta T}\right)_{\Delta p-\Delta\pi}\Big/\left(\frac{J_v}{\Delta p - \Delta\pi}\right)_{\Delta T} = \frac{L_{wT}}{L_w V_w T} = \frac{Q^*}{V_w T} \quad (29)$$

Experimental Section

Materials and Methods. Dense Cellulose Acetate Membranes. Cellulose acetate (Eastman 398-10, 39.8% acetyl content) was dried in a vacuum oven at 85° for 4 hr. A solution was prepared by shaking 20 g of cellulose acetate in 80 ml of acetone (Merck AR) until a clear viscous solution was obtained. Films were prepared by evaporation of the solution spread on a glass plate with a coating knife.

Thickness measurements were made on vacuum dry membranes with a PM-3 comparator, with an applied force of 0.31 kg/cm^2 and an accuracy of ±0.0002 cm. Nine different measurements were made on a 9.4-cm diameter membrane. Individual measurements differed from the mean by no more than 0.0003 cm.

All volume flow measurements were made in thermostated, two compartment cells (Figure 1). The compartments consisted of flat, hollow Perspex cylinders with a free volume of about 52 cm^3. The solutions were stirred by two Perspex propellers connected to magnetic bars driven by a magnetic stirrer.

The membrane was held in place between two Parafilm rings and fitted between two perforated plates machined from Perspex. The exposed area of the membrane was 18.1 cm^2. Volume flow was measured by observing the movement of liquid in two horizontal capillaries graduated to 0.01 ml connected to the cell. At the start of an experiment the initial volume flow caused the membrane to bulge slightly, displacing as much as 0.5 ml of liquid. Volume flow was subsequently always measured against an applied pressure head of 10 cm of H_2O, thus deliberately causing the membrane to bulge before the start of the experiment and eliminating the error. The correction required for the pressure difference was negligible, considering the thermoosmotic pressures involved.

Temperature differences were maintained with a precision of at least ±0.15° by circulating thermostated water in the stainless steel jackets with which the solutions were in direct contact. When temperature gradients were applied, up to 15 hr was allowed for attainment of a steady state. Thermometric expansion and contraction in the capillaries usually lasted for no more than 0.5 to 1 hr.

Water flow was obtained by plotting the volume changes in the capillaries against time. Linearity was found in all cases. Differences between the volume increase in one compartment and volume decrease in the other were due to small leaks in the assembly and were eliminated by tightening the cells gradually for a few days with an applied torque of 25–30 in.-lb until leakage was less than 0.05 ml in 24 hr.

Thermal conductivities of both water-saturated and vacuum-dry dense cellulose acetate membranes were determined with a heated plate device (see ref 9) in which two identical samples were used, one on each side of the heat source. The electrical power required to maintain a constant temperature difference across the samples was read on a precise (±0.2 W) wattmeter and the temperature of the source was determined with thermistors embedded in

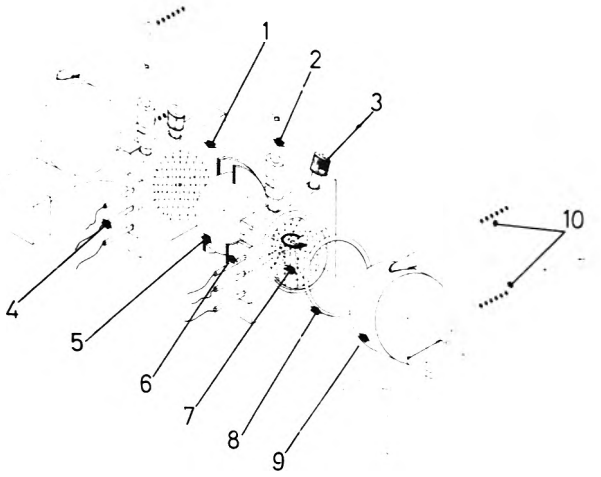

Figure 1. Thermoosmotic apparatus: (1) perforated support plate, (2) pipets for measuring volume flow, (3) sampling port, (4) resistance thermometer, (5) membrane, (6) polyethylene ring, (7) stirrer, (8) rubber O-ring, (9) steel thermostating jacket, (10) thermostating fluid inlets.

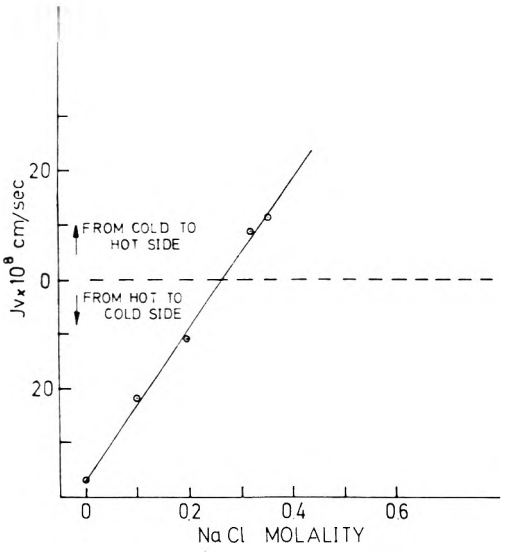

Figure 2. Volume flow for $\Delta T_i = 6.2°$ temperature difference across the membrane at different osmotic gradients. Water was in the cold and NaCl solution in the hot compartment: membrane 1 (74 μ); mean temperature, $T_m = 25°$.

the metal of the heated plate. The whole apparatus was contained in a glove box held at approximately 0.5° below the steady state temperature reached by the heater, thus minimizing radial heat leakage. Heat loss from the sample edges also was negligible for the thin (0.01–0.05 cm) samples used, so that heat flowed primarily from the heated plate through both material samples, and was carried away by the thermostated water running through two steel cooling jackets in contact with the samples.

The thermal resistance of the empty apparatus was found to vary from experiment to experiment while the thermal resistance of the apparatus with membrane samples introduced was constant within 5%, provided the same torque (30 in.-lb) was used to clamp the parts together. As it seemed therefore that good thermal contact was difficult to obtain with the empty apparatus, the overall resistance in the series thermal circuit was measured for a number of membranes having different, known, thicknesses and the thermal resistance of the apparatus found from extrapolation to zero membrane thickness.

Results and Discussion

Volume flow driven by temperature gradients and osmotic pressure differences was measured in cellulose acetate membranes, and it was found that with pure water in both compartments the thermoosmotic volume flow is directed to the cold side.

A series of experiments was conducted with a dense cellulose acetate membrane in which a temperature gradient was applied which produced a thermoosmotic flow in a direction opposite to the flow generated by an osmotic gradient (Figure 2): the salt solutions were in the hot compartment and pure water in the cold compartment. At low salt concentrations the resulting net volume flow is directed to the cold side whereas at gradually higher concentrations the flow decreases and finally changes its direction. The intercept in Figure 2 shows that, with the temperature gradient applied here, volume flow vanishes with water on one side of the membrane, and a 0.27 N solution of sodium chloride on the other, the osmotic pressure of which is 12 atm.

The actual temperature difference across the membrane, ΔT_i, calculated for this experiment (see Table II) is 6.2°. In other words, in this case, a temperature difference of 6.2° constitutes a driving force to the flow of water through the membrane equivalent to a pressure of 12 atm.

Osmotic flows were measured under isothermal conditions at different temperatures. Experimental conditions were chosen so that dilution of the sodium chloride solutions was about 2%, and always less than 4%. The hydraulic permeabilities decreased with increasing membrane thickness but not quite linearly. Values of l_w and the specific hydraulic permeability, $L_p\Delta x$, at zero pressure head can be calculated from the relation $(J_v)_{\Delta T} = -(V_w^2 l_w/\Delta x)\Delta\pi$ (*cf.* Table I).

We do not think that pinholes are responsible for the nonlinearity, as all volume flow experiments were performed with the flow directed against a small hydrostatic pressure. It has been shown[10] that membrane properties depend on conditions of casting and evaporation, and scatter of such magnitude is not uncommon in laboratory-cast cellulose acetate membranes.[11,12]

Figure 3 summarizes several thermoosmotic experiments with pure water on both sides of the membrane, at a mean temperature, $T_m = 25°$, and with temperature differences (ΔT_t) between 10 and 50° maintained between the thermostats. As thermoosmotic flow always occurred from the hot to the cold side, the heat of transfer is positive, and the osmotic pressure difference in the stationary state ($J_v = 0$) has the same sign as ΔT. The hydrostatic pressure required at this stationary state, the thermoosmotic pressure, would, of course, be negative.

It is apparent that the large differences in thickness in the membranes used are not reflected in the flows obtained. This is not surprising, as a different part of the externally applied temperature gradient is dissipated in the unstirred liquid layers in the vicinity of the membrane and on the membrane proper, according to its thickness. The difference in temperature, ΔT_l, between the membrane surfaces can be calculated from the relative thicknesses and from the thermoosmotic water flows. To this end two assumptions are needed: (a) that only the membrane constitutes a barrier to the thermoosmotic volume flow; (b) that the thermal resistance between the two cell compartments

TABLE I: Hydraulic Permeabilities of Dense Cellulose Acetate Membranes

Membrane no.	4	2	4	2	4	2	2	1
t, °C	10	10	25	25	45	45	60	25
$10^4\Delta x$, cm	26	77	26	77	26	77	77	74
$10^{18}l_w$, mol² cm⁻² sec⁻¹ dyn⁻¹	0.65	0.20	1.09	0.33	1.49	0.64	0.92	0.57
$10^{16}L_p\Delta x$, cm⁴ sec⁻¹ dyn⁻¹	2.10	0.65	3.54	1.07	4.84	2.07	2.98	1.85

TABLE II: Thermoosmotic Flows and Calculated Temperature Differences[a]

Volume flow 10^8J_v, cm sec⁻¹	Average thickness $10^4\Delta x$, cm	Temperature differences ΔT_t, °C	ΔT_b, °C	ΔT_i, °C
39	25.5	50	27	2.5
33	75.5	50	27	6.2
23	25.5	30	11	1.8
17.5	75.5	30	11	4.0
7.1	25.5	10	4.5	0.5
5.8	75.5	10	4.5	1.2

[a] ΔT_t = differences in temperature between thermostats. ΔT_b = differences in temperature measured in bulk solutions. ΔT_i = actual temperature differences on membrane sides calculated from eq 31, 32, and 33. Mean temperature = 25°. Pure water in both compartments. Values reported are the average on at least two runs each, on two membranes. Deviations of individual determinations from the average were less than 10%. The thicknesses given are the average thicknesses of a pair of membranes. The pairs were chosen among membranes which differed in thickness by not more than 3 μ. The volume flow is the average flow of each pair.

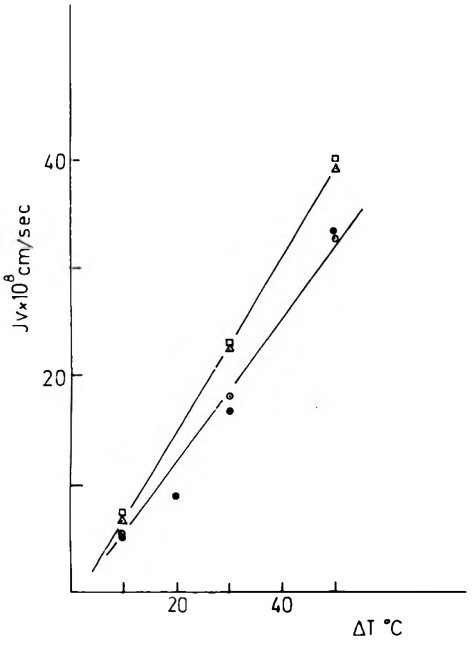

Figure 3. Thermoosmosis at T_m = 25° plotted against the temperature differences ΔT_t maintained between thermostats. For actual temperature differences ΔT_i across membranes, see Table II. □ 25 μ; △ 26 μ; ○ 74 μ; ● 77 μ.

consists of two resistances in series. The one, unchanged from one experiment to another, consists of the unstirred water layers which remain constant as long as the cell geometry and the stirring rate are constant, and the other of the thermal resistance of the membrane itself. This is assumed to be proportional to the membrane thickness.

For two membranes, i and j, of identical composition, of thicknesses Δx_i, Δx_j, and having a thermal conductivity coefficient λ, the flow of heat, J_q, per unit area and time can be written as

$$J_{qi} = \lambda\frac{\Delta T_i}{\Delta x_i} = \lambda_w\frac{\Delta T_{wi}}{\Delta w} \tag{30}$$

where λ_w is the thermal conductivity coefficient of water, Δw, the effective thickness of the unstirred layers, and ΔT_i, ΔT_{wi} the temperature drop across membrane i and the unstirred layers, respectively. For the total temperature difference, measured in the bulk of the solutions, we write

$$\Delta T_b = \Delta T_i + \Delta T_{wi} \tag{31}$$

Corresponding equations can be written for membrane j, and finally, since both thermoosmotic volume flow and heat flow are proportional to the temperature gradient on the membrane itself

$$\left(\frac{J_{qi}}{J_{qj}}\right)_{\Delta T} = \left(\frac{J_{vi}}{J_{vj}}\right)_{\Delta T} = \frac{\Delta T_i}{\Delta x_i}\Big/\frac{\Delta T_j}{\Delta x_j} \tag{32}$$

From eq 30, 31, and 32, ΔT_i is related to the total temperature difference by

$$\Delta T_i = \frac{1 - J_{vi}/J_{vj}}{1 - \Delta x_j/\Delta x_i}\Delta T_b \tag{33}$$

The values for the actual gradients across the membranes are given in Table II for different externally applied temperatures. With these values for ΔT_i, total heats of transport were derived from the osmotic and thermoosmotic flows. Table III shows that the total heats of transports are of the order of 0.1 kcal/mol.

While Q^* depends on the mean temperature, this dependence is much weaker than that of each of the flows separately, as is clearly seen in Figure 4. Hydraulic permeabilities of the cellulose acetate membranes used in this investigation remained constant for a period of 6 months and more, but decreased after heating to 55° (Table IV). The apparent temperature dependence of the flow parameters may thus contain irreversible changes of membrane structure. Since heat annealing decreases volume flow, the increase of the l's with temperature was somewhat underestimated in a sequence of experiments starting with low temperatures.

From the flow equations given above it is clear that the direction of thermoosmosis depends on both the sign and the absolute values of heat of solution and of the heat of transport in the membrane phase. The enthalpy of dissolution of water in cellulose acetate has been reported to be −1.3 kcal/mol.[13] Thus the observed thermoosmosis from the hot to cold side reflects the heat of transport Q_m, partly compensated by the enthalpy change accompanying the transfer from aqueous to polymer phase and *vice versa*.

The total heat of transport and ΔH^s were found to have opposite signs also in another system we examined: polyvinylchloride membranes plasticized with a high percentage of tributylphosphate (TBP).[14] Here too, thermoosmosis

TABLE III

Membrane no.	10^4 Δx, cm	T_m, °K	10^{12} (l_{wT}/T), cm^{-1} sec^{-1} deg^{-1}	Q^*, cal/mol	$10^{-6}(\Delta P/\Delta T)_{J_v}$, dyn cm^{-2} deg^{-1}
2	77	283	10.7	370	−3.02
2	77	298	18.2	390	−3.00
2	77	318	36.4	440	−3.15
2	77	328	58.9	500	−3.50
4	26	298	18.2	120	−0.94

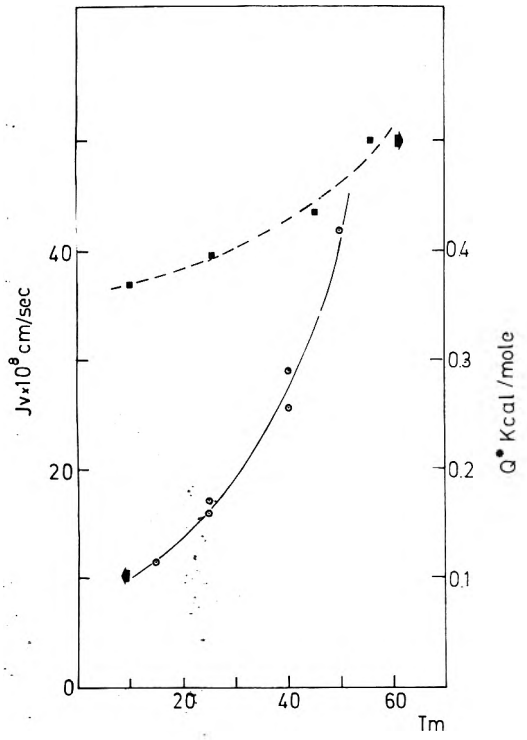

Figure 4. Dependence on mean temperature, T_m, of thermoosmosis (solid line) and heat of transfer Q^* (broken line): temperature difference across membrane, $\Delta T_i = 4°$; membrane 2 (77 μ).

was directed from hot to cold, *i.e.*, total heat of transport positive. The enthalpy of dissolution of water in TBP is $\Delta H^s = -1.05$ kcal/mol,[15,16] giving rise to an opposite heat effect. In sulfonated polyethylene cationic and anionic membranes we found a large thermoosmotic flow toward the hot compartment. The temperature dependence of water uptake in these membranes is not known and will be the subject of further investigation. The question whether Q_m and ΔH^s in a given system always have opposite signs is of both theoretical and practical interest. For ΔH^s and Q_m of equal sign very high thermoosmotic pressures might be obtained.

The values obtained here for Q^* may be compared to those in the literature for other aqueous membrane–water systems (Table V). If we take account of the fact that the values reported there make no allowance for temperature drops in the solutions, the values of Q^* quoted are too small by a factor of perhaps 10. Even so, the heats of transfer found by us for water in cellulose acetate membranes are larger by at least 1 or 2 orders of magnitude.

Although the structure of cellulose acetate membranes and the mechanism of water permeation are not completely understood, high salt rejection and low water permeability

TABLE IV: Decrease in Osmotic Fluxes Caused by Temperature Annealing or Slow Evaporation Rate of Solvent After Casting

NaCl, M	$10^6 J_v$, cm/sec			
	a	*b*	*c*	*d*
0.10	0.62	0.66	0.41	0.30
0.20	1.22	1.28	0.81	0.62
0.35	1.98		1.25	1.01
0.50	3.12	3.13	1.85	1.61
0.68		4.26	2.50	

[a–c] Osmotic fluxes measured at 25°. *a*, *b*, and c, performed on 26-μ membrane cast from 20% cellulose acetate in acetone at room temperature and evaporated in room atmosphere: (*a*) before thermoosmosis experiments; (*b*) after 6 months of thermoosmosis experiments at T_m = 25°; (c) after thermoosmosis experiments at T_m = 55°. [d] Membrane cast as above, at room temperature, but evaporated in 80% saturated acetone atmosphere.

TABLE V: Cellophane + Water

T, °C	$(\Delta p/\Delta T)_0$, dyn/cm² deg	Q^*, cal/mol
	Rastogi, *et al.*	
46	-0.85×10^3	0.137
54	-0.91×10^3	0.128
50	-0.63×10^3	0.088
	Haase, *et al.*	
10.9	-1.97×10^3	2.43
32.2	-7.8×10^3	1.03
71.4	2.64×10^3	−0.40
76.9	2.98×10^3	−0.46

are connected with high density. High density is achieved by slow evaporation of solvent (achieved by controlling its vapor pressure in the casting chamber) and by high annealing temperatures.

It has been found previously that thermoosmosis is decreased by large pore size. It is also intuitively apparent that, while reduced pore size should, all other parameters being unchanged, increase the resistance to flow, it increases the interaction between matrix and diffusant which is essential to thermoosmosis. There is no definite evidence which would allow us to decide whether the permeation of water through dense cellulose acetate is entirely diffusional or partly pore flow.[11,12,17–19] Whatever the detailed structural interpretation, it has been shown that in annealed, less permeable, membranes, the water–matrix interaction is increased relative to the water–water interaction. It seems that only in membranes with this type of interaction, *i.e.*, low g value[17] can strong thermoosmosis be expected.

In any attempt to apply thermoosmosis to desalination by the use of waste heat, the thermodynamic efficiency of the process will be limited by the degree of coupling.[20] It is thus of interest to consider the tightness of coupling between the flow of heat and the flow of water. A convenient operational definition of the degree of coupling in the present system arises from the relative magnitudes of the flows under different conditions. For given ΔT, J_q at $\Delta p - \Delta\pi = 0$ is compared to J_q at $J_w = 0$

$$(J_q)_{J_w}/(J_q)_{\Delta p-\Delta\pi} = 1 - q^2 \qquad (34)$$

In a similar manner, for a given $\Delta p - \Delta\pi$

$$(J_w)_{J_q}/(J_w)_{\Delta T} = 1 - q^2 \qquad (35)$$

For complete coupling, both flows are stopped simultaneously, and q^2 is near to unity. If the flows of heat and water are independent of each other, each flow is proportional to its conjugate force only, and $q = 0$. In other words, for $q = 0$, the cross coefficients of eq 13, 14 and 25 are zero. It can be shown from eq 34 or 35 and 25 that

$$q^2 = L_{wT}^2/L_w L_T = (Q^*)^2(l_w/\lambda T) \quad (36)$$

The thermal conductivity of water-saturated dense cellulose acetate membranes, as determined with the apparatus described in the Experimental Section, is equal to $\lambda = 11.5 \times 10^{-4}$ cal cm^{-1} sec^{-1} deg^{-1}. Introducing this quantity, the heat of transport, and the water permeability into eq 36 we calculate values of q not in excess of 2.5×10^{-3} or about 0.25%. This is, of course, a very low value. Even with the relatively large thermoosmotic coefficient observed in cellulose acetate, coupling between the flow of heat and the flow of water is quite loose. Obviously, thermal leak through the membrane between the compartments is an extremely large fraction of the total energy expended.

Considering the alternate paths available for the passage of heat from one compartment to the other, a thermoosmotically efficient membrane should, among other things, be both very permeable to matter and a good heat insulator. As the conditions of minimal resistance to material flow and maximal resistance to thermal flow appear to be mutually exclusive in solid or liquid membranes of conventional design, only systems with very high Q^* values can attain a reasonable measure of efficiency.

Acknowledgment. We thank Miss C. Bailis for her capable technical assistance.

References and Notes

(1) K. D. Denbigh, *Proc. Roy. Soc. Ser. A*, **210**, 377, 518 (1952).
(2) C. W. Carr and K. Sollner, *J. Electrochem. Soc.*, **109**, 616 (1962).
(3) R. Haase and H. J. De Greiff, *Z. Naturforsch. A*, **26**, 1773 (1971).
(4) R. P. Rastogi, K. Singh, and B. M. Misra, *Desalination*, **3**, 32 (1967).
(5) C. Dirksen, *Soil Sci. Soc. Amer., Proc.*, **33**, 821 (1969).
(6) H. Voellmy and P. Lauger, *Ber. Bunsenges. Phys. Chem.*, **70**, 165 (1966).
(7) S. R. De Groot and P. Mazur, "Non-Equilibrium Thermodynamics," North-Holland Publishing Co., Amsterdam, 1963, pp 273, 417.
(8) O. Kedem in "Reverse Osmosis Membrane Research," H. K. Lonsdale and E. H. Podall, Ed., Plenum Press, 1972.
(9) H. Schenck, "Heat Transfer Engineering," Longmans Green and Co., New York, N.Y., 1960.
(10) B. Kunst and S. Sourirajan, *J. Appl. Polym. Sci.*, **14**, 723 (1970).
(11) H. K. Lonsdale, U. Merten and R. L. Riley, *J. Appl. Polym. Sci.*, **9**, 1341 (1965).
(12) H. E. Grethlein, *Desalination*, **12**, 45 (1973).
(13) H. R. Manesberger, Ed., "Textile Fibers," Wiley, New York, N.Y., 1954, p 886.
(14) R. Bloch, A. Finkelstein, O. Kedem, and D. Vofsi, *Ind. Eng. Chem., Process Des. Develop.*, **6**, 231 (1967).
(15) C. J. Hardy, D. Fairhurst, H. A. C. McKay, and A. M. Wilson, *Trans. Faraday Soc.*, **60**, 1626 (1964).
(16) D. R. Olander, L. Donadien, and M. Benedict, *AIChE J.*, **7**, 153 (1961).
(17) G. Thau, R. Bloch, and O. Kedem, *Desalination*, **1**, 129 (1966).
(18) P. Meares, *Eur. Polym. J.*, **2**, 241 (1966).
(19) E. Gluekauf and P. J. Russell, *Desalination*, **8**, 351 (1970).
(20) O. Kedem and S. R. Caplan, *Trans. Faraday Soc.*, **61**, 1897 (1965).

Biological Ion Exchanger Resins. VI. Determination of the Donnan Potentials of Single Ion-Exchange Beads with Microelectrodes

Michael Goldsmith,* Doris Hor, and Raymond Damadian

Department of Medicine and Program in Biophysics, State University of New York at Brooklyn, Brooklyn, New York *(Received September 3, 1974)*

Publication costs assisted by the National Institutes of Health

Donnan potentials of Dowex 50W X 2 ion-exchange beads were determined by direct puncture of the single beads with microelectrodes. The voltages were found to be independent of the size of the bead and to vary in a nernstian manner with external salt activities below approximately 80 m*m*. Counterion activity coefficients inside the bead were calculated from the voltage, and the chemical determination of the internal molality. The single-ion activity coefficient for potassium was found to be approximately constant (at 0.27) below an external KCl activity of 0.08 *m*.

Introduction

One of the most consistent properties of biological systems is the presence of a voltage across the cellular surface. The mechanism whereby this voltage arises is still in dispute, with one school of thought holding it to be a diffusion potential.[1] Ling gives cogent arguments against this concept, and suggests the voltage to be an adsorption potential.[2] More recently, a concept that ion exchanger resins can be utilized as a useful representation of living cells has been advanced.[3-9]

Since the biological diffusion potential requires the presence of a cell membrane, we had particular interest in the magnitude of the voltages that might be generated by fixed charge systems in the absence of membranes. Consequently we undertook the determination of resin bead potentials by direct puncture.

Since ion-exchange beads meet all the criteria of Donnan systems, theoretical treatments have assumed the existance of potential differences across the bead–solution interface (Donnan potentials). Experimental evaluation of these

Donnan potentials has been limited, and restricted to investigations on macroscopic ion exchanger membranes separating two aqueous compartments. To the best of our knowledge, this paper represents the first determination of the Donnan potentials of single resin beads by direct puncture with microelectrodes.

Experimental Section

All of the studies described below were performed on Dowex 50W X 2 ion exchanger resin (50–100 mesh size). This exchanger was obtained in the H^+ form from BioRad Laboratories (Richmond, Calif.). The beads were column equilibrated against 2 *M* KCl until the effluent pH became constant. The column was then washed with deionized-distilled water until the effluent contained no potassium as measured by flame photometry. The beads were then air dried and stored until needed.

Potassium concentrations were determined by flame photometry on an Instrumentation Laboratory Model 143 flame photometer (Boston, Mass.).

The activity of KCl in the various suspending mediums was obtained by multiplying the concentration by the mean activity coefficient of KCl. For concentrations less than 1×10^{-2} *m*, the mean activity coefficient was assumed equal to the single-ion activity coefficient and was calculated from Debye–Hückel theory. For external concentrations greater than this value, the mean activity coefficient was interpolated from the data of Harned and Owen.[10] Micropipet tip diameters were less than 2 μ as judged by optical microscopy. Electrode resistances were in the range between 8 and 30 megohms in 10 m*M* KCl. The micropipets were filled by boiling in 1 *M* KCl and fitted into a permanent silver–silver chloride inner reference cell designed to allow disposal of used micropipet tips. All measurements were made against a Radiometer saturated calomel electrode with a KCl salt bridge (either of porous pin junction Types K 4112 or K 401).

In order to guard against tip potential artifacts, the electrode pair was calibrated in KCl solutions ranging from 2 *M* to distilled water. All the voltages reported in the text have been corrected for the tip potential artifact. All potential difference measurements were made on a Radiometer pHM 26C millivolt meter (Radiometer Corp., Copenhagen, Denmark) with an input impedance of better than 10^{11} ohms.

Experimental work was accomplished under a 72× dissecting microscope using a highly reflective surface as a work platform. A small quantity of K^+ form beads (30–50) were suspended in KCl medium of varying concentrations using half of a petri dish as a container, and allowed to equilibrate overnight. The reference electrode was placed in the suspending medium, and the microelectrode was advanced into the bead slowly with the aid of a micromanipulator. The advance was made at an angle of 40–50° from the plane of the platform. The slightest penetration of the resin bead caused an immediate jump in the recorded voltage. The microelectrode would then be advanced further in small increments until no further rise in voltage was obtained. Usually, the voltage was at its highest point in the initial penetration. It was found that visible cracking of the bead surface (by too deep a penetration with the electrode) resulted in anomalously low readings, probably by shorting the microelectrode to the external medium. A slow increase in the magnitude of the voltage with time was observed after penetration of the bead. The increase amounted to approximately a 3–4% change over 5 min at lower external salt concentrations. The effect became negligible as the salt concentration of the suspending medium increased. The likely cause for this drift was leakage of KCl from the microelectrode into the bead. All voltages presented in the text are the voltage at time zero. Confirmation of the penetration of the bead came from the observation that lifting of the electrode toward the surface resulted in the lifting of the bead as well, together with the fact that a rise in voltage occurred with penetration. As external salt concentration increased, the resin beads became more difficult to penetrate. Their consistency varied from the appearance of a soft gel (below 100 μm) to a hard plastic (in 1 *m* salt). Although the studies discussed were all made on 2% cross-linked beads, preliminary studies showed that beads with higher cross linking can be successfully punctured with glass microelectrodes.

The potassium content per gram dry weight was determined as follows. An aliquot of beads was dried to constant weight at 103 ± 1°. The beads were then suspended in a large excess of concentrated sulfuric acid of known volume and were equilibrated (with agitation) at ambient temperature for 5 days. At the end of this time period, the potassium content of the supernatant sulfuric acid was determined by flame photometry, and potassium content of the dry beads calculated.

The solvent uptake per gram dry weight was determined by the centrifugation technique of Pepper, *et al.*,[11] with the exception that no correction was made for residual water remaining between the beads.

Results and Discussion

The Donnan potential of a resin bead cannot be directly measured since it is a single electrode potential and as such is undefined.[12] It is usually evaluated by placing two salt bridge electrodes across the Donnan interface. The liquid junction potentials (at the salt bridge surfaces) are either approximated by calculation or more usually, assumed to cancel. If one of the Donnan phases has a substantial nonaqueous component (such as the polystyrene backbone of a resin bead), neither of these procedures is quite satisfactory. However, the use of salt bridge electrodes remains the only direct means of obtaining Donnan potential data. Since the ion-exchange beads in solution are a largely aqueous phase, we assumed the liquid junction potentials to be those arising in simple KCl solutions of equivalent ionic strength. Under these conditions we would expect the junction potential errors (generally less than 4 mV) to fall within experimental scatter.

Figure 1 is a plot of the Donnan potential *vs.* the mean activity of KCl in the suspending medium. Each point represents the mean reading of 7 or more beads with a total of 144 beads studied. The standard deviation of each point was better than ±10% of the voltage indicated. The potential was found to be independent of the size of the bead under study, indicating a high degree of homogeneity in the preparation of the ion exchanger. Such homogeneity has been previously noted.[13]

It should be observed that the curve has a nernstian slope for external activities less than approximately 80 m*m*. For external activities greater than this value, the slope deviates from ideality. This deviation probably reflects contraction of the bead in high external salt. Such a contraction would raise the internal molality.

Since the bead Donnan potential varies in a nernstian

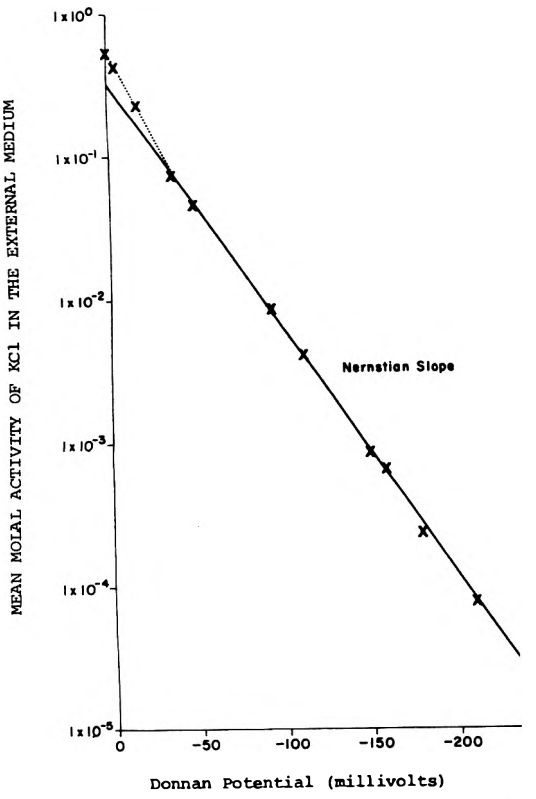

Figure 1. Microelectrode determination of the Donnan potential of Dowex 50 W X 2 (K^+ form) *vs.* external KCl activity at 22°.

manner with the external potassium chloride activity, we may calculate the internal potassium activity from the voltage using the Nernst equation. Column 3 in Table I indicates the internal potassium activity calculated in this manner. Column 4 gives the internal concentration of potassium as determined through chemical analyses. Column 4 does not include a correction for the quantity of nonexchange electrolyte. Such a correction would be negligible for the first three values listed and would be small for the fourth. By dividing the values in column three by those in column four, we obtained the single-ion activity coefficients of potassium inside the bead (column 5). Published values of intrabead activity coefficients represent the mean activity coefficient of the counterion and coion. In order to facilitate comparisons, column 6 gives the mean intrabead activity coefficient of KCl assuming an intrabead activity coefficient of unity for chloride. The mean activity coefficients calculated in this manner are in good agreement with those obtained by Freeman, *et al.*, for this system.[14]

The data given in Table I include measurements at very low external salt activities. Such measurements have previously been unavailable due to the restrictions of the purely chemical techniques used. The results indicate that the potassium activity coefficient within the resin phase remains constant down to very low external salt activities. Thus, the data presented in Table I support the conclusion of Freeman, *et al.*,[14] that intraresin activity coefficients are constant below 0.1 *m* external salt, and extends the validity of this conclusion to at least 1×10^{-4} *m* external salt activity.

TABLE I: Resin Phase Activity Coefficients for K^+ in Dowex 50 W X2[a]

Media (KCl), *m*	Donnan potential, mV	Internal (K^+), *m*	Internal $[K^+]$, *m*[b]	Internal $\bar{\gamma}_{K^+}$	Internal $\bar{\gamma}_{KCl}$[c]
9.8×10^{-5}	−204 ± 17	0.31	1.16	0.27 ± 0.05	0.52
9.6×10^{-4}	−146 ± 13	0.31	1.14	0.27 ± 0.05	0.52
8.5×10^{-3}	−90 ± 8	0.30	1.11	0.27 ± 0.07	0.52
7.3×10^{-2}	−38 ± 3	0.33	1.26	0.26 ± 0.07	0.51

[a] Bead fixed charge capacity was 5.21 ± 0.03 mequiv/gm dry wt (H^+ form). Parentheses indicate molal activity and brackets indicate molal concentrations. [b] Uncorrected for nonexchange electrolyte. [c] Assuming $\bar{\gamma}_{Cl^-} = 1.00$.

The results of this study indicate the value and feasibility of making microelectrode measurements directly in the resin phase. In addition to providing a direct means of observing the intrabead environment, the use of microelectrodes extends the range of experimental observation to very low medium salt activities.

Acknowledgments. This work was performed under a grant from the National Institutes of Health (AM-14890).

The authors wish to thank Mrs. Anne Russo for her secretarial assistance in the preparation of this manuscript.

References and Notes

(1) A. L. Hodgkin and B. Katz, *J. Physiol.*, **108**, 37 (1949).
(2) G. N. Ling, "A Physical Theory of the Living State," Blaisdell Publishing Co., New York, N.Y., 1962, Chapter 10.
(3) R. Damadian, *Biophys. J.*, **11**, 739 (1971).
(4) R. Damadian, M. Goldsmith, and K. S. Zaner, *Biophys. J.*, **11**, 761 (1971).
(5) R. Damadian, *Biophys. J.*, **11**, 773 (1971).
(6) F. W. Cope and R. Damadian, *Physiol. Chem. Phys.*, **6**, 17 (1974).
(7) M. Goldsmith and R. Damadian, *Physiol. Chem. Phys.* **6**, 51 (1974).
(8) R. Damadian, *Ann. N.Y. Acad. Sci.*, **204**, 211 (1973).
(9) L. Minkoff and R. Damadian, *Ann. N.Y. Acad. Sci.*, **204**, 249 (1973).
(10) H. S. Harned and B. B. Owen, "The Physical Chemistry of Electrolytic Solutions," 3rd ed, Reinhold, New York, N.Y., 1958.
(11) K. W. Pepper, D. Reichenberg, and D. K. Hale, *J. Chem. Soc.*, 3129 (1952).
(12) F. Helferrich, "Ion Exchange," McGraw-Hill, New York, N.Y., 1962, p 371.
(13) W. D. Moseley, Jr., and D. H. Freeman, *J. Phys. Chem.*, **67**, 2225 (1963).
(14) D. H. Freeman, V. C. Patel, and T. M. Buchanan, *J. Phys. Chem.*, **69**, 1477 (1965).

Crystal Spectra of Cobalt(II) Chloride Hexahydrate

Hubert W. Joy and Norman Fogel*[1,2]

Department of Chemistry, University of Oklahoma, Norman, Oklahoma 73069 *(Received July 8, 1974)*

The polarized and unpolarized spectra of $CoCl_2 \cdot 6H_2O$ have been studied at room temperature and at liquid nitrogen temperature. The spectra have been fitted using axially elongated tetragonal distortion (D_{4h}) symmetry with the ligand field parameters Dq = 954 K, Ds = 718.5 K, Dt = 228.5 K, the Racah parameter B = 853, and the ratio B/C = 4.323. A limited form of spin–orbit coupling indicates that $\lambda = -170$ K. The spectrum can be fitted reasonably using these parameters, although the site symmetry (C_{2h}) must be used to explain the polarized spectra and some of the fine structure details. The split components of the $^4T_{2g}(F)$, and $^2T_{1g}(P)$ (both in O_h symmetry) are located, as well as some split components of other symmetries in the near infrared and ultraviolet.

Introduction

The spectrum of cobalt(II) chloride hexahydrate has been previously reported by Gielessen,[3] Pappalardo,[4] and by Ferguson.[5] Gielessen was uninterested in analyzing the band structure, although he pointed out that the spectrum was anisotropic. Pappalardo studied the effect of temperature and analyzed the band structure by assuming octahedral (O_h) symmetry. Ferguson, from a study of the polarized spectrum, and a knowledge of the actual crystal symmetry, discussed the band structure qualitatively on the basis of the site symmetry (C_{2h}) and established the symmetry of many of the transitions.

The cobalt(II) chloride hexahydrate contains a $Co(H_2O)_4Cl_2$ unit which is basically an axially extended octahedron. The complex unit has two chloride ions trans to each other, and a square of four water molecules perpendicular to the Cl–Co–Cl, so the molecular symmetry is approximately D_{4h}.[6] The water molecules do not form a true square, but a rectangle that is approximately square, so the molecular symmetry is reduced to D_{2h}. Calculations assuming tetragonal symmetry have been carried out using matrices developed from the weak-field approximation of crystal-field theory. Approximate spin–orbit coupling corrections have been used and the spectrum can be fitted very reasonably with these approximations.

Experimental Section

Reasonably large, well-developed crystals were grown from a water solution of cobalt(II) chloride hexahydrate. The crystal was cleaved and the crystal plate formed was polished to produce two good horizontal planes. The crystal was then mounted over a hole in an aluminum plate and placed in the sample beam of a spectrophotometer. The reference beam was diminished by a series of masks. Room temperature spectra, polarized and unpolarized, were studied in a Cary 14 spectrophotometer at Oak Ridge from 400 to 1800 nm. The low-temperature spectrum (liquid nitrogen temperature) was studied in a Beckman DK-1 spectrophotometer at the University of Oklahoma from about 400 to 800 nm for the polarized spectra and from 350 to 1800 nm for the unpolarized spectrum. The low-temperature spectra were measured in an atmosphere of dry nitrogen so there was no condensation on the crystal.

The cobalt(II) chloride hexahydrate used was analytical reagent grade, recrystallized once before the final crystals were grown. The crystals were analyzed by dehydrating a sample and measuring the weight lost. The chloride ion was analyzed in the dehydrated sample by dissolving the weighed sample in water and titrating for chloride ion by standard methods. *Anal.* Calcd: Cl^-, 54.61; H_2O, 45.44. Found: Cl^-, 54.57 ± 0.07; H_2O, 45.05 ± 0.2.

Crystal Structure of $CoCl_2 \cdot 6H_2O$

The structure has been reported by Mizuno.[6] The unit cell is monoclinic with a = 10.34 Å, b = 7.06 Å, c = 6.67 Å, and β = 122° 20′. The space group is C^3_{2h}–$C2/m$ with two molecules in the unit cell. The cleavage plane is parallel to the (001) face which is well developed in the crystals grown from solution. Cleavage parallel to the (001) face is easy. Figure 1 shows the projections of the $Co(H_2O)_4Cl_2$ units on the (001) face since the light was incident to this face. The Co–Cl bonds lie in the ac plane at right angles to the b axis, which is parallel to the (001) face.

The square of water molecules around the central ion is actually a rectangle with sides of 3.05 and 2.94 Å, so the true molecular symmetry is D_{2h}.[7] This is probably a small perturbation since the spectra can be reasonably well calculated using D_{4h} symmetry. The two waters external to the inner coordination sphere are held by hydrogen bonds and are at some distance from the central ion, and so were not considered in the molecular symmetry. The site symmetry is C_{2h} from a consideration of the closest chloride ions in the adjacent molecular unit.[5,6]

Calculations

The calculations used matrices for all the doublet and quartet states arising from tetragonally distorted d^3–d^7 electronic configurations. The matrices were calculated using the weak-field formalism and off-diagonal elements between states of the same symmetry and spin are included. These matrices were checked against the matrices calculated by Perumareddi[8] using the strong-field formalism. Agreement was to the sixth figure, satisfactory for single precision.

A simplified form of spin–orbit coupling can be calculated which appears only on the diagonal elements of the matrices. The eigenfunctions were tensors, so spin–orbit matrices could be set up following Abragham and Pryce.[9] Ig-

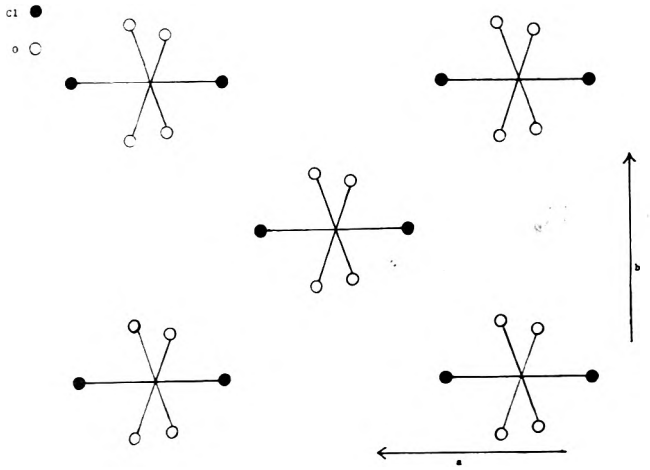

Figure 1. Crystal structure of cobalt(II) chloride hexahydrate, projections of the $Co(H_2O)_4Cl_2$ units on the (001) face.

noring off-diagonal elements and using the invariance of the trace, the matrices can be solved simply. For quartet states the three roots are

$$E = (3/2)\alpha\lambda \quad \text{sixfold degenerate} \quad (1)$$
$$E = -\alpha\lambda \quad \text{fourfold degenerate} \quad (2)$$
$$E = -(5/2)\alpha\lambda \quad \text{twofold degenerate} \quad (3)$$

For doublet states, the two roots are

$$E = 1/2\alpha\lambda \quad \text{fourfold degenerate} \quad (4)$$
$$E = -\alpha\lambda \quad \text{twofold degenerate} \quad (5)$$

where λ is the spin–orbit coupling constant for the term which by standard methods can be related to the spin–orbit coupling constant for the ground state (^4F).[10] α is a constant (in first order) for each symmetry state. α can be evaluated by applying the operators L_x, L_y, and L_z to the eigenfunctions in a symmetry state.[9,10] The first-order values are listed in Table I. The approach is to use octahedral symmetry to calculate the roots and then to assign the roots to the split state produced by a lower symmetry. This was done by solving the spin-matrix and finding the wave functions for each.

The wave functions are the same in octahedral and tetragonal symmetries, since in tetragonal symmetry there are no new off-diagonal elements if spin–orbit coupling is not included in the Hamiltonian. The symmetry of the wave function can then be determined for both symmetries (O_h and D_{4h}). For tetragonal symmetry (D_{4h}) it can be shown that roots (1), (2), and (3) belong to wave functions with ^4E_g symmetry, while roots (1) and (2) can be assigned to wave functions belonging to a singlet state ($^4A_{2g}$ or $^4B_{2g}$). These states rise from the triply degenerate state (T_{1g} or T_{2g}) in O_h symmetry. For the doublet states, roots (4) and (5) can be assigned to wave functions with ^2E_g symmetry and root (4) to the wave functions belonging to singly degenerate states.[11] The roots were added to the appropriate diagonal elements in the ligand-field matrices. For simpler calculations only roots (1) and (3) were used for the ^4E_g states, since root (2) could be interpolated very easily. This is not an exact solution since it ignores off-diagonal elements for spin–orbit states and is useful if the spin–orbit coupling constant (λ) is relatively small as it is in cobalt(II) compounds. This approach produces an approximate value for the spin–orbit coupling constant which can be used for more exact calculations if desired.

The matrices were used in a Fortran IV program which diagonalizes the matrices and varies each parameter to attain the best possible agreement with the experimentally observed band position.[12] This depends on the correct assignment for the bands, but reasonable assignments can usually be made.

TABLE I: Values of the Parameter α

State	α
$^4T_{1g}(F)$, $^2T_{1g}(F)$	−3/2
$^4T_{2g}(F)$, $^2T_{2g}(F)$, $^2T_{1g}(G)$	1/2
$^4T_{1g}(P)$, $^2T_{1g}(P)$	1.0
$^2T_{1g}(G)$	5/2
$^2T_{2g}(H)$	−5/2
$a^2T_{1g}(H)$	15/8
$b^2T_{1g}(H)$	−11/8
$^2T_{2g}(D)$	−1.0

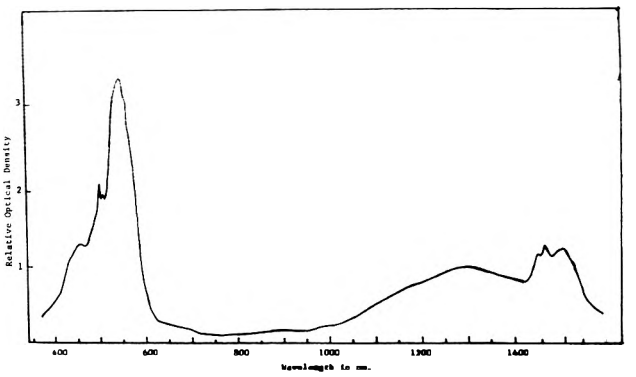

Figure 2. Unpolarized crystal spectrum of $CoCl_2 \cdot 6H_2O$ at room temperature.

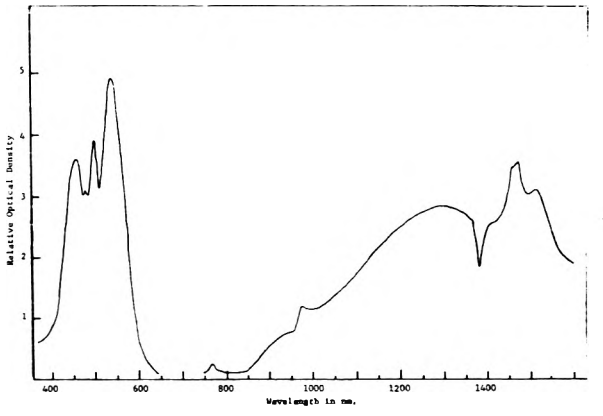

Figure 3. Crystal spectrum of $CoCl_2 \cdot 6H_2O$ polarized perpendicular to the *b* axis at room temperature.

Results and Discussion

The results are in Figures 2–6 and in Table IV. The results are in reasonably good agreement with the work of previous investigators. The room temperature spectrum has considerable structure, but some of the bands are misleading since they are hot bands and arise from an excited vibrational state. The room temperature spectrum is however the only one that has the polarized spectra for the region from 1800 to 800 nm. The spectrum at liquid nitrogen temperature is clearer and with this as a guide, the assignments can usually be made with little trouble.

Ferguson[5] has shown that the polarized spectra must be discussed in terms of the site symmetry (C_{2h}), not the mo-

TABLE II: Correlation Table for the Symmetries O_h, D_{4h}, and C_{2h}[a]

O_h	D_{4h}	C_{2h}
A_{1g}	A_{1g}	A_g
A_{2g}	B_{1g}	A_g
E_g	$B_{1g} + B_{2g}$	$A_g + A_g$
T_{1g}	$A_{2g} + E_g$	$B_g + A_g + B_g$
T_{2g}	$B_{2g} + E_g$	$B_g + A_g + B_g$

[a] Only g representations.

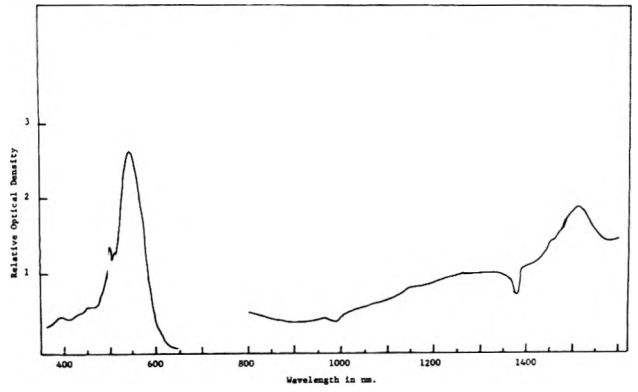

Figure 4. Crystal spectrum of $CoCl_2 \cdot 6H_2O$ polarized parallel to the *b* axis at room temperature.

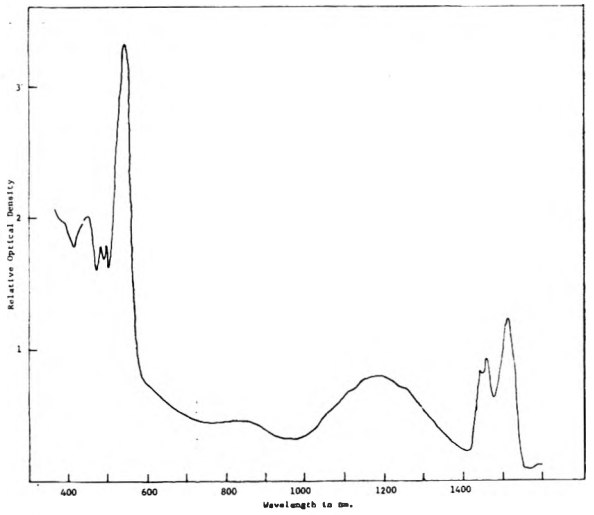

Figure 5. Unpolarized crystal spectrum of $CoCl_2 \cdot 6H_2O$ at liquid nitrogen temperature.

lecular symmetry (D_{2h}). Since the calculations were carried out with tetragonal symmetry (D_{4h}), the symmetry of the transitions will be related to tetragonal or octahedral symmetry where appropriate. The *Z* axis is coincident with the *b* crystal axis and is identical with the C_2 axis which bisects the H_2O–Co–H_2O angle which is perpendicular to the Cl–Co–Cl axis. The correlation table between the symmetries is in Table II. It has been suggested by Ferguson[5] that the intensity of the bands is due to the Cl–Co stretching frequency which has β_u symmetry (α_{2u} in D_{4h}). The vibronic representation in D_{4h} and C_{2h} symmetries for single groups are in Table III.

It has been shown that the polarization indicates that the ground state is of ^4B_g symmetry[5] and this correlates with the $^4A_{2g}$ (in D_{4h}) ground state expected from a com-

TABLE III: Vibronic Representations in D_{4h} and C_{2h} Symmetries for $CoCl_2 \cdot 6H_2O$ (Product of Ground Electronic State, Excited Electronic State, and Perturbing Vibration)

D_{4h} symmetry $^4A_{2g}$ ground state Excited state/ vibrational state	A_{1g}	A_{2g}	B_{1g}	B_{2g}	E_g
2 α_{2u}	A_{1u}	A_{2u}	b_{1u}	b_{2u}	e_u
β_{2u}	b_{1u}	b_{2u}	a_{1u}	a_{2u}	e_u
3 E_u	e_u	e_u	e_u	e_u	a_{2u}

Note: *x*,*y* axis = e_u, *z* axis = a_{2u}, α_{2u} is the high-intensity perturber

C_{2h} symmetry ^4B_g ground state Excited state/ vibrational state	A_g	B_g
6 β_u	a_u	b_u
3 α_u	b_u	a_u

Note: *x*,*y* axis = b_u, *z* axis = a_u, β_u is the high intensity perturber

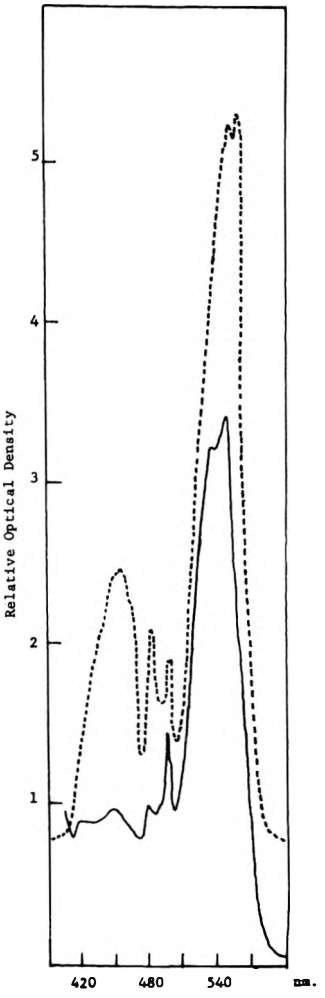

Figure 6. Polarized crystal Spectrum of $CoCl_2 \cdot 6H_2O$ at liquid nitrogen temperature: (————) polarized parallel to the *b* axis, (- - -) polarized perpendicular to the *b* axis.

TABLE IV: Symmetry and Peak Positions for $CoCl_2 \cdot 6H_2O$ (in Kaysers) in D_{4h} Symmetry Observed at Liquid N_2 Temperature

Symmetry	Unpolarized	Polarized spectra		Calcd[a]
		b parallel	*b* perpendicular	
$^4A_{2g}(T_{1g})$				0
				587.0
$^4E_g(T_{1g})$	5,995			222
	5,666			891
$^4B_{2g}(T_{2g})$	6,289 shldr			1,201
	6,579 shldr			6,375
	6,614			6,587
	6,640			
	6,689			
	6,757			
	6,873			
	6,949			
$^2A_1(E_g)$	7,976			8,000
$^4E_g(T_{2g})$	8,197 brd band			8,139
	8,490			8,357
				8,486
$^2B_1(E_g)$	11,494			11,497
$^2E(T_{1g})$	14,492			
$^2A_2(T_{1g})$				14,786
	brd			15,011
$^4B_1(A_{2g})$	shldr			15,570
				16,042
$^2E(T_{2g})$				16,679
				16,849
$^2B_2(T_{2g})$	17,240			17,570
$^4E_g(T_{1g})$	18,450 int	18,467 int	18,484 int	18,416
		18,692 shldr	18,692 shldr	18,811
	18,797 int	18,903 int	18,832 int	19,048
$^2E_g(T_{1g})$	20,243 shldr	20,242 shldr	20,202	20,106
	20,855	20,899	20,855	20,502
	20,576 wk	20,450 shldr wk	20,375 wk	
		20,618 shldr wk		
$^2A_{2g}(T_{1g})$	20,160 shp	20,161 shldr	20,129 shp	20,194
$^2A_{1g}(A_{1g})$	21,978 shldr	22,026 shldr	21,978 shldr	22,070
$^4A_{2g}(T_{1g})$	22,360	21,739 shldr	21,834 shldr	21,807
	22,472	22,222 wk	22,300 int	22,182
$^2B_{2g}(T_{2g})$	24,096 shldr	23,980 shldr	24,272 shldr	24,460
$^2E_g(T_{2g})$	24,875 shldr	24,875 shldr	24,752 shldr	24,761
				24,774
$^2A_{2g}(T_{1g})$				24,725
$^2E_g(T_{1g})$	26,316 shldr			26,383
$^2B_{1g}(E_g)$	27,100 shldr			26,449
$^2A_{1g}(E_g)$	27,624 shldr			27,178
				27,430

[a] Calculated higher states not included since measurement stopped at 350 nm for unpolarized spectra and at 400 for polarized spectra. Shldr = shoulder, wk = weak, int = intense, brd = broad.

plex with axially elongated tetragonal symmetry. Magnetic moment calculations using this ground state were in excellent agreement with the experimental data from 77° A to room temperature. The intense band centered at 18.6 kK is assigned to $^4E_g(P)$ and the band at 22.2 kK is assigned to the $^4A_{2g}(P)$, both split components of the $^4T_{1g}(P)$ in octahedral symmetry. As expected from the C_{2h} symmetry the $^4E_g(P)$ is split into a ^4A_g and ^4B_g which on the basis of the polarized spectra are respectively at 19 and 18.4 kK. This assignment was made because the band at 19 kK shows the same intensity changes in the polarized spectrum as the band at 22.2 kK which has ^4B_g symmetry as can be seen in Figure 6.

The low-intensity bands between 20.1 to 20.9 kK can be assigned to the split components of the $^2T_{1g}(P)$ in O_h symmetry. Since this has the same configuration as the ground state (with one spin reversed) these bands should be relatively sharp as can be observed in Figures 5 and 6. The polarization behavior will be the same as that observed for the quartet states, since in the double groups Γ_8^+ (high spin in O_h) $\rightarrow 2\Gamma_4^+ + 2\Gamma_3^+$ (in C_{2h})[13] while the Γ_6^+ (low spin in O_h) $\rightarrow \Gamma_4^+ + \Gamma_3^+$ (in C_{2h}). This band will be split

into a ^2E_g and a $^2A_{2g}$ in D_{4h} symmetry. The ^2E_g will be split by spin–orbit coupling and by the actual symmetry into ^2A_g and a ^2B_g, while the $^2A_{2g}(P)$ will change to a ^2B_g. The sharp, more intense bands in this region are observed at 20.16, 20.24, and 20.85 kK. The polarized spectra show that the bands at 20.16 and 20.85 kK have the same behavior and can thus be assigned to the ^2B_g symmetry while the band at 20.24 kK with the opposite behavior can be assigned to the ^2A_g. Initial assumptions would put the split components of the $^2E_g(P)$ at 20.16 and 20.24 kK, and the $^2A_{2g}(P)$ at 20.85 kK, but the $^2A_{2g}(P)$ is expected to be lower than the $^2E_g(P)$ and the calculations indicate that this band should be at 20.2 kK. The polarization spectra thus indicates that the first transition at 20.16 kK is the $^2A_{2g}$ (B_g in C_{2h}) and that the two bands at 20.24 and 20.85 kK are the split components of the $^2E_g(P)$ (respectively the ^2A_g and ^2B_g). The actual calculations put the lowest component of the ^2E_g below the $^2A_{2g}(P)$, however, the splitting caused by the site symmetry has not been included in the calculations.

Another point of interest is that the sharp peaks which can be measured with some precision are slightly different in the *b* perpendicular (20.13, 20.20, and 20.85 kK) than in the *b* parallel (20.16, 20.24, and 20.90 kK) spectrum. This can be explained by using the site symmetry. The ground state in the double group[13] can be either Γ_3^+ or Γ_4^+, while for the excited $^2T_{1g}(P)$ (in O_h) the state will be split into Γ_3^+ and Γ_4^+ for the C_{2h} symmetry. Since the β_u vibration is the intensity perturber it appears that for either ground state, the transition $\Gamma_n^+ \leftarrow \Gamma_n^+$ (where $n = 3$ or 4) is intense along the *Z* axis, and of low intensity along the *X* or *Y* axis, whereas the $\Gamma_m^+ \leftarrow \Gamma_n^+$ ($n \neq m = 3$ or 4) is of high intensity along the *X* or *Y* axis and of low intensity along the *Z* axis. Therefore in the *b* parallel spectrum we see the $n \leftarrow n$ transition and in the *b* perpendicular spectrum we see the other transition. This would indicate that the peaks will be shifted in the two polarized spectra as can be seen by the data in Table IV, and as has been observed by others,[3,5] Some of the peaks are broad enough so that the small shift cannot be detected, although it can be observed for the $^4A_{2g}(P)$ peak at 22.2 kK.

Several other puzzling features of the spectra of $CoCl_2 \cdot 6H_2O$ can now be explained. Since the distortion indicated by the splitting of the $^4T_{1g}(P)$ (O_h) is relatively large, it would be expected that the band due to the transition to the $^4T_{2g}(F)$ (O_h) should also be split. The broad band centered around 8.5 kK has been assigned to this transition. Calculations indicate that the split component of this transition belonging to the $^4B_{2g}$ (in D_{4h}) is much lower than this (6.6 kK) and is actually part of the band usually assigned to the overtones of water. The relative complexity of this band is in agreement with this assignment and the polarization spectra indicate that this is the approximate position of $^4B_{2g}(F)$ while the band at 8.5 kK can be assigned to the $^4E_g(F)$ with some doublet transitions included.

Also predicted is the position of a low-intensity band at about 11 kK which can be assigned to the $^2B_{1g}$ split component of the $^2E_g(G)$ in O_h symmetry. The low-intensity transitions to the $^2T_{1g}(G)$ and $^2T_{2g}(G)$ and $^4A_{2g}(F)$ are placed in the weak band stretching from 14.5 to 17 kK. The spectra are therefore described quite well by the use of tetragonal symmetry with an approximate spin–orbit coupling correction.

The crystal field parameters used to calculate these assignments are Dq = 954 K, Ds = 718.5 K, and Dt = 228.5 K. The value of the Racah parameter B was 853 K, and the ratio of B/C was 4.323. The spin–orbit coupling constant (λ) value was −170 K. These values are in the area expected and are in good agreement with the values of Dq and B calculated by Pappalardo,[4] although higher than some previous values.[14] The ordering of the one-electron orbitals is regular and in D_{4h} symmetry the ground state is $e_g^4 b_{2g}^1 b_{1g}^1 a_{1g}^1$ leading to the expected $^4A_{2g}$ symmetry for the ground state. In the site symmetry the e_g will be split, but the splitting is small enough so that it can be ignored for all but fine details.

Acknowledgment. One of us (N.F.) wishes to acknowledge a grant from the Oak Ridge Associated Universities, as well as the help extended by the Metal and Ceramics Division at Oak Ridge where much of the preliminary work was done. We also wish to thank the University of Oklahoma for a grant to help with the computations.

References and Notes

(1) Address correspondence to this author at the Department of Chemistry, University of Oklahoma, Norman, Okla.
(2) O.R.A.U. Fellow 1966–1967, Oak Ridge National Laboratory, Oak Ridge, Tennessee.
(3) J. Gielessen, *Ann. Phys.*, **22**, 537 (1935).
(4) R. Pappalardo, *Phil. Mag.*, **4**, 219 (1959).
(5) J. Ferguson, *J. Chem. Phys.*, **32**, 533 (1960).
(6) J. Mizuno, *J. Phys. Soc. Jap.*, **15**, 1412 (1960).
(7) F. A. Cotton, "Chemical Applications of Group Theory," Wiley-Interscience, New York, N.Y., 1963.
(8) J. R. Perumareddi, *J. Phys. Chem.*, **71**, 3144 (1967).
(9) A. Abragam and M. H. L. Pryce, *Proc. Roy. Soc., Ser. A*, **206**, 173 (1951).
(10) C. J. Ballhausen, "Introduction to Ligand Field Theory," McGraw-Hill, New York, N.Y., 1962.
(11) In first order only T_{1g} or T_{2g} states are split by spin–orbit coupling in an octahedral symmetry.
(12) For more information on the program, communicate with H. W. Joy, P. O. Box 6083, Athens, Ga.
(13) G. F. Kester, *et al.*, "Properties of the Thirty Two Point Groups," MIT Press, Cambridge, Mass., 1963.
(14) L. C. Lewis and N. Fogel, *J. Chem. Soc. A*, 1141 (1970).

Raman Spectra of Sodium Tetrasulfide in Primary Amines. Evidence for S_4^{2-} and S_8^{n-} in Rhombic Sulfur–Amine Solutions

Francis P. Daly and Chris W. Brown*

Department of Chemistry, University of Rhode Island, Kingston, Rhode Island 02881 *(Received March 25, 1974; Revised Manuscript Received November 11, 1974)*

Raman spectra of rhombic sulfur dissolved in ethylenediamine, *n*-propylamine, and monomethylamine have been reported previously. Bands due to new species were observed at 400, 440, 462, 510, and 535 cm^{-1}. Bands at 535 cm^{-1} in the Raman spectra and at 585 cm^{-1} in the infrared spectra were assigned to the symmetric and antisymmetric stretching vibrations of S_3^-, respectively. The bands previously reported at 400, 440, and 510 cm^{-1} are now assigned to the polysulfides, S_4^{2-} and S_8^{n-}. In addition, the Raman spectrum of solid Na_2S_4 is reported for the first time.

Introduction

With the introduction of stricter emission controls on the effluents from the combustion of fossil fuels, it will be necessary to remove sulfur and sulfur compounds either prior to combustion or immediately afterwards.[1] This will increase the currently abundant supply of sulfur; thus, intensive studies for new applications of sulfur have been initiated. Since the interaction of sulfur and amines could prove to be important in a number of chemical reactions, particularly in the catalysis of reactions of sulfur by amines,[2] we have been investigating the composition of the species in sulfur–amine solutions by measuring their vibrational spectra.

Solutions of sulfur and amines are characterized by unusual colors, high conductivities, and free-radical formation.[2] Previously, we reported the presence of the S_3^- species in several primary amine solutions.[3] Further experiments have been performed and an elucidation of the previously unexplained Raman bands is now presented.

Experimental Section

Materials. (a) Rhombic sulfur (Alfa Inorganics) was 99.999% pure. (b) Monomethylamine (Matheson) was 98.0% pure and was used without further purification. (c) Ethylenediamine (EDA) and *n*-propylamine (both from Matheson Coleman and Bell) were distilled under atmospheric conditions and then under vacuum prior to being used. (d) NaHS necessary for the synthesis of Na_2S_4 was prepared by the reaction of hydrogen sulfide (Matheson, 99.5%) and sodium ethoxide in benzene.[4] The NaHS was dried *in vacuo* at approximately 110° for 8 hr. (e) Na_2S_4 was prepared by the reaction of NaHS and S_8 in liquid ammonia under vacuum.[5] The Na_2S_4 was dried at 120° under vacuum for 6 hr. (f) Stock solution of Na_2S_4 in H_2O (Pfaltz and Bauer) had a concentration of 40% by weight and a specific gravity of 1.335 g/ml.

Physical Measurements. Raman spectra were measured using a Spex Industries Model 1401 double monochromator with photon counting detection and a C.R.L. Model 52-A argon ion laser emitting at 4880 Å (≤150 mW power at the sample). All spectra were measured with a spectral slitwidth <8 cm^{-1}. EDA, *n*-propylamine, and H_2O solutions were contained, at 24 ± 1°, in sealed Pyrex capillary tubes with an inner diameter greater than 1.2 mm. Monomethylamine was liquified under vacuum in a Raman cell designed for low-temperature liquids[6] using a Dry Ice–acetone slush bath. A measured amount of sulfur or Na_2S_4 was added to this solvent without breaking the vacuum.

Results

The Raman spectra of solid Na_2S_4 with bands in the S–S stretching region at 424, 448, and 481 cm^{-1} and of Na_2S_4 dissolved in H_2O (~3 *M*) with bands at 414, 448, and 497 cm^{-1} are shown in Figure 1. The spectrum of Na_2S_4 in H_2O is similar to that reported by Ward,[7] who found bands at 419, 454, and 493 cm^{-1}. Spectra are shown only in the 100–600-cm^{-1} region, since all of the new bands associated with polysulfides are in this region.

Dilute solutions (10^{-3} *M*) of Na_2S_4 in EDA are emerald green in color and are similar to 10^{-3} *M* solutions of rhombic sulfur in EDA. The Raman spectrum of Na_2S_4 in EDA with bands at 433, 471 (solvent), 503, and 534 cm^{-1} is shown in Figure 2a. The band at 434 cm^{-1} has a broad shoulder at ~400 cm^{-1}. A spectrum of 10^{-3} *M* rhombic sulfur in EDA is shown in Figure 2c. The major difference between this spectrum and that of Na_2S_4 in EDA is the presence of the band at 400 cm^{-1} in the spectrum of sulfur in EDA. However, the intensity of this band decreases considerably after 24 hr and is almost absent from the spectrum (Figure 2b).

At higher concentrations (10^{-1} *M*) both rhombic sulfur and Na_2S_4 have essentially the same Raman spectrum when dissolved in EDA, and the changes in the spectra with time are the same. The Raman spectrum of 10^{-1} *M* rhombic sulfur in EDA is shown in Figure 3c; the band at 400 cm^{-1} is by far the strongest in the spectrum. However, after 24 hr the relative intensity of this band has decreased considerably as is shown in Figure 3b, and after 72 hr only a shoulder on the band at 440 cm^{-1} remains (Figure 3a). After the time lapse the spectrum of 10^{-1} *M* sulfur (or Na_2S_4) in EDA is the same as the spectrum of 10^{-3} *M* sulfur in EDA after 24 hr and the spectrum of 10^{-3} *M* Na_2S_4 in EDA measured immediately after preparation.

The Raman spectrum of a 3×10^{-2} *M* solution of rhombic sulfur in *n*-propylamine (light orange color) has bands in the S–S stretching region at 397, 438, 465 (solvent), 505,

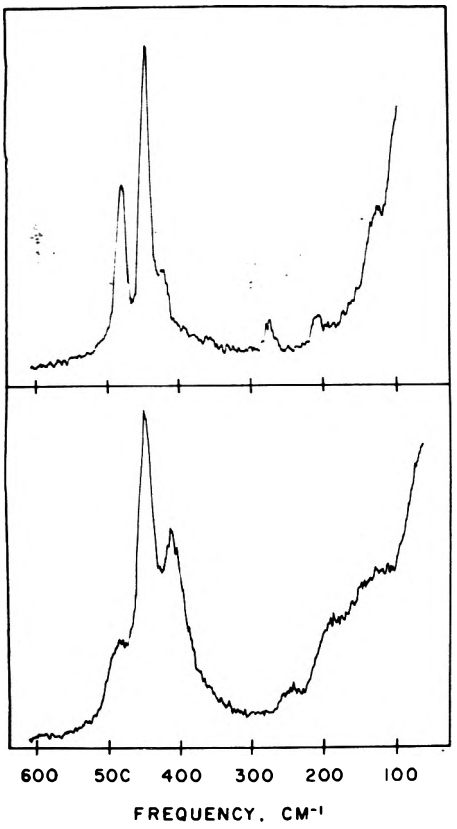

Figure 1. Raman spectra of solid Na_2S_4 (top) and of Na_2S_4 dissolved in H_2O (bottom).

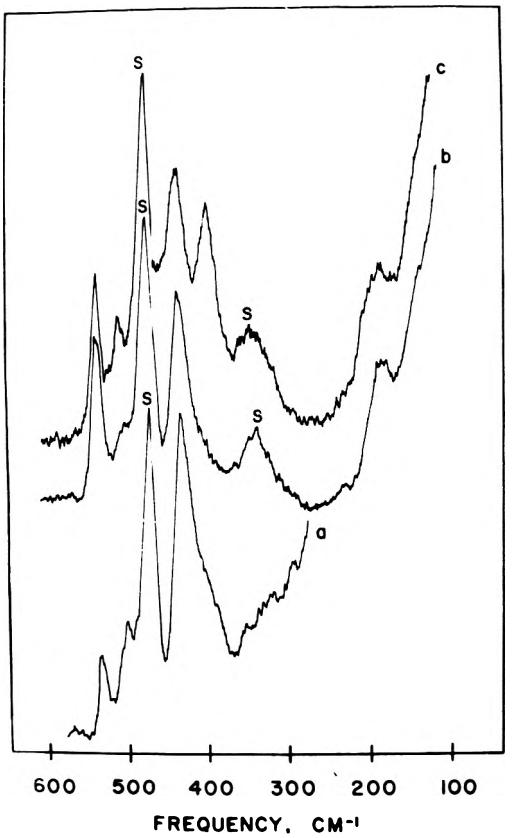

Figure 2. Raman spectra of Na_2S_4 and rhombic sulfur in EDA: (a) 10^{-3} *M* solution of Na_2S_4 in EDA; (b) 10^{-3} *M* solution of rhombic sulfur in EDA after 24 hr; (c) 10^{-3} *M* solution of rhombic sulfur in EDA measured immediately after preparation.

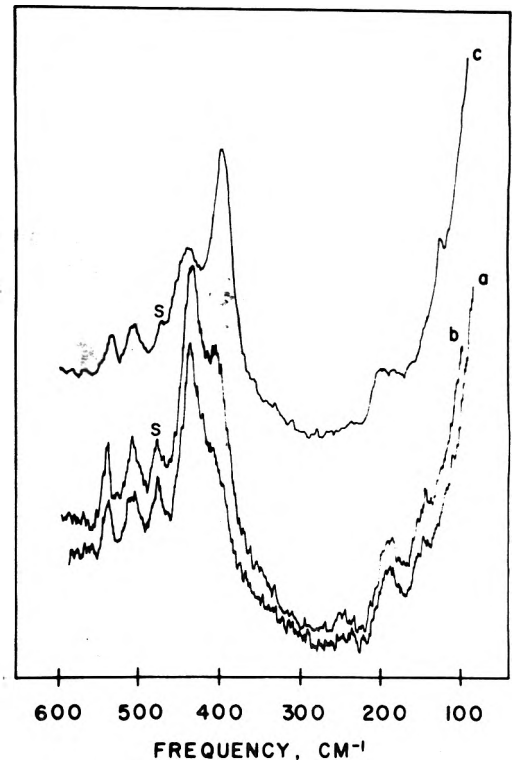

Figure 3. Raman spectra of rhombic sulfur in EDA: (a) 10^{-1} *M* solution measured after 3 days; (b) 10^{-1} *M* solution measured after 24 hr; (c) 10^{-1} *M* solution measured immediately after preparation.

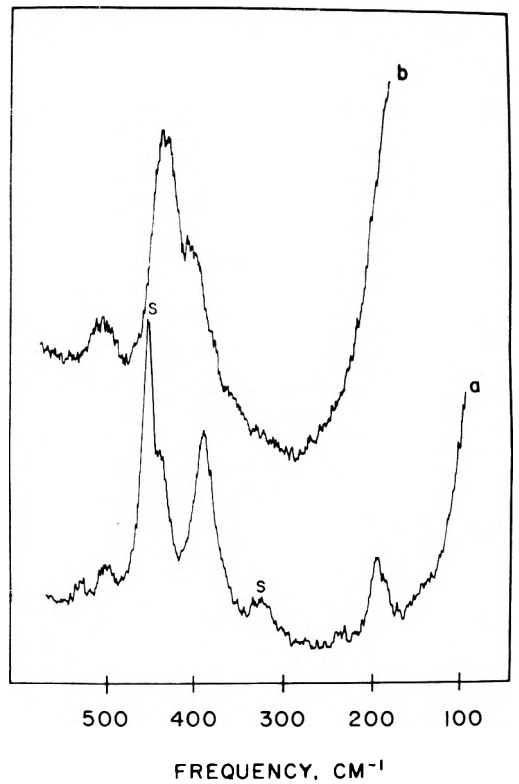

Figure 4. Raman spectra of (a) a 3×10^{-2} *M* solution of Na_2S_4 in *n*-propylamine and of (b) a 3×10^{-2} *M* solution of Na_2S_4 in monomethylamine.

and 534 cm^{-1}. The spectrum of Na_2S_4 in *n*-propylamine (3×10^{-2} *M*) has bands at 393, 442, 460 (solvent), 502, and 535 cm^{-1} as is shown in Figure 4a. After 24 hr the weak

TABLE I: Vibrational Frequencies (cm^{-1}) of Rhombic Sulfur–Amines, Na_2S_4–Amines, and Pure Na_2S_4

Sulfur in EDA	Na_2S_4 in EDA	Sulfur in $C_3H_7NH_2$	Na_2S_4 in $C_3H_7NH_2$	Sulfur in CH_3NH_2	Na_2S_4 in CH_3NH_2	Na_2S_4 in water	Solid Na_2S_4	Assignment
						115	123	S_4^{2-}
188	190							Solvent band
195	196	193	195			191	209	S_4^{2-}
245	240	242	242			245	278	S_4^{2-}
297	300							?
340	335	333	333					Solvent band
396	400	397	393	399	398	414	424	S_4^{2-} and S_8^{n-}
434	433	438	442	437	433	448	448	S_4^{2-}
471	472	465	460	462[a]				Solvent band
502	503	505	502	502	503	497	481	S_4^{2-}
533	534	534	535	535				S_3^-

[a] Raman band of glass container.

band at 535 cm^{-1} increases slightly in intensity, but the remaining bands do not change for either sulfur or Na_2S_4 in *n*-propylamine.

The Raman spectrum of a 3×10^{-2} *M* solution of rhombic sulfur in monomethylamine (straw yellow color) has bands at 399, 437, 462, 502, and 535 cm^{-1}, whereas the spectrum of Na_2S_4 in monomethylamine shown in Figure 4b has bands at 398, 433, and 503 cm^{-1}. This spectrum is almost identical with that of Na_2S_4 in H_2O. There are no significant changes in the spectra of either sulfur or Na_2S_4 in monomethylamine with time.

The observed frequencies for rhombic sulfur–amines, Na_2S_4–amines, and pure Na_2S_4 are listed in Table I. The frequencies of the bands in the present study have been calibrated using emission lines from a neon glow tube and, therefore, tend to differ slightly from those reported previously.[3] There is a very close similarity between the spectra of rhombic sulfur and those of Na_2S_4 in all three amine solutions. The 462-cm^{-1} band previously reported in the spectrum of sulfur–monomethylamine solution is absent in the Na_2S_4–monomethylamine solution. This band was very broad and is likely due to the Raman band of the glass container. Furthermore, the band due to S_3^- at 535 cm^{-1} is also absent from the spectrum of the Na_2S_4–monomethylamine solution. This is probably related to a lower reaction rate of Na_2S_4 to form S_3^- at the lower temperature (−80°).

As mentioned above the Raman spectrum of the aqueous solution of Na_2S_4 reported by Ward[7] was similar to the spectrum we measured. However, when a commercial stock solution of Na_2S_4 in H_2O was diluted to one third of its original concentration the band at 414 cm^{-1} increased in intensity and became as strong as the band at 440 cm^{-1} (Figure 5a, b). Further dilution caused a slight decrease in the intensity of the 414-cm^{-1} band (as is shown in Figure 5c,d,e), but there was also an increase in the turbidity of the solution with the formation of a white-yellow precipitate. The Raman spectrum of this precipitate indicated that it was rhombic sulfur.[8] Thus, the intensity of the band at 414 cm^{-1} is strongly concentration dependent; it first increases with dilution, and then it decreases accompanied by precipitation or rhombic sulfur.

In another experiment solid Na_2S_4 was exposed to air for several weeks. The color of the solid changed from yellow-orange to white-yellow. The spectrum of this solid indicated that rhombic sulfur had formed. Ward[7] observed a similar characteristic of Na_2S_4, namely, that large orthorhombic sulfur crystals could be grown from saturated solutions of Na_2S_4, which were allowed to stand in air for several days.

Discussion

Previously, it has been reported that a possible reaction mechanism for sulfur with triphenylphosphine is the nucleophilic displacement of a sulfur atom on the sulfur molecule by a phosphorus atom of the phosphine.[9] This results in opening the sulfur ring to form an octasulfide chain as follows:

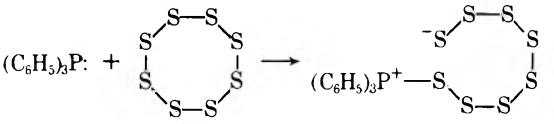

Since nitrogen has a higher electronegativity than phosphorus it is less likely to donate a lone pair of electrons to the S_8 molecule to open the ring. However, Davis and Nakshbendi[2] suggest that removal of a proton from a primary or secondary amine would result in the opening of the ring, and they propose the following mechanism:

$$R_2NH + S_8 \rightleftharpoons \underset{\text{I}}{R_2N^+H{-}S_8^-}$$

$$R_2N^+H{-}S_8^- + R_2NH \rightleftharpoons R_2N^+H_2 + \underset{\text{II}}{R_2N{-}S_8^-}$$

where I is a strong acid and II a weak base. They also suggest that open chain polysulfides (pure sulfur) could be responsible for the unusual colors and conductivities of the sulfur–amine solutions. This is consistent with our observations, since Raman bands between 400 and 500 cm^{-1} have been attributed to the S–S stretching modes of polysulfides. However, the frequency shifts among the various S_8–amine solutions are rather small, the largest being 4 cm^{-1}. This suggests that free open chain polysulfides are present rather than polysulfides bonded to the amine.

The appearance of six Raman bands in the spectra of Na_2S_4–H_2O and solid Na_2S_4 indicates that the species is a tetraatomic molecule with C_2 symmetry as suggested by Ward,[7] who observed five Raman bands in the spectrum of a Na_2S_4–H_2O solution. An ion with the geometry illustrated in Figure 6 has four symmetric vibrations (symmetry species A) and two antisymmetric vibrations (symmetry species B) as defined by the symmetry coordinates listed in Table II.

A normal coordinate calculation was performed using the Wilson FG matrix method[10] and the Schachtschneider

TABLE II: Symmetry Coordinates

Symmetry coordinate	Species	Assignments in H_2O, cm^{-1}
$S_1 = 1/\sqrt{2}(r_1 + r_2)$	A	448
$S_2 = 1/\sqrt{2}(\alpha_1 + \alpha_2)$	A	191
$S_3 = r_3$	A	414
$S_4 = \tau$	A	115
$S_5 = 1/\sqrt{2}(r_1 - r_2)$	B	497
$S_6 = 1/\sqrt{2}(\alpha_1 - \alpha_2)$	B	245

[a] Torsional twist.

TABLE III: Observed and Calculated Frequencies

Obsd freq, cm^{-1}	Calcd freq, cm^{-1}	Difference, cm^{-1}	% error[a]
448.0	449.9	−1.9	−0.430
414.0	410.0	4.0	0.968
191.0	197.7	−6.7	−3.516
115.0	109.0	6.0	5.224
497.0	497.6	−0.6	−0.130
245.0	243.8	1.2	0.481

[a] Average error = 3.41 cm^{-1} or 1.792%.

TABLE IV: Force Constants

Force constant	Our value, mdyn/Å	Ward's value,[a] mdyn/Å
$k_{s-s'}$	1.936	1.84
$k'_{s-s'}$	−0.312	−0.34
k_{s-s}	1.595	1.84
δ	1.115	0.335
δ'	−0.084	0.044
β	0.294	...

[a] Reference 7.

computer programs.[11] The geometrical parameters used in the calculations were the same as those suggested by Ward: $r_1 = r_2 = r_3 = 2.04$ Å; $\alpha_1 = \alpha_2 = 105°$; dihedral angle = 90°. The observed *vs.* the calculated frequencies and their dispersions are listed in Table III. Six force constants were calculated and their values are listed in Table IV. The terms k_{s-s}, $k_{s-s'}$, δ, and β are the force constants for the squared terms of the potential function and $k'_{s-s'}$ and δ' are for the cross terms. Table V lists the potential energy distribution of each frequency for the various force constants.

The observed frequencies for S_4^{2-} are in good agreement with the calculated frequencies and can be used to explain the Raman spectrum of Na_2S_4 in H_2O. Since similar bands are present in the S–S stretching region (400 (shoulder), 433, and 503 cm^{-1}) for Na_2S_4–amine solutions as well as S_8–amine solutions, this is a strong indication that the S_4^{2-} ion exists in these solutions.

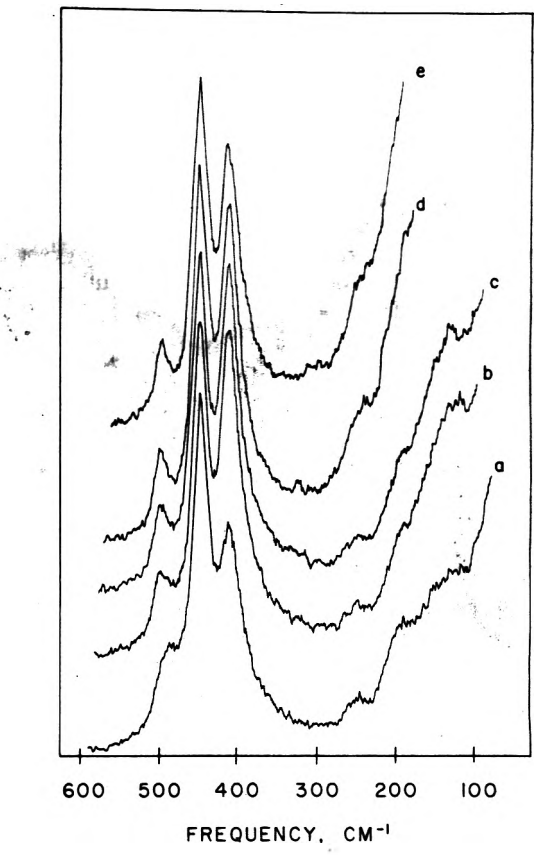

Figure 5. Raman spectra of Na_2S_4 in H_2O (commercial stock solution in the following concentrations: (a) 3.07 *M*; (b) 0.88 *M*; (c) 0.51 *M*; (d) 0.36 *M*; (e) 0.12 *M*.

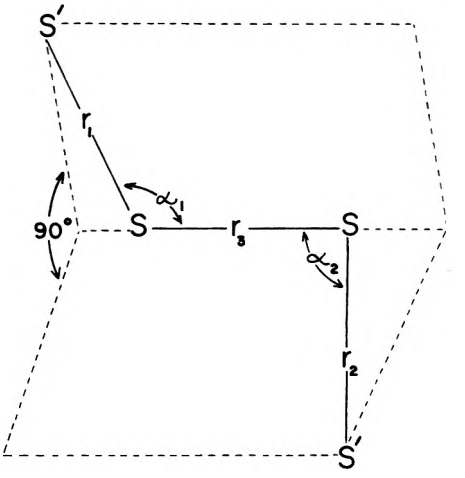

Figure 6. Geometry of S_4^{2-} species.

TABLE V: Potential Energy Distribution

Freq, cm^{-1}	$k_{s-s'}$	$k'_{s-s'}$	k_{s-s}	δ	δ'	β
449.9	0.5424	−0.0874	0.5386	0.0066	−0.0005	0.0003
410.0	0.5448	−0.0878	0.3307	0.2227	−0.0168	0.0065
197.7	0.0916	−0.0148	0.1013	0.5585	−0.0422	0.3056
109.0	0.0131	−0.0021	0.0295	0.2941	−0.0222	0.6875
497.6	0.8178	0.1318	0.0	0.0469	0.0035	0.0
243.8	0.0434	0.0070	0.0	0.8829	0.0667	0.0

Our previous results[3] showed that S_3^- is present in sulfur–amine solutions and the present results indicate that S_4^{2-} is also present. Furthermore, the results suggest the existence of a third species. The band at ~400 cm^{-1} in the spectra of 10^{-1} and 10^{-3} M sulfur in EDA and in the spectrum of the 10^{-1} M solution of Na_2S_4 in EDA decreases with time. The band at approximately the same frequency in the spectrum of Na_2S_4 in H_2O (Figure 5) first increases in intensity with increasing dilution and then decreases with the accompanied formation of rhombic sulfur. We feel that all of this evidence points to the fact that this band is due to S_8^{n-}. In Na_2S_4–amine or water solutions S_8^{n-} could be formed by the dimerization of S_4^{2-}, and in the rhombic sulfur–amine solutions from S_8 rings. In the spectrum of the latter solution the disappearance of the band with time could be accounted for by the formation of smaller polysulfides (e.g., S_3^- and S_4^{2-}) from S_8^{n-} chains.

Acknowledgments. We wish to express our appreciation to the National Science Foundation for a matching grant which made possible the purchase of the Raman instrumentation. One of us (F.P.D.) gratefully acknowledges financial support in the form of a NDEA Title IV Fellowship.

References and Notes

(1) T. Chivers and I. Drummond, *Chem. Soc. Rev.*, **2**, 233 (1973).
(2) R. E. Davis and H. F. Nakshbendi, *J. Amer. Chem. Soc.*, **84**, 2085 (1962); W. G. Hodgson, S. A. Buckler, and G. Peters, *ibid.*, **85**, 543 (1963).
(3) F. P. Daly and C. W. Brown, *J. Phys. Chem.*, **77**, 1859 (1973).
(4) A. Rule, *J. Chem. Soc.*, **99**, 558 (1911).
(5) R. E. Eibeck, University Microfilms, L.C. Card No. Mic 61-1608; *Diss. Abstr.*, **21**, 3254–5 (1961).
(6) A. G. Hopkins, F. P. Daly, and C. W. Brown, *Appl. Spectrosc.*, **28**, 194 (1974).
(7) A. T. Ward, *Nat. Res. Bull.*, **4**, 581 (1969).
(8) R. E. Barletta and C. W. Brown, *J. Phys. Chem.*, **75**, 4059 (1971).
(9) P. D. Bartlett and G. Meguerian, *J. Amer. Chem. Soc.*, **78**, 3710 (1956).
(10) E. B. Wilson, J. C. Decius, and P. C. Cross, "Molecular Vibrations," McGraw-Hill, New York, N.Y., 1955.
(11) J. H. Schachtschneider, "Vibrational Analysis of Polyatomic Molecules. VI.," Shell Development Co., Emeryville, Calif., 1964.

Spectroscopic Evidence for the Tetraamminecopper(II) Complex in a Y-Type Zeolite

D. R. Flentge, J. H. Lunsford,*

Department of Chemistry, Texas A&M University, College Station, Texas 77843

P. A. Jacobs, and J. B. Uytterhoeven

Laboratorium voor Oppervlaktescheikunde, University of Leuven, 3030 Heverlee, Belgium *(Received August 26, 1974)*

Publication costs assisted by the National Science Foundation (USA) and the National Fonds voor Wetenschappelijk Onderzook (Belgium)

The changes in the epr and ir spectra of copper(II)–ammine complexes in a Y-type zeolite have been studied as a function of the amount of ammonia adsorbed. The intensity of the epr spectrum increased linearly until the ratio of the number of ammonia molecules to the number of cupric ions was 4:1, at which point the addition of excess ammonia failed to change the spectrum. The same behavior was noted in the ir spectrum for the symmetric deformation band of ammonia coordinated to cupric ions. Adsorption of deuterated ammonia on a low-exchanged sample produced an epr spectrum which revealed the superhyperfine splitting of four equivalent nitrogen nuclei in the parallel as well as the perpendicular region of the spectrum. These data provide additional evidence that the $[Cu(NH_3)_4]^{2+}$ complex is formed within the zeolite structure. This complex may be detected in the presence of excess ammonia and oxygen at temperatures up to 180°. The change in the epr spectrum of a moderately exchanged sample upon adsorption of ammonia indicates that the copper ions move out of the small cavities, and most of the complexes are formed in the large cavities of the zeolite.

Introduction

A number of recent studies have demonstrated that it is possible to synthesize fully coordinated transition metal complexes within a zeolite structure.[1–5] Normally, the metal ion is first exchanged in from an aqueous solution, the zeolite is dehydrated, and the complex is formed by adsorbing the ligand from the gas phase. X-Ray diffraction data provide convincing evidence that in the process of forming the complexes the metal ions move, and if large ligands are involved, one must conclude that the complexes form within the large cavities.[5,6] Furthermore, epr results for copper–ammine complexes indicate that all of the copper in moderately exchanged CuY is involved in complex formation, therefore, the metal ions must be able to move from the relatively hidden sites (sites I and I′) to more accessible locations.[2–4,7] Such motion is, of course, important if one wishes to utilize these transition metal ions in catalytic reactions.

Much of the published work has been carried out on Cu^{2+}-exchanged zeolites because this d^9 ion may be conveniently studied by epr techniques.[1–4,7–11] The nitrogen hyperfine structure observed upon the adsorption of excess ammonia in a CuY zeolite confirms that at least four ammonia mole-

cules are adsorbed per Cu^{2+} ion. The most reasonable structure is a square-planar $[Cu(NH_3)_4]^{2+}$ complex.[2,3] A similar conclusion may be reached about the Cu(II)–py complex; however, the nitrogen super hyperfine structure is difficult to interpret.[1,2,7]

One would ultimately like to study these complexes under usual reacting conditions, *i.e.*, 100–300°, but here the epr technique fails because at 25° and higher temperatures the spectra are poorly resolved. Infrared spectroscopy, on the other hand, can be extended to much higher temperatures. In the present work we have attempted to relate in a fairly quantitative manner the epr and the infrared spectrum of the square-planar $[Cu(NH_3)_4]^{2+}$ complex. As will be subsequently shown, the results provide additional evidence that the square-planar complex is selectively formed even without an excess of ammonia and that the complex may be detected at temperatures up to 180° in the presence of excess ammonia. In a separate study it has been shown that the $[Cu(NH_3)_4]^{2+}$ is an active intermediate in the catalytic oxidation of ammonia over a CuY zeolite.[12]

Experimental Section

Zeolite Samples. A Linde NaY sample was treated with an excess of 0.1 *N* NaCl solution and washed with distilled water to remove cation impurities and to avoid a cation deficiency. Aliquots of this sample were treated with $Cu(NO_3)_2$ solutions of different concentrations ($N < 0.1$) in order to obtain samples with different Cu^{2+} content. The samples were washed to remove excess electrolyte, dried at room temperature, and stored over a saturated ammonium chloride solution in order to obtain a constant level of hydration. The samples will be denoted as CuY followed by a figure indicating the exchange level of Cu^{2+} in per cent of the total cation exchange capacity. The samples CuY-4.3, CuY-17, CuY-41, CuY-55, and CuY-75 contained 1.2, 4.9, 11.4, 15.4, and 21 Cu^{2+} ions per unit cell, respectively. A $Cu(NH_3)_4Y$ sample was prepared from an aqueous 0.1 *N* $CuCl_2$ solution containing an excess of NH_3. During the exchange process the deep blue color of the $[Cu(NH_3)_4]^{2+}$ complex was transferred from the solution to the zeolite.

Sample Pretreatment. Self-Supporting films of zeolites were prepared by compressing the zeolite powder between stainless steel dies under a pressure of 3.3 tons/cm^2 of film. The thickness of these films ranged between 1.4 and 3.0 mg of dry zeolite/cm^2. These films, cut to 1 × 2 cm plates, were mounted in a vacuum infrared cell described elsewhere.[13] For epr experiments similar films were prepared and cut into squares with dimensions of less than 3 mm. These platelets packed uniformly in the epr cell.

Each epr and ir sample was outgassed at room temperature at a pressure of 10^{-5} Torr. Samples were then outgassed up to 400° using one of the following sets of conditions: set I: heating *in vacuo* to 400° in 15 min; outgassing was continued at that temperature for another 15 min; set II: heating *in vacuo* to 400° in 15 min; the sample was then exposed to oxygen pressure of 0.5 atm for 5 min and subsequently evacuated at 400° for 10 min; set III: heating *in vacuo* to 400° using increments of 100°/hr; the maximum temperature was maintained for 1 hr; set IV: heating *in vacuo* to 400° using increments of 100°/hr; after 1 hr at 400° oxygen was introduced and removed as in set II.

During the final outgassing the pressure was 10^{-5} Torr. The samples were cooled to room temperature under a dynamic vacuum.

Adsorption of Ammonia. Anhydrous ammonia of high purity was used (Matheson for the epr experiments, J. T. Baker for the ir experiments). It was purified by a repeated freeze–pump–thaw technique. The NH_3 was admitted to the samples in slugs of 30–50 μmol for the epr experiments and of approximately 10 μmol for the ir experiments. Initial epr experiments indicated that 4 hr was needed for the adsorbed NH_3 to reach equilibrium with the Cu^{2+} ions after adsorption at room temperature. Raising the adsorption and equilibrium temperature to 36° reduced the equilibrium times to 30 min. In the ir experiments equilibrium times of less than 30 min were found. During the ir experiments the film was constantly in the beam and a temperature of 35–40° is estimated. Some authors have reported temperatures as high as 80°.[14]

Nonuniform adsorption of NH_3 was evident when the zeolite was packed in a column. This was easily observed by noting the presence of the pale green color of dehydrated CuY in addition to the characteristic blue color of the copper–ammine complex. The problem was minimized by spreading the CuY platelets over the maximum possible area within the epr cell. Adsorption of NH_3 on such samples led to immediate uniformity of color and, presumably, of adsorption. No effects due to nonuniform adsorption were evident in the ir experiments.

Epr Spectroscopy. Epr spectra were recorded with the sample at −196° using a Varian E-6S spectrometer with a TE_{102} mode cavity. A sample of pitch in KCl was used as a reference standard for intensity. The *g* values are reported relative to a 2,2-diphenyl-1-picrylhydrazil (dpph) standard with $g = 2.0036$. The estimated error in the *g* values is ±0.005 and in the hyperfine splitting is ±2 G.

Spectra were recorded after each addition of ammonia. An oil bath was used to keep the zeolite at 36° for adsorption and equilibrium studies on the samples.

Infrared Spectroscopy. The ir spectra were recorded using a Beckman IR-12 spectrophotometer in the double-beam absorbance mode. The slit width and gain were adjusted on each film to give 55% deflection of the pen at 1300 cm^{-1} in the single-beam transmission mode. The films were outgassed to 400° before these adjustments were made. The resolution in the bending region was better than 3 cm^{-1}. The ir spectra for the adsorption studies were recorded at room temperature with the only heating of the sample arising from energy absorbed from the ir beam. Spectra were recorded after each addition of ammonia. An ir spectrum was taken on a CuY-55 sample at 180°. For this sample the second chopper on the spectrometer was stopped to avoid interference from the emission of the sample.

Quantitative Interpretation of the Epr and Ir Spectra. The concentration of the copper–ammine complex in the zeolite was determined for the epr experiments by measuring the area under the low-field ($m_I = -\frac{3}{2}$) component of the parallel region of the copper–ammine spectrum. To determine the intensity of this component the background due to the uncomplexed copper was interpolated in the region of the spectrum where the copper–ammine complex appeared. The height of the complex peak from the background was measured at 2-mm (5-G) intervals. These values were then replotted and the height of the peak times the square of the width at half-maximum was taken as a relative measure of the complex concentration denoted by Δ. The intensity of the sample of pitch in KCl was used to correct for instrument variations. The error in such area measurements was ±10%.

The concentration of the copper–ammine complex in the zeolite for the ir experiments was determined by measuring the intensity of the absorption band occurring at 1275 cm^{-1}. This band arises from the symmetric deformation vibration of ammonia coordinated with copper. It is sensitive to the cation as well as the valence of that cation. It is, therefore, an excellent quantitative measure of the amount of ammonia coordinated with copper because coordination with other cations present in the zeolite gives rise to absorption bands at frequencies different from 1275 cm^{-1}. Since the 1275-cm^{-1} band rests on the shoulder of intense skeletal vibrations, only the area of the high frequency half of this band was measured. A flat base line was extrapolated from two points in the ir spectrum at which absorption is a minimum. A perpendicular was dropped from the absorption curve at 1275 cm^{-1} to the base line, and the area enclosed by the perpendicular, the base line, and the absorption curve was then measured using a rolling-disk planimeter. The same technique was used on the outgassed films before NH_3 adsorption to determine the area due to the background absorption of the film. This value was then subtracted from each area measured after adsorption of NH_3. This produced an area which was solely due to NH_3 complexed with Cu^{2+} ions. The insert in Figure 5 illustrates the manner in which the crosshatched area (the background) was subtracted from the total area. The dashed line in the curve represents the shape of the absorption curve for an outgassed film.

A procedure similar to that described for measuring the intensity of the low-field component of the epr spectrum was also used to subtract out the background under the peak at 1275 cm^{-1} for several samples. After the peak had been replotted, the area was determined by triangulation of the peak. The results provided essentially the same information as the method just described. For convenience, the first method was used for all ir results reported here.

Results

The Epr Data. The epr results are reported only for the CuY-4.3, CuY-17, and CuY-41 samples, since at higher copper-exchange levels spin-exchange interactions between paramagnetic ions makes it impossible to resolve the spectra of the complexed and uncomplexed copper ions. The epr spectra for CuY-55 and CuY-75 consisted of a totally symmetric line, which did not change shape upon adsorption of ammonia. There was a shift in g value, however, indicating a change in the coordination of the Cu^{2+}.[11]

The dehydrated CuY-4.3 sample yielded spectra containing two sets of isolated Cu^{2+} ions characterized by $g^1_\parallel = 2.38$ and $g^2_\parallel = 2.30$ with $|A^1_\parallel| = 108$ G and $|A^2_\parallel| = 175$ G. The intensity of the lines for the second species was much lower than that of the first species. Figure 1a shows the spectrum of CuY-4.3 exposed to a pressure of 0.5 atm of ND_3. Not only are the superhyperfine lines due to the interaction between the copper and nitrogen resolved in the perpendicular region of the spectrum, but they are also resolved in the $m_I = -3/2$ component of the spectrum. The superhyperfine splitting of the low-field component has been observed by Derouane, *et al.*,[15] in $Cu(py)_4(NO_3)_2$ and frozen $Cu(py)_5^{2+}$ but has not been previously observed for a surface species. Figure 1b shows the low-field component on an expanded scale. The perpendicular region of the spectrum as well as the low-field component has been simulated, assuming four equivalent nitrogen nuclei and the results are shown in Figure 1. In the former case, values of

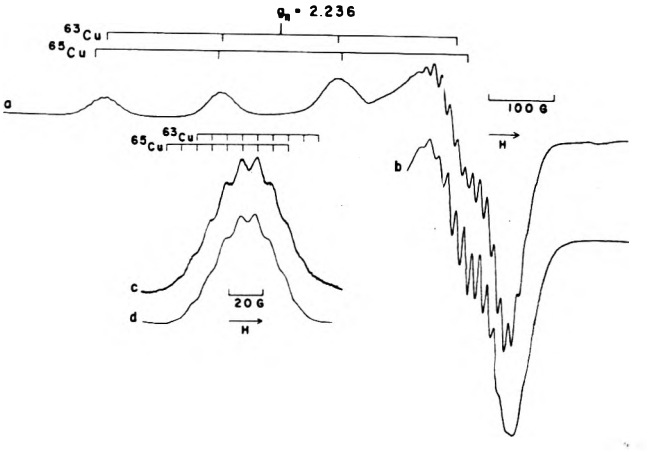

Figure 1. Epr spectra of CuY-4.3 with 0.5 atm of ND_3: (a) experimental spectrum; (b) simulated spectrum in the perpendicular region; (c) low-field component with the receiver gain 3 times the value of spectrum a; (d) simulated spectrum of the low-field component.

$|A_\perp{}^{Cu}| = 20$ G and $|A_\perp{}^{N}| = 12.4$ G with $g_\perp = 2.035$ were used in the calculation. For the parallel direction it was necessary to incorporate hyperfine splittings for both the ^{63}Cu isotope (69% abundance) and the ^{65}Cu isotope (31% abundance). The respective values were $|A_\parallel{}^{63Cu}| = 172$ G and $|A_\parallel{}^{65Cu}| = 184$ G. A hyperfine splitting of 9 G was used for $|A_\parallel{}^{N}|$ with $g_\parallel = 2.236$.

For the dehydrated CuY-17 three sets of isolated Cu^{2+} ions yield spectra characterized by $g^1_\parallel = 2.38$, $g^2_\parallel = 2.30$, and $g^3_\parallel = 2.36$ with $|A^1_\parallel| = 108$ G, $|A^2_\parallel| = 175$ G, and $|A^3_\parallel| = 125$ G. These experimental values of $A_\parallel$ probably reflect the hyperfine splitting of the more abundant copper isotope, within experimental error. Upon addition of excess ammonia the spectrum of the $[Cu(NH_3)_4]^{2+}$ complex appeared with $g_\parallel = 2.24$ and $|A_\parallel| = 168$ G. The parameters for the copper–ammine complex are in agreement with data published by other workers, although our interpretation of the spectra for the uncomplexed Cu^{2+} differs somewhat from previous work.[1-4,7]

One-half atmosphere of oxygen was adsorbed on a CuY-17 sample which had previously been exposed to a small quantity of ammonia (less than four molecules ammonia per cupric ion). The spectrum due to the copper(II)–ammine complex was broadened beyond detection, and a weak spectrum remained which had $g_\parallel = 2.38$ and $|A_\parallel| = 113$ G. This spectrum is very similar to one observed in the dehydrated CuY-4.3 sample.

As shown in Figure 2a the epr spectrum of the dehydrated CuY-41 sample is dominated by a broad symmetric line which has been attributed to nonlinear pairs of Cu^{2+} ions undergoing spin-exchange interactions.[11] These Cu^{2+} ions are believed to be in site I′ positions within the same sodalite unit. One may also observe small peaks on the low-field side of the spectrum which are due to isolated Cu^{2+} ions. Upon addition of ammonia the large symmetric line is converted to the anisotropic spectrum of *isolated* copper–ammonia complexes with $g_\parallel = 2.24$ and $|A_\parallel| = 175$ G. The spectrum of this new complex is depicted in Figure 2b and c. In Figure 2b there may be a small residue of the spin-exchanged copper ions; however, in general, the copper ions that were undergoing spin exchange reacted more rapidly than the isolated copper ions which contributed to the low-field peaks.

In order to follow the increase in concentration of the copper–ammonia complex the Δ of the low-field ($m_I = -3/2$)

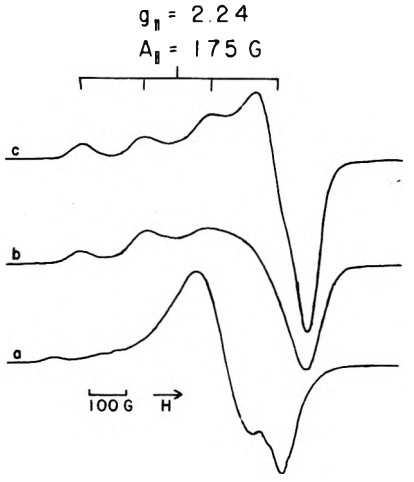

Figure 2. Epr spectra of CuY-41: (a) after outgassing to 400°; (b) after approximately four NH_3 molecules had been adsorbed per Cu^{2+} ion; (c) after addition of 0.5 atm of NH_3.

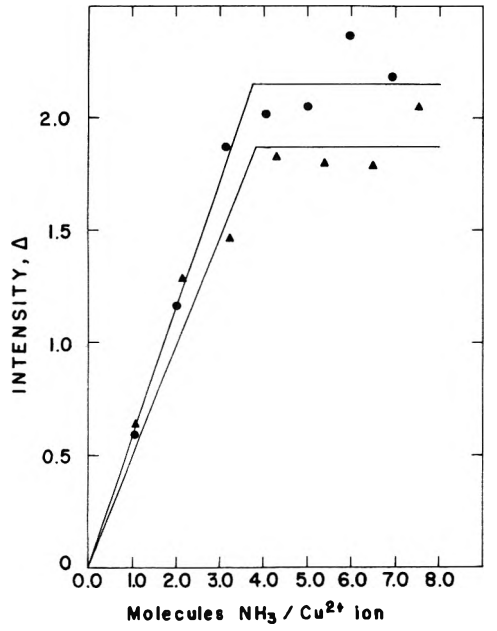

Figure 3. Intensity, Δ, of the $m_I = -3/2$ component of the copper-ammine epr spectrum *vs.* molecules of NH_3 adsorbed per Cu^{2+} ion for CuY-41: ▲, pretreatment conditions of set II; ●, pretreatment conditions of set IV.

TABLE I: Infrared Bands (cm^{-1}) and Their Assignments

Before Adsorption of NH_3	
3650–3660	OH str vib; w
3550–3560	
1640	H_2O bend; w, br
After Adsorption of NH_3	
3400	NH str vib
3380	
3320	
3270	
3220	
3190	
1675	Def vib of NH_4^+
1485	
1435	
1632	Doubly degenerate anti-sym def vib of NH_3
1618	
1275	Sym def of NH_3 coordinated to Cu^{2+}

hyperfine component of the complex was measured following the addition of known amounts of ammonia. A plot of Δ *vs.* the amount of adsorbed ammonia is shown in Figure 3. One should note that these plots for the CuY-41 samples treated according to the conditions of set II and set IV yield data which can be divided into two linear regions—one with a positive slope and one with a zero slope. Within experimental error the inflection point occurs at the point where the ratio of molecules of ammonia to cupric ions is 4:1. This feature seems to be independent of pretreatment conditions.

The Ir Data. Table I lists the bands which appeared upon adsorption of NH_3 on the outgassed films. Figure 4 shows spectra of NH_3 adsorbed on CuY-55 films which were treated according to the conditions of set III and set IV. As depicted in spectrum a, well-defined bands were observed at 1275, 1435, 1485, 1618, 1632, 3190, 3220, 3275, 3320, and 3385 cm^{-1}. Spectrum b shows the same basic bands, indicating that the two different outgassing procedures produced essentially identical environments within the zeolite. A spectrum recorded at 180° with the zeolite in the presence of excess NH_3 showed bands at 1275, 1450, 1618, and 1632 cm^{-1}.

Figure 5 illustrates the changes in the spectra of CuY-75 in the NH deformation region as the amount of adsorbed NH_3 was increased. The sample was pretreated under the conditions of set IV. Spectra b–d were taken with increas-

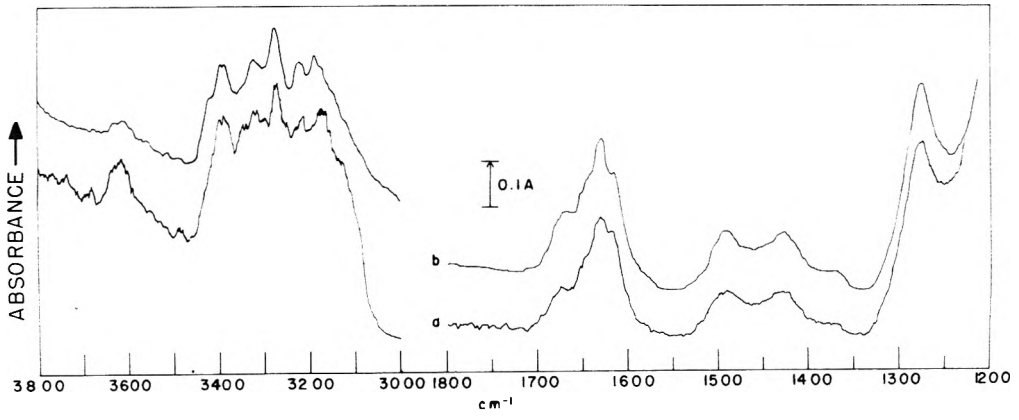

Figure 4. Infrared spectra of CuY-55: (a) pretreated according to conditions of set IV; (b) pretreated according to conditions of set III.

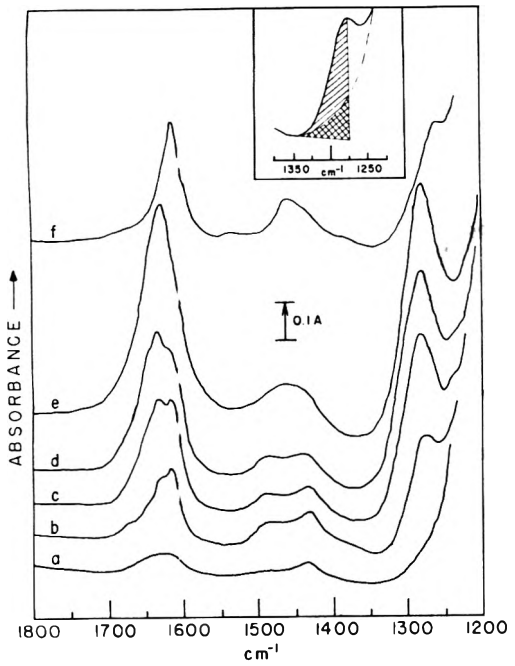

Figure 5. Infrared spectra for stepwise adsorption of NH_3 on CuY-75: (a) pretreated under conditions of set IV; (b) 1.0 molecule of NH_3 adsorbed per Cu^{2+} ion; (c) 1.9 molecules of NH_3 adsorbed per Cu^{2+} ion; (d) 2.9 molecules of NH_3 adsorbed per Cu^{2+} ion; (e) P_{NH_3} = 7 Torr; (f) sample evacuated overnight at 100°.

ing amounts of NH_3 present but without residual pressure, and spectrum e was taken in the presence of excess NH_3, while spectrum f was taken after outgassing overnight at 100°. The bands due to NH_4^+ (1435, 1485 cm^{-1}) are weak and reach maximum intensity after introduction of the first slug. The 1275-cm^{-1} band increased regularly with increasing amounts of NH_3. A quantitative measure of the intensity of this band was made, the results of which will be discussed later. Upon outgassing at 100° this band was considerably reduced in intensity and was shifted to lower wave numbers (1260 cm^{-1}).

Two bands occurred in the region of the doubly degenerate deformation vibration of the ammonia molecule. As seen in Figure 5, they absorb at 1618 and 1632 cm^{-1}. Initially (spectrum b), the band at 1618 cm^{-1} was more intense than the one at 1632 cm^{-1}; however, the 1632-cm^{-1} band became predominant after addition of larger amounts of ammonia. In the presence of excess ammonia only one peak at 1630 cm^{-1} was observed. Removal of the excess NH_3 at room temperature brought back the 1618- and 1632-cm^{-1} bands. Overnight outgassing removed the component at 1632 cm^{-1} but the one at 1615 cm^{-1} remained (spectrum f). This band is probably identical with the 1618-cm^{-1} component of spectra b and c.

Figure 6 shows plots of the intensity of the 1275-cm^{-1} band as a function of the amount of NH_3 adsorbed expressed as NH_3 molecules per Cu^{2+} ion for the CuY-41, CuY-55, and CuY-75 samples. Here too the curves can be broken down into straight lines, one with a positive slope and the second with approximately zero slope. The points of inflection come in the area where four molecules of NH_3 have been added per Cu^{2+} ion. For all points on these curves the adsorption of NH_3 was quantitative and no gas-phase NH_3 was present in the cell, except where noted in the figure caption. Addition of excess NH_3 did not influence the intensity of this band. The effect of different pretreatment conditions on the intensity of the band is also shown in Figure 6. Although there is considerable scatter in the data, a plot of the maximum intensity of the 1275-cm^{-1} band *vs.* the Cu^{2+} content of the zeolite for different conditions produces a linear increase with increasing Cu^{2+} concentration.

The zeolite sample into which a $[Cu(NH_3)_4]^{2+}$ complex was exchanged contained a band at 1275 cm^{-1}, as well as very intense bands around 1460 and 1640 cm^{-1}. These last two are probably due to ammonium ions and water plus ammonia on the zeolite, respectively. Evacuation of the sample caused a decrease in the intensity of the 1275-cm^{-1} band, but readsorption of ammonia restored it in full.

The ir spectrum of the dehydrated zeolite has a weak residual absorption at 1640 cm^{-1}. In the hydroxyl stretching region bands at 3555 and 3655 cm^{-1} appeared on samples CuY-55 and CuY-75 which were treated under the conditions of sets I and III. These bands were not found for the oxygen-treated samples. Due to the important light scattering by zeolite particles in the region 3000–4000 cm^{-1}, the intensity of these bands could not be measured accurately; however, on a qualitative basis a comparison can be made. The area of the hydroxyl bands for CuY-75 was roughly twice that for CuY-55. A plot of the peak areas *vs.* per cent Cu^{2+} in the zeolite indicates that the spectra of CuY-41 should contain no hydroxyl bands. Experimentally this was found to be true. Spectra of the CuY-17 and CuY-41 samples did not exhibit these bands. The hydroxyls on the CuY-55 and CuY-75 samples reacted with NH_3 to form ammonium ions.

Discussion

The previously reported epr spectra of Vansant and Lunsford[3] demonstrated that the $d_{x^2-y^2}$ orbital of Cu^{2+} in a zeolite interacted with four equivalent nitrogen atoms in a $[Cu(NH_3)_4]^{2+}$ complex. The spectra in Figure 1 provide additional evidence that four ammonia molecules interact with each cupric ion. The presence of two sets of nine hyperfine lines on the $m_I = -3/2$ component of the copper spectrum means that four nitrogen atoms with $I = 1$ interact to give $2NI + 1 = 9$ lines. The splitting in the perpendicular region also confirms this.

If one assumes that the ammonia is preferentially adsorbed on Cu^{2+} ions in the zeolite, then it follows that a plot of Δ from the epr spectrum *vs.* the amount of ammonia adsorbed should give a linear increase until all cupric ions have their most favorable coordination, at which point the slope of the line should go to zero. This inflection point should give the stoichiometry of the complex. The results of Figure 3, therefore, confirm that essentially all of the Cu^{2+} ions are bound up in such a tetraamine complex when a stoichiometric amount of NH_3 is added to the CuY zeolite. Furthermore, since the copper hyperfine splitting and the g values do not change upon the addition of excess NH_3, one may conclude that any interaction with a fifth ammonia molecule is weak, if it exists at all.

From the standpoint of catalysis it is important that the complex be located in the supercage. The sodalite cage has a free diameter of 6.6 Å,[16] and the longest distance across the square-planar $[Cu(NH_3)_4]^{2+}$ complex is approximately 5.5 Å; hence, it is conceivable that the complex is in the sodalite cage. We believe, however, that the experimental evidence favors the formation of most of the complexes in the large cavities. The strongest piece of evidence which favors this viewpoint is the "decoupling" of the exchange-coupled

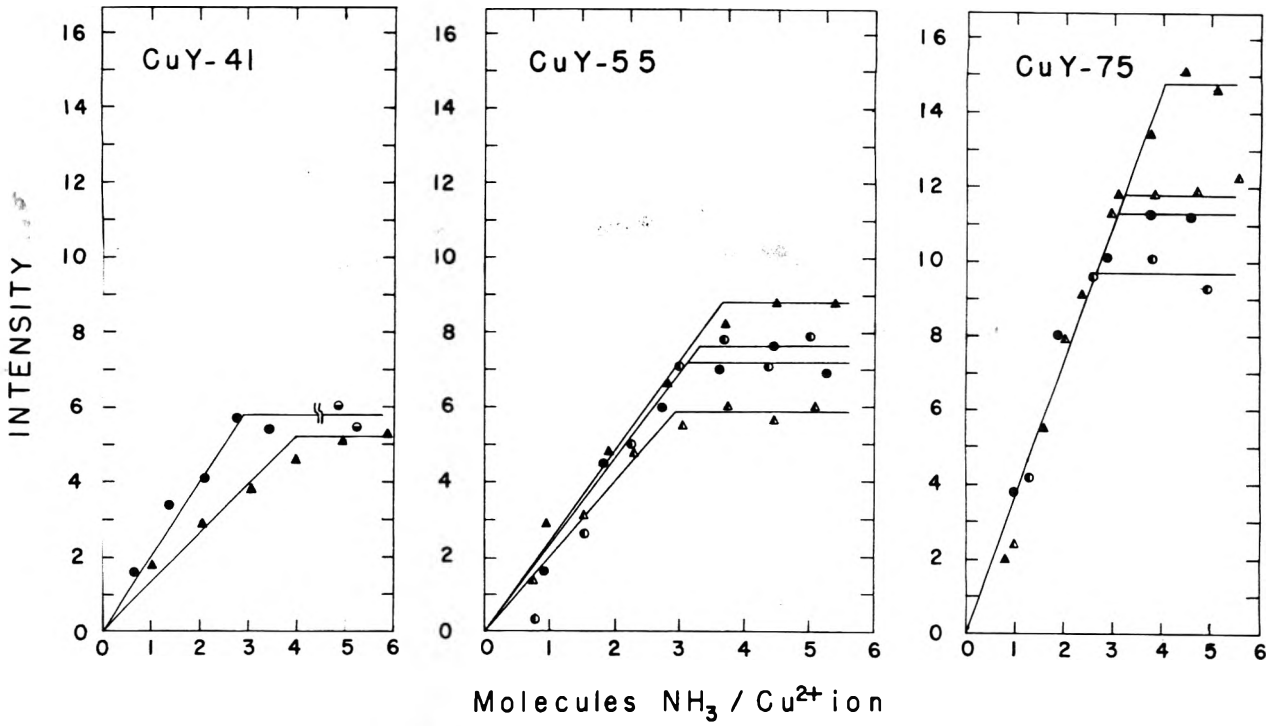

Figure 6. Intensity of infrared band at 1275 cm^{-1} for CuY-41, CuY-55, and CuY-75 as a function of molecules of a NH_3 adsorbed per Cu^{2+} ion. Effect of pretreatment conditions on intensity is shown: ◐, set III; ● set IV; ⊖, set IV, gas-phase NH_3 present in cell; ▲, set I; ▲, set II.

Cu^{2+} ions in the CuY-41 sample as indicated by the spectra of Figure 2. For such decoupling to occur upon the adsorption of ammonia, the copper ions in the same sodalite cages must move away from each other. For a CuY-41 sample there are 1.5 copper cations, on the average, in each small cavity. Therefore, at least one-third of the copper ions must move out into the large cavities, where they form complexes. In the higher exchanged samples, there are a number of large cavities with at least two complexes, and in such cases spin exchange may again occur.

The oxygen broadening experiments provide another piece of evidence for the location of the complexes in the supercages. Oxygen is not thought to enter the sodalite cages at room temperature. Since the signal of the copper(II)–ammine complexes was broadened by interaction with the molecular oxygen, it seems that these complexes are located in the supercage. The signal which remains is from isolated Cu^{2+} ions located within the small cages.

As mentioned previously, one of the primary objectives of this work was to relate the epr and the ir spectra of the $[Cu(NH_3)_4]^{2+}$ complex in the same sample. According to Nakagawa and Shimanouchi[17] this complex in salts such as the sulfate has infrared adsorption bands at 3270 cm^{-1} [ν(N-H)], 1610 cm^{-1} [$\delta(NH_3)_d$], 1270 and 1240 cm^{-1} [$\delta(NH_3)_s$], 713 cm^{-1} [δ(N-Cu-N)], and 420 cm^{-1} [ν(Cu-N)]. Because of intense absorption from zeolite lattice vibrations, the region below 1200 cm^{-1} was very difficult to study. There was a shoulder in the region 720–700 cm^{-1} upon ammonia adsorption but it was poorly resolved. No change was observed in the spectrum around 420 cm^{-1}. Vedrine, *et al.*,[7] claimed to have observed a Cu–N stretching band for a $[Cu(NH_3)_n]^{2+}$ complex at 317 cm^{-1}. Using epr hyperfine coupling data a Cu–N stretching frequency of 70 cm^{-1} was calculated for a species thought to be $[Cu(NH_3)_4]^{2+}$. The large shift in the stretching frequency in the first case was attributed to hydrogen bonding while in the latter case it was proposed that the complexes were interacting with one another in the supercage. It should be mentioned that the infrared bands taken alone are not definitive evidence for the square-planar complex. For example, $Cu(NH_3)_5(BF_4)_2$ has absorption bands at 1633, 1272, 1180, 720, 509, and 397 cm^{-1} [18] and β-$CuCl_2(NH_3)_2$ has bands at 1603, 1277, and 1253 cm^{-1}.[19]

In view of the excellent agreement between the growth behavior of the 1275-cm^{-1} band and the epr spectrum of the square-planar complex upon the addition of ammonia, we believe that in the zeolite this band is characteristic of the tetraamine complex. The observation that the peak area did not increase after the 4:1 stoichiometric amount of ammonia had been added is further evidence that the complex has only four ammonia molecules per copper ion. This symmetric deformation band appears to be moderately sensitive to the coordination of the copper, since removal of the ammonia at 100° results in a tetrahedral complex with one NH_3 ligand as determined from the epr spectrum[3] and the [$\delta(NH_3)_s$] for this new complex was shifted to 1260 cm^{-1}.

In addition to the ir band at 1275 cm^{-1}, other less characteristic bands of the $[Cu(NH_3)_4]^{2+}$ complex were observed in the regions 1615–1635 and 3190–3385 cm^{-1}. These bands are typical of the antisymmetric deformation and the N–H stretching modes of adsorbed ammonia, respectively. A plot of the peak area of the band at 1615–1635 cm^{-1} *vs.* molecules of ammonia added per cupric ion did not show a change in slope at a 4:1 stoichiometry; therefore, the ir absorption in this region is not restricted to the ammonia in the copper complex. The antisymmetric deformation vibration for ammonia is doubly degenerate and the removal of the degeneracy to produce two bands is one possible explanation for the presence of the bands at 1618 and 1632 cm^{-1}. Since the bands have unequal intensities at most points during the stepwise adsorption and since a

change in symmetry for the NH_3 molecule is not achieved by coordination with Cu^{2+} ions, it is unlikely that this is the case. There is significant hydrogen bonding with oxide ions of the lattice as is evidenced by the wide range of N–H stretching frequencies observed; however, this hydrogen bonding could produce two deformation frequencies only if the interaction was strong enough to hinder the rotation around the Cu–N bond.

The samples which had hydroxyl bands present after pretreatment yielded bands at 1435 and 1485 cm^{-1} upon adsorption of ammonia. These bands are due to NH_4^+ deformations, as described by Uytterhoeven, *et al.*,[20] for NH_4Y zeolites.

It is evident from the ir data in Figure 6 that the stoichiometry of the ammonia adsorption is a function of the extent of exchange and of the pretreatment conditions. The epr data show that for the lower exchanged samples all the Cu^{2+} ions are complexed with four NH_3 molecules. The ir data obtained with the sample CuY-41 confirm this. For the lower exchanged samples the differences between the effects of the different sets of pretreatments are rather small.

For the higher exchanged samples (CuY-55 and CuY-75) apparent stoichiometries between 3 and 4 are observed for the complexes. Values lower than 4 indicate that a given fraction of the Cu^{2+} ions are not participating in the complexation reaction, probably because they are in sites unaccessible for NH_3 molecules, presumably S_I sites. Migration of these cations into the supercage would result in a high accumulation of positive charges in these cages. We consider it unlikely that complexes with stoichiometry other than 4 are formed to a large extent.

The stoichiometry of the complex formation, derived from the intensity of the 1275-cm^{-1} band, is systematically lower than 4 after the sets of pretreatment which did not include an oxygen treatment at 400°. This can be ascribed to the fact that a fraction of the Cu^{2+} ions was reduced and was not participating in the complex formation. The data in Figure 6 for CuY-55 and CuY-75 further reveal that only a very quick heating to 400° combined with an oxygen treatment yields a maximum stoichiometry of 4. A slow increase of the temperature resulted systematically in a lower apparent stoichiometry. This indicates that the mode of pretreatment has a very important effect on the location of the cations and their availability for complex formation.

Conclusions

By comparison of epr and ir data we conclude that adsorption of even small quantities of ammonia in a CuY zeolite results in the formation of a square-planar $[Cu(NH_3)_4]^{2+}$ complex. The ir spectrum of the complex may be observed at temperatures up to 180° in the presence of excess ammonia. As the complexes are formed in moderately exchanged zeolites, the nonlinear pairs of Cu^{2+} ions are separated, and the cupric ions must move from S_I and $S_{I'}$ sites into the supercage where they are probably distributed among several possible sites.

Acknowledgments. The authors wish to acknowledge the support of this cooperative program by the National Science Foundations of Belgium (NFWO) and the United States (NSF). P.A.J. acknowledges a grant as "Aangesteld Navorser" from NFWO (Belgium). We also wish to thank Drs. G. P. Lozos and B. M. Hoffman for the computer program which was used to simulate the epr spectrum and Dr. R. F. Howe for his computational assistance.

References and Notes

(1) C. Naccache and Y. Ben Taarit, *Chem. Phys. Lett.*, **11**, 11 (1971).
(2) J. Turkevich, Y. Ono, and J. Soria, *J. Catal.*, **25**, 44 (1972).
(3) E. F. Vansant and J. H. Lunsford, *J. Phys. Chem.*, **76**, 2860 (1972).
(4) I. R. Leith and H. F. Leach, *Proc. Roy. Soc., Ser. A*, **330**, 247 (1972).
(5) J. H. Lunsford and E. F. Vansant, *J. Chem. Soc., Faraday Trans. 2*, **69**, 1028 (1973).
(6) P. Gallezot, Y. Ben Taarit, and B. Imelik, *J. Catal.*, **26**, 295 (1972).
(7) J. C. Vedrine, E. G. Derouane, and Y. Ben Taarit, *J. Phys. Chem.*, **78**, 531 (1974).
(8) J. T. Richardson, *J. Catal.*, **9**, 172 (1967).
(9) H. B. Slot and J. L. Verbeek, *J. Catal.*, **12**, 216 (1968).
(10) I. D. Mikheikin, V. A. Shvets, and V. B. Kazanskii, *Kinet. Katal.*, **11**, 747 (1970).
(11) C. C. Chao and J. H. Lunsford, *J. Chem. Phys.*, **57**, 2890 (1972).
(12) W. B. Williamson, D. R. Flentge, and J. H. Lunsford, accepted for publication in *J. Catal.*
(13) J. B. Uytterhoeven, P. Jacobs, K. Makay, and R. Schoonheydt, *J. Phys. Chem.*, **72**, 1768 (1968).
(14) R. L. Goldsmith, M. V. Mathieu, and B. Imelik, *Spectrochim. Acta, Part A*, **27**, 247 (1971).
(15) E. G. Derouane, J. N. Braham, and R. Hubin, *Chem. Phys. Lett.*, **25**, 243 (1974).
(16) D. W. Breck, *J. Chem. Educ.*, **41**, 678 (1964).
(17) I. Nakagawa and T. Shimanouchi, *Spectrochim. Acta*, **22**, 759 (1966).
(18) A. A. G. Tomlinson and B. J. Hathaway, *J. Chem. Soc. A*, 1905 (1968).
(19) R. J. H. Clark and C. S. Williams, *J. Chem. Soc. A*, 1425 (1966).
(20) J. B. Uytterhoeven, L. G. Christner, and W. K. Hall, *J. Phys. Chem.*, **69**, 2117 (1965).

Equilibrium Studies by Electron Spin Resonance. X. Thermodynamics of Ion-Pair Dissociation by the Use of Time-Averaged Coupling Constants

Antonio E. Alegría, Rosario Concepción, and Gerald R. Stevenson*

Department of Chemistry, University of Puerto Rico, Rio Piedras, Puerto Rico 00931 *(Received September 23, 1974)*

Publication costs assisted by the University of Puerto Rico

The addition of salt (KI) to solutions of para-substituted nitrobenzene anion radicals in hexamethylphosphoramide (HMPA) results in the formation of ion pairs, which in the presence of free ion can result in one of the following observations upon esr analysis: (a) simultaneous observation of the spectra due to the free ion and ion pair, (b) dramatic line width alternation of the nitrogen hyperfine lines due to a rapid interconversion of the free ion and ion pair, and (c) complete time averaging of the spectra for the free ion and ion pair. When the σ value for the para substituent is less than about 0.6, the rate of ion-pair formation and dissociation is slow on the esr time scale and simultaneous recording of the two spectra is observed. When the para substituent is strongly electron withdrawing, as for the case of *p*-dinitrobenzene, complete time averaging is observed. For intermediate cases, as *p*-nitrobenzaldehyde, *p*-cyanonitrobenzene, and *p*-nitrobenzophenone, the esr spectra exhibit line width alternation. Thus, the larger the charge density on the NO_2 group the slower the rate of ion-pair formation and dissociation. The rate of ion-pair formation and dissociation was found to be fast on the esr time scale for the 2,6-di-*tert*-butylbenzosemiquinone system in contrast to that for the benzosemiquinone. This is attributed to a decrease in the charge density on the oxygen atom on the 4 carbon due to the presence of the two *tert*-butyl groups. For the systems where the rate of interconversion between ion pair and free ion is sufficiently fast on the esr time scale the esr coupling constants were algebraically related to the ion-pair dissociation constant, and the thermodynamic parameters for this process were obtained. The results agree qualitatively with those predicted by a Hammett plot previously reported.

The apparent special solvating power of hexamethylphosphoramide (HMPA) for alkali metal cations has rendered this solvent particularly useful for the study of ion pairing for a variety of organic anion radicals.[1,2] Many anion radicals in HMPA are fully dissociated.[1] However, the addition of alkali metal salts to these anion radical solutions often results in the formation of ion pairs.[3]

The appearance of the ion pair in solution with the free ion can result in two completely different effects upon the observed esr pattern. If the time between ion association–dissociation events is short on the esr time scale, the resulting spectrum is that of a time-averaged species. This is normally the case in the ethereal solvents.[4,5] However, in HMPA where these association dissociation reactions are slowed down, presumably due to the high affinity the HMPA has for the cation and the relatively high viscosity of this solvent, simultaneous observation of the esr spectra for both the free ion and ion pair is often the case.[6] Simultaneous observation of the two spectra is not ruled out in the ethereal solvents and has been observed for several anion radical systems.[7,8] It is still not well understood why for some systems the spectra for the free ion and that of the ion pair are observed simultaneously and for others only the time-averaged spectrum can be recorded. Our intention in this report is in part to detail the factors that control the rate of ion-pair dissociation and formation in HMPA.

For the systems where the ion pair and free ion can be observed simultaneously, it is a relatively simple matter to determine experimentally the thermodynamic parameters controlling the concentrations of the ion pair and free ion. This is true since their relative spin concentrations are proportional to the respective esr line intensities. For systems where time averaging of the two species is observed one must rely on weighted-average equations in order to determine the thermodynamic equilibrium constant (K_{eq}) controlling the dissociation of the ion pair (β) to form the free ion (α), eq 1 and 2.

$$\beta \rightleftharpoons \alpha + M^+ \tag{1}$$

$$K_{eq} = (\alpha)(M^+)/(\beta) \tag{2}$$

If the observed coupling constant ($\bar{A}$) is the result of a time average between the coupling constant for the free ion (A°) and that for the ion pair (A'), then

$$\bar{A} = [A^\circ(\alpha) + A'(\beta)]/[(\alpha) + (\beta)] \tag{3}$$

Combining this expression with that for K_{eq} (eq 2) leads to

$$K_{eq} = (A' - \bar{A})(M^+)/(\bar{A} - A^\circ) \tag{4}$$

If accurate estimates for A° and A' can be made, K_{eq} can be determined from the observed coupling constant and eq 4. This is the general type of analysis that has been used by Hirota[5] and by Hermann, *et al.*[9]

Some of the problems in this type of analysis have recently been pointed out by Szwarc and coworkers.[10] The main difficulty is that it is very difficult to obtain accurate values for A'. Error in the chosen value for A' will lead to large error in K_{eq}. It is best if K_{eq} can be obtained without having to rely upon assumed values for A'. The best way to utilize weighted-average coupling constants is first to rearrange eq 4, which leads to

$$1/(\bar{A} - A^\circ) = K_{eq}/(M^+)(A' - A^\circ) + 1/(A' - A^\circ) \tag{5}$$

Now a plot of $1/(\bar{A} - A^\circ)$ *vs.* $1/(M^+)$ should be linear and have a slope of $K_{eq}/(A' - A^\circ)$ and an intercept of $1/(A' - A^\circ)$.

Equation 5 is simply an adaptation of a general expression used for the determination of equilibrium constants for the formation or dissociation of weak molecular complexes by the use of spectroscopic measurements to esr.[11] Deranleau[12] has recently discussed in detail the errors involved in these types of experimental measurements. He has pointed out that the equilibrium constants are most reliable when they are based upon data that extend as much as possible into the region where the saturation factor (s) is between 0.2 and 0.8. For the esr experiments discussed here

$$s = (\beta)/[(\alpha) + (\beta)] = (\bar{A} - A^\circ)/(A' - A^\circ) \quad (6)$$

Here we wish to report on the use of weighted-average equations in terms of esr coupling constants for the determination of the thermodynamic parameters controlling ion-pair dissociation and the conditions under which these equations can be used. In a preliminary communication we reported the determination of the equilibrium constant for the dissociation of the 2,6-di-*tert*-butylsemiquinone ion pair in HMPA by the use of eq 5.

Results and Discussion

The reduction of 2,6-di-*tert*-butylbenzoquinone in HMPA with potassium metal results in the formation of the free anion radical, which exhibits an esr signal consisting of a triplet due to two equivalent protons with a coupling constant of 2.346 ± 0.005 G[13] and a small splitting due to the 18 methyl protons of 0.037 G. Successive addition of potassium iodide to this solution results in a gradual decrease in the large coupling constant. This decrease is due to the formation of the ion pair, which exists in rapid equilibrium with the free ion, eq 1. Since the observed coupling constant ($\bar{A}$) smoothly decreases with the addition of potassium ion[14] (Figure 1), this coupling constant must be a weighted average between the coupling constant for the free ion (A°) and that for the ion pair (A') as expressed in eq 3.

If the two-jump model expressed in eq 1 (ion pair to free ion) is correct, the data should behave linearly with respect to eq 5. Treated in this manner our data (Table I) did yield a straight line at each of the temperatures studied, Figure 2. The equilibrium constants at the various temperatures are given in Table II. The data in Table II were treated in the normal manner to yield the values −1.52 ± 0.1 kcal/mol and −9.6 ± 1 eu for the enthalpy and entropy, respectively.

We must note here that the plot of $1/(\bar{A} - A^\circ)$ *vs.* $1/(K^+)$ should be linear only if there is no formation of triple ions (ion pairs consisting of one anion and two cations). The free ion can be in equilibrium with either of the two possible ion pairs (structures I and II) or with both of them as shown.

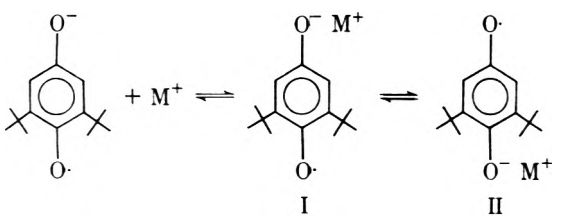

I II

The existence of both ion pairs would not necessarily give curvature to the plot since the two structures could be in rapid equilibrium and only the time average between them observed. However, if either the interconversion between structures I and II is slow on the esr time scale or the triple ion is formed, curvature of this plot (Figure 2) would be expected. The fact that neither of these two possibilities occurred for the potassium system is probably due to the fact that the potassium cation is sterically hindered from entering the side of the ring in which the carbonyl group is sandwiched by the two *tert*-butyl groups. A smaller cation, however, might not be so hindered. Further, smaller alkyl substituent groups may allow the formation of triple ions even for the potassium reduction.

TABLE I: Representative Esr Coupling Constants for the Anion Radical of 2,6-Di-*tert*-butylbenzoquinone in HMPA at 23°

$(K^+)_{total}$, M	$\bar{A}$, G	$(K^+)_{total}$, M	$\bar{A}$, G
0	2.346	0.2839	2.134
0.0493	2.242	0.2999	2.132
0.1271	2.195	0.3605	2.081
0.1801	2.170	∞	2.06

TABLE II: Equilibrium Constants for the Dissociation of the Ion Pair of 2,6-Di-*tert*-butylsemiquinone in HMPA with Added KI

T, °C	K_{eq}, M	T, °C	K_{eq}, M
−5	0.134	18	0.105
−2	0.130	20	0.105
5	0.121		

Addition of sodium iodide to the free anion radical of 2,6-di-*tert*-butylbenzoquinone in HMPA also results in a decrease in the observed coupling constant for the α protons, but a plot of $1/(\bar{A} - A^\circ)$ *vs.* $1/(Na^+)$ is not linear. Further, an asymmetry is observed in the esr line widths. That is, the line widths increase with decreasing magnetic field. This spectrum is obviously due to the formation of two different ion pairs with slightly different coupling constants and g values. If the radical with the smaller coupling constant also possesses the smaller g value, then the difference in the positions of the lines due to the two ion pairs will decrease with the magnetic field. One of the two ion pairs is probably the triple ion. A similar effect has been observed for the benzoquinone anion radical in HMPA saturated with KI[3] and for durosemiquinone in tetrahydrofuran.[15] The approach of the sodium ion to the carbonyl sandwiched between the two *tert*-butyl groups is not as sterically hindered as it is for the potassium ion due to the smaller size of the sodium cation. From this argument we would expect the addition of LiI to the free ion in HMPA to result also in the observation of an asymmetric esr spectrum.[16] Experimentally this is the case.

Addition of $NaClO_3$ to solutions of the free anion radical of *p*-dinitrobenzene results in a smooth increase in the nitrogen coupling constant, which is also due to the formation of a time-averaged ion pair.[17,18] The rapid rate of exchange of cation for this system is further evidenced by the fact that the two nitrogens remain equivalent for all obtainable concentrations of alkali metal cation.[18]

For para-substituted nitrobenzenes with σ values for the substituent less than 0.6 or 0.7, depending upon the cation used, no time averaging of the two species was observed; but the esr spectra of the two species were observed simultaneously (the spectra for the free ion and ion pair were superimposed).[6]

Addition of KI or $NaClO_3$ to the free anion radical of *p*-

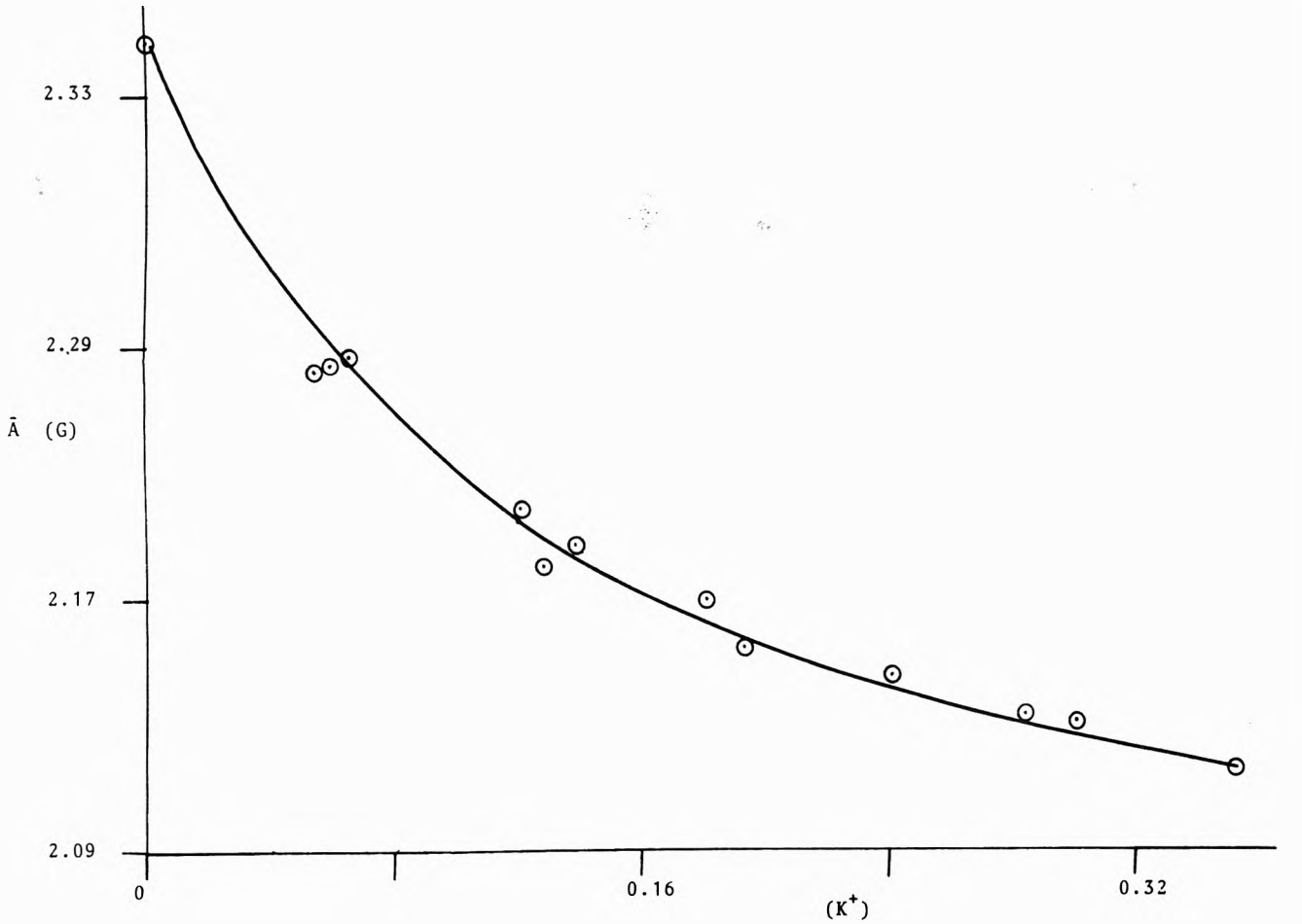

Figure 1. Plot of the α-proton coupling constant for the anion radical of 2,6-di-*tert*-butylbenzoquinone *vs.* the total potassium ion concentration in moles per liter.

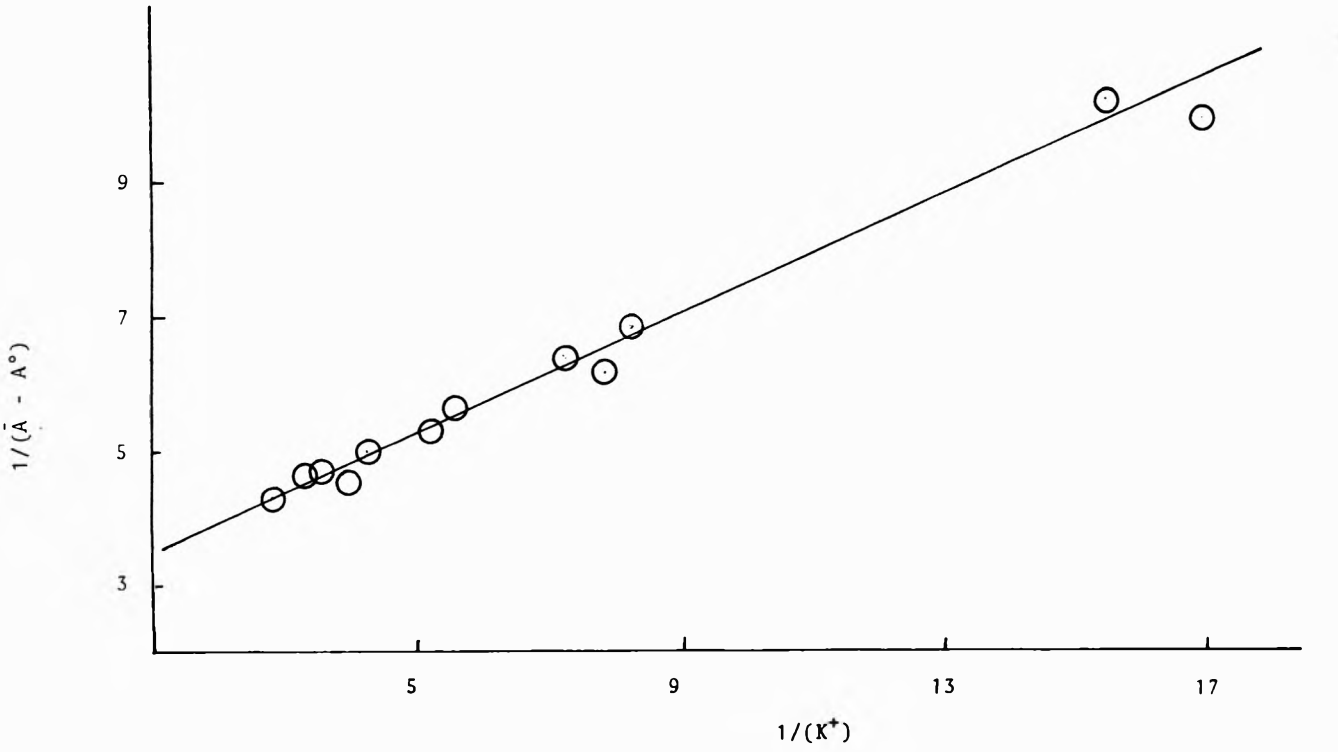

Figure 2. Plot of $1/(\bar{A} - A^{\circ})$ *vs.* the reciprocal of the potassium ion concentration for the 2,6-di-*tert*-butylbenzoquinone system.

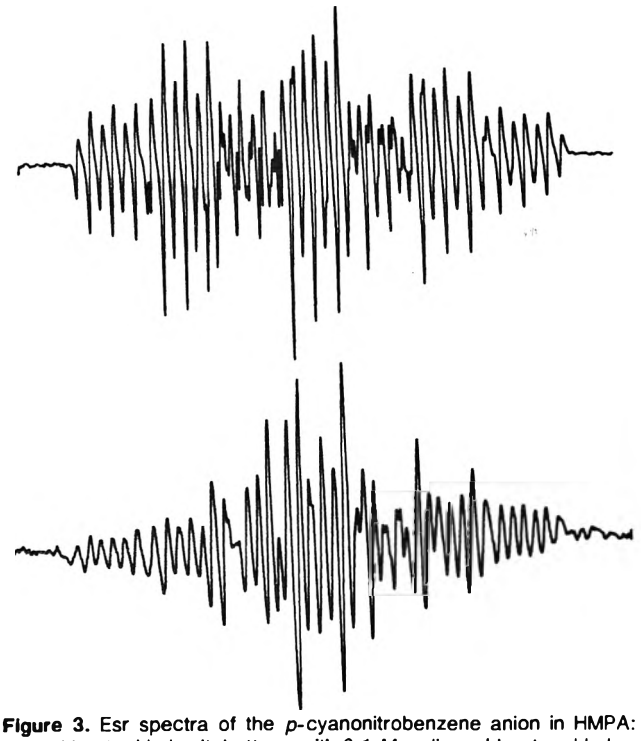

Figure 3. Esr spectra of the *p*-cyanonitrobenzene anion in HMPA: top, without added salt; bottom, with 0.1 *M* sodium chlorate added.

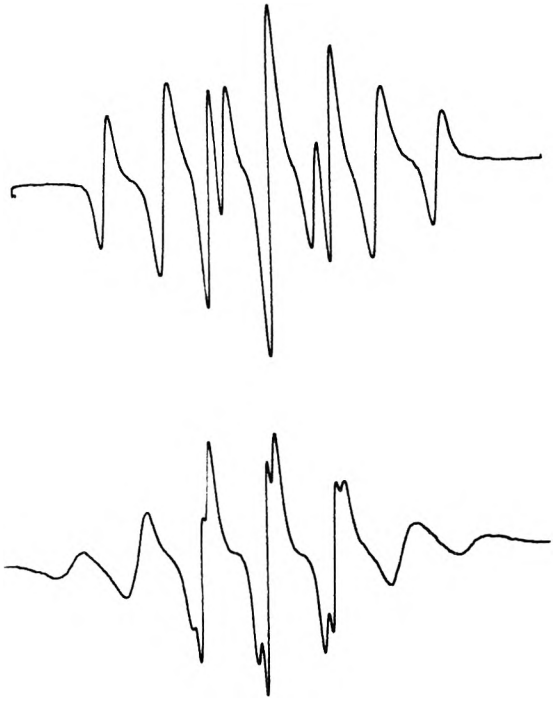

Figure 4. Esr spectra for the anion radical of *p*-nitrobenzophenone in HMPA. The lower spectrum is for a solution containing 0.2 *M* KI.

cyanonitrobenzene in HMPA leads to dramatic line width alternation, Figure 3. The $m = +1$ and $m = -1$ lines of the nitro group nitrogen are broadened, but the $m = 0$ lines remain sharp. This is in agreement with what is expected for a rapid modulation of the nitrogen hyperfine coupling constant due to the rapid interconversion between the free ion and ion pair.

Similar results are observed for the anion radical of *p*-nitrobenzophenone in HMPA upon addition of potassium

TABLE III: Thermodynamic Parameters Controlling the Ion-Pair Dissociation of the Potassium Salt of the Systems

System	$K_{eq}(25°)$, M	$\Delta H°$, kcal/mol	$\Delta S°$, eu
p-Dinitrobenzene	0.7[a]	−1.9	−9.3
p-Nitrobenzophenone	0.059 ± 0.005	−0.89 ± 0.1	−8.6
p-Nitrobenzaldehyde	0.060 ± 0.005	0	−5.6

[a] This value was taken from ref 17 and 18.

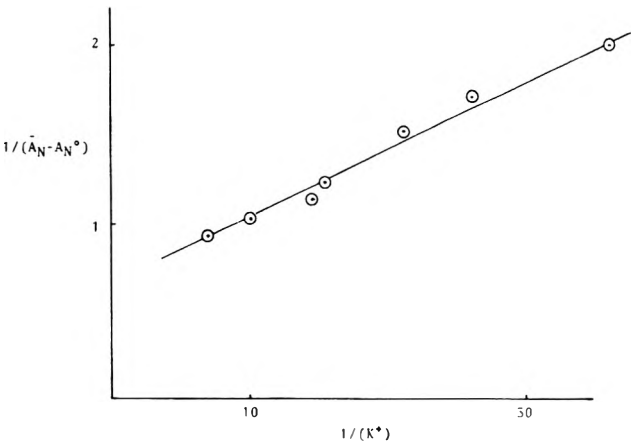

Figure 5. Plot of $1/(\bar{A}_N - A_N°)$ *vs.* the reciprocal of the potassium ion concentration for the *p*-nitrobenzophenone system.

iodide, Figure 4. However, in this case the line width alternation is light and the time-averaged esr coupling constant for the nitrogen-14 nucleus can be accurately measured. A plot of $1/(\bar{A}_N - A_N°)$ *vs.* $1/(K^+)$ is linear, Figure 5, and the resulting thermodynamic parameters for eq 1 are given in Table III. The entropy and enthalpy functions were determined in the usual manner.

The electron-withdrawing ability of the benzoyl group is large enough to allow time averaging of the ion pair and free ion yet small enough so that some line width alternation is observed. The same situation should be observed for other substituents with similar properties such as the aldehyde function.

Addition of KI to the free anion radical of *p*-nitrobenzaldehyde in HMPA results in an increase in A_N together with strong line width alternation. This line width alternation results in large errors in the measurements of A_N. However, the total line width of the spectrum (distance from the first line to the last line) rises proportionally with A_N; thus the time-averaged equation (eq 5) can be written in terms of the total line width (Δw_t). A plot of $1/(\Delta\bar{w}_t - \Delta w_t°)$ *vs.* the reciprocal of the potassium ion concentration is linear, and the resulting thermodynamic parameters are given in Table III. The slope and intercept of this plot, Figure 6, are independent of the temperature and thus $\Delta H°$ is near zero.

Conclusions

It is clear that the time between ion association–dissociation events in the para-substituted nitrobenzene systems is roughly inversely proportional to the electron-donating ability of the para substituent. When the $\sigma+$ value for the substituent is less than about 0.6, as it is for the substituents H, alkyl, and Cl, the rate of ion-pair formation and

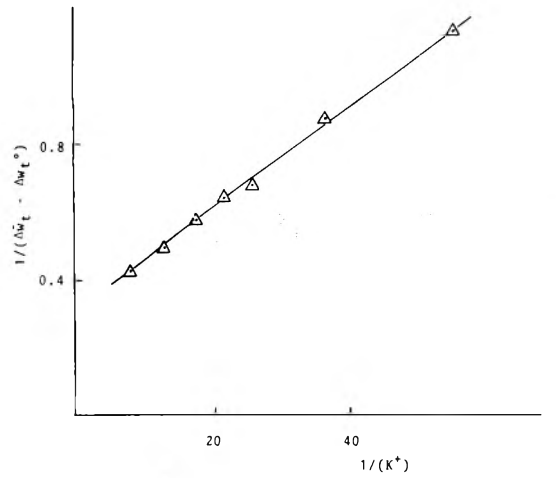

Figure 6. Plot of $1/(\Delta\bar{w}_t - \Delta w_t^\circ)$ *vs.* the reciprocal of the potassium ion concentration for the *p*-nitrobenzaldehyde system.

dissociation is slow on the esr time scale and simultaneous recording of the two spectra is observed. When this $\sigma+$ value is very large, as is the case for *p*-dinitrobenzene, complete time averaging of the spectra for the ion pair and free ion is observed.[3] All of this indicates that the larger the charge density on the NO_2 group the slower is the rate of ion-pair formation and dissociation.

A plot of the enthalpy of dissociation of the ion pair *vs.* the $\sigma+$ value for the para substituent yields a ρ value of -23.[3] This plot predicts enthalpies for the *p*-nitrobenzaldehyde and *p*-nitrobenzophenone systems of about zero. Experimentally this is the case. Even though this Hammett plot was constructed for system yielding simultaneous observation of the two spectra, it predicts resonable values for the enthalpies for systems which yield time averaging.

The rate of ion-pair formation and dissociation for the *p*-benzoquinone anion radical in HMPA is slow on the esr time scale. However, that for the 2,6-di-*tert*-butylbenzosemiquinone system in HMPA is fast. This is probably due to the decrease in the charge density on the oxygen atoms due to the presence of the alkyl substituents. The fact that the potassium cation was unable to approach the oxygen that is sandwiched between the two *tert*-butyl groups indicates not only that ion pairing is controlled by coulombic and solvation forces but also that steric considerations are also of importance.

The work presented here shows that time-averaged esr coupling constants can be used to determine ion-pair dissociation constants, but care must be taken to be sure that the system can be represented by a single ion pair and free ion or, if more than one ion pair exists, that they are rapidly interconverted and the equilibrium between the two is not a function of the counterion concentration.

Finally, it has already been mentioned that the reliability of the equilibrium constants measured for the ion-pair dissociation reaction (eq 1) is determined in part by the saturation factor (s). This factor is defined by eq 6. For the calculation of s for the *p*-nitrobenzophenone and *p*-nitrobenzaldehyde systems A is, of course, replaced by A_N and Δw_t, repectively. It is clear from Table IV that our s values extend well into the range of reliability.

TABLE IV: Saturation Factors for the Systems

System	Range for s
2,6-Di-*tert*-butylbenzoquinone	0.36–0.93
p-Nitrobenzophenone	0.29–0.69
p-Nitrobenzaldehyde	0.24–0.65

Experimental Section

All of the organic compounds used were purchased from Aldrich Chemical Co. and recrystallized before use. The potassium iodide was purchased from Alpha Inorganics and was stored in a vacuum oven for 48 hr at 100° prior to use.

The method of reduction of the neutral molecule to form the anion radicals and the purification of the HMPA have been previously described.[19]

X-Band esr spectra were recorded on a Varian E-9 esr spectrometer equipped with a Varian temperature controller calibrated with a copper–constantan thermocouple.[20]

Acknowledgments. The authors are grateful to Research Corp. and the National Institutes of Health for support of this work. The NIH support was from Grant No. RR-8102 from the Division of Research Resources.

References and Notes

(1) (a) J. Chaudhuri, S. Kume, J. Jagur-Grodzinski, and M. Szwarc, *J. Amer. Chem. Soc.*, **90**, 6421 (1968); (b) A. Cserhegyi, J. Jagur-Grodzinsky, and M. Szwarc, *ibid.*, **91**, 1892 (1969); (c) A. Cserhegyi, J. Chaudhuri, E. Franta, J. Jagur-Grodzinsky, and M. Szwarc, *ibid.*, **89**, 7129 (1967); (d) G. Levin, J. Jagur-Grodzinsky, and M. Szwarc, *ibid.*, **92**, 2268 (1970).
(2) G. R. Stevenson, L. Echegoyen, and L. R. Lizardi, *J. Phys. Chem.*, **76**, 1439 (1972).
(3) G. R. Stevenson and L. Echegoyen, *J. Phys. Chem.*, **77**, 2339 (1973).
(4) For examples of semiquinones see T. E. Gough and P. R. Hindle, *Can. J. Chem.*, **49**, 1529 (1971).
(5) N. Hirota, *J. Phys. Chem.*, **71**, 127 (1967).
(6) G. R. Stevenson and A. E. Alegria, *J. Phys. Chem.*, **77**, 3100 (1973).
(7) R. D. Allendoerfer and R. J. Papez, *J. Phys. Chem.*, **76**, 1012 (1972).
(8) R. Chang and C. S. Johnson, Jr., *J. Amer. Chem. Soc.*, **88**, 2338 (1966).
(9) A. M. Hermann, A. Rembaum, and W. R. Carper, *J. Phys. Chem.*, **71**, 2661 (1967).
(10) K. Hofelmann, J. Jagur-Grodzinski, and M. Szwarc, *J. Amer. Chem. Soc.*, **91**, 4645 (1969).
(11) W. B. Pearson, *J. Amer. Chem. Soc.*, **87**, 167 (1965).
(12) D. A. Deranleau, *J. Amer. Chem. Soc.*, **91**, 4044 (1969).
(13) All errors are reported as standard deviations.
(14) It has been previously observed that salts like KI are fully dissociated in HMPA: see P. Bruno, M. D. Monica, and E. Reghetti, *J. Phys. Chem.*, **77**, 1258 (1973).
(15) T. E. Gough and P. R. Hindle, *Can. J. Chem.*, **49**, 1529 (1971).
(16) It should be noted that some asymmetry in the esr spectra is expected even with the formation of only one ion pair that is in rapid equilibrium with the free ion as explained by S. K. Fraenkel, *J. Phys. Chem.*, **71**, 139 (1967). However, this effect is small.
(17) G. R. Stevenson and R. Concepción, *J. Amer. Chem. Soc.*, **96**, 4696 (1974).
(18) G. R. Stevenson and R. Concepción, submitted for publication in *J. Amer. Chem. Soc.*
(19) G. R. Stevenson, L. Echegoyen, and L. R. Lizardi, *J. Phys. Chem.*, **76**, 1439 (1972).
(20) The purchase of the E-9 esr spectrometer was made possible by a grant-in-aid from the Research Corp.

Dimerization. Study by Dipolar Broadening of Electron Spin Resonance Lines

E. Roland Menzel and John R. Wasson*

Department of Chemistry, University of Kentucky, Lexington, Kentucky 40506
(Received April 19, 1974; Revised Manuscript Received August 27, 1974)

Publication costs assisted by the Universtiy of Kentucky Tobacco and Health Research Institute

The solution esr spectra of several copper(II) dithiocarbamates in a variety of solvents were investigated at room temperature in the concentration range from 5×10^{-4} to 10^{-1} M. A very pronounced broadening of the magnetic resonance lines was observed at the higher concentrations. This broadening far exceeds estimates based on motional theoretical treatments of line widths for liquid systems. The method of moments developed by Van Vleck for crystalline magnetic systems is adapted to liquid systems involving molecules with correlation times sufficiently long to allow a "rigid liquid" formulation. The major weakness of the method of moments is the difficulty of characterization of line shapes, particularly in the near-Lorentzian case. A procedure is developed by which line shapes can be closely approximated such that the characterization of the line shape by the second moment alone becomes possible. First principle calculation based on the "rigid liquid" model agrees reasonably well with the data for the copper dithiocarbamates. The agreement between theory and experiment is satisfactory also for esr spectra of free radicals in solution. In solutions containing dimers in addition to monomers, the dimer concentration (in the range of 10^{-4} M) could be obtained from study of the esr line broadening. The dimer concentration had the expected linear dependence on sample concentration.

Introduction

The study of line widths and line shapes has been more extensively pursued in magnetic resonance than in any other branch of spectroscopy. Line widths are often small compared to the transition frequency in optical spectra and the number of mechanisms affecting line widths is large so that theoretical treatment is difficult. In the microwave region one needs to consider only magnetostatic interactions between atoms or molecules for purposes of line width study and, for liquids and gases, rotations and translations of molecules. Thus, magnetic resonance lines are amenable to thorough theoretical treatment.

The theory for liquid systems was pioneered by Bloembergen, Purcell, and Pound[1] who employed a Brownian motional model in which the tumbling and translations of ions or molecules produce an averaging effect on the static dipolar interactions of magnetic systems which results in linewidth narrowing. An excellent discussion of the physical reasons underlying this narrowing is given in their paper. For crystalline systems, where these motions do not apply, the method of moments treatment of Van Vleck[2] comprises the pioneering work. This method was extended to magnetically dilute crystalline systems by Kittel and Abrahams.[3]

Since the classic work of Bloembergen, Purcell, and Pound[1] and Van Vleck[2] theoretical treatments[4-10] and a number of recipes to calculate magnetic resonance line shapes have been developed.[11] Interpretation of nmr and esr spectral widths and shapes by these theories has generally been satisfactory. Curiously, however, study of the concentration dependence of esr line widths for solutions at relatively high concentrations ($\sim 10^{-1}$ to 10^{-2} M) of paramagnetic species has only rarely received attention to the best of our knowledge.[12] Neither has the possibility of study of dimerization and cluster formation by investigation of magnetic resonance line widths either in liquids or crystals been extensively explored, except in qualitative discussion[13] and in cases where dimers show pronounced triplet spectra superposed on monomer doublet spectra.[14-17] In the latter situation experiments are performed at low temperatures where the samples are no longer liquids and the analysis is based on relative intensities rather than study of line widths or line shapes.

Herein the esr spectra of several copper(II) dithiocarbamates in solution at concentrations ranging from 10^{-4} to 10^{-1} M are reported. This work was undertaken in order to examine the concentration dependence of esr line widths and explore the possibility of studying dimerization using concentration and line width data. It is well known that many copper(II) compounds[18] and free radicals are dimeric in the solid state. A number of dithiocarbamates of biological significance are also known.[19] It was thought that this work would not only be of importance in studying association of copper(II) compounds and other species in solution but also be of relevance to a number of analytical problems encountered in our studies of free radicals from tobacco smoke.[20]

Esr spectra of a number of copper(II) dithiocarbamates have been studied in solution at a concentration of 2×10^{-3} M by Gibson.[21] The temperature dependence of esr line widths of 5×10^{-4} M solutions of bis(diethyldithiocarbamato)copper(II) has also been reported.[22] These studies were concerned with the variation of line widths of the four hyperfine components with nuclear magnetic quantum number. Interpretation employed the theories of Kivelson[8] and McConnell.[7] The former is based on the work of Kubo and Tomita,[5] the latter on the work of Bloembergen, Purcell, and Pound.[1] Both the Kivelson[8] and McConnell[7] treatments show a conspicuous absence of concentration dependence since intermolecular interactions were considered negligible. However, our data (described in a later section) show a very pronounced broadening of esr lines with concentrations between 10^{-2} and 10^{-1} M, whereas at lower concentrations line widths are essentially constant and reasonably well described by the theories of Kivelson[8] and

McConnell.[7] The motional model of Bloembergen, Purcell, and Pound[1] predicts only a small broadening at the higher concentrations of interest here while the treatments of Kivelson[8] and McConnell[7] provide no concentration dependence. At first thought it might be expected that interactions not contained in the theoretical formulations obtain at the higher concentrations. This could be the reason concentration dependence of esr line widths at higher concentrations has apparently escaped detailed interpretation. The present work will hopefully remedy that deficiency by developing a model based on established theory which yields reasonably good agreement with experiment for esr spectra of solutions and which has a tractable simplicity.

The extension of Van Vleck's method of moments[2] to magnetically dilute crystal systems[3] includes an explicit concentration dependence. The rigid lattice model would appear not to be directly applicable to solution cases since molecular motions are not accounted for. The model of Bloembergen, Purcell, and Pound[1] has been reexamined in order to determine the effect of inclusion of intermolecular interactions on esr line widths. Their theory was considered because it is attractive to experimentalists in terms of detail shown in their paper and clarity of exposition which cannot necessarily be said of some of the other cited references.

Intermolecular Interactions in the Motional Model

Our data for copper(II) dithiocarbamates (shown below) indicate an esr line broadening of ~15 G at 10^{-1} M (in absence of aggregation) over the constant line widths of ~10 G at low concentrations for room temperature spectra obtained at X-band frequencies (~10^{10} Hz). Equation 50 of ref 1 shows the effect of intermolecular interactions on the relaxation rate $1/T_1$ arising from nonsecular terms in the magnetic dipolar Hamiltonian. In the relaxation rate framework quantities $1/T$ correspond to line width according to the relation

$$1/T \simeq 2\pi\Delta\nu$$

where $\Delta\nu$ is the line width. For our case an estimate of $1/T_1$ based on the motional model yields $1/T_1 \sim 5 \times 10^7$ sec^{-1} at 10^{-1} M, roughly an order of magnitude too low compared to experiment ($1/T \sim 5 \times 10^8$ sec^{-1} for 25-G line width). The intermolecular contribution to the relaxation rate $1/T_2'$ arising from the secular terms of the magnetic Hamiltonian is given by eq 52 of ref 1. For our case the translational correlation time $\tau_c = r^2/12D$ (r = distance between molecules; D = diffusion coefficient) is small compared to $1/T_2'$ so that $1/T_2' \sim (6/\pi)C_1\tau_c$ (ref 1, p 704) where $C_1 = (3/10)g^4\beta^4/h^2r^6$ and the symbols have their usual meanings. Radial integration from the distance of closest intermolecular approach to infinity, as done for $1/T_{1n}$ (ref 1, eq 49) yields $1/T_2' \sim 1.5 \times 10^7$ sec^{-1} at 10^{-1} M which corresponds to a line width of ~1 G. The Bloembergen, Purcell, and Pound[1] treatment, therefore, predicts only a small line broadening, much less than that observed experimentally, and substantially smaller than the low concentration line widths. This accounts for the neglect of intermolecular interactions in the Kivelson[8] and McConnell[7] formulations. In terms of the relaxation rate $1/T_1$ the broadening is still smaller than shown by the above order-of-magnitude evaluation since the assumption $4\pi^2\nu_0^2\tau_c^2 \ll 1$ appropriate in nmr spectroscopy of liquid systems does not hold here. For $\nu_0 \sim 10^{10}$ Hz and assuming that the distance of closest approach between molecules (excepting dimerization) is ~10 Å, which will be justified shortly, $4\pi^2\nu^2\tau_c^2 \gg 1$ which reduces the theoretical $1/T_1$ on the basis of the model of Bloembergen, Purcell, and Pound (*cf.* eq 46 of ref 1) drastically. Unless effects other than motional effects on magnetic dipolar interactions take place, one is led to suspect that the translational correlation time is sufficiently long so that molecular translations are no longer important at high concentrations. Significant changes in viscosity take place only at much higher concentrations than those of interest here.

A model considering the statistical distribution of distances between molecules uniformly distributed in a "rigid liquid" would seem to be a reasonable approach to the secular intermolecular dipolar interactions described by $1/T_2'$. Intramolecular effects and interactions described by $1/T_1$ would be neglected in this approach, the former because it yields no concentration variation, the latter since it does not result in significant broadening. A statistical distribution approach was very successfully taken by Förster[23] in his classic treatment of the somewhat analogous problem of radiationless intermolecular energy transfer as related to concentration depolarization of fluorescence in liquids. If, then, a statistical distribution of molecules is considered and the secular magnetic Hamiltonian is taken to describe the line broadening, while the time-dependent terms are neglected, the translational correlation time needs no longer be considered. A treatment by the method of moments of Van Vleck[2] suitably adapted to liquids by introduction of a distribution probability function can be employed. One could alternately consider parameterizing the translational correlation time in order to obtain agreement with experiment. In fact, even the "rotational" correlation time $4\pi\eta a^3/3kT$ evaluated from first principles does not produce agreement with experiment, so that a somewhat empirical approach needs to be taken.[21] The parameter approach is not physically satisfying, and, in addition, would result in a linear concentration dependence (see eq 49 of ref 1) which does not correspond to experimental findings. We will, therefore, demand instead that the model developed along the above outlined procedure must be amenable to first principle calculation which yields reasonably good agreement with experiment, thus allowing one to test the legitimacy of the approach. An important criterion in the development of this model will be sufficient simplicity to allow straightforward use by investigators who are more at home with instrumentation than with operators and correlation functions.

Adaptation of the Method of Moments to Liquids

Proceeding along the above proposed lines we make immediate use of Van Vleck's equations[2] and the treatment of Kittel and Abrahams[3] for magnetically dilute systems. Explicit account of the possibility of dimerization yields the following for the second moment of an esr line:

$$\langle\Delta\nu^2\rangle_{av} = \frac{S(S+1)}{3h^2}\left[(1-f)\sum_{\substack{k\\k\neq j_1}} B_{j_1k}^2 + f\sum_{\substack{k\\k\neq j_2}}\left[B_{j_2k}^2 + B_{\Delta_d}^2\right]\right] \quad (1)$$

where the fraction of molecules involved in dimerization is denoted by f. Monomer "sites" are denoted by j_1, dimer sites by j_2. The term $B_{\Delta_d}^2$ explicitly accounts for the dipolar interaction between dimer partners. With regard to the first term of eq 1 we note that the interaction of a monomer j with a distant dimer k is practically indistinguishable

from the interaction between j and two monomers near each other. In the summation over k all molecules are, therefore, treated as monomers. Adaptation to the liquid state is made by replacing sums by integrals, by averaging over all relative orientations of molecules and orientations of the intermolecular distances with respect to the static magnetic field, and by introducing the probability distribution function $e^{-\xi}\,d\xi$.[23] This function describes the probability of finding a neighbor to a given molecule at a distance between r and $r + dr$. Here $\xi = NCV$ with $N = 6 \times 10^{23}$ molecules/mol, C is the concentration in moles/liter (M), and $V = 4/3\pi r^3$ corresponds to volume in liters. The use of $e^{-\xi}\,d\xi$ implies interaction between a molecule j and a single molecule k only. In other words, the assumption is made that the probability of finding a third molecule in the same vicinity is small. This may apply for distances near the distance of closest approach, but is not legitimate for large distances. At large distances interactions become weak, however, so that we expect that the use of the above probability function will yield a reasonably close approximation, provided the probability of finding the above-mentioned third molecule is indeed small. If we let $C = 10^{-1}\,M$ and $r \sim 10$ Å and let $dV \sim \Delta V \sim V$, then $d\xi \sim \Delta\xi \sim \xi$. The probability of finding two neighboring molecules within dV ($\sim V$) is then $(e^{-\xi}\Delta\xi)^2$, which is sufficiently small to be neglected to first approximation. Averaging over all orientations (see eq 11–14 of ref 2) results in

$$\langle \Delta\nu^2 \rangle_{av} = \frac{3}{5}\beta^4 g^4 h^{-2} S(S+1)\left\{\int_{\zeta}^{\infty} \frac{e^{-\xi}\,d\xi}{r^6} + \frac{f}{\Delta_d^6}\right\} \quad (2)$$

where ζ denotes the distance of closest approach between the magnetically active ions of two interacting molecules, excepting dimerization, r, the Cu–Cu distance for neighboring monomers, Δ_d, the Cu–Cu distance in a dimer configuration and $d\xi = NC\,4\pi r^2\,dr$. The integral in eq 2 can be expanded into two terms

$$[e^{-\xi}/\xi]_Z \quad \text{and} \quad \int_Z^{\infty} (e^{-\xi}/\xi)\,d\xi$$

where Z denotes the value of ξ at $r = \zeta$. For $\xi \lesssim 10$ Å, Z is in the range 0.1 to 0.2. Figure 1 shows the magnitude of both terms as a function of Z. The term $[e^{-\xi}/\xi]_Z$ is seen to dominate. After making the substitution $\Delta\nu_{ms} = 2[\langle \Delta\nu^2 \rangle_{av}]^{1/2}$ for Gaussian line shape and letting $g \simeq 2$, $S = 1/2$ appropriate to the copper dithiocarbamates we obtain

$$\Delta\nu_{ms} = \frac{6\beta}{\sqrt{5}}\left[\frac{4\pi}{3}\frac{NC}{\zeta^3} + \frac{f}{\Delta_d^6}\right]^{1/2} \quad (3)$$

with $\Delta\nu_{ms}$ = broadening of peak-to-peak width of the derivative shape. The broadening $\Delta\nu_{ms}$ of the peak-to-peak width in the derivative spectrum is given in Gauss, since the substitution $\Delta H = h\Delta\nu/g\beta$ has been made. $\Delta\nu_{ms}$ is not simply the peak-to-peak width of the broadened line minus that of the unbroadened line. This is discussed below. Even though widths of hyperfine components are measured, the influence of the nuclear magnetic moments is neglected, since the nuclear Bohr magneton is much smaller than the electronic one. Equation 3 is the final form of our model. It computes the line broadening corresponding to the increase of peak-to-peak width of lines in the esr derivative spectrum assuming Gaussian line shape. Extension to other line shapes will be made shortly. If the sample concentration is known and dimerization does not occur ($f = 0$), then $\Delta\nu_{ms}$ can be computed immediately and compared to esr data if ζ can be estimated. If C and ζ are known, substitution of

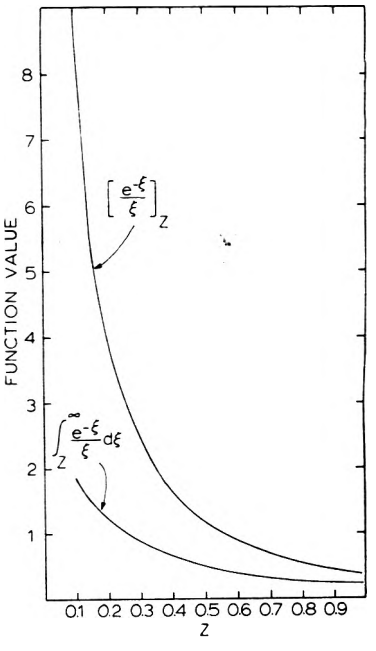

Figure 1. Values of the functions $[e^{-\xi}/\xi]_Z$ and $\int_Z^{\infty}(e^{-\xi}/\xi)\,d\xi$. See text for definition of symbols.

experimental values $\Delta\nu_{ms}$ into the left side of eq 3 yields the dimer concentration, $0.5Cf$. For the copper dithiocarbamates investigated and chloroform solutions $\zeta \sim 8.7$ Å and eq 3 becomes

$$\Delta\nu_{ms} \simeq 2.5 \times 10^{-20}[3.8 \times 10^{42}C + 5.45 \times 10^{44}f]^{1/2} \quad (4)$$

for Gaussian line shape, with $\Delta\nu_{ms}$ in Gauss and C in moles/liter.

Distance of Closest Approach and Dimer Distance

An estimate of ζ and Δ_d can be made by essentially a hard-sphere model using the van der Waals radii of elements and known bond distances. For the distance of closest approach of the two copper atoms in two neighboring molecules we make the reasonable assumption that one "layer" of solvent molecules is interposed between the two chelate molecules such that closest packing and closest Cu–Cu distance results. Figure 2 depicts the configuration, although parallel arrangement of the two chelates is not necessary. One obtains $\zeta \sim 8.7$ Å for Cu–DIPA (Cu–DIPA = bis(diisopropyldithiocarbamato)copper(II), $Cu[S_2CN(C_3H_7)_2]_2$) and for Cu–P (bis(pyrrolidinyldithiocarbamato)copper(II), $Cu[S_2CNC_4H_8]_2$). We defer discussion of the accuracy of this estimate until a later section. The dimer configuration is shown in Figure 3 where the molecules are assumed to be in a parallel arrangement. The perpendicular arrangement is less favorable due to less tight packing of atoms. The Cu–Cu distance $\Delta_d \simeq 3.5$ Å and the orientation between the dimer partners are in agreement with the literature.[15,18,24] We defer the question of dimer tumbling to a later section.

Determination of $\Delta\nu_{ms}$ for Non-Gaussian Line Shapes

The major weakness of the method of moments lies in the difficulty of determination of line shapes. In principle, one wants to describe the broadening of a spectral line, *i.e.*, the increase in half width, Γ, of the line by the quantity

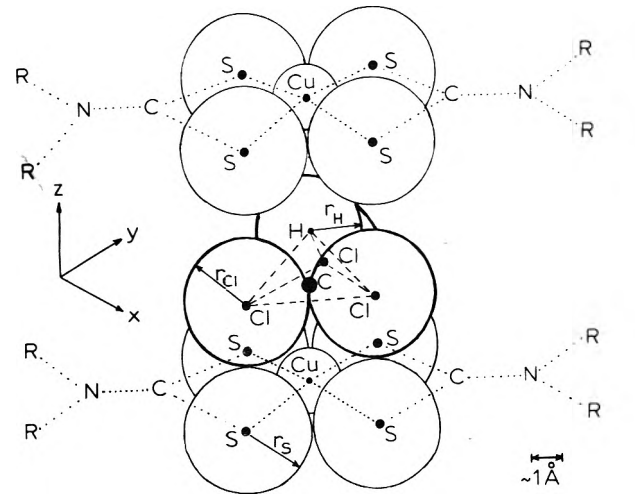

Figure 2. Schematic representation of the configuration of closest approach of two copper(II) dithiocarbamate monomers in chloroform.

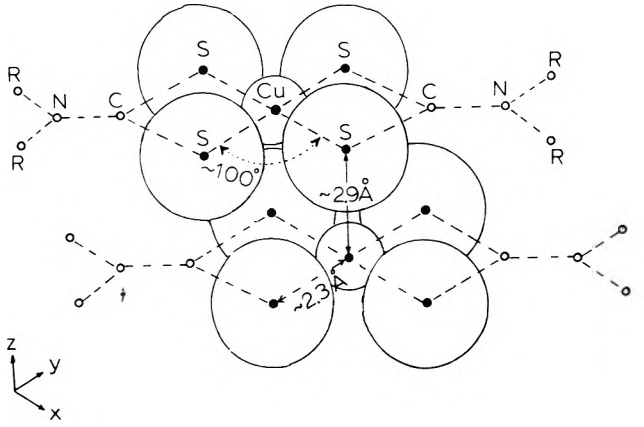

Figure 3. Schematic representation of the dimer configuration of copper(II) dithiocarbamates.

$\langle \Delta\nu^2 \rangle_{av}$ which is obtained by the method of moments. If necessary, higher moments $\langle \Delta\nu^{2n} \rangle_{av}$ can be obtained and ratios of the moments be taken to characterize the line shape. For instance, for Gaussian shape $[\langle \Delta\nu^4 \rangle_{av}]^{1/4} = 1.32[\langle \Delta\nu^2 \rangle_{av}]^{1/2}$, whereas for rectangular shape the corresponding factor would be 1.16. Customarily one is interested in Gaussian and Lorentzian line shapes. While the Gaussian line shape is tractable, the method of moments breaks down for Lorentzian shape since the integrals $\int_0^\infty L\,\nu^2\,d\nu$, $\int_0^\infty L\,\nu^4\,d\nu$, etc., cannot be evaluated in the limit $\nu \to \infty$ where $L = \Gamma^2/(\Gamma^2 + \nu^2)$ and Γ is the half-width at half-height. One recourse is to treat the Lorentzian shape as cut off at a point $\nu = \alpha \gg \Gamma$. One then obtains[3] $\langle \Delta\nu^2 \rangle_{av} = 2\Gamma\alpha/\pi$, $\langle \Delta\nu^4 \rangle_{av} = 2\Gamma\alpha^3(3\pi)^{-1}$. We let $\alpha = K\Gamma$ with $K \gg 1$ and obtain $\langle \Delta\nu^2 \rangle_{av}\pi(2K)^{-1} = \Gamma^2$ and $\langle \Delta\nu^4 \rangle_{av}3\pi(2K^3)^{-1} = \Gamma^4$. The ratio $[\langle \Delta\nu^2 \rangle_{av}]^{1/2}/[\langle \Delta\nu^4 \rangle_{av}]^{1/4}$ is essentially undetermined, depending on K, hence, on the choice of cut-off point, and is therefore not useable for the characterization of line shape. An additional difficulty is the very rapidly increasing complexity of the equations for $\langle \Delta\nu^{2n} \rangle_{av}$. To see this it suffices to compare eq 10 and 21 of ref 2. It therefore becomes essential from the practical view to find a procedure by which line shapes varying from Gaussian to very nearly Lorentzian can be characterized by $\langle \Delta\nu^2 \rangle_{av}$ only. This characterization would take the following form. Suppose a line is Gaussian ($e^{-\ln 2\nu^2/\Gamma^2}$). Then, $\Gamma^2 = 2 \ln 2 \langle \Delta\nu^2 \rangle_{av}$ (Γ is not the "full half-width" $\Delta\nu_{1/2}$ of Van Vleck[2] but $\Gamma = \frac{1}{2}\Delta\nu_{1/2}$). For a triangular line one would obtain $\Gamma^2 = \frac{3}{8}\langle \Delta\nu^2 \rangle_{av}$. If now the value of $\langle \Delta\nu^2 \rangle_{av}$ for Gaussian shape is computed by, for instance, eq 3 of this paper, one could adapt this equation to a different line shape by means of a correction factor to be applied to the corresponding measured quantity, Γ^2 in this case. For instance, the correction factor to be applied to the measured Γ^2 in case of triangular shape would be (16 ln 2)/3. For nearly Lorentzian shape the adaptation proceeds as follows. We consider the frequency distribution $[\Gamma^2/(\Gamma^2 + \nu^2)]^2$, *i.e.*, a square-Lorentzian line shape. The square-Lorentzian shape reasonably well approximates the Lorentzian shape, being slightly more "bell shaped" near the peak and dropping off slightly faster in the wings. In terms of esr spectra one is interested in the derivative of the frequency distribution. Figure 4 compares the derivative Lorentzian and square-Lorentzian (suitably scaled) shapes. The two are nearly identical. In terms of experimentally obtained derivative curves of esr spectra the square-Lorentzian distribution constitutes a very close approximation to the Lorentzian distribution. We next note that the square-Gaussian distribution $e^{-2\ln 2\nu^2/\Gamma^2}$ is itself Gaussian with half-width reduced from Γ to $\Gamma/\sqrt{2}$. We denote Gaussian, square-Gaussian, Lorentzian, and square-Lorentzian shapes by G, G^2, L, and L^2, respectively, and denote the derivative shapes by the prefix d. Plots of dL and dG with the same Γ are shown in Figure 5A. Plots of dL^2 and dG^2 with the same Γ (which is no longer the half-width of either G^2 or L^2) are shown in Figure 5B. Comparison of the two figures shows that in terms of derivative spectra one can relate Gaussian and Lorentzian shapes to good approximation by instead relating G^2 and L^2. The use of G^2 is not necessary, however. One could just as well relate G and L^2 by introduction of a suitable scaling of Γ in L^2. The results in terms of the above-mentioned correction factors which are to be applied to the measured $\Delta\nu_{ms}$ would be the same. We choose to use G^2 purely for convenience. We now note that the second moment of L^2 can be readily computed, which is the reason for having introduced L^2 to begin with. We obtain $\langle \Delta\nu^2 \rangle_{av} = \Gamma^2$ for L^2, and $\langle \Delta\nu^2 \rangle_{av}$ 4 ln 2 = Γ^2 for G^2. In terms of the peak-to-peak width in the derivative spectrum, the quantity usually measured in esr spectra to obtain the line broadening, ${}^{L^2}\Delta\nu_{ms} = 2\langle \Delta\nu^2 \rangle_{av}/\sqrt{5}$ and ${}^{G^2}\Delta\nu_{ms} = 2\langle \Delta\nu^2 \rangle_{av}$, where left superscripts signify the line shape. This means that eq 3 must yield a value $\sqrt{5}$ larger for nearly Lorentzian shape than for Gaussian shape. In effect, one can apply eq 3 to nearly Lorentzian shape provided one multiplies the measured $\Delta\nu_{ms}$ by a correction factor $\sim\sqrt{5}$. Unfortunately, the above procedure can be applied to good approximation only when the line broadening is substantially larger than the "natural line width" (obtained at concentrations $\lesssim 10^{-3}$ M). The "natural shape" at low concentrations is found to be nearly Lorentzian for the compounds studied in this paper. The question arises whether the broadening is Gaussian, Lorentzian, or intermediate. As long as the broadening is considerably smaller than the natural line width (near 10^{-2} M for the present systems) the change in line shape resulting from the broadening is not easily measured. For large broadening (near 10^{-1} M in our case) changes in the observed line shapes are readily determined, however, and the required correction factor for $\Delta\nu_{ms}$, which allows extension of eq 3 to line shapes other than Gaussian, can be obtained. In the region of small broadening one can

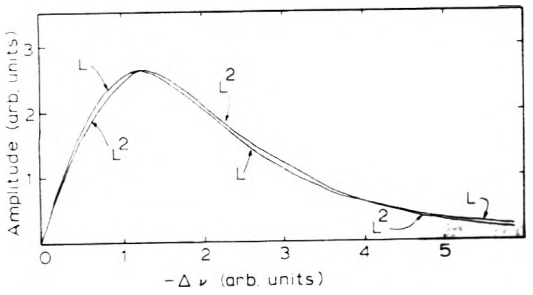

Figure 4. Comparison of Lorentzian and "square-Lorentzian" derivative line shapes (suitably scaled).

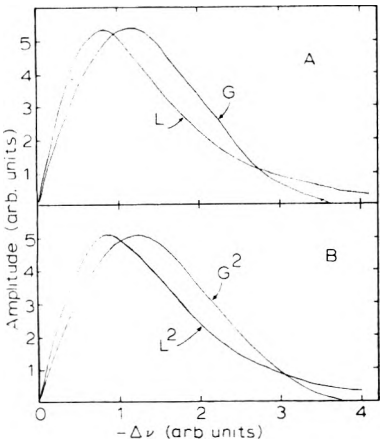

Figure 5. Comparison of Gaussian and Lorentzian with square-Gaussian and square-Lorentzian derivative shapes (suitably scaled).

either plead ignorance and establish the limits within which $\Delta\nu_{ms}$ lies (Gaussian shape and nearly Lorentzian shape), or one can approximate line shapes by extrapolating back linearly from the line shapes found at the lowest concentration at which the change in line shape becomes readily measurable, to the low concentration line shapes. We have taken the latter approach. We will consider the resulting cases of "mixed line shape" below. A procedure which allows determination of the correction factors to be applied to eq 3 as function of the observed line shape will be described.

Experimental Section

Bis(diisopropyldithiocarbamato)copper(II), Cu–DIPA, and bis(dipyrrolidinyldithiocarbamato)copper(II), Cu–P, were prepared[25] and purified by procedures similar to those described[26] for the related chromium(III) compounds. 2,2,5,5-Tetramethyl-3-pyrrolin-1-oxyl-3-carboxylic acid *N*-hydroxysuccinimide ester free radical was obtained from Eastman Organic Chemicals, Rochester, N.Y., and used without further purification.

Esr spectra were obtained using instrumentation and techniques described previously.[26] Esr spectra in chloroform and chlorobenzene solutions at concentrations ranging from 5×10^{-4} to 10^{-1} *M* were obtained at room temperature at X-band frequencies. Figures 6 and 7 show the variation in the peak-to-peak widths of the four observed hyperfine lines ($S = 1/2$, $I = 3/2$) with sample concentration for Cu–DIPA in chloroform. We note that the ^{65}Cu in addition to the more abundant ^{63}Cu is seen at low concentrations *via* the structure on the "negative-slope" half of the high-field line and the slight broadening of the "positive-slope" half of the low-field line, as seen in Figure 6. The two intermediate-field lines show no discernible asymmetry. At the higher concentrations, which are of primary interest in the present paper, the large broadening obliterates the ^{65}Cu effect, which is therefore ignored at these concentrations. At the lower concentrations the peak-to-peak widths in the derivative spectra were taken to be those of the two intermediate-field lines and were deduced for the low- and high-field lines by consideration of only the negative-slope and positive-slope portions, respectively. The assumption was made that the "real" positive-slope half of the low-field line equals the negative-slope half in shape and that the "real" negative-slope half of the high-field line equals the positive-slope half in shape. Figure 8 shows the estimated variation of broadening with half-width. The value of the half-width at zero broadening represents the intrinsic half-width, which is normalized to unity in Figure 8. The shape of the curve can be deduced readily by consideration of, for instance, superposition of closely spaced triangular shaped lines. Since the peak-to-peak width in the derivative spectrum is directly proportional to the half-width, Figure 8 also gives $\Delta\nu_{ms}$ as function of the observed peak-to-peak width. Figure 9 shows the resulting variation of $\Delta\nu_{ms}$ with sample concentration for Cu–DIPA in chloroform. The solid line in Figure 9 shows the predicted variation on the basis of eq 4 in absence of dimerization. Figure 10 shows the variation of $\Delta\nu_{ms}$ for chlorobenzene solution. For chlorobenzene solution the observed line shapes are nearly Gaussian at 10^{-1} *M* and more nearly Lorentzian at 10^{-2} *M*. The dashed line in Figure 10 gives the limits of Gaussian broadening. The experimental points in Figures 9 and 10 include averaging over the four hyperfine components. The variation of line shapes with concentration was accounted for *via* the method discussed in the section entitled Mixed Line Shapes. For Cu–DIPA in chloroform the line shapes were found to be nearly Lorentzian at 10^{-2} *M*, becoming slightly more Lorentzian still in appearance at 10^{-1} *M*. Cu–P was not sufficiently soluble to allow obtention of data at the higher concentrations. The comparison of calculated and observed $\Delta\nu_{ms}$ is summarized in Table I for 10^{-2} *M* sample concentration. Also given in Table I are the distances of closest monomer approach for the various solvent cases, computed on the basis of the previously discussed "hard-sphere model." In this computation the tumbling of solvent molecules is neglected. For chloroform solution inclusion of tumbling of the solvent molecules in the monomolecular layer interposed between two monomer copper dithiocarbamate molecules in the configuration of closest approach reduces the calculated broadening by a factor of about 1.2 (to be discussed in a latter section) and similarly also for the other solvents. The Gaussian limit in Table I for the calculated broadening is possibly the better approximation than the near-Lorentzian limit, since the broadening at higher concentrations in absence of dimerization (Cu–DIPA in chlorobenzene) is Gaussian. The excess broadening for Cu–DIPA in chloroform suggests the occurrence of dimerization. Tendency for dimerization is in fact to be expected.[18,24] The absence of this excess broadening in chlorobenzene solution, hence apparently little dimerization, if we assume for the moment that dimerization is the cause for the excess broadening in chloroform solution, may be related to solvent size and geometry.

Dimerization

The parameter *f* in eq 3 of the present model can be fit

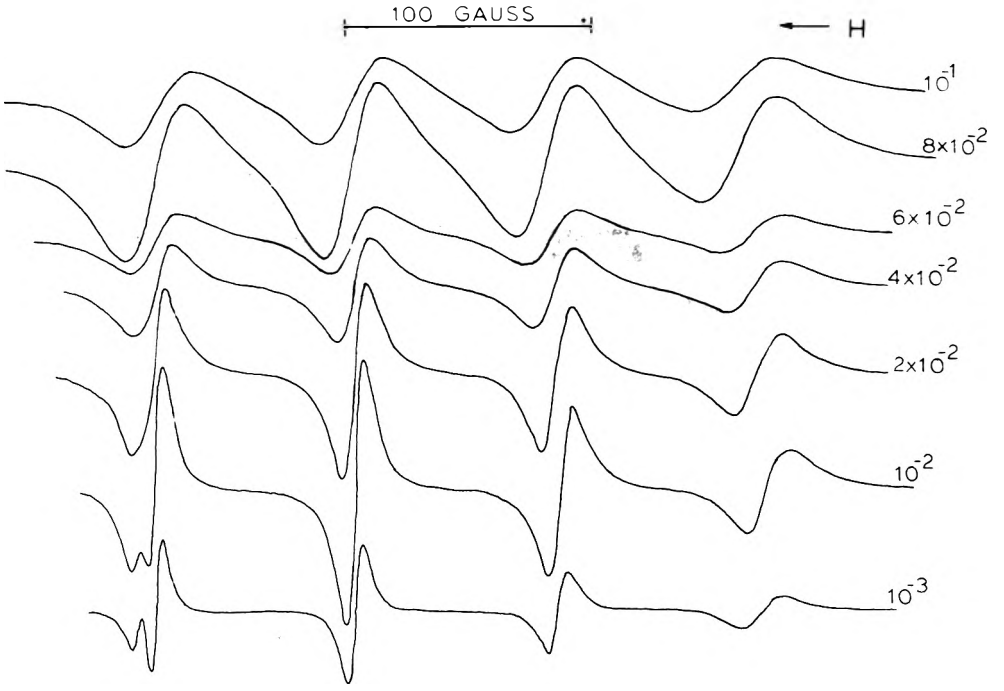

Figure 6. Observed esr spectra of Cu-DIPA in chloroform. The numbers in the figure are concentrations in moles per liter.

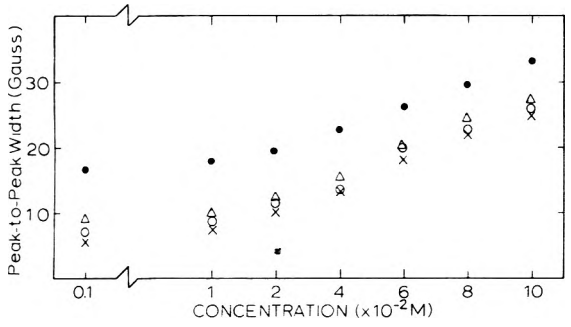

Figure 7. Concentration dependence of peak-to-peak widths of the four hyperfine lines of Cu-DIPA in chloroform. Widths are denoted by ●, Δ, C, × for the lines from low to high field, respectively.

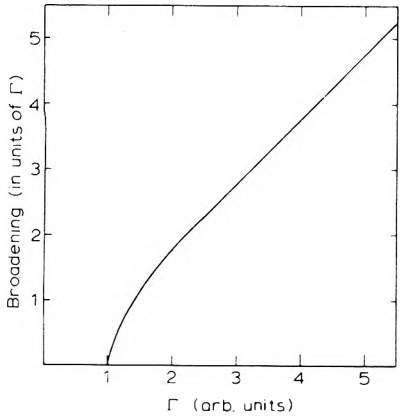

Figure 8. Dependence of broadening on half-width. The intrinsic half-width is taken to be 1.0.

to any concentration dependence of broadening, if treated purely empirically, which tells us little about the legitimacy of our approach unless the variation of f follows prediction for concentration dependence of dimerization. From equilibrium considerations we have $2M \rightarrow D$, where M denotes monomers and D, dimers. The equilibrium constant k =

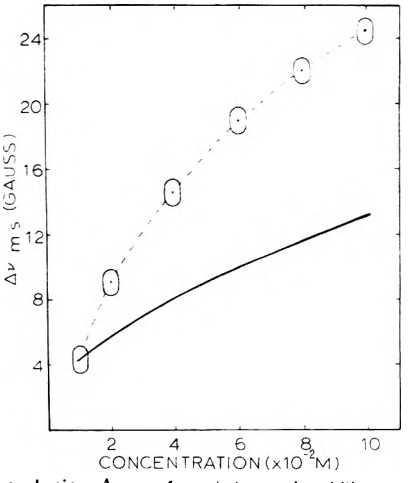

Figure 9. Broadening $\Delta\nu_{ms}$ of peak-to-peak width as a function of concentration for Cu-DIPA in chloroform. The solid line gives the predicted broadening in absence of dimerization. Ellipses are experimental values.

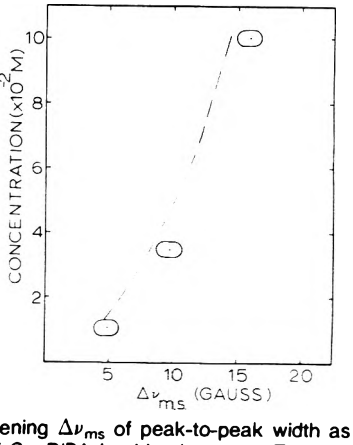

Figure 10. Broadening $\Delta\nu_{ms}$ of peak-to-peak width as a function of concentration of Cu-DIPA in chlorobenzene. The dashed line gives predicted broadening assuming Gaussian line shape. Ellipses are experimental values.

TABLE I: Dipolar Broadening in Solution at 10^{-2} *M* Concentration

Compd	Solvent	ζ,[a] Å	Calcd broadening G			Expt broadening, G (±1 G)
Cu–DIPA[b]	Chloroform	8.7	4.7[d]	4[e]	6.5[f]	4.5
Cu–P[c]	Chloroform	8.7	4.7	4	6.5	4
Cu–P	Dichloromethane	8.5	4.9	4	6.5	5
Cu–P	Bromoform	9.2	4.3	3	5	3.5
Cu–DIPA	Chlorobenzene	8.0	5.3	3.5	5.5	5

[a] ζ = distance of closest Cu-Cu approach, excepting dimerization. Tumbling of solvent molecules is neglected. [b] Cu-DIPA = $Cu[S_2CN(CHCH_3CH_3)_2]_2$. [c] Cu-P = $Cu[S_2CNC_4H_8]_2$. [d] Gaussian broadening is assumed, tumbling of solvent molecules is neglected. [e] Gaussian broadening is assumed, tumbling of solvent molecules is accounted for. [f] Near-Lorentzian broadening is assumed, tumbling of solvent molecules is accounted for.

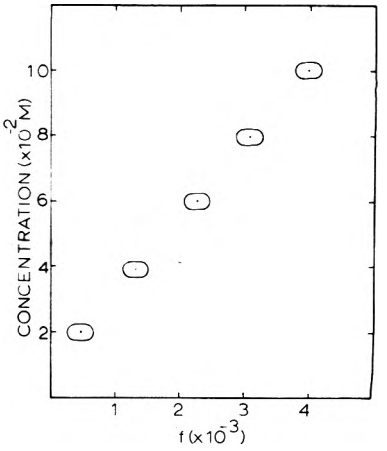

Figure 11. Fraction, *f*, of molecules involved in dimerization as a function of sample concentration for Cu–DIPA in chloroform. The dimer concentration is $0.5Cf$ where C is the sample concentration.

$[D][M]^{-2}$. As long as [D] is small we have $[M] \cong C$ where C is the sample concentration. Since $Cf = 2[D]$, we have $f = k'C$. We demand that the values of f obtained on the basis of eq 4 for Cu–DIPA in chloroform be proportional to the sample concentration, if our model is to be valid. The obtained variation of f is shown in Figure 11. The necessary correction factor which needs to be applied to $\Delta\nu_{ms}$ in eq 4 to yield the results shown in Figure 11 was obtained by computer simulation of the observed line shapes using a mixed shape $AL^2 + BG^2$. Good agreement with observed line shapes was found for $A = 0.7$ to 0.8 and $B = 0.3$ to 0.2 corresponding to a correction factor of about 1.6 (see Appendix). The points shown in Figure 11 should follow a straight line through the origin. The slight deviation from this linearity for the points corresponding to small broadening arises from difficulty in exact $\Delta\nu_{ms}$ as well as correction factors in the region of small broadening. The points corresponding to larger broadening ($C \gtrsim 6 \times 10^2$ *M*) are more reliable and follow the expected linearity, indicating that the "excess broadening" of Cu–DIPA in chloroform is due to dimerization.

We have ignored the possibility of occurrence of trimers and higher aggregates. Suppose we assume that the molecules stack in these clusters, which would seem resonable in view of the molecular geometry. One would obtain broadening given by factors $(4/3)^3f/\Delta_d^6$ and $(3/2)^4f/\Delta_d^6$ as compared to $^2f/\Delta_d^6$ for dimers, left superscripts on f denoting trimers, tetramers, and dimers, respectively. It is most unlikely that the trimer and tetramer formation constants ^3k and ^4k are much larger than the dimerization constant ^2k. But ^3f and ^4f depend on C^2 and C^3, respectively (C = sample concentration), and can therefore be confidently expected to be very substantially smaller than ^2f. Thus, higher aggregates contribute little to the line broadening.

Since the distances of closest approach between monomers for the systems studied do not show much variation, the distressing possibility of purely fortuitous coincidence between calculation and experiment arises. To ensure that this is not the case we have also studied the broadening for 2,2,5,5-tetramethyl-3-pyrrolin-1-oxyl-3-carboxylic acid *N*-hydroxysuccinimide ester free radical. Concentrations in chloroform solution ranged from 10^{-4} to 4×10^{-2} *M*. For this free radical the distance of closest approach ζ was computed to be about 12 Å, quite different from that of the copper compounds. Broadening was found to be appreciable in the concentration range $C \gtrsim 10^{-2}$ *M*. Experimental values of $\Delta\nu_{ms}$ were 2.2 and 4 G at 1.2×10^{-2} and 4×10^{-2} *M*, respectively. The line shapes were approximately 50% Gaussian according to our mixed Gaussian-square Lorentzian procedure. The corresponding correction factor of about 1.5 must be applied to the above values for comparison with values calculated from eq 3. Calculated values of 3.6 and 6.5 G for the above concentrations, respectively, were found from eq 3. These are preliminary results. A more detailed study on a number of free radicals will be reported in a later paper.

Assumptions in the "Rigid Liquid" Model

The reasonably close agreement between calculated and observed line broadening for the copper compounds and the free radical case and the obtained $f \simeq kC$ dependence for dimerization indicate the validity of the utilized model. Preceding acceptance of the validity, however, some of the assumptions made in the development of the model need closer scrutiny.

Regarding the distance of closest monomer approach ζ, one might alternately proceed as follows. The minimum distance can be obtained by considering two copper chelate molecules rotating about their long axes and situated near each other such that no solvent molecules are interposed between them. The distance ζ would correspond to about four sulfur van der Waals radii, *i.e.*, about 7.5 Å for chloroform solution. One could instead assume parallel planes of two chelate molecules separated by a monomolecular layer of tumbling solvent molecules yielding $\zeta \sim 10$ Å for chloroform solution. This latter method of computation of ζ represents perhaps the best approximation to reality. The former alternative is unlikely in view of the results of Table I since a definite solvent dependence is observed.

The viscosity should not enter in terms of our model. Moreover, the viscosity of bromoform is considerably higher than that of chlorobenzene, yet the broadening is smaller. In any event, the alternative of rotating chelates would result in an increase of calculated broadening of only a factor 1.2, the alternative involving tumbling solvent molecules would result in a decrease of calculated broadening by a factor of roughly 1.2. The details of the model employed for estimation of ζ thus produces no drastic variation in

computed broadening as seen in Table I. If one is satisfied with an approximate prediction of the line width at a given concentration or if one allows for a semiempirical determination ζ, these details are not crucial. The variation with concentration is not affected, remaining proportional to $C^{1/2}$ in absence of dimerization.

A somewhat more serious problem might be the tumbling of a dimer, which was neglected in our formulation. To ensure that this assumption is not catastrophically unwarranted we return to the theory of Bloembergen, Purcell, and Pound and consider the ratio $2\tau_c/T_2''$ with $T_2' \rightarrow T_2''$ and T_2'' corresponding to the rigid lattice picture. If this ratio is substantially larger than 1, then the rigid liquid approach taken is valid and the dimer tumbling can be ignored. The dimer case is described by our model when f is set equal to 1, near-Lorentzian shape is assumed, and the term involving $NC\zeta^{-3}$ is dropped in eq 4 yielding $\Delta\nu_{ms} \sim 200$ G. This corresponds to $1/T_2'' \sim 10^{10}$ sec^{-1}. For the radius of the tumbling dimer we take an approximate configuration of eight sulfur atoms forming a cube yielding $a \gtrsim 10$ Å. A correlation time $\tau_c \gtrsim 10^{-9}$ results. The above ratio is then substantially larger than 1 and dimer tumbling is apparently not important. We note that the use of $e^{-\xi}\,d\xi$ underestimates the broadening somewhat, so that motional narrowing, which undoubtedly takes place to some extent, even though a strong averaging out of the secular dipolar interactions does not result, is at least partially compensated for.

Variation of Line Shape with Concentration

The fact that the line shapes for Cu–DIPA in chloroform become more Lorentzian in appearance at the higher concentrations, where dimerization becomes appreciable, suggests the possibility that exchange, which has been ignored so far, might be important. In terms of the evaluation of $\langle\Delta\nu^2\rangle_{av}$ this interaction does not figure because of commutation relations.[2] Should exchange not be significant, however, then our model must also be capable of predicting a tendency toward more nearly Lorentzian line shape as the sample concentration increases. This tendency is described by increase of the ratio $\langle\Delta\nu^4\rangle_{av}/[\langle\Delta\nu^2\rangle_{av}]^2$ as the line shape becomes more nearly Lorentzian. The terms involved in $\langle\Delta\nu^4\rangle_{av}$ are of the form[3] $B_{jk}{}^2B_{jl}{}^2$, $B_{jk}{}^2B_{jl}B_{kl}$ and $B_{jk}{}^4$. We have (Σ_{jk}' meaning that $j \neq k$)

$$\sum_{jkl}' B_{jk}{}^2B_{jl}{}^2\Big/\left(\sum_{jk}' B_{jk}{}^2\right)^2 \sim \sum_{jkl}' B_{jk}{}^2B_{jk}B_{kl}\Big/\left(\sum_{jk}' B_{jk}{}^2\right)^2 \sim \frac{4\pi NC}{3\zeta^3}\left[\frac{4\pi NC}{3\zeta^3} + \frac{f}{\Delta_d{}^6}\right]\left[\frac{4\pi NC}{3\zeta^3} + \frac{f}{\Delta_d{}^6}\right]^{-2} \sim 0.3$$

for Cu–DIPA in chloroform at 10^{-1} M *vs.* 1.0 at low concentrations, and

$$\sum_{k>j} B_{jk}{}^4\Big/\left(\sum_{jk}' B_{jk}{}^2\right)^2 \sim \left[\frac{4\pi NC}{3\zeta^3} + \frac{1}{f}\left(\frac{f}{\Delta_d{}^6}\right)\right]^2\Big/\left[\frac{4NC}{3\zeta^3} + \frac{f}{\Delta_d{}^6}\right]^2 \sim \frac{1}{4f} \sim 60$$

for Cu–DIPA in chlorofrom at 10^{-1} M *vs.* 1 at the lower concentrations. As a result of the latter term the ratio $\langle\Delta\nu^4\rangle_{av}/[\langle\Delta\nu^2\rangle_{av}]^2$ increases appreciably, indicative of tendency toward Lorentzian line shape.

In order to estimate the importance of exchange we have computed Cu–Cu and Cu–S[25] overlap integrals as function of internuclear distance. These are shown in Figures 12 and 13. The Cu–S overlap could conceivably enter through a second-order effect. The small values of the overlap integrals at the internuclear distances for the copper dithiocarbamates indicate that exchange is not appreciable. The magnetic dipolar interactions alone are not sufficiently strong to destroy the validity of the individual Cu electron spin quantum number, since the magnitude of the spin–spin interaction between two copper atoms separated by ~3.5 Å is much smaller than the Zeeman splitting and can therefore be thought of as a small perturbation. We need, therefore, not be concerned with the formation of triplet species.

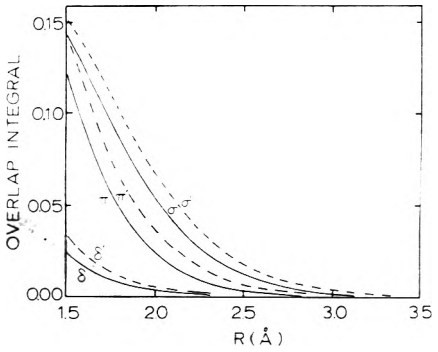

Figure 12. Copper–copper d–d overlap integrals as a function of internuclear distance. The primed σ, π, and δ overlap lines were calculated using an orbital exponent reduced 5% from that for the free ion. Slater orbitals with an exponent equal to 3.080 were employed.

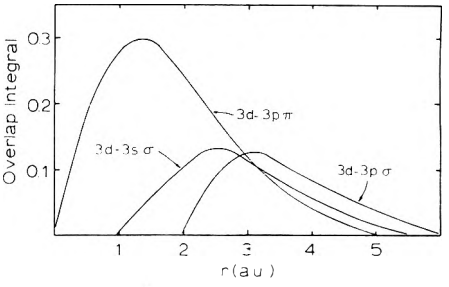

Figure 13. Copper–sulfur overlap integrals. Slater orbital exponents are Cu-μ_{3d} = 3.080; S-μ_{3s} = 2.1223; S-μ_{3p} = 1.8273.

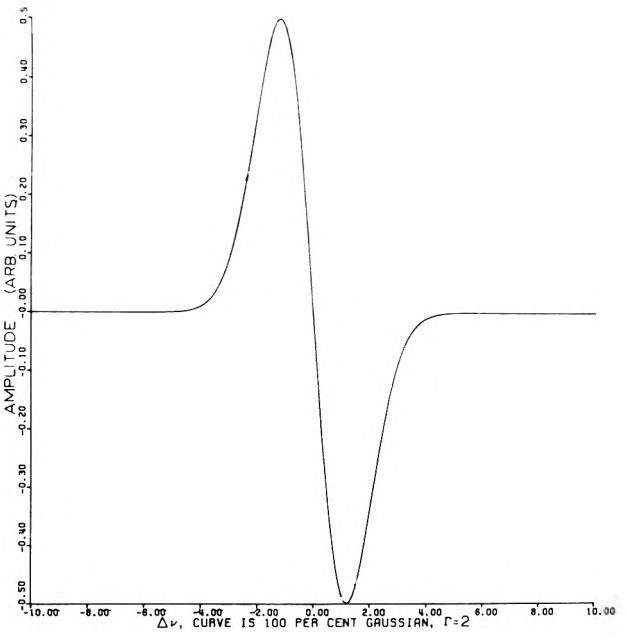

Figure 14. Mixed Gaussian–square-Lorentzian derivative shape with 100% Gaussian contribution. $\Gamma = 2$.

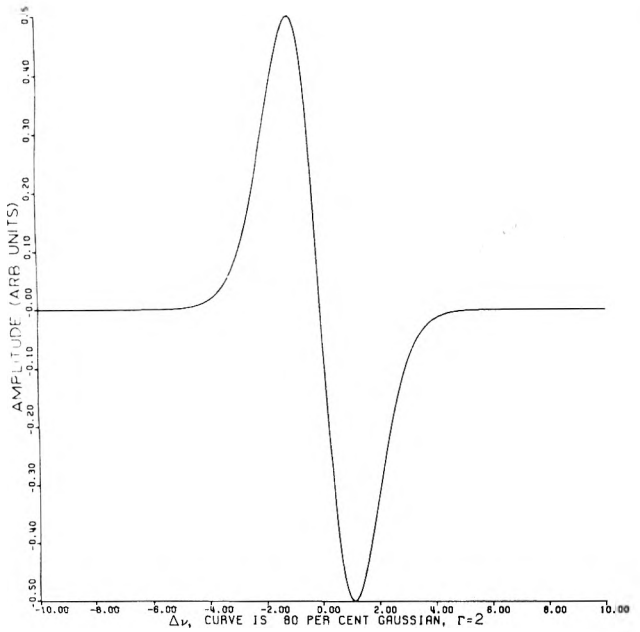

Figure 15. Mixed Gaussian–square-Lorentzian derivative shape with 80% Gaussian contribution. $\Gamma = 2$.

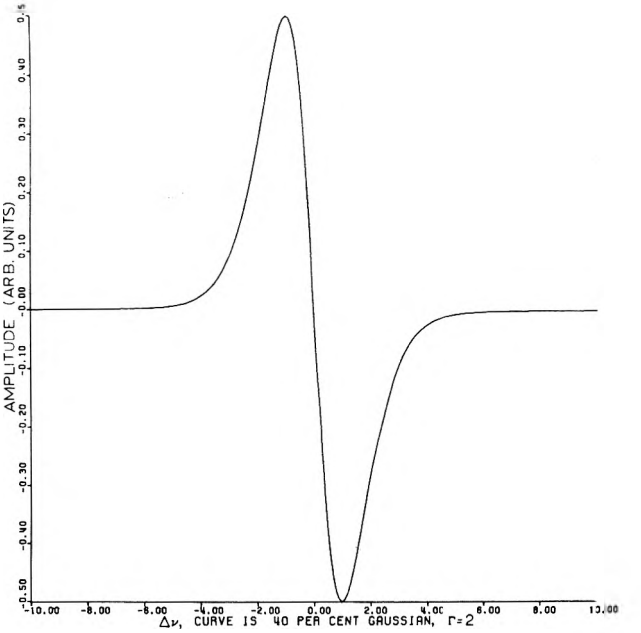

Figure 17. Mixed Gaussian–square-Lorentzian derivative shape with 40% Gaussian contribution. $\Gamma = 2$.

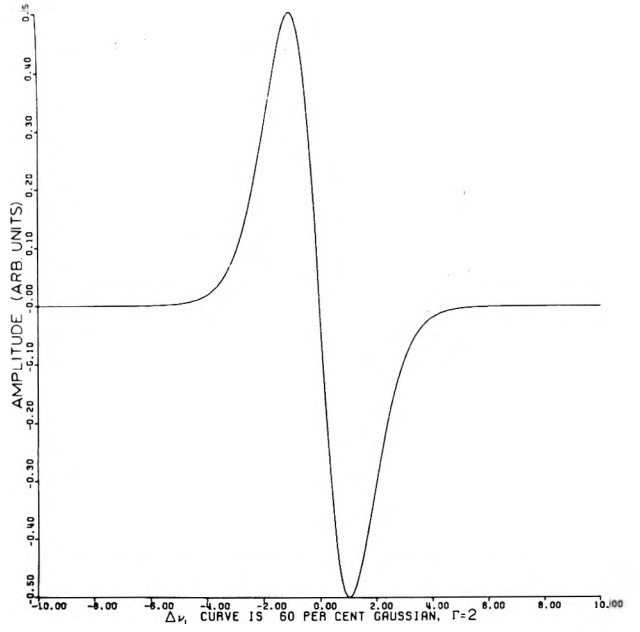

Figure 16. Mixed Gaussian–square-Lorentzian derivative shape with 60% Gaussian contribution. $\Gamma = 2$.

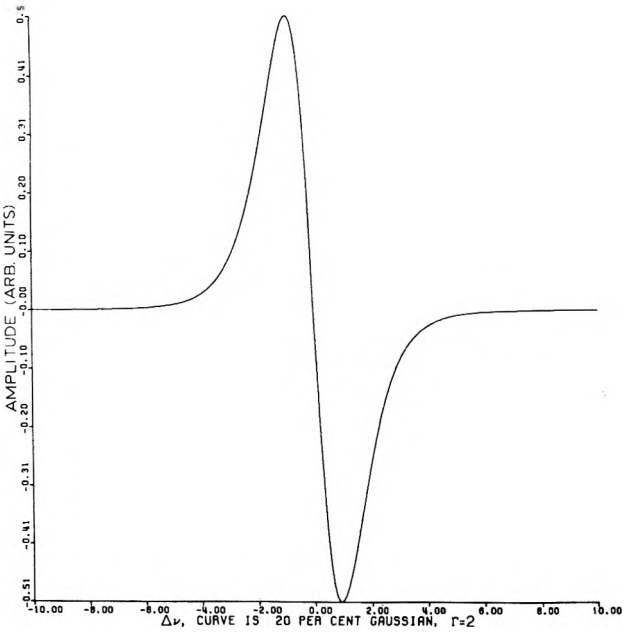

Figure 18. Mixed Gaussian–square-Lorentzian derivative shape with 20% Gaussian contribution. $\Gamma = 2$.

Mixed Line Shapes

Changes in line shapes can be accommodated in our model by multiplication of the measured $\Delta\nu_{ms}$ by a suitable correction factor. The corrected $\Delta\nu_{ms}$ can then be used directly in the left side of eq 3. The correction factor is obtained by the use of the L^2 line shape which approximates the Lorentzian shape closely in terms of the derivative spectra. If the line shape is very nearly Lorentzian a correction factor $\sqrt{5}$ obtains. To facilitate the treatment of mixed line shapes, where the correction factors lie between 1 and $\sqrt{5}$, we have computer simulated mixed L^2–G^2 shapes, with Gaussian contribution varying from 0 to 100% in steps of 10% and square Lorentzian contribution varying correspondingly from 100 to 0%. Both shapes were set to have maximum amplitude 1 and the same parameter Γ. With appropriate scaling of experimentally found line shapes by straight superposition onto the computer plots we found invariably a reasonably close match with one of the computer plots. In the Appendix such simulated mixed shapes are shown with Gaussian contribution (see Figures 14–19) varying in steps of 20% (which we found to be sufficiently small steps for reasonably close approximation to observed shape). For obvious reasons we have kept the number of plots shown in the Appendix at a reasonable minimum. If more accurate fit to experimental shapes is desired the parameter Γ need not be the same for G^2 and L^2. One could consider contributions from more than two

TABLE II: Values of $\langle\Delta\nu^2\rangle_{av}$ and $\Delta\nu_{ms}$ for Mixed Gaussian-Square-Lorentzian Line Shapes[a]

% Gaussian contribution	$\langle\Delta\nu^2\rangle_{av}$[b]	$\Delta\nu_{ms}$[c]	Correction factor[d]
100	1.44	2.42	1
80	1.98	2.30	1.22
60	2.48	2.16	1.46
40	3.01	1.95	1.78
20	3.51	1.86	2.02
0	4.00	1.79	2.24

[a] $\Gamma = 2$, see text for discussion. [b] Values of $\langle\Delta\nu^2\rangle_{av}$ can be evaluated exactly once the mixed G^2, L^2 approximation of the line shape is made. [c] Values $\Delta\nu_{ms}$ are obtained from Figures 14-19. [d] $\Delta\nu_{ms} = (2/x)[\langle\Delta\nu^2\rangle_{av}]^{1/2}$.

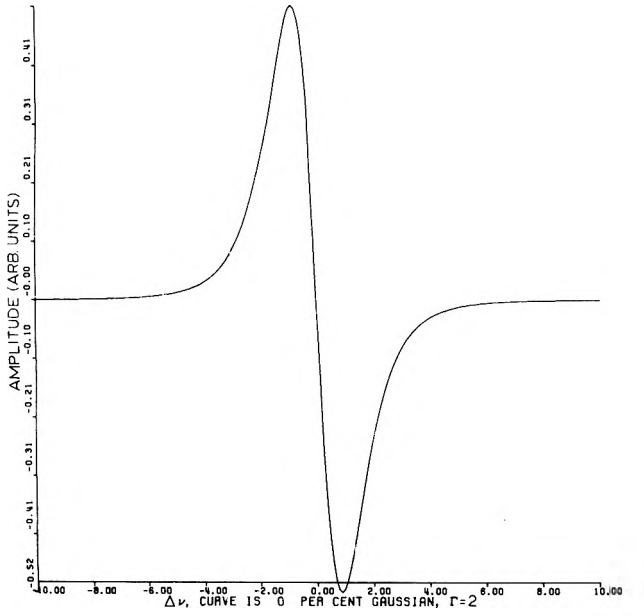

Figure 19. Mixed Gaussian–square-Lorentzian derivative shape with 0% Gaussian contribution. $\Gamma = 2$.

components also. For the mixed shapes shown in the Appendix the corresponding values of $\langle\Delta\nu^2\rangle_{av}$ in units of Γ are given (Table II) to allow straight forward obtention of the correction factors X of $\Delta\nu_{ms}$ which are also given in Table II.

Conclusions

We have set out to and believe to have succeeded in developing a readily usable model for the interpretation of esr line broadening in liquid systems with high concentration of a magnetically active species. The model is based on established theory and reasonable assumptions and is applicable to molecules which are sufficiently large to have motional correlation times which are long, so that intermolecular dipolar interactions are not averaged out. Since the copper dithiocarbamates and the free radical we studied are only of moderate size, the "rigid liquid" model appears to have a wide range of applicability.

Our results indicate that dimerization can be studied by means of esr line broadening, even if dimer concentrations are low, and suggest the possibility of usefulness of line broadening as a means to determine the concentration of elusive magnetic species in solution.

Acknowledgments. The authors are indebted to Mr. William R. Vincent for his capable assistance with the computer programming and plotting and to the Kentucky Tobacco and Health Research Board for research support.

Appendix

Figures 14–19 and Table II given herein are designed to facilitate interpretation of esr line broadening in those cases, where line shapes are nearly Lorentzian or intermediate between Gaussian and Lorentzian. As discussed previously, the Lorentzian shape is approximated by the square-Lorentzian function $L^2 = [\Gamma^2/(\Gamma^2 + \nu^2)]^2$. Mixed line shapes are simulated by plots of the function $A\,dL^2 + B\,dG^2$, where G^2 is given by $e^{-2\ln 2\nu^2/\Gamma^2}$ and where dL^2 and dG^2 are the respective derivatives. A and B are the percentages of contribution by dL^2 and dG^2 to the mixed shape. In Figures 14–19, A varies from 0 to 100% in steps of 20%, B varies correspondingly from 100 to 0%. Γ was arbitrarily set to 2. The figures were calculated and plotted by computer. The corresponding values of $\langle\Delta\nu^2\rangle_{av}$ can be evaluated by hand. Suitably scaled experimental lines can be superposed onto the mixed shapes shown here to hopefully allow a sufficiently close match yielding the appropriate correction factor to be used in conjunction with eq 3. This is done by taking $\Delta\nu_{ms}$ from the computer plot which matches an experimental line and the corresponding $\langle\Delta\nu^2\rangle_{av}$. Then, $\Delta\nu_{ms} = (2/x)[\langle\Delta\nu^2\rangle_{av}]^{1/2}$ and x is the appropriate correction factor.

References and Notes

(1) N. Bloembergen, E. M. Purcell, and R. V. Pound, *Phys. Rev.*, **73**, 679 (1948).
(2) J. H. Van Vleck, *Phys. Rev.*, **74**, 1168 (1948).
(3) C. Kittel and E. Abrahams, *Phys. Rev.*, **90**, 238 (1953).
(4) M. H. L. Pryce and K. W. H. Stevens, *Proc. Phys. Soc., Ser. A*, **63**, 36 (1950).
(5) R. Kubo and K. Tomita, *J. Phys. Soc. Jap.*, **9**, 888 (1954).
(6) P. W. Anderson, *J. Phys. Soc. Jap.* 9, 316 (1954).
(7) H. M. McConnell, *J. Chem. Phys.*, **25**, 709 (1956).
(8) D. Kivelson, *J. Chem. Phys.*, **33**, 1094 (1960).
(9) A. Hudson and G. R. Luckhurst, *Chem. Rev.*, **69**, 191 (1969), and references cited therein; L. T. Nuus and P. W. Atkins, Ed., "Electron Spin Relaxation in Liquids," Plenum Press, New York, N.Y., 1972; P. W. Atkins, *Advan. Mol. Relaxation Processes*, **2**, 121 (1972).
(10) H. Sillescu, *J. Chem. Phys.*, **54**, 2110 (1971).
(11) For example, J. C. Gill, *J. Phys. C.: Solid State Phys.*, **4**, 1720 (1971); G. W. Canters and C. S. Johnson, Jr., *J. Magn. Resonance*, **6**, 1 (1972).
(12) For example, T. A. Miller and R. N. Adams, *J. Amer. Chem. Soc.*, **88**, 5713 (1966); J. C. Danner and T. R. Tuttle, Jr., *ibid.*, **85**, 4052 (1963); M. T. Jones, *J. Chem. Phys.*, **38**, 2892 (1963).
(13) S. J. Wyard, *Proc. Phys. Soc.*, **86**, 587 (1965).
(14) H. Yokoi and T. Isobe, *Bull. Chem. Soc. Jap.*, **44**, 1446 (1971); **46**, 447 (1973); M. Chikira and T. Isobe, *ibid.*, **45**, 3006 (1972).
(15) A. D. Toy, S. H. H. Chaston, J. R. Pilbrow, and T. D. Smith, *Inorg. Chem.*, **10**, 2219 (1971).
(16) H. Yokoi and T. Isobe, *Chem. Lett.*, 95 (1972).
(17) A. D. Toy, M. D. Hobday, P. D. W. Boyd, T. D. Smith, and J. R. Pilbrow, *J. Chem. Soc., Dalton Trans.*, 1259 (1973), and references therein.
(18) J. F. Villa and W. E. Hatfield, *Inorg. Chem.*, **10**, 2038 (1971); J. F. Villa and W. E. Hatfield, *Inorg. Chim. Acta*, **5**, 145 (1971); G. O. Carlisle, G. D. Simpson, and W. E. Hatfield, *Inorg. Nucl. Chem. Lett.*, **9**, 1247 (1973).
(19) For example, G. D. Thorn and R. A Ludwig, "The Dithiocarbamates and Related Compounds," Elsevier, Amsterdam, 1962.
(20) L. De Salles de Hys, H. E. Francis, G. L. Seebach, and J. R. Wasson, "ESR Spin Trapping Studies of Cigarette Smoke," Tobacco and Health Research Workshop, Lexington, March 26–28, 1973 (Abstracted in "Directory of On-Going Research in Smoking and Health" published by the U. S. Department of Health, Education and Welfare).
(21) J. F. Gibson, *Trans. Faraday Soc.*, **60**, 2105 (1964).
(22) A. A. Shklysev, F. M. Bumerov, and V. F. Anufrienko, *Zh. Strukt. Khim.*, **13**, 406 (1972).
(23) Th. Förster, *Ann. Phys.*, **2**, 55 (1943).
(24) A. K. Gregson and S. Mitra, *J. Chem. Phys.*, **49**, 3696 (1968).
(25) E. R. Menzel, D. R. Lorenz, and J. R. Wasson, to be submitted for publication.
(26) E. R. Price and J. R. Wasson, *J. Inorg. Nucl. Chem.*, **36**, 67 (1974).

Fluorine-19 and Hydrogen Contact Shifts of Lewis Acids Hydrogen Bonded to a Stable Free Radical. Non-Curie Law Behavior[1]

Roger E. Cramer,* Phillip L. Dahlstrom, and Hilda Heya

Department of Chemistry, University of Hawaii, Honolulu, Hawaii 96822 *(Received June 5, 1974)*

The possible sources of the non-Curie law behavior for the temperature dependence of the contact shifts induced by the spin labeling of Lewis acids with the stable free-radical 2,2,6,6-tetramethylpiperidine nitroxide have been investigated. The probable cause is the temperature dependence of the hyperfine coupling constants which results from varying populations of thermally excited vibrational states over the temperature range available for investigation.

Introduction

Contact shifts induced by the spin labeling of solvent molecules with a stable organic free radical can be a powerful tool for the investigation of weak intermolecular interactions. Unfortunately the shifts found for one such system[2] have been reported to deviate badly from the zero intercept predicted for the expected Curie law behavior, thus complicating their interpretation. In addition, while Morishima, *et al.*[3] have reported that ^1H and ^{13}C contact shifts of this kind have the expected Curie law temperature dependence, in fact, the contact shifts which they report have a linear $1/T$ relationship but a nonzero intercept. Because of the importance of hydrogen bonding and the potential usefulness of this technique, it is of some interest to determine the cause of this non-Curie law behavior. To this end we report here the results of a study of the ^1H and ^{19}F contact shifts induced by the interaction of the series of simple fluorophenols with the 2,2,6,6-tetramethylpiperidine nitroxide free radical.

Experimental Section

The alcohols, *m*-fluorophenol (MFP), o-fluorophenol (OFP), and 1,1,1,3,3,3-hexafluoro-2-propanol (HFIP), were obtained from Pierce Chemical Co. at the highest purity available. They were dried over Linde type 4A molecular sieves then distilled with only the middle fraction used. The solid *p*-fluorophenol (PFP, Pierce) was sublimed twice under vacuum. The purified alcohols were stored in light-tight containers over P_2O_5 under refrigeration. Methylcyclohexane (MCH, Aldrich), *p*-fluoroanisole (PFA, Aldrich), *m*-fluoroanisole (MFA, Aldrich), *o*-fluoroanisole (OFA, PCR, Inc.) 3,3,5,5-tetramethylcyclohexanone (TMCH, Pfaltz and Bauer), and cyclohexane (MCB) were dried over Linde type 4A molecular sieves for several days prior to use.

The free radical, 2,2,6,6-tetramethylpiperidine nitroxide (TMPNO), was prepared by the method of Briere, Lemaire, and Rassat.[4] The crude product was purified by elution through a chromatography column of neutral activated alumina with 20% diethyl ether in cyclohexane. The middle fraction was collected and the solvent removed under vacuum. The resulting free radical was sublimed under vacuum at room temperature and stored in the manner previously described.

Samples were prepared under anhydrous conditions in a drybox supplied with dry air from a Pall Trinity Micro Corp. Model 10HA1 air drier.

Nmr spectra were recorded on a Varian HA-100 spectrometer. Proton chemical shifts were obtained at 100.0 MHz, ^{19}F chemical shifts were obtained at 94.1 MHz. Temperatures were measured directly to $\pm 0.5°$ by means of a thermocouple inserted in the variable-temperature probe of the spectrometer by a modification previously reported.[5] Proton chemical shifts were measured relative to internal TMS (10% v/v). ^{19}F chemical shifts were measured relative to the appropriate *o*-, *m*-, or *p*-fluoroanisole as an internal standard with the spectrometer locked on an external capillary of 1,4-dibromotetrafluorobenzene–toluene or perfluorocyclohexene.

Visible spectra were recorded on a Beckman DB-G spectrophotometer.

The volume magnetic susceptibility of the TMPNO free radical was measured by the nmr method reviewed by Mulay.[6] TMPNO was dissolved in methylcyclohexane containing approximately 10% (v/v) TMS. The paramagnetic sample was placed in a sealed capillary centered in the nmr sample tube with pieces of Teflon. The outer portion of the sample tube contained only the solvent mixture.

The equilibrium quotient and limiting chemical shift for a 1:1 complex were determined from the concentration dependence of the chemical shifts in the fast exchange region by use of a computer program[7] which utilizes an iterative minimization procedure.[8]

Results and Discussion

The isotropic nmr shift is expressed as the difference between the chemical shift in a paramagnetic system and in a closely analogous diamagnetic system.

$$\Delta\nu_{iso} = \Delta\nu_{para} - \Delta\nu_{dia} \quad (1)$$

Since the dipolar contribution to the isotropic shift is negligible for organic free radicals, the entire shift can be considered a Fermi contact shift.

The choice of a suitable diamagnetic reference base for TMPNO presents a difficult problem. The most suitable candidate we were able to envision, which was commercially available, was TMCH. Taft and coworkers[9] have found the ^{19}F nmr of PFP to be a very sensitive probe of the interactions of the hydroxyl group. We observe substantial ^{19}F chemical shifts for PFP on addition of either the diamagnetic, TMCH, or paramagnetic, TMPNO, proton acceptor. The concentration dependence of the fluorine chemical shifts for 0.1 *M* PFP with TMCH and with TMPNO was analyzed *via* the computer program to deter-

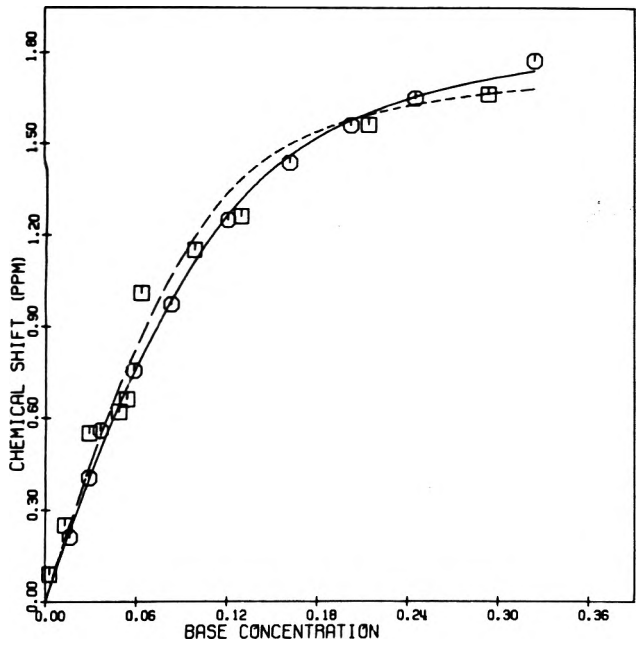

Figure 1. Plot of the theoretical concentration dependence of the ^{19}F chemical shifts for 0.1 *M* PFP with TMPNO (- - - -) and TMCH (——): (○) diamagnetic and (□) paramagnetic experimental data.

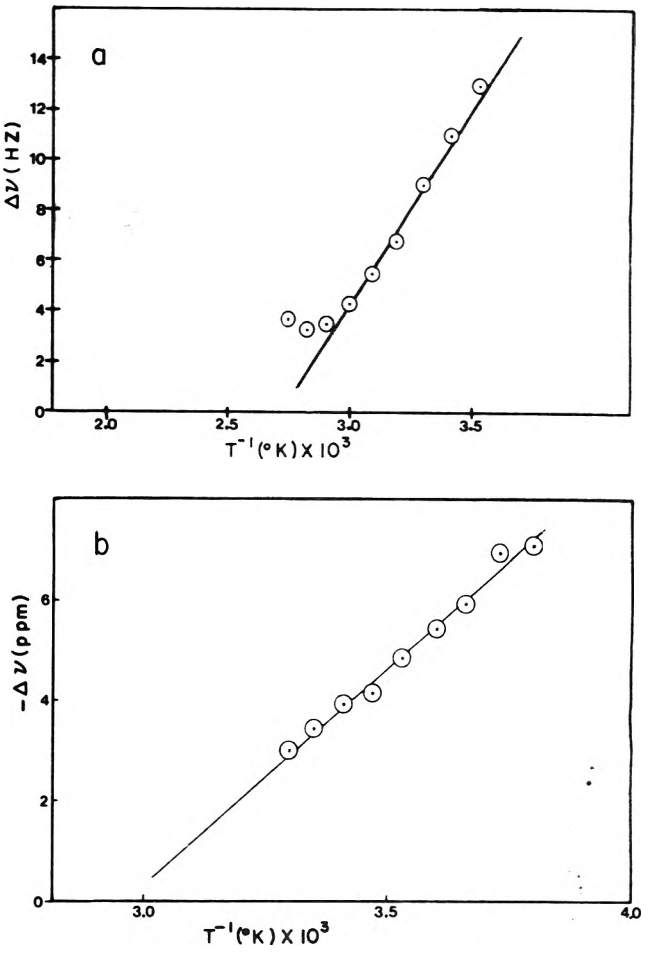

Figure 2. (a) Temperature dependence of the observed hydroxyl proton contact shifts for 0.1 *M* OFP and 5 × 10^{-4} *M* TMPNO, A_0/B_0 = 200. (b) Temperature dependence of the limiting ^{19}F contact shift for the adduct of MFP with TMPNO.

mine the equilibrium quotients and the limiting chemical shifts. The upfield shifts of the fluorine resonance for the diamagnetic and paramagnetic systems reach a limiting value of 1.94 ± 0.09 and 1.8 ± 0.2 ppm, respectively. Thus, within the experimental accuracy, no contact shift is observed for the para fluorine, presumably due to the large distance from the unpaired electron. However, the similarity between the concentration dependence curves (Figure 1) and the existence of the same limiting chemical shift for the diamagnetic and paramagnetic systems indicates very similar interactions with the two bases. We conclude that the choice of TMCH as a diamagnetic reference base for the TMPNO free radical is a fairly good one.

Initially several factors were thought to be possible contributors to the non-Curie law behavior of the contact shifts of the hydrogen bonded Lewis acids. In the region of fast exchange on the nmr time scale, the observed chemical shift is the weighted average of the chemical shifts of the free and complexed acid, and any shift in their ratio as a function of temperature will be reflected in the temperature dependence of the observed shift. The ratio of free to complexed acid is determined by several possible equilibria all of which are temperature dependent. These equilibria include the formation of the 1:1 adduct itself, the self-association of the acid, and equilibria involving adducts of other than 1:1 stoichiometry. In other paramagnetic systems which have previously been studied,[10] shifts in equilibria have been found to be large enough to produce substantial deviations from the expected Curie law temperature dependence. The non-Curie law behavior could also be the result of nonequilibrium phenomena. The paramagnetic susceptibility of the free radical itself would be expected to obey the Curie law. If this were not the case, then the isotropic shifts of the adduct would not have Curie law temperature dependence. Lastly, the non-Curie law dependence could be characteristic of the hydrogen-bonding interaction itself.

In order to eliminate the possibility that the nonzero intercept results from self-association of the acid, we studied the OFP–TMPNO and MFP–TMPNO systems. Considerable self-association of OFP at the concentrations studied is indicated by a concentration dependence of the hydroxyl ^{1}H chemical shift. For 0.2 *M* OFP it was found that the temperature dependence of the self-association completely screens any temperature-dependent chemical shift which might be due to the formation of a complex with the diamagnetic reference TMCH. However, the paramagnetic base, TMPNO, produces a contact shift large enough to be measured. A plot of the observed contact shift *vs.* $1/T$ for the hydroxyl proton of 0.1 *M* OFP as determined from the difference of the chemical shifts for the diamagnetic (4 × 10^{-4} *M* TMCH, A_0 (acid concentration)/B_0 (base concentration) = 250) and paramagnetic (5 × 10^{-4} *M* TMPNO, A_0/B_0 = 200) systems is shown in Figure 2a. The linear portion of the curve has an intercept at 268 ± 8 K. The temperature dependence of the observed hydroxyl proton contact shift was obtained in a similar manner for solutions of diamagnetic and paramagnetic bases with 0.17 *M* MFP (A_0/B_0 = 400). The linear plot (Figure 3a) has an intercept on the temperature axis at 262 ± 9 K. These intercepts are very similar to the 235 ± 2 K intercept reported by Lim and Drago[2] for neat trifluoroethanol and TMPNO (A_0/B_0 ≃ 210) for which the acid is very highly associated. The

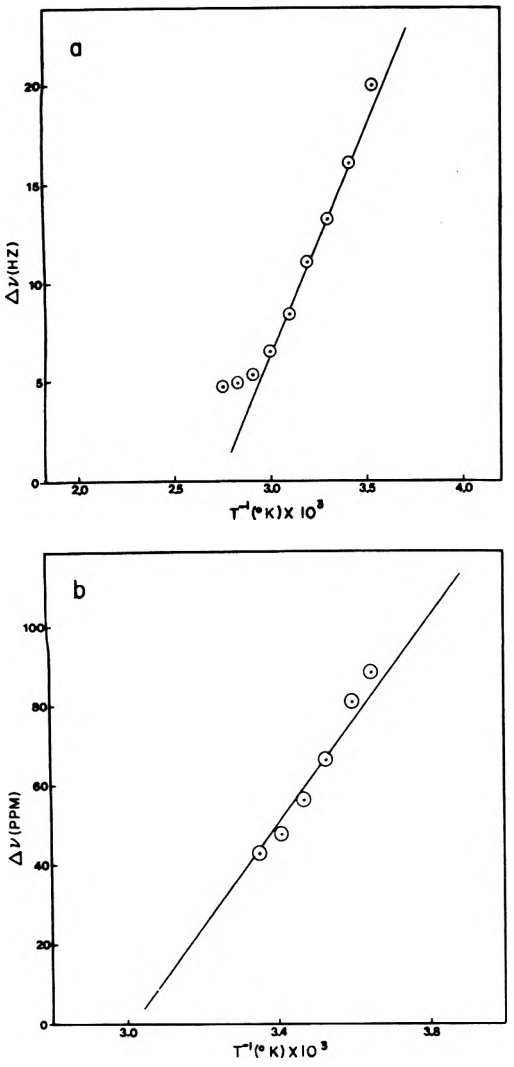

Figure 3. (a) Temperature dependence of the observed proton contact shift for 0.17 *M* MFP and 4 × 10^{-4} *M* TMPNO, A_0/B_0 = 400. (b) Temperature dependence of the limiting proton contact shift for the adduct of MFP with TMPNO.

fact that similar intercepts result from both the neat solution and in our relatively dilute ones indicates that no significant deviation from Curie law dependence is produced by self-association.

While the data in both Figures 2a and 3a produce good straight lines, the last two or three points in each case show some curvature. The magnitude of the deviation could be accounted for by the decrease in the equilibrium quotient at the higher temperatures, but the deviation is in the wrong direction. It is possible that the curvature may be due to some systematic error occurring in the high temperature region. However the curvature may well be real since extrapolation of the linear portion of the curve through zero shift to very high temperature leads to the unrealistic prediction of increasing shift with increasing temperature. A study in a higher boiling solvent would be needed to resolve this point.

In order to eliminate the possiblility that the nonzero intercept might be caused by the temperature dependence of the hydrogen-bonding equilibrium quotient, one can plot the limiting chemical shifts rather than those observed in the fast exchange region. Techniques for the determination of both the equilibrium quotient and the limiting chemical

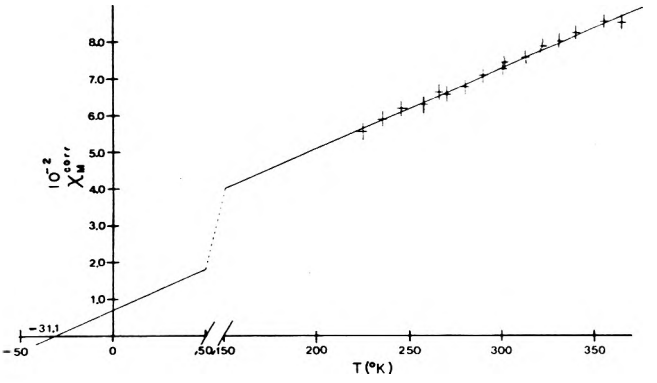

Figure 4. Temperature dependence of the paramagnetic susceptibility of 0.102 *M* TMPNO.

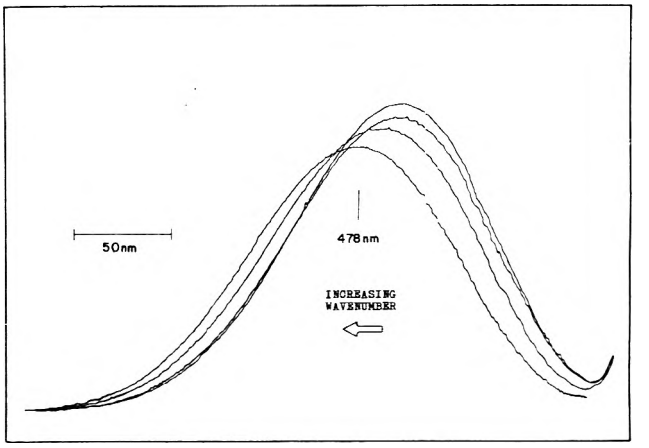

Figure 5. Isosbestic point for the n → π* absorption of 0.0228 *M* TMPNO with HFIP.

shift are well known and have been discussed elsewhere.[11] The applicable method requires that the chemical shift be followed over a wide range of acid–base ratios. Unfortunately addition of TMPNO rapidly broadens the hydroxyl proton resonance precluding a study over the necessary concentration range. One way to overcome this difficulty is to utilize nuclei which are at a greater distance from the unpaired electron and whose signals are consequently broadened to a lesser extent. Since shifts as large as possible are also desirable, and since contact shifts of ^{19}F substituents are generally larger than those of corresponding ^{1}H substituents, ^{19}F nmr is favorable for such studies.

The monofluorophenols were chosen as a well-characterized group of hydrogen-bonding Lewis acids which meet these requirements. However no contact shift was observed for PFP, *vide supra*, and the ^{19}F resonance of OFP broadened too rapidly with addition of TMPNO to permit study of a suitable range of concentrations. For the remaining member, MFP, sufficiently large shifts and sharp lines were obtained so that the necessary study could be carried out.

^{19}F chemical shifts for 0.1 *M* MFP, with both TMPNO and TMCH added over the concentration range allowed by the line broadening, were measured and the limiting chemical shifts and equilibrium quotients were obtained over a range of temperatures. As expected, the limiting diamagnetic shift is found to be independent of the temperature. The limiting fluorine contact shift was obtained from the difference of the limiting diamagnetic and paramagnetic chemical shifts and its temperature dependence is shown in

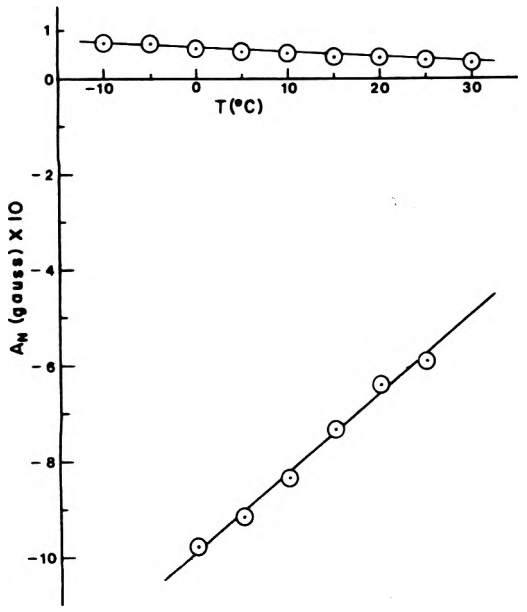

Figure 6. Temperature dependence of the calculated hyperfine coupling constants for the MFP–TMPNO adduct: A_F, upper curve; and A_H for the hydroxyl proton, lower curve.

Figure 2b. The linear plot has an intercept on the temperature axis of 240 ± 5 K.

With the equilibrium quotient obtained from the ^{19}F study the concentration of both the 1:1 complex and the free acid can be obtained. From this information and the observed hydroxyl proton shifts the limiting hydroxyl shifts can be calculated at those temperatures for which the equilibrium quotient is known. Its temperature dependence yields a linear plot (Figure 3b) with an intercept on the temperature axis of 247 ± 2 K.

For each of these cases, we see that the limiting contact shift has approximately the same intercept on the temperature axis as the observed contact shift. Thus, the temperature dependence of the equilibrium quotient must make no significant contribution to the deviation of the contact shift from Curie law behavior.

In order to eliminate the possibility that the non-Curie law behavior might be due to the magnetism of the free radical, the magnetic suceptibility of a 0.102 M solution of TMPNO in methylcyclohexane was determined over a range of temperatures. The experimentally determined volume susceptibilities were corrected for the temperature dependence of the density of methylcyclohexane.[12] This correction is the major source of error in the nmr determination of the temperature dependence of the magnetic susceptibility and is inherent in the method since the volume susceptibility is the experimentally determined quantity. The molar susceptibilities were corrected for the temperature-independent diamagnetic contribution which was calculated to be -110.4×10^{-4} erg G^{-2} mol^{-1}. A plot of the resulting X_M^{-1} *vs.* T (Figure 4) gives an intercept of −31 ± 8 K. It is seen that the temperature dependence of the paramagnetic susceptibility of the TMPNO free radical follows the Curie law within experimental accuracy.

In order to establish that only a 1:1 adduct is formed in solution we examined the n → π* electronic transition for a 0.0228 *M* solution of TMPNO in *n*-heptane, varying the concentration of HFIP from 0 to 0.0285 *M*. Only one isosbestic point was found, at 491 ± 3 nm (Figure 5). Similar results have been reported for the DTBNO–phenol system.[13] We conclude that only the 1:1 hydrogen bonded complex is important, and formation of adducts of other than 1:1 stoichiometry do not contribute significantly to the non-Curie law behavior of the contact shift.

The evidence presented thus far indicates that the deviation from the expected Curie law behavior of the Fermi contact shift is characteristic of the system. Since it does not occur for the free base but only for the adduct it would seem to be a property of the hydrogen bond. If the adduct were susceptible to temperature-dependent distortions of the hydrogen bond, then the hyperfine coupling constants would be temperature dependent and the contact shifts would show non-Curie law behavior. Using the appropriate values for the magnetic susceptibility of TMPNO and the limiting proton and fluorine contact shifts the appropriate hyperfine coupling constants were calculated from eq 2[10c] at each temperature.

$$\frac{\Delta\nu}{\nu_0} = \frac{-A_n}{Ng_N\beta_N} X_M \qquad (2)$$

The hyperfine coupling constants are seen to exhibit a linear decrease in magnitude with increasing temperature over the range of temperatures studied (Figure 6). Since the source of the deviation of the contact shift from Curie law behavior is proposed to be the hydrogen bond, the effect on both A_H and A_F should be the same. The fact that the temperature dependence of both hyperfine coupling constants have the same intercept on the temperature axis (66 ± 3°) indicates that the same mechanism is indeed affecting both nuclei.

Wiley and Miller[15] have found that in contrast to most chemical shifts, the limiting proton chemical shift of $HCCl_3$ hydrogen bonded to various Lewis bases is temperature dependent. A model which accounts for this temperature dependence was proposed earlier by Muller and Reiter.[16] They note that for weak hydrogen bonds the potential well is shallow and anharmonic with low lying excited vibrational states. As the temperature is increased the population of the excited states is increased causing the bond to lengthen and the magnetic environment of the observed nucleus to approach that of the free acid. While such an effect is relatively small for diamagnetic systems it would be expected to be quite large for paramagnetic systems and such a model is completely in accord with our observations.

Another closely related model, similar to that proposed to account for the temperature dependence of the proton hyperfine coupling constants of the CH_3 radical,[17] could also explain our data. The unpaired spin in the nitroxide is believed to reside in a π orbital.[4] As evidenced by the upfield contact shift, net down spin is placed at the proton. If the hydrogen bond were to bend, the proton could directly overlap the up spin in the nitroxide π orbital thus reducing the net down spin felt at the proton and decreasing the contact shift. Thermal energy would excite such bending modes and produce the observed change in the hyperfine coupling constants.

At this point we cannot select which of these models might be producing the observed trends in the hyperfine coupling constants. It is however clear that the observed effect is real and that it can be accounted for by temperature-dependent distortions of the hydrogen bond.

References and Notes

(1) Abstracted in part from the M.S. thesis of P.L.D., 1973, University of Hawaii, Honolulu, Hawaii 96822.
(2) Y. Y. Lim and R. S. Drago, *J. Amer. Chem. Soc.*, **93**, 891 (1971).

(3) (a) I. Morishima, K. Endo, and T. Yonezawa, *Chem. Phys. Lett.*, **9**, 203 (1971); (b) *J. Amer. Chem. Soc.*, **93**, 2048 (1971); (c) I. Morishima, T. Inubushi, K. Endo, T. Yonezawa, and K. Goto, *ibid.*, **94**, 4812 (1972); (d) I. Morishima, K. Endo, and T. Yonezawa, *J. Chem. Phys.*, **58**, 3146 (1973).
(4) R. Briere, H. Lemaire, and A. Rassat, *Bul. Soc. Chim. Fr.*, **11**, 3273 (1965).
(5) P. L. Dahlstrom, J. L. Loo, and R. L. Harris, *J. Magn. Resonance*, in press.
(6) L. N. Mulay, "Magnetic Susceptibility," Interscience, New York, N.Y., 1963.
(7) (a) F. L. Slejko, R. S. Drago, and D. G. Brown, *J. Amer. Chem. Soc.*, **94**, 9210 (1972); (b) T. D. Epley, Ph.D. Thesis, 1967, University of Illinois, Urbana, Ill. 61801.
(8) The general minimization routine, SIMPLEX, has been copyrighted by J. P. Chandler of the University of Indiana, 1965.
(9) R. W. Taft, E. Price, I. R. Fox, I. C. Lewis, K. K. Anderson, and G. T. Davis, *J. Amer. Chem. Soc.*, **85**, 3146 (1963).
(10) (a) G. N. La Mar and E. O. Sherman, *J. Amer. Chem. Soc.*, **92**, 2691 (1970); (b) M. F. Rettig and R. S. Drago, *ibid.*, **88**, 2966 (1966); (c) W. D. Perry and R. S. Drago, *ibid.*, **93**, 2183 (1971).
(11) D. A. Deranleau, *J. Amer. Chem. Soc.*, **91**, 4044 (1969).
(12) (a) G. Egloff, "Physical Constants of Hydrocarbons," Vol. 2, ACS Monograph Series, Reinhold, New York, N.Y., 1940; (b) J. Timmermans, "Physico-Chemical Constants of Pure Organic Compounds," Elsevier, New York, N.Y., 1950.
(13) Y. Murata and N. Mataga, *Bull. Chem. Soc. Jap.*, **44**, 354 (1971).
(14) C. J. Jameson and H. S. Gutowsky, *J. Chem. Phys.*, **51**, 2790 (1969).
(15) R. Wiley and S. I. Miller, *J. Amer. Chem. Soc.*, **94**, 3287 (1972).
(16) N. Muller and R. C. Reiter, *J. Chem. Phys.*, **42**, 3265 (1965).
(17) I. A. Zlochower, W. R. Miller, Jr., and G. K. Fraenkel, *J. Chem. Phys.*, **42**, 3339 (1965).

Computation of the Intermolecular Vibrational Modes of a Tetrahedral Water Pentamer at the Core of an Ice-Like Water Cluster[1]

Lester L. Shipman[2a] and Harold A. Scheraga*[2b]

Department of Chemistry, Cornell University, Ithaca, New York 14853 *(Received May 23, 1974)*

The Shipman–Scheraga intermolecular potential energy function for water (SS potential) has been used to calculate the intermolecular vibrational modes of a tetrahedral water pentamer at the core of an ice-like water 17-mer. The calculated intermolecular vibrational spectrum was compared to the experimental infrared and inelastic neutron scattering spectra of ice I_h. Comparison of the vibrational frequencies of the pentamer at the core of the 17-mer with the vibrational frequencies of a single water molecule at the core of a tetrahedral pentamer water cluster indicates that vibrational coupling among the central water molecule and its four nearest neighbors increases the width of the librational and hindered translational bands, while leaving the mean librational and hindered translational frequencies almost unchanged. Integrated infrared absorptivities have been calculated for each intermolecular normal vibrational mode of the pentamer, and these integrated absorptivities have been summed to give the total integrated absorptivities for the librational and translational bands, for three different models for the calculation of the total dipole moment of the 17-mer. The calculated integrated infrared absorptivities for the hindered translational and librational bands were compared to the corresponding experimental values for ice I_h.

I. Introduction

The intermolecular vibrational spectrum of ice I_h (ordinary ice) has been investigated experimentally by the infrared,[3-14] neutron scattering,[15-29] and Raman[3,30-35] spectroscopic techniques. In addition, there have been several theoretical studies[27,29,36-44] of these intermolecular vibrations.

While most theoretical studies[27,29,36-43] have used harmonic force constant models (O···O···O bending, O···O stretch, etc.), the present study made use of the recently derived[45] Shipman–Scheraga six-dimensional pair potential for water (SS potential). Intermolecular vibrational frequencies have been calculated from the multidimensional intermolecular potential in a manner similar to that of several previous studies.[44,46,47] The aims of the present study were to investigate the effects of vibrational coupling among the central water molecule and its four nearest neighbors in an ice I_h arrangement and to compare several models for the induced dipoles in water in condensed phases. It was not the aim of our study to calculate the *detailed* intermolecular vibrational spectrum of ice I_h; such a calculation would require a consideration of the dynamics of *many* water molecules in a large portion of the ice lattice in order to properly account for long-range coupling; our aim was to obtain an understanding at the molecular level of the effects of short-range coupling on the intermolecular vibrations of water molecules in ice-like environments.

The model used for the study[48] was a 17-mer consisting of a central water molecule, its 4 nearest neighbors, and its 12 next-to-nearest neighbors,[49] with the outer 12 molecules held fixed and the inner core of 5 molecules allowed to undergo intermolecular vibrations. Intramolecular vibrational modes were not considered, and the structure of each monomer was held fixed at the experimental infrared-microwave structure[50] of the water monomer. The proton arrangement of the 17-mer was that of the smallest hexagonal unit cell,[51] C^3_{6V} ($P6_3cm$), for proton-ordered ice I_h. In real ice I_h, the protons are known to be disordered on the basis of entropic considerations[52] and neutron diffraction evidence.[53] This ordered proton arrangement was used (or

all calculations in the present study; Prask, *et al.*,[29] have found that proton-ordered and proton-disordered ice give essentially the same vibrational spectrum. The SS potential was used to calculate the intermolecular normal vibrational modes of the central water molecule and its four nearest neighbors in the field of its 12 fixed next-to-nearest neighbors. The integrated infrared absorptivity was calculated for each of the intermolecular normal vibrational modes of the pentamer under the assumption that the total dipole moment of the 17-mer arose by three different mechanisms, *viz.*, permanent dipoles only, permanent plus molecule-induced dipoles, and permanent plus atom-induced dipoles (see section III for a discussion of these three models).

II. Calculation of the Intermolecular Normal Vibrational Frequencies

The structure of the 17-mer for which the normal vibrational frequencies were calculated was obtained by minimizing the empirical SS intermolecular potential energy[45] with respect to the 30 intermolecular degrees of freedom of the tetrahedral water pentamer at the core of the 17-mer, starting from the proton-ordered ice I_h structure with an O···O distance of 2.7493 Å. This particular distance was chosen previously[45] as an estimate of the O···O distance in real ice I_h at 0°K. The outer 12 molecules of the 17-mer were held fixed for all calculations. The intermolecular degrees of freedom were rotations about the three principal axes for the moments of inertia and translations of the center of mass along three space-fixed cartesian axes (a total of six degrees of freedom per water) for the central water and each of its four nearest neighbors (a total of 30 degrees of freedom). The five molecules (tetrahedral pentamer) that were allowed to rotate and translate during the minimization translated and rotated only very slightly from starting to final positions (the average absolute translation along the cartesian axes was 0.03 Å and the average absolute rotation about the principal axes was 2°).

The harmonic force constant matrix (mass included) was calculated numerically at the minimum-potential-energy structure, and subsequent diagonalization of this matrix gave the normal modes (eigenvectors of the force constant matrix) and normal vibrational frequencies [$1/(2\pi c)$ times the square roots of the eigenvalues of the force constant matrix] in cm^{-1}. The resulting normal vibrational frequencies are given in Table I. Examination of the eigenvectors of the force constant matrix revealed that the first 15 frequencies are predominantly librations, and the last 15 frequencies are predominantly hindered translations. These frequencies may be compared to the normal vibrational frequencies (730, 714, 660, 205, 192, and 188 cm^{-1})[45] for the intermolecular vibrations of the central water molecule in the field of its four fixed nearest neighbors. Vibrational coupling of the central water molecule with its four nearest neighbors increases the width of the librational band from 660–730 to 634–830 cm^{-1}, whereas the mean librational frequency increases only 5 cm^{-1} (from 701 to 706 cm^{-1}). This same coupling increases the width of the hindered translational band from 188–205 to 80–268 cm^{-1}, with a decrease in the mean frequency of only 6 cm^{-1} (from 195 to 189 cm^{-1}). Thus, the effect of this short-range vibrational coupling is to leave the mean frequencies about the same (within 6 cm^{-1}), but increases the width and asymmetry of both the librational and hindered translational bands.

TABLE I: Normal Mode Frequencies and Integrated Absorptivities of a Tetrahedral Pentamer in an Ice-Like Environment

Modes	ω, cm^{-1}	$10^{-6}\int K(\omega)\, d\omega$, cm^{-2}		
		a	*b*	*c*
Librational	830	0.334	0.320	0.186
	803	0.002	0.003	0.002
	792	0.240	0.217	0.131
	728	0.315	0.318	0.200
	718	0.290	0.304	0.208
	715	0.098	0.093	0.057
	705	0.000	0.000	0.000
	690	0.114	0.112	0.077
	690	0.074	0.072	0.046
	689	0.033	0.032	0.024
	666	0.032	0.032	0.019
	656	0.112	0.118	0.067
	641	0.028	0.033	0.017
	636	0.001	0.001	0.000
	634	0.017	0.020	0.010
Hindered translational	268	0.001	0.003	0.005
	262	0.000	0.004	0.009
	258	0.002	0.007	0.012
	208	0.002	0.006	0.010
	202	0.000	0.002	0.006
	199	0.000	0.002	0.008
	186	0.002	0.007	0.011
	184	0.000	0.004	0.011
	182	0.000	0.003	0.006
	180	0.000	0.001	0.001
	179	0.001	0.004	0.007
	169	0.000	0.001	0.004
	100	0.000	0.000	0.000
	83	0.000	0.002	0.002
	80	0.001	0.003	0.004

[a] Permanent dipoles only. [b] Permanent plus molecule-induced dipoles. [c] Permanent plus atom-induced dipoles.

There is general agreement among the inelastic neutron scattering studies[15-29] on ice I_h that the hindered translational band extends from quite low frequencies (<50 cm^{-1}) to 350–450 cm^{-1} and the librational band extends from 350–450 to 1100–1300 cm^{-1}. As expected, because long-range coupling is absent from the present calculation, the calculated band widths are smaller than the experimental band widths; the present results show that there is considerable broadening of the bands as the motions of the water molecules are coupled to the motions of their nearest neighbors, and certainly that further broadening would be expected with the inclusion of longer-range coupling in the calculation.

III. Integrated Infrared Absorptivities

Unlike the inelastic neutron scattering spectrum which is not greatly affected by selection rules, the infrared spectrum of ice I_h differs significantly from the actual frequency distribution because the integrated absorptivity per normal mode is nonuniform across the hindered translational and librational bands. For this reason as well as others, there are significant differences between the inelastic neutron scattering and infrared spectra of ice I_h. The differences are most obvious for the librational band where the

TABLE II: Integrated Absorptivities of the Infrared Spectrum of a Tetrahedral Pentamer in an Ice-Like Environment

Model	Integrated absorptivity $10^{-6}\sum_i \int_{\text{line } i} K(\omega)\, d\omega$, cm^{-2}	
	Libration	Hindered translation
Permanent dipoles	1.690	0.009
Permanent plus molecule-induced dipoles	1.675	0.049
Permanent plus atom-induced dipoles	1.044	0.096
Experimental (for ice I_h)[13]	0.85	0.238

infrared spectrum[9] has a single broad peak with a maximum near 840 cm^{-1}, and the inelastic neutron scattering spectrum[15-29] has one broad peak near 600–690 cm^{-1} and another one near 820–970 cm^{-1}.

The absorptivity, $K(\omega)$, at frequency ω (in cm^{-1}) is related to light intensity as follows:

$$I(\omega) = I_0(\omega) \exp[-K(\omega)l] \tag{1}$$

where the light intensity is I_0 and I, respectively, before and after traveling through a distance l in the medium. The integrated infrared absorptivity over the line corresponding to the ith normal mode is related to the first derivative of the dipole moment of the system, μ, with respect to the ith normal mode, Q_i, as follows:[13]

$$\int_{\text{line } i} K(\omega)\, d\omega = \frac{N_i \pi}{3c^2}\left[\frac{\partial \mu}{\partial Q_i}\cdot\frac{\partial \mu}{\partial Q_i}\right] \tag{2}$$

where N_i is the number of oscillators per unit volume (taken here as one normal mode per volume of five water molecules in ice I_h), and c is the speed of light. The integrated infrared absorptivity of a *band* is obtained by summing over the integrated absorptivities of all the lines in the band. The calculated integrated infrared absorptivities of the various normal modes (for three different models for the dipole moment of the 17-mer; see below) are given in Table I. The calculated and experimental integrated absorptivities for the librational and hindered translational bands are given in Table II. The derivatives, $(\partial\mu/\partial Q_i)$, of the 17-mer were calculated numerically by taking the ratio of the small changes in μ brought about by small changes along Q_i from the equilibrium structure. Three different models were considered for the total dipole moment of the 17-mer, *viz.*, (A) permanent dipoles only, (B) permanent plus molecule-induced dipoles, and (C) permanent plus atom-induced dipoles (see below for a description of these three models).

The calculated integrated absorptivities differ significantly for the various normal modes. In particular, the absorptivity for the librational band is highest at the high-frequency end of the band; this is consistent with the aforementioned qualitative differences between the infrared and inelastic neutron scattering spectra (*i.e.*, the region of the high-frequency inelastic neutron scattering peak at 820–970 cm^{-1} is much more prominent in the infrared spectrum than the region of the 600–690 cm^{-1} inelastic scattering peak). The calculated results in Table II for the librational and hindered translational bands show a tendency to approach the experimental results in going from model A to B to C. Thus, the model of atom-induced dipoles seems to be better than the models of molecule-induced dipoles or no induced dipoles. However, it must be pointed out that the calculated integrated absorptivities are still significantly different from the experimental results even for model C. It is of interest that, for the librations, the calculated values in Table II are higher than the experimental value, and it is clear that the contribution from induced dipoles is in opposition to the contribution from the permanent dipoles. The small nonzero value for model A (permanent dipoles only) for the hindered translational modes arises from weak coupling with the librations, which introduces some librational motion into each predominantly translational mode (for a purely translational mode and permanent dipoles only, $\partial\mu/\partial Q_i$ is the zero vector).

A. Permanent Dipole Moments Only. The dipole moment of the 17-mer was taken as the sum of the permanent dipole moments of the 17 water molecules.

$$\mu = \sum_{i=1}^{17} \mu_i(\text{perm}) \tag{3}$$

The magnitude of the permanent dipole moment was taken as the experimental value[55] of 1.884 D, the same as used in the derivation[45] of the SS potential.

B. Permanent Plus Molecule-Induced Dipole Moments. The dipole moment of the 17-mer was taken as the sum of the permanent dipole moments of each of the 17 water molecules plus the sum of the dipole moments induced in each of the 17 water molecules by the other 16 molecules.

$$\mu = \sum_{i=1}^{17} \mu_i(\text{perm}) + \sum_{i=1}^{17} \mu_i(\text{ind}) \tag{4}$$

where μ_i (ind) was calculated classically[56] using the following formula:

$$\mu_i(\text{ind}) = \alpha \sum_{j=1}^{17}{}' \left\{\frac{3[\mu_j(\text{perm})\cdot\mathbf{R}_{ij}]\mathbf{R}_{ij}}{R_{ij}^5} - \frac{\mu_j(\text{perm})}{R_{ij}^3}\right\} \tag{5}$$

where α is the polarizability of the water monomer (taken as 1.444 $(Å)^3$),[57] $\mathbf{R}_{ij}$ is the vector from the center of mass of molecule i to the center of mass of molecule j, and the primed summation means that the ith term is skipped.

C. Permanent Plus Atom-Induced Dipole Moments. The dipole moment of the 17-mer was taken as the sum of the permanent dipole moments of each of the 17 water molecules plus the sum of the dipole moments induced in each of the 51 atoms of the 17-mer by the charges on the 48 atoms on the 16 other water molecules.

$$\mu = \sum_{i=1}^{17} \mu_i(\text{perm}) + \sum_{i=1}^{51} \mu_i(\text{ind}) \tag{6}$$

where μ_i(ind) was calculated using the following formula:[58]

$$\mu_i(\text{ind}) = -\sum_{j=1}^{51}{}' \frac{\alpha_i \delta_j \mathbf{R}_{ij}}{R_{ij}^3} \tag{7}$$

where δ_j is the charge centered on the jth atom, α_i is the polarizability of the ith atom, and the primed summation means that those terms for the water molecule containing the ith atom are skipped. The δ's for hydrogen and oxygen were taken as $+0.3348e$ and $-0.6696e$, respectively. These charges were chosen to reproduce the experimental permanent dipole moment (1.884 D[55]) of the water monomer at

the experimental infrared-microwave structure[50] of water monomer. The polarizability of hydrogen and oxygen in the water molecule were taken as 0.424 and 0.596 $(Å)^3$, respectively.[59]

V. Conclusions

From the dynamical behavior of a tetrahedral water pentamer at the core of an ice-like 17-mer water cluster, we have shown that the coupling of the motions of a central water molecule with the motions of its four nearest neighbors in an ice-like arrangement broadens the librational and hindered translational bands considerably while hardly shifting the mean frequencies of the two bands. It has been shown that, among the models of permanent dipoles only, permanent plus molecule-induced dipoles, and permanent plus atom-induced dipoles, the model of permanent plus atom-induced dipoles comes closest (under the simple short-range dynamical model used here) to reproducing the experimental integrated infrared absorptivities of the librational and hindered translational bands of ice I_h. It has been shown that the integrated absorptivity across the librational band in the infrared spectrum is quite uneven and the higher integrated absorptivities tend to be at the high-frequency end of the band; this result is consistent with the qualitative difference between the experimental infrared and inelastic neutron scattering spectrum of ice I_h. The present calculations show that some librational modes are essentially invisible to the infrared (*e.g.*, the mode at 803 cm^{-1} has a negligibly small integrated absorptivity). The calculated hindered translational and librational band positions are in approximate agreement with the experimental inelastic neutron scattering spectrum of ice I_h, although the experimental band widths are significantly larger than the calculated band widths. The difference in band widths may reasonably be attributed primarily to the neglect of long-range vibrational coupling in the present calculation.

References and Notes

(1) This work was supported by research grants from the National Science Foundation (GB-28469X3) and from the National Institute of General Medical Sciences of the National Institutes of Health, U.S. Public Health Service (GM-14312).
(2) (a) NIH Postdoctoral Fellow, 1972–1974. (b) To whom requests for reprints should be addressed.
(3) See N. Ockman, *Advan. Phys.*, **7**, 199 (1958), for a review of infrared and Raman studies published before October, 1957.
(4) D. F. Hornig, H. F. White, and F. P. Reding, *Spectrochim. Acta*, **12**, 338 (1958).
(5) N. Ockman and G. B. B. M. Sutherland, *Proc. Roy. Soc., Ser. A*, **247**, 434 (1958).
(6) C. Haas and D. F. Hornig, *J. Chem. Phys.*, **32**, 1763 (1960).
(7) R. Zimmerman and G. C. Pimentel, *Proc. Int. Meeting Molecular Spectrosc.*, **2**, 726 (1962).
(8) P. A. Giguere and J. P. Arraudeau, *C. R. Acad. Sci.*, **257**, 1692 (1963).
(9) J. E. Bertie and E. Whalley, *J. Chem. Phys.*, **40**, 1637 (1964).
(10) J. E. Bertie and E. Whalley, *J. Chem. Phys.*, **46**, 1271 (1967).
(11) W. M. Irvine and J. M. Pollack, *Icarus*, **8**, 324 (1968).
(12) E. Whalley, *Develop. Appl. Spectrosc.*, **6**, 277 (1968).
(13) J. E. Bertie, H. J. Labbé, and E. Whalley, *J. Chem. Phys.*, **50**, 4501 (1969).
(14) E. Whalley in "Physics of Ice," N. Riehl, B. Bullemer, and H. Engelhardt, Ed., Plenum Press, New York, N.Y., 1969, p 73.
(15) B. N. Brockhouse, *Phys. Rev. Lett.*, **2**, 287 (1959).
(16) D. J. Hughes, H. Palevsky, W. Kley, and E. Tunkelo, *Phys. Rev.*, **119**, 872 (1960).
(17) T. Springer, *Nukleonik*, **3**, 110 (1961).
(18) T. Springer and W. Wiedemann, *Z. Phys.*, **164**, 111 (1961).
(19) A. D. B. Woods, B. N. Brockhouse, M. Sakamoto, *and R. N.* Sinclair in "Inelastic Scattering of Neutrons in Solids and Liquids," International Atomic Energy Agency, Vienna, 1961, p 487.
(20) K. E. Larsson and U. Dahlborg, *J. Nucl. Energy, Parts A/B*, **16**, 81 (1962).
(21) K. E. Larsson and U. Dahlborg in "Inelastic Scattering of Neutrons in Solids and Liquids," International Atomic Energy Agency, Vienna, 1963, p 317.
(22) V. V. Golikov, I. Zukovskaja, S. L. Sapiro, A. Skatula, and E. Janik, *Inelastic Scattering Neutrons, Proc. Symp., 1964*, p 201 (1964).
(23) J. O. Burgman, J. Sciesinski, and K. Skold, *Phys. Rev.*, **170**, 808 (1968).
(24) H. Prask, H. Boutin, and S. Yip, *J. Chem. Phys.*, **48**, 3367 (1968).
(25) O. K. Harling, *J. Chem. Phys.*, **50**, 5279 (1969).
(26) B. Renker, *Phys. Lett. A*, **30**, 493 (1969).
(27) B. Renker and P. v. Blankenhagen in "Physics of Ice," B. Bullemer, H. Engelhardt, and N. Riehl, Ed., Plenum Press, New York, N.Y., 1969, p 287.
(28) P. v. Blankenhagen, *Ber. Bunsenges. Phys. Chem.*, **76**, 891 (1972).
(29) H. J. Prask, S. F. Trevino, J. D. Gault, and K. W. Logan, *J. Chem. Phys.*, **56**, 3217 (1972).
(30) V. I. Val'kov and G. L. Maslenkova, *Opt. Spectrosk.*, **1**, 881 (1956).
(31) M. J. Taylor and E. Whalley, *J. Chem. Phys.*, **40**, 1660 (1964).
(32) G. E. Walrafen, *J. Chem. Phys.*, **40**, 3249 (1964).
(33) G. E. Walrafen, *J. Chem. Phys.*, **44**, 1546 (1966).
(34) P. K. Faure, *J. Phys.*, 214 (1969).
(35) P. T. T. Wong, D. D. Klug, and E. Whalley in "Physics and Chemistry of Ice," E. Whalley, S. J. Jones, and L. W. Gold, Ed., Royal Society of Canada, Ottawa, 1973, p 87.
(36) E. Forslind, *Sve. Forkningsinst. Cem. Betong Kgl. Tek. Hoegsk. Stockholm, Handl.*, **21**, 1 (1954).
(37) P. Faure and A. Kahane, *J. Phys. (Paris)*, **28**, 944 (1967).
(38) Y. Nakahara, *J. Nucl. Sci. Technol.*, **5**, 635 (1968).
(39) S. Trevino, H. Prask, T. Wall, and S. Yip in "Neutron Inelastic Scattering," International Atomic Energy Agency, Vienna, 1968, p 345.
(40) P. Faure, *J. Phys. (Paris)*, **30**, 214 (1969).
(41) T. M. Haridasan and J. Govindarajan, *Chem. Phys. Lett.*, **4**, 11 (1969).
(42) R. E. Shawyer and P. Dean, *Discuss. Faraday Soc.*, **48**, 102 (1969).
(43) P. Bosi, R. Tubino, and G. Zerbi in ref 35, p 98.
(44) B. R. Lentz, A. T. Hagler, and H. A. Scheraga, *J. Phys. Chem.*, **78**, 1844 (1974).
(45) L. L. Shipman and H. A. Scheraga, *J. Phys. Chem.*, **78**, 909 (1974).
(46) O. Weres and S. A. Rice, *J. Amer. Chem. Soc.*, **94**, 8983 (1972).
(47) A. Warshel and S. Lifson, *J. Chem. Phys.*, **53**, 582 (1970).
(48) The SS potential was derived using a water pentamer model to calculate the average librational frequency of ice I_h, but the potential is independent of this choice of model because nearest-neighbor coupling shifts the calculated average librational frequency only slightly (see section II).
(49) There is a 13th second-nearest neighbor of the central water molecule that, unlike the other 12 second-nearest neighbors, is not hydrogen bonded to a nearest neighbor of the central water. This 13th second nearest neighbor has not been included in the present calculations since it should not have as great an effect on the vibrations studied as the other 12 second-nearest neighbors.
(50) W. S. Benedict, N. Gailer, and E. F. Plyer, *J. Chem. Phys.*, **24**, 1139 (1956).
(51) J. D. Bernal and R. H. Fowler, *J. Chem. Phys.*, **1**, 515 (1933).
(52) L. Pauling, *J. Amer. Chem. Soc.*, **57**, 2680 (1935).
(53) S. W. Peterson and H. A. Levy, *Acta Crystallogr.*, **10**, 70 (1957).
(54) A partial summary of peak positions found in neutron scattering studies can be found in ref 44. That summary complements the summary of the extent of the inelastic neutron scattering spectrum found in the present study.
(55) M. Lichtenstein, V. E. Derr, and J. J. Gallagher, *J. Mol. Spectrosc.*, **20**, 391 (1966).
(56) J. A. Barker, *Proc. Roy. Soc., Ser. A*, **219**, 367 (1953).
(57) J. B. Hasted in "Water. A Comprehensive Treatise," Vol. 1, F. Franks, Ed., Plenum Press, New York, N.Y., 1972, p 257.
(58) This formula is an expression of the usual assumption (see ref 56) that the induced dipole moment is equal to the polarizability times the inducing field.
(59) J. Ketelaar, "Chemical Constitution," Elsevier, New York, N.Y., 1958, p 91. We have modified the values reported by Ketelaar in the third significant figure so that $2\alpha_H + \alpha_O = 1.444$ $(Å)^3$, the experimental value[57] for the polarizability of water.

An Algorithm for Simulation of Transient and Alternating Current Electrical Properties of Conducting Membranes, Junctions, and One-Dimensional, Finite Galvanic Cells

James R. Sandifer and Richard P. Buck*

William Rand Kenan Laboratories of Chemistry, University of North Carolina, Chapel Hill, North Carolina 27514 *(Received May 9, 1974)*

Publication costs assisted by the National Science Foundation

An algorithm for computer simulation of transient concentration profiles and both transient and ac electrical properties of conducting membranes has been developed and described. Applications include transport by several ions with different mobilities and valences in permselective membranes, totally blocked cells, and finite galvanic cells. The algorithm is based on the Nernst–Planck system of equations coupled with Poisson's equation, introduced *via* the displacement current; therefore, electroneutrality is not assumed and migration effects are included automatically. Simulations of transient and steady-state properties as well as ac impedances are compared with solutions obtained analytically. Conventional linearization of field equations is not required to obtain transient responses. However, conversion from time to frequency using the Fourier transform to obtain impedances is theoretically limited to dimensionless currents and voltages less than unity. We have demonstrated versatility of the algorithm by simulating a case of biological interest—the inductive behavior of the squid giant axon.

Introduction

Impedance characteristics of membranes and galvanic cells have been studied both theoretically and experimentally for many years. In 1899 Warburg[1] considered diffusion-limited faradaic impedance and derived the now familiar expressions which bear his name. A few years later, Krüger[2] combined Warburg's theory with Helmholtz's double layer concept to establish perhaps the most widely accepted theory of polarization in electrochemistry. It was recognized by Jaffé,[3] however, that the older theories were restricted to galvanic cells containing supporting electrolyte because they neglected current perturbation of space charge, electric field nonlinearity, migration terms, and effects of ion recombination. Accordingly, he developed a more general theory applicable to a variety of polarizable media in which these various effects could be taken into account. After 20 years Jaffe's original work, which assumed that no ions could pass electrode or membrane interfaces (completely blocked), was extended to more general cases including electrode discharge of current carriers. These extensions of basic ideas treat ac polarization effects due to charge motion in semiconductors[4] and electrolyte solutions.[5] Discharge at the electrodes was described[5] as a first-order process governed by a rate constant, the "Chang–Jaffé" parameter. Subsequently Macdonald[6] extended Jaffé's work for blocked electrodes, included more general cases, and simplified or removed some of the approximations. Friauf[7] followed soon after with a similar treatment.

In the early years, considerable experimental work was done by Kohlrausch, Wien, and others. This verification of theory, reviewed by Jones and Christian,[8] was extended by Jaffé and Rider.[9] Studies by Randles,[10] Ershler,[11] and Gerischer[12] established an equivalent circuit for a single rate-controlling electrode process which describes well the impedance of semiinfinite cells containing inert electrolyte and identifies resistance caused by the activation polarization of the electrode reaction. This so-called "Randles' circuit" is of fundamental importance to electrochemists although it is limited to supported electrolytes where migration can be ignored. Research groups in Sluyters' and Delahay's laboratories made major contributions in this area after 1960 and Sluyters' chapter in Bard's series[13] may be consulted for a general treatment of the impedances of semiinfinite electrolytic cells.

After Friauf's paper in 1954 there was little theoretical activity until the work of Beaumont and Jacobs in 1967,[14] which is based on the Macdonald–Friauf theory. Since that time numerous papers have appeared. Macdonald[15–18] extended and refined his closed form impedance theory to include virtually all possible cases involving two mobile charge carriers plus immobile, noncombining positive and negative (donor/acceptor) charges. His theory now applies to solids and liquids with both electronic and ionic conduction, varying rates of discharge at the electrodes, and arbitrary mobilities and valences. It also includes contributions from extrinsic charge defect producers in the medium; therefore, semiconductors, ordinary solid and liquid electrolytes, Kerr and liquid crystal display cells, and to some extent fused salts can be treated.

Prior to Macdonald's 1971 paper, closed form impedance expressions were obtained from linearized sets of equations which resulted from expressing the variables in the form of

$$V = V_0 + V_1 e^{j\omega t} \qquad (1)$$

and substituting this set into the Poisson and Nernst–Planck equations. V is a general symbol representing the time and distance variation of some arbitrary variable such as potential, concentration, or electric intensity. V_0 is the equilibrium value of the arbitrary variable, $j = \sqrt{-1}$, ω is the angular frequency, and t is time. This linear system was then solved analytically with appropriate boundary conditions. Results obtained in this way are valid for univalent charge carriers only if the sinusoidal voltages are less than RT/F, where R is the gas constant, T is the absolute temperatures, and F is the Faraday.

Macdonald[16–18] begins with the nonlinear transport equations including the displacement current and obtains closed form expressions for the impedance-frequency response in the linear region. The results are analyzed nu-

merically in detail to discover frequency ranges over which impedances may be approximated by equivalent circuits. Often as many as three circuits must be employed to cover a complete spectrum depending on the boundary conditions and kinetic and transport parameters. Reduced (dimensionless) expressions for the circuit parameters are supplied with the approximate frequency ranges over which the circuits are valid. In addition, a set of graphs is given which illustrate expected responses for a variety of conditions. Some closed form impedance expressions which result from the analysis are included. Further details may be obtained from the latest paper.[18] Other approaches to these problems have been worked out and are described in detail by Arndt and Roper.[19]

Although these approaches are undoubtedly valid within the limitations of the transport equations, they lack simplicity. The practicing electrochemist, solid state physicist, or membrane biologist depends upon theoreticians to treat specific cases which may be of interest to him. A general, uninvolved, easily understood approach to the solution of complicated membrane impedance problems is needed in order to interpret data in which space charge, migration, or kinetic effects are known or suspected to play an important and unavoidable role. We feel that we have developed such an approach. Valuable insights into the processes occurring in a membrane or similar material may be gained even in very complicated cases involving many ions and kinetic effects.

Mathematical Formulation

Our algorithm is similar to the finite difference (digital simulation) scheme outlined by Feldberg,[20] except that migration and space charge effects are included. Feldberg's original approach used only Fick's diffusion laws; nevertheless, it has found widespread acceptance among electrochemists as a convenient means of solving complicated transport problems in the presence of inert supporting electroyte. Time and distance are discretized into intervals so that concentration derivatives may be approximated as finite differences. The distance intervals are called "volume elements" and are here designated by subscript j. The number of elements into which a membrane is divided is "NVE;" but the thickness of the membrane D will be (NVE $-$ 1)d, where d is the thickness of an element, because we choose to place the interfaces (electrodes) in the middle of the first and last elements[21] instead of at the edges. Concentrations are initially assigned in the middle of each element and electric intensities are assigned at interfaces between elements.

Flux, J_{ij}, of each species is given by the dilute solution form of the Nernst–Planck equations:

$$J_{ij} = -u_i RT \frac{dC_{ij}}{dx} + z_i u_i C_{ij} F E_j \qquad (2)$$

The subscript i designates the species; C_{ij} is its concentration in the jth volume element, z_i is its valence, and u_i is its mobility. E_j is the electric intensity at the jth interface, between the j and the $j + 1$ elements. Other symbols were defined above. A one-dimensional system in which x is the distance variable is assumed. This equation may be written in dimensionless form[22] by introducing the following parameters:

$$\bar{J}_{ij} = J_{ij}d/u_0C_0RT \qquad \bar{u}_i = u_i/u_0$$
$$\bar{x} = x/d \qquad \bar{C}_{ij} = C_{ij}/C_0$$
$$\bar{E}_j = E_jdF/RT \qquad \bar{V} = VF/RT$$

Symbols with bars are dimensionless. V is the potential difference between points within the membrane and is a function of distance and time; however, we evaluate only the total potential difference across the membrane interior so the subscript j has been deleted. Later we will obtain the total membrane potential by combining interior and interfacial components. Parameters u_0 and C_0 are the scaling mobility and concentration, respectively. u_0 is chosen to be about 10% greater than twice the mobility of the fastest charged species. C_0 is chosen within a power of ten of the membrane salt concentration. For problems involving transport of ions of only one sign through thin membranes such as lipid bilayers, de Levie and Moreira[23] find a suitable scaling factor is the concentration obtained by equating the Debye and membrane thickness, *e.g.*, $C_0 = \epsilon RT/F^2d^2$. Equation 2 may now be written in the finite difference form:

$$\bar{J}_{ij} = -\bar{u}_i\Delta\bar{C}_{ij}/\Delta\bar{x} + z_i\bar{u}_i\bar{C}_{ij}\bar{E}_j \qquad (3)$$

It is convenient to let $\Delta\bar{x} = 1$ in eq 3, so that distance is normalized by the thickness of a volume element rather than by the thickness of the membrane. The second term on the right side of eq 3 is the contribution of migration to the total flow.

The current density through the membrane is given by the following dimensionless finite difference equation:

$$\bar{I} = \sum_i z_i\bar{J}_{ij} + \bar{K}\Delta\bar{E}_j/\Delta\bar{t} \qquad (4a)$$

where the dimensionless parameters are:

$$\bar{I} = Id/u_0C_0FRT \qquad (4b)$$

$$\bar{t} = tu_0RT/d^2 \qquad (4c)$$

$$\bar{K} = k\epsilon RT/C_0d^2F^2 = 2.35 \times 10^{-20}k/C_0d^2 \qquad (4d)$$

In these equations, I is the current density, which is assumed to be constant throughout the membrane. Only current clamp responses are considered. The dimensionless term, $\bar{K}$, is a function of the dielectric constant where ϵ is the permittivity of free space and k is the conventional dielectric constant. $\bar{K}$ is also a ratio of the time required for an ion to diffuse one Debye thickness to the time required to diffuse one half of the volume element. The second term on the right-hand side of eq 4a is the displacement current, which accounts for accumulation of space charge due to current. Equation 4a is related to Poisson's equation in that both are differential forms of Gauss' law, one with respect to time, the other with respect to distance. We take $\Delta\bar{t} = 1$ in the simulations, and because time is normalized by the diffusion time, d^2/u_0RT, real times may be made quite small inasmuch as thickness of a volume element, d, may be small.

From eq 3, the flux of each ion between volume elements may be computed when $\bar{E}_j$ is known at the element interfaces since the concentration gradient can be approximated as a finite difference. An iterative equation for the computation of $\bar{E}_j$ from past values of this variable, called $\bar{E}_j'$, may be derived by rewriting eq 4a as below:

$$\bar{I} = \sum_i z_i\bar{J}_{ij} + \bar{K}(\bar{E}_j - \bar{E}_j') \qquad (5)$$

Now if eq 3 and 5 are combined and rearranged:

$$\bar{E}_j = \frac{\bar{I} + \bar{K}\bar{E}_j' + \sum_i z_i\bar{u}_i\Delta\bar{C}_{ij}}{\bar{K} + \sum_i z_i^2\bar{u}_i\bar{C}_{ij}} \qquad (6)$$

$\bar{E}_j$ values can be computed iteratively from eq 6 if $\bar{C}_{ij}$ is approximated as the average concentration between elements j and $j + 1$.

Equation 6 is similar to one derived by Cohen and Cooley,[22] except that they set $\bar{K} = 0$. It may be shown that eq 6 is the iterative form of eq 7 when ΔC_{ij} is constant.

$$\bar{E}_j = \bar{E}_{j\infty}(1 - e^{-\bar{t}/\bar{\tau}}) \qquad (7)$$

$\bar{E}_{j\infty}$ is the limiting value of $\bar{E}_j$ as $\bar{t} \to \infty$ and $\bar{\tau}$ is a time constant. These parameters may be computed as follows:

$$\bar{E}_{j\infty} = \left(\bar{I} + \sum_i z_i \bar{u}_i \Delta \bar{C}_{ij}\right) \Big/ \sum_i z_i^2 \bar{u}_i \bar{C}_{ij}$$

$$\bar{\tau} = \bar{E}_{j\infty}\bar{K}/\bar{I}$$

If $\Delta \bar{C}_{ij} = 0$, $\bar{E}_{j\infty}/\bar{I}$ is simply the bulk resistivity of the medium. $\bar{E}_j$ values computed from eq 6 may be substituted into eq 3 to compute fluxes so that new concentration profiles may be determined from the finite difference form of Fick's second law

$$\bar{C}_{ij} = \bar{C}_{ij}' - (\bar{J}_{ij+1} - \bar{J}_{ij}) \qquad (8)$$

where $\bar{C}_{ij}'$ is the past value of $\bar{C}_{ij}$. The sequence now returns to eq 6 for a new set of $\bar{E}_j$ values, then eq 3 for new $\bar{J}_{ij}$ values, and again to eq 8 for a new concentration profile. This process is repeated until a steady state is reached.

It might be objected that this procedure requires too much storage—a concentration array and a flux array for each species, as well as an electric intensity array. We have not found this to be a handicap because at most 50 volume elements are needed to obtain 1% or better accuracy for the test systems reported in the Results sections. Nevertheless, the entire algorithm could be restructured to eliminate flux arrays by using second-order derivatives.

Two voltages are defined: $\bar{V}_m$, which is the voltage drop across the interior bulk of the medium, and $\bar{V}_i$, which is the interfacial potential resulting from equality of electrochemical potentials between ions just inside the interface and the external phase (electrode or bathing solution). $\bar{V}_m$ may be computed from the equation:

$$\bar{V}_m = -\sum_{1}^{NVE-1} \bar{E}_j \qquad (9)$$

and $\bar{V}_i$ may be computed from

$$\bar{V}_i = \pm \ln (\overline{CSALT2}/\overline{CSALT1}) \qquad (10)$$

This calculation gives the sum of the two interfacial potentials. $\overline{CSALT1}$ is the mean salt concentration at the interior of the first interface while $\overline{CSALT2}$ refers to the second interface. The positive sign is taken in eq 10 when the cations are in rapid, reversible equilibrium while anions are blocked at both interfaces. The negative sign is used when anions are in rapid, reversible equilibrium while cations are blocked. It is further assumed that the external bathing solutions contain the reversible ion and the external phases are in every way identical on the two sides of the membrane so that the standard chemical potentials and identical external salt activities will cancel. Rapid stirring of the external solutions assures uniform concentrations even though current flows through the membrane. For membranes containing only a univalent salt

$$\overline{CSALT} = \sqrt{\bar{C}_+ \bar{C}_-} \qquad (11)$$

where $\bar{C}_+$ and $\bar{C}_-$ refer to the interfacial concentrations of the positive and negative ions, respectively. The total potential drop across the membrane will be the sum of $\bar{V}_m$ and $\bar{V}_i$. By expressing total measurable membrane potential as the sum of eq 9 and 10, we are applying the general segmented potential model of Teorell–Meyer–Sievers. For positive current (+ charge moving from side 1 to side 2) the total membrane potential $\bar{V}_m + \bar{V}_i$ is negative, and both $\bar{V}_m$ and $\bar{V}_i$ are negative. In Figures 1–4, the absolute values of the reduced potentials are plotted.

It is assumed that only ions of one sign cross the interface (permselectivity); therefore, the interfacial concentrations (activity coefficients are assumed to be unity) of these ions in an electrically neutral environment will determine the potential. It is also assumed that the rate of transfer across the interface is infinite. Both assumptions may be easily removed, either by introducing heterogeneous rate constants[20,24,25] or Chang–Jaffé parameters.[5] The mean salt concentration must be used in eq 10 as the appropriate quantity at the interface where interfacial space charge exists. Verification of this approach on theoretical grounds was given by Buck[26] and will be given further verification later in this paper for a univalent salt.

The algorithm described so far is suitable only for the simulation of transient responses. To pass from time to the frequency domain it is necessary to Fourier transform the transient potential values. This approach is theoretically justified for potential excursions in the linear range, *i.e.*, $\bar{V}_m$ less than 1. This method has been used by numerous experimentalists in recent years,[27–31] especially since the advent of the "Fast Fourier Transform" algorithm.[32] Our examples are confined to the linear region.

The pertinent equations are:

$$\bar{Z}^* = \bar{V}^*/\bar{I}^* \qquad (12)$$

$$\bar{V}' = \int_0^\infty [\bar{V}(\bar{t}) - \bar{V}_\infty] \cos(\bar{\omega}\bar{t})\, d\bar{t} \qquad (13)$$

$$\bar{V}'' = \int_0^\infty [\bar{V}(\bar{t}) - \bar{V}_\infty] \sin(\bar{\omega}\bar{t})\, d\bar{t} + \bar{V}_\infty/\bar{\omega} \qquad (14)$$

$$\bar{I}' = 0 \qquad (15)$$

$$\bar{I}'' = -\bar{I}/\bar{\omega} \qquad (16)$$

The first of these, eq 12, is the impedance for linear systems. Equations 13 and 14 are proper forms for time responses which do not die off at long times. These results and eq 15 and 16 depend upon use of the Riemann–Lebesque lemma.[33] The stars indicate that the values are complex; primes represent in-phase values, and double primes represent out-of-phase values. $\bar{V}(\bar{t})$ is the time-dependent voltage resulting from the constant current $\bar{I}$. $\bar{V}_\infty$ is the limiting value of $\bar{V}(\bar{t})$ as $\bar{t} \to \infty$ and $\bar{\omega} = \omega/\omega_0$ is the dimensionless radial frequency. The normalizing angular frequency is $\omega_0 = 2\pi u_0 RT/d^2$. Integrals in eq 13 and 14 are evaluated *via* Simpson's rule.

Results Assuming Electroneutrality ($\bar{K} = 0$) and a Single Uni-univalent Salt

Cohen and Cooley have simulated the voltage response of an equivalent membrane (actually a constrained Planck junction) subjected to a current step. They assume electroneutrality and also that interfacial concentrations do not change with time. Since this latter assumption precludes time-dependent interfacial potentials, we have avoided this assumption but retained the electroneutrality condition only for the time being.

Consider the case of a permselective membrane contain-

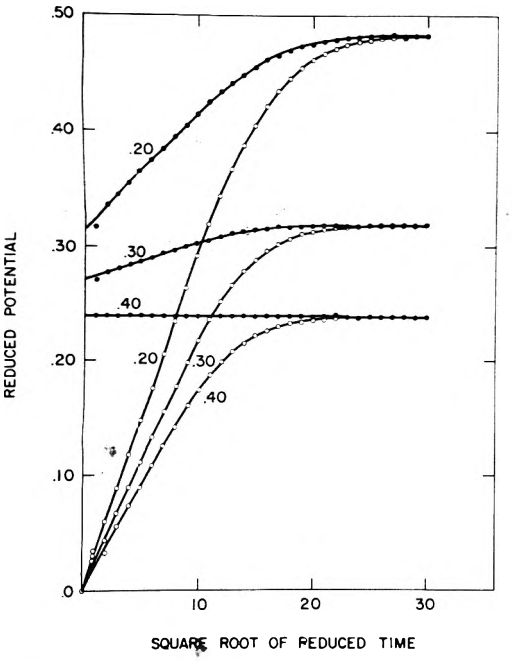

Figure 1. Potential *vs.* $(\bar{t})^{1/2}$ curves for cation permselective liquid membrane between symmetric bathing solutions containing a permselective ion salt. The mobility of the permselective ion is shown on each curve. The counterion, which is constrained within the membrane, has a mobility of 0.40 in every case: $\bar{I} = 0.01$, $\bar{C} = 1$, $\bar{K} = 0$, $z_+ = z_- = 1$, and NVE = 20; $\bar{V}_m$ (●), $\bar{V}_i$ (O). $\bar{I}$ flows left to right.

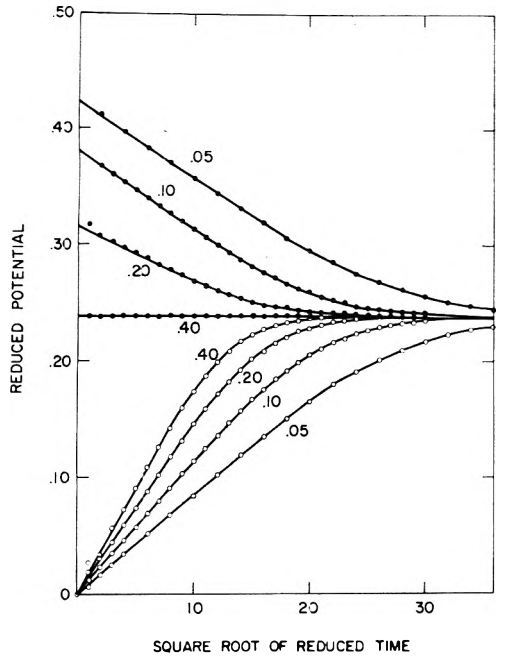

Figure 2. Potential *vs.* $(\bar{t})^{1/2}$ curves for cation permselective liquid membrane between symmetric bathing solutions containing a permselective ion salt. The mobility of the permselective ion is 0.40 in every case. The counterion has the mobility shown on each curve. $\bar{I} = 0.01$, $\bar{K} = 0$, and NVE = 20; $\bar{V}_m$ (●), $\bar{V}_i$ (O).

ing only a univalent salt. The permselective ion, by definition, carries all the faradaic current at the interfaces, while both ions contribute to bulk transport and displacement current prior to the steady state. (See the chronopotentiometry section of ref 21 for a full description of the interfacial current simulation.) Absolute responses, $\bar{V}_m$ and $\bar{V}_i$, for such a system, assuming lower mobility for the permselective ion, are shown in Figure 1. Both voltage responses rise with $(\bar{t})^{1/2}$ dependencies to the same limiting value, indicating that the total voltage drop across the membrane as $t \to \infty$ is equally divided between the bulk and the interface. Similar response is shown in Figure 2, where the permselective ion has the higher mobility. If the total voltage is Fourier transformed into the complex impedance plane and the out-of-phase impedance component plotted against the in-phase component (Cole–Cole plot) the result has the shape of the familiar finite Warburg function.[34] The curve intersects the real axis in two places, the high and low frequency limits. As shown in Table I, these limits are within 1% of those obtained at $\omega \to \infty$ by Macdonald's methods[18] and Buck's methods[26] in the nonlinear range for $\bar{\omega} \to 0$. Macdonald's result at $\bar{\omega} \to 0$ for exceedingly small currents such that $\bar{C}'' = \bar{C}'$ is also shown.

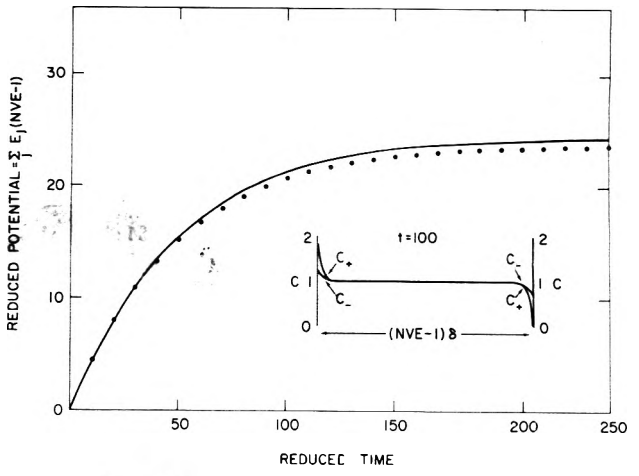

Figure 3. $\bar{V}_m$ *vs.* $\bar{t}$ curves of liquid membranes, as in Figures 1 and 2, at short times with the electroneutrality condition relaxed. $u_+ = u_- = 0.01$, $\bar{K} = 1.0$, NVE = 50, $\bar{I} = 0.01$, $z_+ = z_- = 1$, and $\bar{C} = 1$. The results are linear in the sense that raising $\bar{u}_+$ and $\bar{u}_-$ by a factor of 100 or decreasing $\bar{I}$ by 100 gives $\bar{V}_m$ reduced by 100.

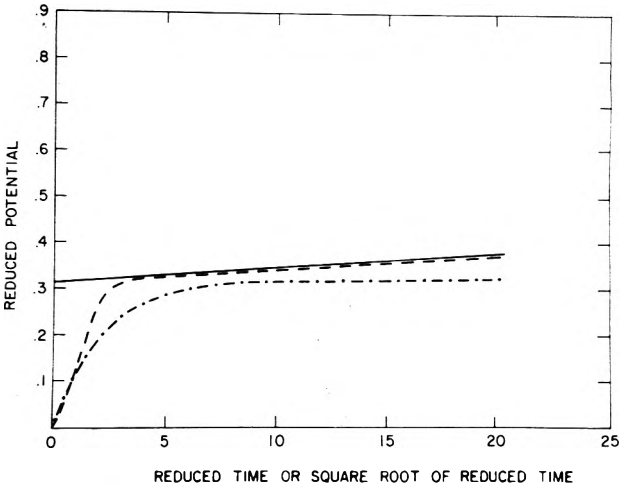

Figure 4. Simulation of short time portion of the uppermost curve in Figure 1. $\bar{V}_m$ is plotted against both $\bar{t}$ (– · –) and $(\bar{t})^{1/2}$ (– –) for comparison. Values used are $\bar{u}_+ = 0.2$, $\bar{u}_- = 0.4$, $\bar{K} = 0.1$, $\bar{I} = 0.01$, NVE = 20, $z_+ = z_- = 1$, and $\bar{C} = 1$.

Because electroneutrality was assumed, charging voltages do not appear in these figures. Instead $\bar{V}_m$ rises instantaneously to its high-frequency limiting value and no high-frequency semicircle characteristic of the bulk resistance, geometrical capacitance combination appears in the

TABLE I: Comparison of Electroneutrality Simulations with Rigorous Analytical Results[a]

Mobilities		$\bar{R}(\bar{\omega} \rightarrow 0)$			$\bar{R}(\bar{\omega} \rightarrow \infty)$	
Permselective	Counter	Simulation	Ref 26	Ref 18	Simulation	Ref 18
0.20	0.40	96.8	96.8	95.0	**31.4**	31.7
0.30	0.40	63.8	63.9	63.3	**27.1**	27.1
0.40	0.40	47.6	47.5	47.5	23.8	23.8
0.40	0.20	47.6	47.5	47.5	31.6	31.7
0.40	0.10	47.6	47.5	47.5	38.0	38.0
0.40	0.05	47.6	47.5	47.5	42.2	42.2

[a] References 18 and 26. $\bar{R}$ represents the dimensionless resistance at the limiting frequency specified. Values indicated by Macdonald were calculated from the following linearized equations. These equations are reduced parameter versions of eq 10 and 12 (ref 18). Nonlinear equations follow from Eq 14b and 15b (ref 26).

$$R(\omega \rightarrow \infty) = \frac{D}{F^2(z_+^2 u_+ C_+ + z_-^2 u_- C_-)} = \frac{D}{F^2(u_+ + u_-)C}$$

(the latter for $z_+ = z_- = 1$)

$$\bar{R}(\bar{\omega} \rightarrow \infty) = (\mathrm{NVE} - 1)/(\bar{u}_+ + \bar{u}_-)$$

$$R(\omega \rightarrow 0)(\text{linearized}) = \frac{D}{F^2 u_+ C}$$

$$\bar{R}(\bar{\omega} \rightarrow 0)(\text{linearized}) = (\mathrm{NVE} - 1)/\bar{u}_+ \bar{C}$$

$$R(\omega \rightarrow 0)(\text{not linearized}) = \frac{D}{F^2 u_+ (C'' - C')} \ln \frac{C''}{C'}$$

$$\bar{R}(\bar{\omega} \rightarrow 0)(\text{not linearized}) = \frac{(\mathrm{NVE} - 1)}{\bar{u}_+ (\bar{C}'' - \bar{C}')} \ln \frac{\bar{C}''}{\bar{C}'}$$

$\bar{C}'$ and $\bar{C}''$ are reduced concentrations of salt at the left and right sides.

complex impedance plane. This characteristic simply reflects the fact that the geometrical capacitance charging will usually take place in much shorter times (higher frequencies) than the diffusional process. Since this behavior is normal, one may generally assume that $\Delta\bar{C}_{ij}$ is zero in eq 6 for the duration of the charging and that the field, $\bar{E}_j$, is constant through the membrane.[35] This result leads directly to eq 7, which transforms into the frequency domain as the missing high-frequency semicircle. We will show the proper way to obtain high-frequency results in the next section.

Results Assuming $\bar{K} \neq 0$

Increasing $\bar{K}$ has the effect of increasing the amount of space charge in the medium. In Figure 3 the expected charging curve for a permselective membrane has been computed directly by allowing $\bar{K}$ to be greater than zero. The solid curve obeys eq 7; the simulated points lie below this curve because the space charge region extends deeply into the membrane, thus lowering its effective thickness. This result can be understood from the concentration profiles in the figure. Conventional current is flowing from left to right; positive ions are being forced into the membrane on the left side and withdrawn on the right. This flow produces positive space charge in the membrane on the left and negative charge on the right. Resistivity of the electrically neutral medium is still given by $\bar{E}_{j\infty}/\bar{I}$ as in eq 7, so the space charge region only decreases the effective thickness of the medium. $\bar{K} = 1$ in this simulation, so that with NVE = 50, $C_0 = 10^{-6}$ mol/cm^3, and $k = 80$, the thickness is

TABLE II: Variation of $\bar{V}_i(\bar{t} \rightarrow \infty)$ with $\bar{K}$ for the Cases Shown in Figure 5[a]

$\bar{K}$	$\bar{V}_i(t \rightarrow \infty)$	$\bar{K}$	$\bar{V}_i(t \rightarrow \infty)$
0.0	0.483	10.0	0.485
0.1	0.485	20.0	0.489
1.0	0.483	100.0	0.499

[a] Theoretical value 0.484.

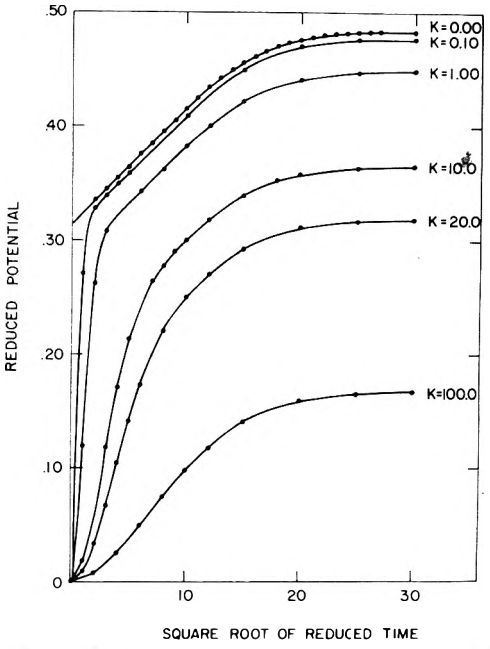

Figure 5. $\bar{V}_m$ *vs.* $(\bar{t})^{1/2}$ curves showing the effect of varying $\bar{K}$: $\bar{u}_+ = 0.20$, $\bar{u}_- = 0.40$, $\bar{I} = 0.01$, NVE = 20, and $\bar{K}$ values are shown on each curve. Conditions are otherwise the same as in Figure 4.

only about 7000 Å and the space charge extends about 350 Å on either side. The ratio of membrane thickness to Debye thickness is $49/\sqrt{2}$. If smaller values of $\bar{K}$ are used, the space charge does not extend so far into the membrane and the simulated response curve follows the theoretical very closely. The time constant of the charging curve is $\bar{K}$ times the bulk resistivity; so, for smaller values of $\bar{K}$, time must be scaled by increasing u_0 thus decreasing all the $\bar{u}_i$'s.

In Figure 4, we have returned to the problem simulated by the uppermost curve in Figure 1. The simulated points using $\bar{K} = 0.1$ are plotted (dashed line) *vs.* $(\bar{t})^{1/2}$ for the first 20. The heavy line represents interpolated values for $\bar{K} = 0$ from Figure 1, and is drawn for comparison also *vs.* $(\bar{t})^{1/2}$. When the medium is very thin, strong deviation from electroneutrality may occur and $\bar{K}$ can be large. For example, a membrane 200-Å thick may show $\bar{K}$ in excess of 100. The effects of large values of $\bar{K}$ on $\bar{V}_m$ are shown in Figure 5 in the case that the $\bar{u}$ of the permselective ion is 0.20 while that of the counter ion is 0.40. Although plotted *vs.* $(\bar{t})^{1/2}$ for comparison, the $\bar{K} = 100$ curve shows that $\bar{V}_m$ grows nearly exponentially at short times and that two time constants are involved. The Fourier transform gives a depressed impedance semicircle, resembling a cycloid, in the complex impedance plane.

These data can also be used to validate our use of CSALT defined previously in the calculation of the interfacial potentials $\bar{V}_i$. Steady-state values of $\bar{V}_i$ are shown for various values of $\bar{K}$ in Table II. The theoretical value 0.484

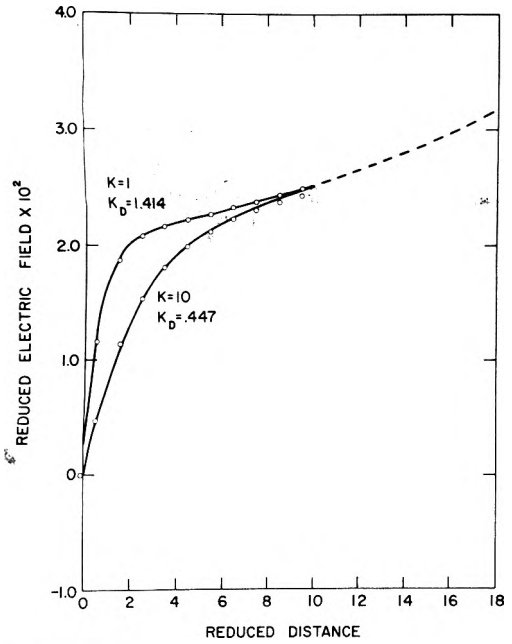

Figure 6. $\bar{E}$ *vs.* $\bar{x}$ curves for cation permselective liquid membrane as in Figure 1 with $\bar{C} = 1$ and $z_+ = z_- = 1$ in which the mobility of the permselective ion is 0.20 while that of the counter ion is 0.40. The curves are shown after 900 iterations with 20 volume elements: $\bar{I} = 0.01$, $\bar{K}$ values are shown on the curves along with the corresponding reciprocal Debye thickness, K_D.

can be computed in the absence of space charge using eq 15b ref 26 according to

$$-\bar{V}_i = \ln\left[\frac{\text{CSALT} + \dfrac{ID}{4RTu_+F}}{\text{CSALT} - \dfrac{ID}{4RTu_+F}}\right] = \ln\left[\frac{1 + \dfrac{(\text{NVE} - 1)\bar{I}}{4\bar{u}_+}}{1 - \dfrac{(\text{NVE} - 1)\bar{I}}{4\bar{u}_+}}\right] \quad (17)$$

for a membrane of thickness D containing a uni-univalent salt of mean concentration CSALT. Variation is about 3% for $\bar{K} = 0$ to 100. This high variation may be due more to integration error than to the CSALT assumption; when $\bar{K} = 0$ (Table I) this particular simulation produces less than a 1% error in $\bar{R}(\bar{\omega} \to 0)$. When mobilities are equal the variation is zero.

According to a recent theory by Buck,[26] the steady-state electric intensity profile through half a discharging membrane from $x = 0$ to $x = D/2$ is

$$E = E_0 e^{-(1+I/L)^{1/2} K_D x} + \frac{RT}{zF}\left[\frac{I}{LD/2 + I(D/2 - x)}\right] \quad (18)$$

where K_D^{-1} is the Debye thickness, $(k\epsilon RT/2C_0F^2)^{1/2}$ for a 1–1 electrolyte at concentration C_0; L is the limiting current $(4RTu_pzFC_0/D)$, where u_p is the mobility of the permselective ion, z is its valence, and D is the membrane or cell thickness. E_0 in eq 18 is given below:

$$E_0 = (1 + I/L)^{1/2}\left[V_0 - V_s - \frac{RT}{zF}\ln(1 + I/L)\right]K_D \quad (19)$$

$V_0 - V_s$ is the potential difference between the outer Helmholtz plane and the center of the membrane.

As shown in Figure 6, where simulated points lie on the curve representing eq 18 in dimensionless form, our algorithm offers verification of Buck's theory. The theory is valid only if electroneutrality prevails at the center of the membrane and so the deviation of points for $\bar{K} = 10$ occurs because this requirement is not met. The center of the membrane is at $\bar{x} = 9.5$ and the dashed line is the extended diffusion field from an extension of eq 18 to cover the region $x > D/2$. When $\bar{K} = 0$ the simulated points lie on this line from one side of the membrane to the other.

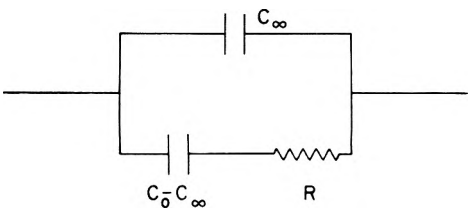

Figure 7. The equivalent circuit of a blocked membrane or galvanic cell containing mobile charge carriers. Subscripts refer to limiting frequency values. C_0 is half the double layer capacitance C_{dl} for each interface. C_∞ is the geometric capacitance; R is bulk resistance.

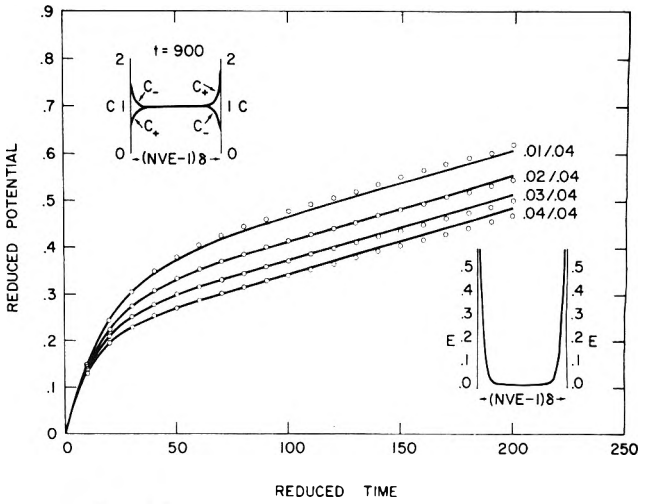

Figure 8. $\bar{V}_m$ *vs.* $\bar{t}$ curves, simulated for a blocked case. The mobilities of the ions $\bar{u}_+/\bar{u}_-$ are shown after each curve: $\bar{K} = 1$, $\bar{I} = 0.001$, NVE = 20, $\bar{C} = 1$, $z_+ = z_- = 1$, and $\delta = d$ = volume element thickness. Inserted diagrams give concentration and field profiles.

If the medium contains no permselective ion there can be no discharge at the interfaces and the cell will be completely blocked. Its equivalent circuit will then be that shown in Figure 7,[6,36] where C_∞ is the geometrical capacitance per cm², C_{dl} is the total double layer capacitance per cm² (C_0 in the figure), and R is the bulk resistance per unit cross section. The total double layer capacitance is $k\epsilon K_D/2$ which, in the dimensionless units defined previously, becomes $\bar{C}_{dl} = (\bar{K}\bar{C}/2)^{1/2}$. The reduction of resistance and capacitance follows from a series of relationships whereby the time reduction must be consistent with the product of factors which render R and C dimensionless. Also, the coefficient of $d\bar{E}/d\bar{t}$ must be a dimensionless capacitance multiplied by a dimensionless distance. Thus $\bar{K}$ must be a dimensionless capacitance per volume element and $\bar{C}_\infty = \bar{K}/(\text{NVE} - 1)$. A consistent set of dimensionalizing factors are:

$$\text{resistance} = (d/u_0C_0F^2)\bar{R} \quad (20)$$

$$\text{capacitance} = (k\epsilon/d\bar{K})\bar{C} \quad (21)$$

TABLE III: Check of Simulation Against Poisson's Equation[a]

Case	$\bar{x}$	$-\Delta\bar{E}$	$-\bar{q}$	% diff
(0.01,200)	1	0.0598	0.05967	0.2
	2	0.01633	0.01632	0.06
	3	0.00511	0.005118	0.2
(0.02,900)	1	0.2968	0.2964	0.1
	2	0.0806	0.08023	0.5
	3	0.02207	0.02207	0
(0.03,200)	1	0.06318	0.06312	0.1
	2	0.01623	0.01612	0.6
	3	0.00418	0.004131	1
(0.04,900	1	0.2980	0.2974	0.2
	2	0.0794	0.07897	0.5
	3	0.02133	0.02085	2

[a] In all cases $\bar{K} = 1$ and the mobility of one ion is 0.04. The mobility of the ion is presented, along with $\bar{t}$, in the form $(\bar{u}_i, \bar{t})$ in the column labeled case.

The voltage–time response of this circuit is given classically as

$$\bar{V}_m = \bar{I}\bar{t}/\bar{C}_0 + \bar{I}\bar{R}\left(1 - \frac{\bar{C}_\infty}{\bar{C}_0}\right)^2\{1 - \exp[\bar{t}/\bar{R}\bar{C}_\infty(1 - \bar{C}_\infty/\bar{C}_0)]\} \quad (22)$$

$\bar{V}_m$ represents the total voltage drop because $\bar{V}_i$ is necessarily zero. The lines in Figure 8 obey this equation for appropriate values of the parameters as defined above. The dots are simulated points. Departure of potential from the equation at longer times is undoubtedly due to replacement of a proper integration by a summation in eq 11. It is naive to think that precise integration of field can be achieved with only 20 volume elements, especially when the electric intensity varies dramatically at the interfaces, as it must in a blocked case to account for the space charge.

Although it does not appear directly in the algorithm, Poisson's equation

$$dE/dx = \rho/k\epsilon \quad (23)$$

where ρ is the volume charge density, must be obeyed. In finite difference, dimensionless form, this means that $\bar{K}\Delta\bar{E}$ between element interfaces must equal $\bar{q} = z_+\bar{C}_+ - |z_-|\bar{C}_-$ within each element. As shown in Table III, this result is indeed achieved.

Inductive Effects

A membrane may separate unlike solutions such that a fast permselective ion will be on one side while a slower one of the same sign will be on the other. The steady-state concentrations within the membrane will vary linearly from initial concentrations of unity (in this case) to zero. To account for electroneutrality, a third ion of opposite charge must be included in the membrane. This ion may not cross the interfaces and we further stipulate that its mobility is zero, although nonzero mobility could just as easily be simulated. If current is now passed through the membrane in a direction such that fast ions are swept through the membrane from left to right, the potential drop ($\bar{V}_m$) will decrease with a $(\bar{t})^{1/2}$ dependency after an initial charging increase until a limiting value is approached. This is an inductive effect. The complex impedance representation of this system is shown in Figure 9: For this simulation, NVE

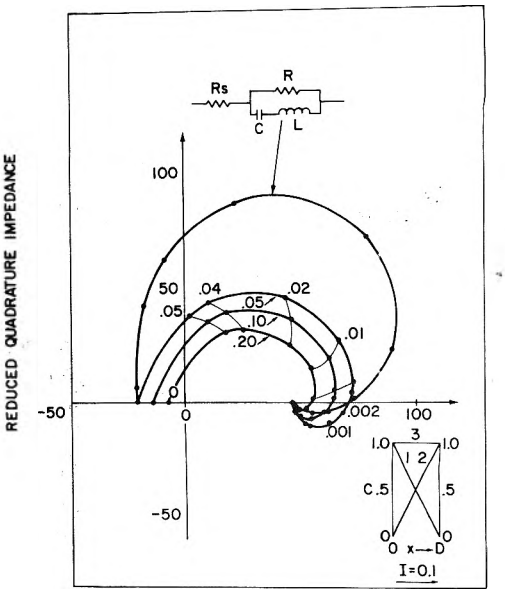

Figure 9. These central curves are simulated Cole–Cole plots for a spontaneous system exhibiting "inductive effects." Permselective ion 1 is faster than permselective ion 2 and has a mobility of 0.4 in all cases. The mobility of ion 2 is shown below each curve; ion 3 is a membrane soluble counter ion. Insert diagram shows the initial, steady-state condition. Left bathing solution is an infinite reservoir of ion 1 salt. Right side contains only ion 2 salt: NVE = 20, $\bar{K} = 1$, and $\bar{I} = 0.1$ Reduced frequencies ($\bar{\omega}$) appear above the curves. The values of suggested equivalent circuit[41] parameters are $R_s = -21$, $R = 68$, $C = 0.342$, and $L = 2140$; all in dimensionless units.

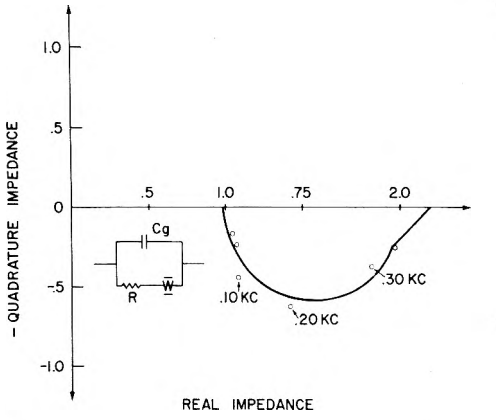

Figure 10. Cole's transcribed data of the squid axon impedance, after C_g has been subtracted out. The values are in units of 10.3 kΩ. The curve through the points is an "inverted," finite Warburg, as described in the text.

= 20, $\bar{u}_1 = 0.4$, $\bar{u}_2 = 0.20$, 0.10, and 0.05, $\bar{K} = 1$, and $\bar{I} = 0.1$ were used. Simulations were also done with smaller currents and for the absence of space charge $\bar{K} = 0$. In the latter case a finite Warburg-like response is observed (the solid line in Figure 10). However $\bar{Z}'(\omega = 0)$ is less than $\bar{Z}'(\omega = \infty)$ so that $\bar{Z}'$ decreases as ω increases. This type of behavior leads to $\bar{Z}''$ with opposite sign compared with normal Warburg behavior. Although not exact except in the limit $\bar{u}_1 \ll \bar{u}_2$, the impedance follows the finite Warburg form:

$$\bar{Z} = \bar{Z}_\infty + (\bar{Z}_0 - \bar{Z}_\infty)\frac{\tanh(j\bar{\omega}\bar{\tau}/2)^{1/2}}{(j\bar{\omega}\bar{\tau}/2)^{1/2}} \quad (24)$$

For the conditions of Figure 9, $\bar{Z}_0 = 47.5$, $\bar{Z}_\infty = 65.8$, 87.8,

and 112.9 for the three $\bar{u}_2$ values listed above. These values are obtained from

$$\bar{Z}_0 = \bar{R}(\bar{\omega} \to 0) = \frac{(\mathrm{NVE} - 1)}{\bar{u}_1 \bar{C}} \qquad (25)$$

and

$$\bar{Z}_\infty = \bar{R}(\omega \to \infty) = \frac{(\mathrm{NVE} - 1)}{\bar{C}(\bar{u}_1 - \bar{u}_2)} \ln \frac{\bar{u}_1}{\bar{u}_2} \qquad (26)$$

for $z_1 \triangleq z_2 = 1$.

Coupling of the space charge capacitance through $\bar{K} = 1$ produces an overlapping of the usual high-frequency semicircle and the Warburg-like diffusional impedance with the results shown in Figure 9. Notice that the high-frequency limiting resistance is negative, consistent with the fact that voltage must be applied to such a membrane in order to maintain zero current. The fact that the curves circle the origin counter-clockwise with increasing $\bar{\omega}$ indicates that the system is unstable according to the Llewellyn criterion,[37] as discussed by de Levie.[38] This is a necessary, but not sufficient, condition for oscillations, which have been observed for such systems.[39,40] In Figure 9 is also shown a circuit consisting of a capacitor shunted by a resistor–inductor series combination, as suggested by Cole.[41] Although this network can be fit at the two points where $\bar{Z}'' = 0$ and at the corresponding frequencies it does not represent the simulated points.

The general shapes of the inductive impedance plots above are very similar to that of the squid giant axon membrane, as reported by Cole.[41] Our results suggest that the equivalent circuit representation of a squid axon may be that shown in Figure 10. $\bar{W}$ represents an "inverted," finite Warburg discussed above and is represented by the solid curve in the figure. The points were obtained by transcribing Cole's data from figure 1:43 of ref 41, converting from impedance to admittance, subtracting the geometrical capacitance obtained at the high frequency limit, and then converting back to impedance. One reduced impedance unit, on the figure, corresponds to about 10.3 kΩ. Our transcribing procedure could not yield precise results; however, the agreement between experimental points and the general shape of the theoretical curve is very good. We have concluded that Cole's circuit cannot represent the squid axon membrane data. A further modification including a frequency dependent resistor, which Cole also suggests, is not very informative.

Simulation Error

The $d\bar{E}/d\bar{t} = \bar{E}_j - \bar{E}_{j'}$ approximation (eq 5) is the poorest finite difference approximation used in the algorithm. Its error may be expressed as an infinite series in which the leading and most important term is $-\Delta t(d^2\bar{E}/d\bar{t}^2)/2$.[42,43] Accordingly, there will be no error if E changes linearly with time in each volume element. Unfortunately, $\bar{E}$ grows exponentially (eq 7) so the error is $-\bar{E}_{j\infty}e^{\bar{t}\bar{\tau}}/2\bar{\tau}^2$ to $-\frac{1}{8}\bar{t}^{3/2}$. Typically, computed values of $\bar{E}_j$ will be in error by at most 0.5%. Reference 42 can be consulted for further information concerning the concentration differentials.

A more serious source of error, which fortunately does not directly affect the simulation itself, is replacement of integration by the summation in eq 9. We are using what amounts to trapezoidal rule integration,[43] which yields no error provided the function is a straight line. Because the electric intensity is nearly exponential close to the interfaces, errors could be as high as 8% for large values of $\bar{K}$. As we have already said, the error is most serious for blocked electrode simulations, and is considerably less than 8% for the other examples used.

Conclusions

The algorithm presented here is simple, concise, and versatile. It may be extended to include kinetic or equilibrium complications as previously described by Feldberg.[20] Virtually any number of ions may be treated and they may have arbitrary valences and concentrations. The algorithm is an explicit method and therefore is subject to the restriction that no mobility may exceed 0.5 reduced units.[20,43] This is a well-known stability condition which must be met; otherwise, simulation of concentrations will oscillate. No difficulties have been experienced so long as mobilities are kept below 0.45, even though widely different values (0.001–0.45) are used in the same simulation. We have not tested stability outside this range. A further limitation, not associated with the algorithm, is the use of the Fourier transform procedure to convert from time to frequency (*i.e.*, calculate $\bar{Z}(\bar{\omega})$ from $\bar{V}(\bar{t})$) which is only applicable for small current clamps such that $\bar{V} \ll 1$. Transient calculations can be quite accurate as demonstrated by comparison with analytical results.

Although this paper describes only current clamp studies, transient voltages due to concentration changes outside the membrane may also be simulated,[44] thus widening further the range of application of the method to include potentiometric problems.

References and Notes

(1) E. Warburg, *Wied. Ann.*, **67**, 493 (1899); *Drud. Ann.*, **6**, 125 (1901).
(2) F. Krüger, *Z. Phys. Chem.*, **45**, 1 (1903).
(3) G. Jaffé, *Ann. Phys.*, **16**, 217, 249 (1933).
(4) G. Jaffé, *Phys. Rev.*, **85**, 354 (1952).
(5) H. Chang and G. Jaffé, *J. Chem. Phys.*, **20**, 1071 (1952).
(6) J. R. Macdonald, *Phys. Rev.*, **92**, 4 (1953).
(7) R. J. Friauf, *J. Chem. Phys.*, **22**, 1329 (1954).
(8) G. Jones and S. M. Christian, *J. Amer. Chem. Soc.*, **57**, 272, 280 (1935).
(9) G. Jaffé and J. A. Rider, *J. Chem. Phys.*, **20**, 1077 (1952).
(10) J. E. B. Randles, *Discuss. Faraday Soc.*, **1**, 11 (1947).
(11) H. Ershler, *Discuss. Faraday Soc.*, **1**, 269 (1947).
(12) H. Gerischer, *Z. Phys. Chem.*, **198**, 286 (1951).
(13) M. Sluyters-Rehbach and J. H. Sluyters in "Electroanalytical Chemistry," Vol. 4, A. J. Bard, Ed., Marcel Dekker, New York, N.Y., 1969.
(14) J. H. Beaumont and P. W. M. Jacobs, *J. Phys. Chem. Solids*, **28**, 657 (1967).
(15) J. R. Macdonald, *Trans. Faraday Soc.*, **66**, 943 (1970).
(16) J. R. Macdonald; *J. Chem. Phys.*, **54**, 2026 (1971).
(17) J. R. Macdonald, *J. Electroanal. Chem.*, **32**, 317 (1971).
(18) J. R. Macdonald, *J. Chem. Phys.*, **58**, 4982 (1973).
(19) R. A. Arndt and L. D. Roper, "Simple Membranes Electrodiffusion Theory," Physical Biological Sciences Misc., Blacksburg, Va, 1972.
(20) S. W. Feldberg in "Electroanalytical Chemistry," Vol. 3, A. J. Bard, Ed., Marcel Dekker, New York, N.Y., 1969.
(21) J. R. Sandifer and R. P. Buck, *J. Electroanal. Chem.*, **49**, 161 (1974).
(22) H. Cohen and S. W. Cooley, *Biophys. J.*, **5**, 145 (1965).
(23) R. de Levie and H. Moreira, *J. Memb. Biol.*, **9**, 241 (1972).
(24) P. Delahay, "New Instrumental Methods of Electrochemistry," Wiley-Interscience, New York, N.Y., 1954, p 32.
(25) P. Delahay, "Double Layer and Electrode Kinetics," Wiley-Interscience, New York, N.Y., 1966, Chapter 7, p 153.
(26) R. P. Buck, *J. Electroanal. Chem.*, **46**, 1 (1973).
(27) A. A. Pilla, *J. Electrochem. Soc.*, **117**, 467 (1970).
(28) A. A. Pilla, *J. Electrochem. Soc.*, **118**, 1295 (1971).
(29) S. C. Creason and D. E. Smith, *J. Electroanal. Chem.*, **36**, App. 1 (1972).
(30) S. C. Creason and D. E. Smith, *J. Electroanal. Chem.*, **40**, App. 1 (1972).
(31) S. C. Creason, J. W. Hayes, and D. E. Smith, *J. Electroanal. Chem.*, **47**, 9 (1973).
(32) J. W. Cooley and J. W. Tukey, *Math Com.*, **19**, 297 (1965).
(33) A. Papoulis, "The Fourier Integral and Its Applications," McGraw-Hill, New York, N.Y., 1962, p 278.
(34) H. Lullies, *Biol. Rev.*, **12**, 338 (1937).
(35) K. S. Cole, "Membranes, Ions and Impulses," University of California Press, Berkeley, Calif., 1965, p 188.

(36) R. P. Buck, *J. Electroanal. Chem.*, **23**, 219 (1969).
(37) F. B. Llewellyn, *Proc. IRE*, **21**, 1532 (1933).
(38) R. de Levie, *J. Electroanal. Chem.*, **25**, 257 (1970).
(39) T. Teorell, *J. Gen. Physiol.*, **42**, 831 (1959).
(40) S. R. Caplan and D. C. Mikulecky in "Ion Exchange," Vol. 1, J. A. Marinsky, Ed., Marcel Dekker, New York, 1966, p 46.
(41) Reference 35, p 81.
(42) J. Crank, "The Mathematics of Diffusion," Oxford University Press, New York, N.Y., 1957, Chapter 10.
(43) B. Carnahan, H. A. Luther, and S. O. Wilkes, "Applied Numerical Methods," Wiley, New York, N.Y., 1969, Chapter 7.
(44) R. P. Buck and J. R. Sandifer, *J. Phys. Chem.*, **77**, 2122 (1973).

Calculated *vs.* Experimental Hydrogen Reaction Rates with Uranium

J. B. Condon[1]

Union Carbide Corporation, Nuclear Division, Oak Ridge, Tennessee 37830 *(Received August 22, 1974)*

Publication costs assisted by Union Carbide Corporation, Nuclear Division

Reaction rates for the hydrogen attack on uranium samples were both measured and calculated. The calculations were made using the model involving the diffusion equation and the equation expressing the kinetics of hydriding. All parameters but one were specified by previous experiments. The model was found to be in excellent agreement with reaction rates determined experimentally provided caution was exercised to randomize the grain structure of the starting sample.

Introduction

The purpose of this paper is to reconcile the previously observed[2a] first-order reaction rate with the normally observed linear reaction rates between hydrogen and uranium samples of reasonable size. To do this, calculations are made utilizing the proposed reactant-diffusion model as presented in the previous paper. These calculations are required for most uranium samples, other than fine powders, to determine reaction rates.

The ranges of sizes for which these calculations are needed is dependent upon temperature and hydrogen pressure. This is rigorously defined in a subsequent report,[2b] which demarks the range of temperatures, pressures, and sample thicknesses in which calculations become necessary. With the assumption of high tenacity for uranium (at least on the time scale of the reaction), the parabolic, first-order and mixed-parabolic and first-order reaction rates were derived.

Tenacity of uranium under stress, however, is not normally observed. The rates of overall reactions are slow enough and the sample size large enough to allow either spalling from a stressed surface or at least loss of integrity. The consequence of this more realistic assumption is a reaction rate which is linear with time and surface area.

Most reaction rates reported in the literature are of the linear type. The exceptions include parabolic rates of Albrecht and Mallett[3] and Alire, *et al.*,[4] first-order rates by Condon and Larson;[2a] and S-shaped dependence by Amilhat-Caralp, *et al.*[5] The former two types were dealt with fair success in the mentioned report;[2b] whereas, the latter is impossible to compare since sample shapes were not specified. Svec and Duke[6] did not report a uranium or surface area dependence but did report an activation energy of 8.2 kcal. Reports of linear dependence include data by Wicke and Otto,[7] Albrecht and Mallett,[3] and Galkin, *et al.*[8]

Reported herein are the results of some additional experiments along with the method and results of the linear reaction-rate calculations. Comparisons of the experimental results with the calculated results should reveal the range of validity of the proposed model.

Method of Calculation

Basic Model Equations. The reactant-phase-diffusion model involves a simple diffusion equation with a sink. This is given in one dimension, x, by

$$D\frac{\partial^2 C}{\partial x^2} = \frac{\partial C}{\partial t} - a\frac{\partial U}{\partial t} \tag{1}$$

where C is the atomic concentration (in mole fraction) of the diffusing species (hydrogen), U the normalized diffusion medium content (uranium content expressed as mole fraction), t is time, and a is the stoichiometric ratio for the reaction (here $a = 3$ mole fraction of H/mole fraction of U). The diffusion coefficient, D, is considered constant even though one would expect it to change with the change in the diffusion medium, in this case a change from pure uranium to uranium with hydride contamination. Since the solubility of hydrogen in uranium is very low and mechanical failure occurs with very low levels of hydride inclusions, D is assumed constant up to the point of metal fracture. To determine the power of the sink term, a second equation is used, that is

$$-\frac{\partial U}{\partial t} = k_1 C U \tag{2}$$

where k_1 is the rate constant determined previously.[2a] The boundary conditions used previously for the two-sided plate problem[2b] were

$$C(x, 0) = 0 \tag{3}$$

and

$$C(0, l) = C(l, l) = C_0 \tag{4}$$

where l was the plate thickness. C_0 is the solubility of hydrogen in the metal and together with D and k_1 is a known function of temperature.

$$k_1 = 10.4 \exp(1592/T) \text{ sec}^{-1} \times \text{(mole fraction of H)}^{-1} \quad \text{(ref 2a)} \quad (5)$$

$$C_0 = 5.58 \times 10^{-4} \exp(-894/T)\, P^{1/2} \times \text{(mole fraction of H) (with } P \text{ in Pa, ref 9, 10)} \quad (6)$$

and

$$D = 1.9 \times 10^{-6} \exp(-5820/T) \text{ m}^2/\text{sec} \quad \text{(ref 9, 10)} \quad (7)$$

In the present case, however, the second boundary condition must be modified. To take into account the loss of integrity of the uranium after a certain fraction has been transformed locally the condition is

$$C(x \leq x_c, t) = C(x \geq l - x_c, t) = C_0 \quad (8)$$

where x_c is defined as the point at which exactly the right amount of transformation has occurred to cause integrity loss. Computationally, this is accomplished with a simple decision ("if") statement.

Up to this point, the calculation has only one adjustable parameter. This parameter, x_c, is dependent on the point in the transformation at which stresses on the uranium are great enough to cause fracture. This could be left as adjustable; however, there are some guidelines as to approximately what its maximum value should be. It should be noted here that the criterion should be dependent upon precise sample geometry as are all fracture problems. In the following, however, a flat surface will be assumed. The criterion derivation will also use the simplest equations since use of more sophisticated equations are not justified by either the data available for the mechanics of uranium or the hydriding kinetic data. An error of approximately 50% in this parameter should be acceptable here.

The x_c Criterion. The parameter x_c in this calculation must be defined in terms of the extent of reaction. If the extent of reaction locally is equal to a defined amount, designated α_c, then the distance from the surface to that locale is x_c. The problem is, therefore, to find a criterion to designate what this extent of reaction should be.

Hopefully this assignment could be made from the metallurgical and physical properties of uranium saturated with hydrogen and β-uranium hydride. Metallurgical properties such as ultimate tensile strain, reduction in area are known for this material.[11-13] However, since it is moderately ductile, there is no reliable method of using this information to calculate the compressive strain in two dimensions required for fracture.

Even if this point of fracture could be calculated, there is still a possibility that the loss of integrity of the uranium might occur before spalling. This would be analogous to the case of uranium oxidation where it has been deduced[14] that crystallographic rearrangements and not spalling determines how closely molecular oxygen may approach the reaction front.

In spite of the foregoing reservations, some crude guidelines should be possible. A maximum allowed compressive strain should be obtainable from the corrected one-dimensional fracture stress and the modulus. Since, generally, metals behave more elastic under compression than tension, the use of idealized elastic equations should provide a reasonable approximation. It will, therefore, be assumed that uranium is reasonably elastic when compressed to less than 1%.

The Von Mises idealized equation for elastic materials written for two-dimensional rectalinear coordinates, Y_1 and Y_2, is

$$C = \sigma_{Y_1}^2 - \sigma_{Y_1}\sigma_{Y_2} + \sigma_{Y_2}^2 \quad (9)$$

when the stresses, σ_{Y_1} and σ_{Y_2}, are written as tensile being positive. It will be noted that the two-dimensional case with two equal compressive stresses and the one-dimensional case yield the same equation. In other words, if either

$$\sigma_{Y_1} = \sigma_{Y_2} \quad (10)$$

or

$$\sigma_{Y_2} = 0 \quad (11)$$

then

$$C = \sigma_{Y_1}^2 \quad (12)$$

Due to plasticity, eq 12 cannot be used directly to find the maximum stress to failure on tensile specimens. The conversion to true fracture stress should, however, eliminate the largest inaccuracy.

The stress–strain data for uranium saturated with hydrogen have been recently obtained by Powell, *et al.*[13] The modulus is approximately 138 ($\sigma \approx 30$) GPa and the true fracture stress is 0.917 ($\sigma \approx 0.030$) GPa. These values are strain-rate dependent but are reliable to within 50%. The required stress level in both the Y_1 and Y_2 directions on a surface to cause fracture is the same as the true fracture stress under one-dimensional tension or approximately 0.92 GPa. This will give a strain of about 0.66% if the modulus under compression is the same as that in tension.

To translate this information into extent of reaction one may conceive of the following steps. First, an increment of the reaction occurs in a small volume and an expansion of the material takes place. The plane of the surface, however, is constrained such that a compressive stress is applied to make the material conform to the original surface area. If this strain is greater than the above 0.66%, then the material fractures and the hydrogen gas can advance past this volume increment. If the strain is less than the 0.66%, the hydrogen advances into and past this volume only by diffusion.

In the reaction step one assumes a small volume expansion fraction, f, where

$$f = \frac{V_{\text{after reaction}}}{V_{\text{pure metal}}} - 1 \quad (13)$$

Under hydrostatic expansion each linear dimension will increase by $\frac{1}{3}f$ (since $(1 + \frac{1}{3}f)^3 \approx 1 + f$ with f small). To conform to the original area, a strain of $\frac{1}{3}f$ must therefore be effected to both dimensions of the surface plane. Thus fracture occurs when $\frac{1}{3}f$ equals or exceeds 0.0066.

Since the density of β-UH_3 is 11.1 and uranium is 19.07, the extent of reaction, α, corresponding to the above fraction expansion can be calculated by

$$f \approx 0.74\alpha \quad (14)$$

which will give the extent of reaction where fracture will occur as being

$$\alpha_c = (3 \times 0.0066)/0.74 \approx 0.027 \quad (15)$$

For pure uranium the modulus is a little higher, ~170 GPa, according to a summary by Holden.[12] The ultimate tensile

strength, however, is considerably lower. It is down to about 0.40–0.60 GPa for randomized material.

From the foregoing discussion, it appears that the loss of metal integrity must occur at rather low values for α_c. That is from the point of view of fracture alone, α_c should be in the neighborhood of 2%. This parameter is so poorly defined, however, that it must be considered an adjustable. The model thus has one adjustable parameter. For calculation purposes, the upper and lower limit of this parameter is taken as 3.0 and 1.6%. It will be shown later that the choice of criterion does not affect the observed (resultant) activation energy, and the 1.6–3.0% value is within the scatter of the best available data.

Performance of Calculations. The numerical calculations were made on a variety of IBM 360 computers. A fully implicit solution scheme was used to generate a tridiagonal system of simultaneous equations.[15] The system was solved and checked for convergence with an allowance for up to five iterations. The error was of the order $\Delta x^2 + \Delta t$ and each of the step sizes had to be continuously adjusted to make certain of proper control. The errors were such that the linear rates determined would be low; however, continued down adjustments of Δx and Δt could be made to check the appropriateness of the step-size choice. A semiinfinite solid problem iterated to a converging linear rate would have been more efficient. The two-sided plate problem was chosen, however, in order to determine the behavior of this reaction problem at the beginning and end of the reaction. This sometimes presented machine storage problems when Δx was very small and the thickness large; therefore, some of the linear rates were calculated at thicknesses not reported in the literature or used here.

Experimental Section

Justification. Hydriding experiments were undertaken to check the literature values available and to obtain values at temperatures not reported for a higher statistical check. With respect to the first reason, there are some minor inconsistencies in the literature. The inconsistencies are outside the limits of error imposed by the 2.2 ± 0.8% extent parameter described above.

Samples and Method. The samples used were nominally 8-mil thick (~0.2 mm), rolled foils which, after electropolishing and pickling, were reduced to a 0.15–0.17 mm thickness. The surface area, counting both sides, was 24.4 cm^2. Chemical analysis revealed that carbon at 98 wppm, iron at 85 wppm, silicon at 60 wppm, aluminum at 38 wppm, and nitrogen at 10 wppm were the principal contaminants. The oxygen analyzed at 660 wppm which is undoubtedly due to surface oxide since metallurgical examination did not justify such a high value. Estimates from this latter method produced a value of $\ll$100 wppm for oxygen content. All other elements were either below level of detection by spark-source mass spectroscopy or below 10 wppm.

Before the kinetic studies, an attempt was made to remove as much surface contamination, especially oxide, as possible. The samples were degreased in ultrasonic baths of perchloroethylene and Freon 113. If any grease was visible after this treatment, it was brushed off using either Freon or ethanol as a solvent and the bath repeated. If the samples had a preliminary heat treatment, then they were first electropolished with direct current in concentrated (RACS) nitric acid. All preliminary heat treatments were done in an ultra-high-vacuum system that had provisions for a rapid water quench. The final cleaning immediately before admission to the balance system consisted of the following steps: (1) a pickle at 80° in 1:2 nitric acid, (2) an ultrasonic cleaning in the same acid at room temperature, (3) a quick rinse in demineralized water, and (4) a rinse in ethanol. The sample was treated as described immediately before admission to the balance to minimize oxidation.

For some of the higher rates, tubular samples were machined out of reactor-grade uranium. The principal contamination in this material was carbon at about 330 wppm. The samples were 14 mm o.d. and 10 mm long with a wall thickness of about 1 mm. These samples were used so that the longer reaction time would make allowances for the balance to settle down after admission of hydrogen or alternatively to allow enough time for a heat up. The thinner samples reacted so rapidly that it was difficult to obtain the steady-state linear reaction rate.

The kinetic studies were performed in a Mettler Model TA1 thermoanalyzer DTA-TGA balance. Immediately after the pickling treatment, the samples were loosely rolled into a cylindrical coil 40 mm in length. These were then placed in an alumina crucible that was 59 mm deep. This depth allowed all the product to remain in the crucible. The crucible was placed in the balance and the vacuum chamber evacuated to 7×10^{-3} Pa (5×10^{-5} Torr). Upon occasion a heat treatment in gettered argon would be performed and the chamber cooled and again evacuated. For samples hydrided under 150° a prehydriding step was performed to eliminate oxide contamination on the surface. This prehydride was performed at 150° and an atmosphere (10^5 Pa) of hydrogen. This prehydriding was continued to about 20% completion at which point the chamber was evacuated. The sample was allowed to degas before the temperature was reduced to the hydriding temperature. All hydriding studies reported here were performed under an atmosphere of hydrogen.

None of the heat-treated samples exhibited exotherms large enough to upset the temperature control of the sample. Some of the nonheat-treated samples exothermed and were erratic in weight gain. Such results were either discounted or corrected for the temperature change. There are several explanations for the erratic exothermic behavior of those samples. It was felt, however, that a pursuit of this question was not central to the point of the present research.

Results

All the acceptable hydriding experiments, that is those without exotherms, displayed three regions to give an overall appearance of an S-shaped weight gain. The first part is a slow start-up or incubation period. This portion can be attributed to two effects: (1) oxygen contamination in the sample near and at the surface, or (2) a start-up to establish a diffusion gradient which is seen in the calculated rates. The central portion at low temperatures or high temperatures with thick samples is nearly linear. It is from this portion that the steady-state rates are extracted for comparison. The final portion is merely the round-off in the rate due to sample depletion. This portion is not a sharp break to a stop in the reaction but is a smooth round-off.

The absolute reaction rates initially obtained were not consistent with values in the literature. The activation energy was approximately that obtained by Wicke and Otto[7] and by Galkin, *et al.*[8] The absolute rate, however, was a factor of 20 lower than those two cited rates. The difference was attributed to the difference in the metal preparation

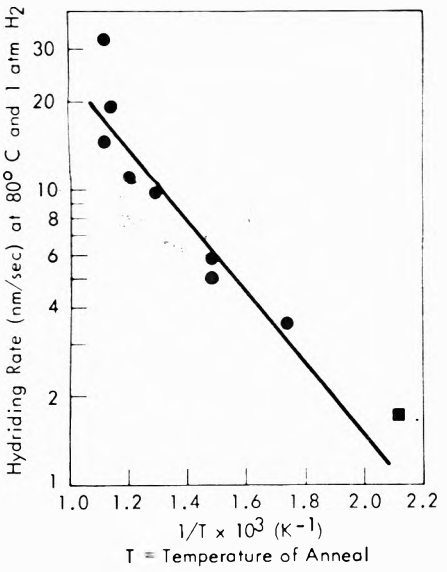

Figure 1. Hydriding rate as a function of a preannealing treatment. ($1/T$ plotted is that of the preanneal sample. The symbol ■ designates an unannealed sample.)

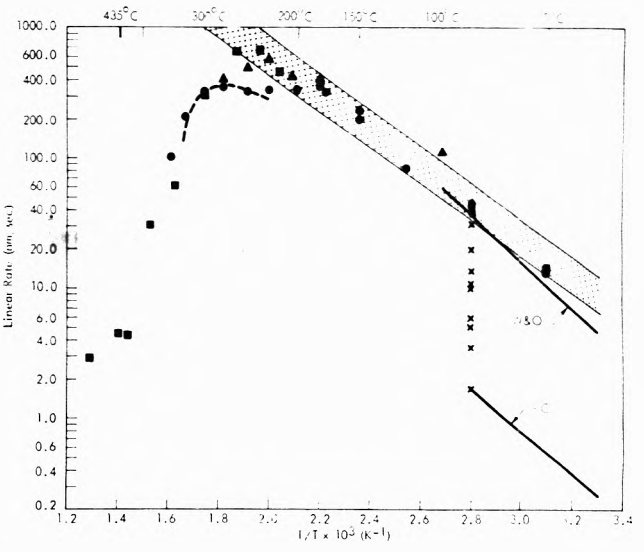

Figure 2. Experimental and calculated linear hydriding rates. Calculations were bracketed by the criterium that cracking occurs at 2.2 ± 0.8% extent of reaction and shown as shaded area. Dotted lines indicate extension of calculation to take into account the dehydriding (with extent of reaction for cracking, 3%). Experimental data as follows: W & O, empirical equation by Wicke and Otto;[7] C, data by present author on as-rolled samples; ■, Galkin, *et al.*,[8] x, present data from Figure 1; ●, present data on 0.15-mm randomized samples; ▲: present data on 1-mm randomized samples.

used here. Wicke and Otto and Galkin, *et al.*, used large, and presumably, as-cast samples; whereas, in this study, highly cold-worked and oriented[16-22] samples were the resultant of preparation. Preferred orientation for the foil samples is an assumption since it was not possible to obtain pole figures on such thin samples. This is a highly reasonable assumption, however, given the experience of other workers.[16-22] In light of this conclusion, it was also assumed that Albrecht and Mallet[3] may have had fiber texture[23] in their rods that would make their rates low.

To test the possibility that the working of the sample makes a difference in hydriding rates, a series of hydridings was carried out on samples that were first annealed. The anneals were performed at various temperatures for several days. These hydriding experiments were then performed at 80° and 1 atm of hydrogen. The linear rates obtained from this series are shown in Figure 1. The Arrhenius-type plotting is shown only for convenience, although one might get an activation energy for grain rearrangement from such a study. It was found that a 425° anneal for 10 days, a 1-day anneal at 600°, or a β-phase quench as prescribed by Turkalo[23] all gave essentially the same hydriding rate. Therefore, one of these treatments was used in all the subsequent work. The latter two were the preferred treatments.

With the prior heat treatment, the results of the experiments were in extremely good agreement with Wicke and Otto and with Galkin. Even the decrease in rate at about 300° followed Galkin's results very closely. This agreement can be seen in Figure 2. The experimental results from nonheat-treated samples and partially heat-treated samples are also shown in the figure for comparison.

Comparison of Results to Calculations

The first favorable comparison between the calculated and experimental curves is the S-shape that both exhibit. The results of a typical calculation for overall rate are shown in Figure 3. It can be seen from Figure 4, where the hydrogen concentration is plotted as a function of distance and time, that the start-up curvature is due to an establishment of a diffusion gradient. The round-off at the end is likewise due to a lag in the first-order rate of conversion.

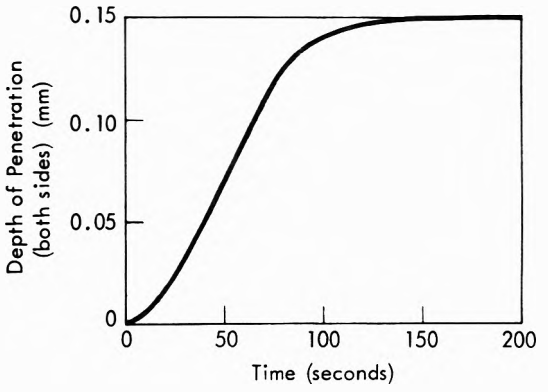

Figure 3. A typical calculated rate curve showing the amount of uranium consumed as a function of time: $T = 300°$; $\alpha_c = 3.0\%$.

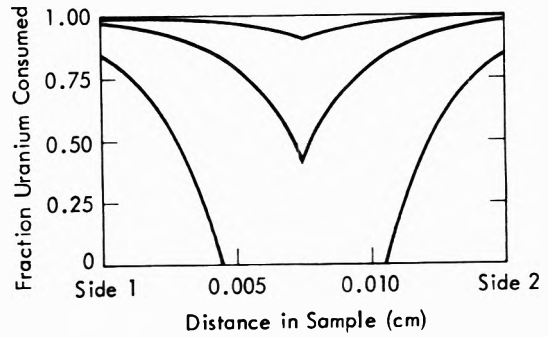

Figure 4. Calculated extent of reaction as a function of distance in the sample: $T = 300°$; $\alpha_c = 3.0\%$; the lines are at 30-sec intervals.

Comparison of Figure 3 with an experimental run in Figure 5 reveals a striking similarity.

It was noticed, however, that although the round-off por-

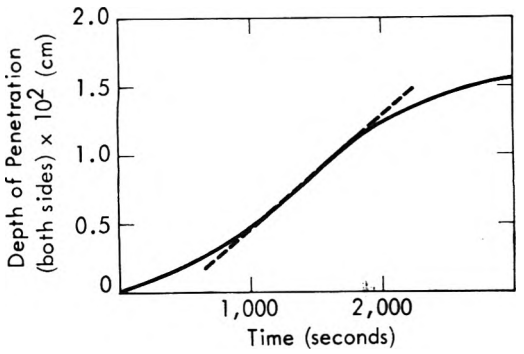

Figure 5. A typical experimental rate curve showing the amount of uranium consumed as a function of time. Dashed line shows the linear portion used to compare rates: $T = 80°$.

tions of the experimental and calculated curves were compatible for the full range of temperatures from 30° to approximately 250°, the calculated incubation times at low temperatures are considerably shorter than those observed. The explanation for this could be in oxygen contamination near or at the surface of the sample. This should be the case even if the sample were prehydrided to spall the oxide since the background pressure was not low enough to meet the criteria previously stated.[2a]

To compare experimental and calculated rates, the linear portion of the weight gain curve was used. This is illustrated in Figure 5 with the extended straight line. The rates of both are expressed in terms of a depth of penetration (as are Wicke and Otto's and Galkin's). This depth of penetration is defined as the distance integral through the sample of the extent of reaction. The rate is then the time rate of change of this integral. The results of the calculated rates with the 3 and 1.6% extent of reaction criteria are shown as the lower and upper limits of the shaded area on Figure 2. There was very little deviation from a linear relationship for these calculations on this Arrhenius plot. The slopes are identical with an activation energy of 6.35 kcal. This value is difficult to explain on the basis of the three starting activation energies. This value is independent of the extent criteria and is the same even if the extent was raised to 50%.

It will be noticed that the extent criteria of 2.2 ± 0.8% brackets the experimental data up to about 275°. At that point a downward trend in experimental rates begins. The reason for this decrease could be either an increase in creep rate observed[12] at this temperature or the competitive effect of the reverse reaction. The reverse local rate has been measured however, and, therefore, one should be able to modify eq 2 to take it into account. The reverse rate is, however, not first-order in remaining uranium but rather a low order, about ⅓, in hydride inventory. This leads mathematically to a contradiction between the thermodynamics and kinetics of the system that has been dealt with elsewhere.[24] Ignoring this problem, however, one can add a term to eq 2 to get

$$-\frac{dU}{dl} = k_1 CU - k_2(1 - U)^{1/3} \qquad (16)$$

where k_2 is the previously determined low-order rate constant for dehydriding. The value for k_2 consistent with the units here is

$$k_2 \approx 7.9 \times 10^4 \exp(-9210/T) \qquad (17)$$

(U is a normalized quantity).

Using this value the extensions of the rates at high temperatures are shown as the dashed lines in Figure 2. As can be seen, the agreement is good even though the *theoretical* foundations for this modification are weak. It must also be kept in mind that neither the dehydriding rate constant nor the dehydriding reaction order are very well known and are very sensitive to the presence of contaminants. It will be noted, however, that the overall effect of the dehydriding term produces a maximum at the correct temperature.

Conclusions

The experimental and calculated hydrogen reaction rates on uranium are in very good agreement. This agreement is true over a large temperature range, where the mechanism of the reaction has been determined. Even above 250° at 1 atm where the overall reaction rate decreases, fair agreement can be obtained by modifying the model with the previously determined dehydriding kinetics. It should also be noted that only one variable parameter was introduced in the model calculations. That introduced parameter expressed the extent of the reaction at which spalling or loss of metal integrity occurred.

The calculations are in agreement with experiment provided care is taken to randomize the grain structure of the sample. Oriented samples generally had lower reaction rates than predicted. Most likely these rate differences could be attributed to anisotropy in the diffusion coefficient. If so, one would expect to be able to orient samples such that the diffusion coefficient could be determined for various crystallographic directions by back calculations from determined corrosion rates.

Finally, the success of the model calculations shown here helps to confirm the correctness of the previously proposed kinetics.[2a] With such a confirmation, the differences between the mathematical expressions for the kinetics and the thermodynamics of this system are easily explained.[24] Any theory to explain the H-UH_3-U system which cannot allow for these apparent differences is inaccurate.

Acknowledgments. I wish to thank L. Steckel of the Y-12 Plant Laboratory Division for all the excellent TGA work presented here. Also I wish to thank James Parks, John Hawthorn, and Margaret Stone of the ORGDP Computer Center for the computer programming and calculations presented. I also thank Dr. G. L. Powell for supplying his most recent fracture mechanics data.

Work performed at Oak Ridge Y-12 plant under Contract No. W-7405-eng-26 with the U.S. Atomic Energy Commission.

References and Notes

(1) Oak Ridge Y-12 Plant, operated for the U.S. Atomic Energy Commission by the Union Carbide Corporation's Nuclear Division.
(2) (a) J. B. Condon and E. A. Larson, *J. Chem. Phys.*, **59**, 855 (1973). (b) J. B. Condon, "Calculations of Nonspalling Isothermal Hydriding Rates for Uranium," Y-1963, Union Carbide Corp., Nuclear Division, Oak Ridge Y-12 Plant, Oak Ridge, Tenn., 1974.
(3) W. M. Albrecht and M. W. Mallett, *J. Electrochem. Soc.*, **103**, 404 (1956).
(4) R. M. Alire, B. A. Mueller, C. L. Peterson, and J. R. Mosley, *J. Chem. Phys.*, **52**, 37 (1970).
(5) F. Amilhat-Caralp, L. Casahourset, and M. Destrian, *Bull. Soc. Chim. Fr.*, 1966, 3594 (1966).
(6) H. J. Svec and F. R. Duke, ISC-105 (1950).
(7) E. Wicke and Kl. Otto, *Z. Phy. Chem. (Frankfurt am Main)*, **31**, 222 (1962).
(8) N. P. Galkin, B. N. Sudarikov, Iu. D. Shishkov, and V. I. Tarasov, *Mosk. Khim-Tekhnol. Inst.*, **No. 43**, 67 (1963).
(9) G. L. Powell and J. B. Condon, *Anal. Chem.*, **45**, 2349 (1973).

(10) M. W. Mallett and M. J. Trzeciak, *Trans. ASM.*, **50**, 981 (1958).
(11) W. D. Davis, KAPL-1548 (1956).
(12) A. N. Holden, "Physical Metallurgy of Uranium," Addison-Wesley, Reading, Mass., 1958.
(13) G. L. Powell, J. Koger, R. Bennett, and R. A. Williamson, private communication (report to be published).
(14) E. W. Haycock, *J. Electrochem. Soc.*, **106**, 771 (1959).
(15) A. Ralston and H. S. Wilf, "Mathematical Methods for Digital Computers," Wiley, New York, N.Y., 1960.
(16) W. Seymour, *Trans. AIME, J. Metal*, Sept 1954, 999 (1954).
(17) C. J. McHargue and L. K. Jetter, *Progr. Nucl. Energy, Ser. 5*, **2**, 430 (1959).
(18) C. M. Mitchel and J. F. Rowland, *Acta Met.*, **2**, 560 (1954).
(19) J. Adam and J. Stephenson, *J. Inst. Metals*, **61**, 561 (1964).
(20) M. H. Mueller, H. W. Knott, and P. A. Beck, *Trans AIME, J. Metal* Nov 1955, 1214 (1955).
(21) E. A. Calnan and C. J. B. Clews, *Phil Mag., Ser. 7*, **43**, 93 (1952).
(22) L. LeNaour, CEA-R-3494 (Mai 1968).
(23) A. M. Turkalo, J. E. Burke, and A. N. Holden, KAPL-428 (1950).
(24) J. B. Condon, *J. Phys. Chem.*, **79**, 42 (1975).

Redox Potentials of Free Radicals. IV. Superoxide and Hydroperoxy Radicals $\cdot O_2^-$ and $\cdot HO_2$

P. S. Rao[1] and E. Hayon*

Pioneering Research Laboratory, U. S. Army Natick Laboratories, Natick, Massachusetts 01760
(Received December 17, 1973; Revised Manuscript Received September 18, 1974)

Publication costs assisted by Natick Laboratories

The fast-reaction technique of pulse radiolysis and kinetic absorption spectrophotometry was used to generate $\cdot O_2^-$ and $\cdot HO_2$ radicals in aqueous solution, and follow their one-electron redox reactions. In the presence of electron acceptors A, the one-electron oxidation of these radicals was monitored by following the formation of $\cdot A^-$ radicals: $\cdot O_2^- + A \rightleftharpoons O_2 + \cdot A^-$. Similarly, the one-electron reduction of $\cdot O_2^-$ was monitored in the presence of electron donors: $\cdot O_2^- + AH_2 \rightarrow H_2O_2 + \cdot A^-$. The efficiencies of these electron transfer processes were found to be dependent on the two-electron redox potentials of the electron donor or acceptor compounds used. From the midpoint (50% electron transfer) of these titration curves the kinetic potentials of some redox couples could be derived (at pH 7.0, ~25°): $E_k^{01} = +0.07$ V for the $O_2|\cdot O_2^-$ couple and $E_k^{01} \geq +0.36$ V for the $\cdot O_2^-|H_2O_2$ couple. The oxidation of $\cdot O_2^-$ was found to take place under reversible equilibrium conditions, whereas the reduction of $\cdot O_2^-$ was not reversible under the experimental conditions used. The observed rate constants of electron transfer reactions involving $\cdot O_2^-$, $\cdot HO_2$, and O_2 with a large number of acceptors and donors have been tabulated and found to be in general agreement with the E_k^{01} values derived for the appropriate redox couples.

Introduction

Many chemical and biological oxidation–reduction reactions occur *via* the intermediary of molecular oxygen, which can act as a mediator in electron transfer processes.[2-4] Many reactions involving oxygen in the ground state also proceed by one-electron steps *via* the superoxide radical $\cdot O_2^-$. The role and importance of $\cdot O_2^-$ in certain enzymatic and nonenzymatic oxidation reactions have been established (see, *e.g.*, ref 3, 5, and 6). The mechanism of reoxidation by oxygen of reduced biochemical systems (*e.g.*, reduced flavins, Fe^{2+} cytochromes, NADH, leuco dyes) has been shown or suggested to proceed in some cases *via* the formation of $\cdot O_2^-$ radicals.

The superoxide radical can undergo acid–base reactions, reaction 1,[7,8] and the physicochemical properties of $\cdot O_2^-$

$$\cdot O_2^- + H^+ \underset{pK_a = 4.85 \pm 0.1}{\rightleftharpoons} \cdot HO_2 \qquad (1)$$

and $\cdot HO_2$ radicals have recently been reviewed.[9,10] The impression has existed among some physical chemists that these radical intermediates are relatively unreactive species. Biochemical studies,[3,5,6] however, have shown that the one-electron oxidation *and* reduction reactions of $\cdot O_2^-$ and $\cdot HO_2$ can be of vital importance in certain biological reactions. No direct experimental determination of the redox potentials of the $\cdot O_2^-|O_2$, $\cdot O_2^-|H_2O_2$, $\cdot HO_2|O_2$, and $\cdot HO_2|H_2O_2$ couples have been obtained, leading to considerable uncertainties in establishing the reaction mechanism of chemical and biological oxidation processes. This work is an attempt to determine experimentally the redox potentials of these couples, based on a method recently developed in this laboratory.[11,12] Preliminary results have been published.[13]

Experimental Section

The $\cdot O_2^-$ and $\cdot HO_2$ radicals were produced in aqueous solution using the technique of pulse radiolysis. The details of the experimental set-up used have been described.[14,15]

The superoxide radical was produced from the reaction of oxygen with hydrated electrons

$$e_{aq}^- + O_2 \longrightarrow \cdot O_2^- \qquad (2)$$

under conditons such that all (>90%) the e_{aq}^- reacted with O_2 and none with the electron acceptor (A) or electron donor (AH_2) molecules used

$$e_{aq}^- + A \longrightarrow \cdot A^- \quad (3)$$

$$e_{aq}^- + AH_2 \longrightarrow \cdot AH_2^- \quad (4)$$

The concentrations of O_2, A, and AH_2 were adjusted based on the known[16] rate constants k_2, k_3, and k_4. The OH radicals produced from the radiolysis of water were, in some cases, scavenged[14] by *tert*-butyl alcohol. The radical produced from this alcohol can react with oxygen to form the corresponding peroxy radical.[14] This peroxy radical does not undergo[14,17,18] acid–base reactions up to pH ≥13, and was found not to interfere with the results obtained in this work (see ref 13 and below). The H atoms produced from the radiolysis of water react mainly with O_2

$$H + O_2 \longrightarrow \cdot HO_2 \quad (5)$$

Depending on the pH of the experiments, the radicals were present either as $\cdot O_2^-$ or $\cdot HO_2$, based on equilibrium 1.

The details of the method used to determine the potentials of organic free radicals ($\cdot R^-$) have been described.[11] This method depends on following the formation of the radicals produced by electron transfer to the acceptors (A), or by electron transfer from the donors (AH_2), *e.g.*

$$\cdot R^- + A \longrightarrow R + \cdot A^- \quad (6)$$

From a plot of efficiency of formation of $\cdot A$ radicals (expressed as percentage) as a function of the known redox potentials of the acceptors, typical titration curves are obtained. From the midpoint (50% electron transfer) of these curves, the potentials of the $\cdot R^-$ radicals can be derived. The redox potentials of the acceptors determined experimentally[19] are usually for two-electron processes.

It has subsequently been shown[11b] that for most of the organic free radicals examined equilibrium conditions did not prevail for reaction 6, under the experimental conditions used. Hence, the Nernst equation cannot be applied and the potentials derived from this method have been referred to as *kinetic* potentials,[11b] since it characterizes the efficiency of a radical to reduce an acceptor (or oxidize a donor) in kinetic competition with other reactions.[11b]

For the $\cdot O_2^-$ radical, it will be shown below that reversible conditions do appear to exist for the one-electron oxidation of $\cdot O_2^-$, equilibrium 7, but not for the one-electron

$$\cdot O_2^- + A \rightleftharpoons O_2 + \cdot A^- \quad (7)$$

$$\cdot O_2^- + AH_2 \longrightarrow HO_2^-(H_2O_2) + \cdot AH \quad (8)$$

reduction of $\cdot O_2^-$, reaction 8. The $\cdot AH$ radical produced can also undergo acid–base equilibration.

$$\cdot AH \rightleftharpoons \cdot A^- + H^+ \quad (9)$$

The percentage efficiencies of the electron transfer processes were obtained based on determination of the 100% efficiency ("blank") for formation of the $\cdot A^-$ or $\cdot AH$ radicals, according to reactions 3 and 10. These "blanks" were

$$e_{aq}^- + A \longrightarrow \cdot A^- \quad (3)$$

$$OH + AH_2 \longrightarrow \cdot AH + H_2O \quad (10)$$

carried out for every acceptor and donor compound each time just prior to carrying out the experiment, under identical experimental conditions of concentration, dose, pH, wavelength, etc. The lowest possible concentration of radicals were used to minimize radical–radical reactions.

Table I lists the acceptors and donors used, and the E^{01} values taken from the literature.[19] The notation $E^{(1)}$ is the value at pH 7.0 and ~25°, and E_m the value at the stated pH of the experiment. The sign of the potentials is in accord with the IUPAC convention.

TABLE I: List of Electron Donors and Acceptors Used

Compound	E^{01},[a] V	λ,[b] nm monitored
1. *N*-Ethylmaleimide	−0.500	335
2. Carbon dioxide	−0.420	
3. NAD•	−0.320	400
4. Lipoate	−0.289	385
5. Anthraquinone-2,6-disulfonate	−0.184	400
6. 2,3-Dimethylnaphthaquinone	−0.070	
7. Vitamin K	−0.060	
8. Cytochrome b_5	−0.055	
9. Menaquinone	−0.002	400
10. Duro-*p*-hydroquinone[c]	−0.042	
11. Methylene Blue	−0.011	580
12. Toluidine Blue O	−0.034	610
13. Duroquinone	+0.068	445
14. Indophenol (pH 9)	+0.089	610
15. Trimethyl-*p*-hydroquinone	+0.108	430
16. 1,4-Naphthaquinone-2-sulfonate	+0.118	400
17. 1,2-Naphthaquinone	+0.143	290
18. 2,5-Dimethyl-*p*-hydroquinone[c]	+0.170	
19. 1,2,4-Trihydroxybenzene[c]	+0.176	
20. 2,5-Dimethyl-*p*-benzoquinone	+0.176	440
21. 1,2-Naphthaquinone-4-sulfonate	+0.217	290
22. Methyl-*p*-hydroquinone[c]	+0.233	430
23. 2-Methyl-*p*-benzoquinone	+0.240	
24. *p*-Hydroquinone[c]	+0.280	430
25. 2,5-Dichloro-*p*-hydroquinone[c]	+0.285	
26. *p*-Benzoquinone	+0.293	430
27. 2,5-Dichloro-*p*-benzoquinone	+0.310	430
28. *N*-Methyl-*p*-phenylenediamine	+0.330	520
29. 3-Dimethyl-*p*-aminophenol	+0.410	385
30. 2,3-Dicyano-*p*-hydroquinone[c]	+0.510	430
31. Diphenoquinone	+0.534	400
32. *p*-Methoxyphenol	+0.564	400

[a] Redox potential at pH 7.0 and 25°; values derived from ref 19. [b] See also ref 11. [c] Compounds used in Figure 2.

The chemicals used were the highest research grade commercially available, and were obtained from Aldrich, Eastman Chemicals, J. T. Baker, K and K Laboratories, and Baker and Adamson. The solutions were buffered with ~1 m*M* phosphate, and perchloric acid and potassium hydroxide were used to adjust the pH. Special care was taken to reduce exposure of the solutions to light.

Results

Determination of the Potential of the $\cdot O_2^-|H_2O_2$ Couple. The one-electron reduction of the $\cdot O_2^-$ radical gives O_2^{2-} which is rapidly protonated by water to give hydrogen peroxide (pK_a^1 of H_2O_2 = 11.75). The electron donors chosen to bring about this reduction, reaction 8, were various hydroquinones, phenols, and *N*-methyl-*p*-phenylenediamine. These were selected on the basis of (a) their stability in oxygenated solutions, and (b) the formation of radical intermediates which absorb at appropriate wavelengths, react very slowly with O_2, and have relatively high molar extinction coefficients. The intermediates produced from these donors are semiquinone radicals (from hydroquinones), phenoxy radicals (from phenols), and aromatic amine cation radicals (from phenylenediamines).

These experiments were carried out in buffered solution at pH 7.0, oxygen-saturated ($[O_2] = 1.25 \times 10^{-3}$ *M*) and

typically 1.0 mM concentration of the electron donors. The OH radicals produced from the radiolysis of water were "converted" to O_2^- radicals by carrying out the experiments in the presence of 0.1 M sodium formate, when the following reactions occur

$$OH + HCO_2^- \longrightarrow \cdot CO_2^- + H_2O$$
$$\cdot CO_2^- + O_2 \longrightarrow \cdot O_2^- + CO_2 \qquad (11)$$

Under the experimental conditions chosen, none of the OH radicals react with AH_2 molecules and all the $\cdot CO_2^-$ radicals form $\cdot O_2^-$ in $\ll 1$ μsec, since k_{11} was found to be $\sim 5.0 \times 10^9$ M^{-1} sec^{-1}.

The percentage efficiencies for electron transfer from the donor molecules to the superoxide radical $\cdot O_2^-$ are presented, in Figure 1a, as a function of the redox potential of the donor compounds. It is seen that with increase (more positive) in the E^{01} of the AH_2 molecules the percentage efficiency decreases from ~100 to 0%. A "titration" type of curve is obtained. It was, unfortunately, not possible to find suitable donors with E^{01} values in the range +0.3 to +0.4 V.

It should be pointed out that, under the experimental conditions used, the $\cdot AH$ or $\cdot A^-$ radicals produced in reaction 8, namely, semiquinones, phenoxy, and aromatic amine cations radicals, react relatively slowly with O_2. Therefore, at the time scale of the experimental measurement essentially none had reacted *via*

$$\cdot AH + O_2 \rightleftharpoons A + \cdot O_2^- + H^+ \qquad (12)$$

Indeed, as will be shown below, the back reaction 12 is prevalent.

The rate constant of the reaction of $\cdot AH$ or $\cdot A^-$ radicals with H_2O_2, the reverse reaction 8, is considerably slower than the forward reaction. Hence reversible equilibrium conditions do not exist for the one-electron reduction of $\cdot O_2^-$ by AH_2, and the Nernst equation cannot be applied. Similar conditions were found[11,12] for the one-electron oxidation of organic free radicals, and the potentials of such couples have been referred to as kinetic potentials.[11b]

From Figure 1a, the midpoint (*i.e.*, 50% electron transfer) on the titration curve corresponds to a E_k^{01} value of $\geq$ +0.36 V, for the $\cdot O_2^-|H_2O_2$ redox couple. This value is based on the two-electron redox potential of the AH_2 donors. It is considered to be a lower limit since insufficient data were available for its determination. The E^{01} value (*i.e.*, the thermodynamic redox potential) for this couple is expected to be higher (*i.e.*, more positive), see more below.

Determination of the Potential of the $O_2|\cdot O_2^-$ Couple. The one-electron oxidation of the $\cdot O_2^-$ radical, reaction 7, can be studied by following the formation of the $\cdot A^-$ radicals from various electron acceptors A. These experiments were carried out in oxygen-saturated solutions at pH 7.0 in the presence of 1.0 M *tert*-butyl alcohol to scavenge the OH radicals. A few experiments were carried out using 0.1 M HCO_2^- as an OH radical scavenger, or a mixture of 13 mM N_2O and 0.7 mM O_2. Essentially similar results were obtained. The concentration of the acceptors used was 5×10^{-5} M (except 2.0–2.5 $\times 10^{-5}$ M when dyes were used), and relatively low $[\cdot O_2^-]$ of ~1–2 μM. Under these conditions, essentially none of the $\cdot O_2^-$ radicals decayed before reaction with the acceptors since reaction 13 is relatively very slow[7]

$$2\cdot O_2^- + 2H_2O \longrightarrow H_2O_2 + O_2 + 2OH^- \qquad (13)$$

The dependence of the efficiency of reaction 7 upon the redox potentials of the acceptors used is given in Figure 1b.

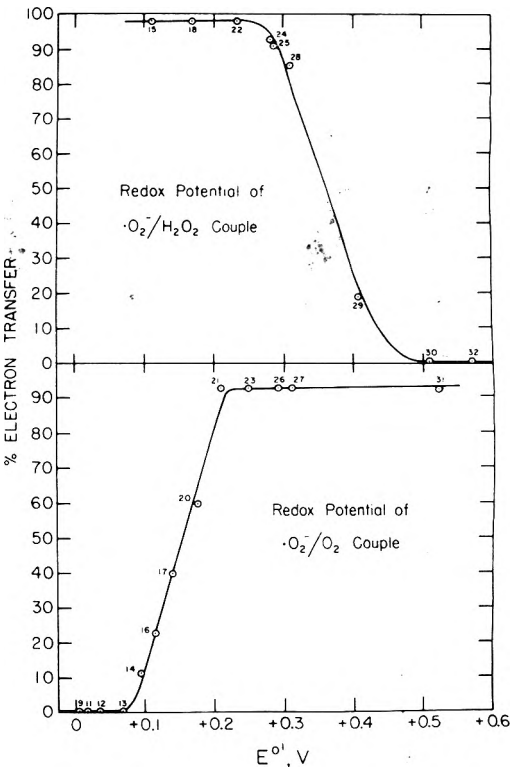

Figure 1. (a) The efficiency (expressed as percentage) of electron transfer from donor molecules to $\cdot O_2^-$ radicals, and (b) the efficiency of electron transfer from $\cdot O_2^-$ to a range of acceptor molecules. Experiments were carried out at pH 7.0 and relatively low concentrations of radicals. For the reduction of $\cdot O_2^-$, [radical] = 8–12 μM, while for the oxidation of $\cdot O_2^-$, [radical] = 1–2 μM. The donors and acceptors used are listed in Table I.

In this case a complete range of acceptors was available. Furthermore, reversible equilibrium conditions were found to exist, under our experimental conditions, for reaction 7.

The two half-cell reactions for this couple are

$$O_2 + e^- \rightleftharpoons \cdot O_2^- \qquad (14)$$
$$A + e^- \rightleftharpoons \cdot A^- \qquad (15)$$

and

$$E_A^0 - E_{O_2}^0 = 0.059 \log \frac{[\cdot A^-][O_2]}{[\cdot O_2^-][A]} \qquad (A)$$

Under equilibrium conditions at the midpoint (50% electron transfer) of the titration curve, eq B can be derived

$$E_{O_2}^0 = E_A^0 - 0.059 \log \frac{2[O_2]_0 - [\cdot O_2^-]_0}{2[A]_0 - [\cdot O_2^-]_0} \qquad (B)$$

where the subscripts "0" denote initial concentrations. Under the experimental conditions used, $[A]_0/[\cdot O_2^-]_0 \sim$ 12–15 and eq B can be reduced to

$$E_{O_2}^0 = E_A^0 - 0.082 \qquad (C)$$

From Figure 1b, a midpoint potential value of +0.15 $\pm$ 0.02 V can be obtained, giving a E_k^{01} = +0.07 $\pm$ 0.02 V for the $O_2|\cdot O_2^-$ redox couple. This value is based on the two-electron redox potential of the electron acceptors used. The earlier value given[13] for this couple was not corrected on the basis of eq C.

Determination of the Potential of the $\cdot HO_2|H_2O_2$ Couple. The hydroperoxy radicals decay bimolecularly with $k_{16} = 2.0 \times 10^6$ M^{-1} sec^{-1}, which is considerably faster

TABLE II: Yields (G Values) of Hydrogen Peroxide Produced from the ^{60}Co γ Radiolysis of Oxygenated Aqueous Solutions of Various Hydroquinones at pH ~0.4

Donor, AH_2	E^{01}, V	$G(H_2O_2)$	Ref
Duro-*p*-hydroquinone	+0.042	~4.40	This work
2,3-Dimethyl-*p*-hydroquinone	+0.170	4.44	20
1,2,3-Trihydroxybenzene	+0.176	4.17	20
Methyl-*p*-hydroquinone	+0.233	4.4 ± 0.5	This work
p-Hydroquinone	+0.280	4.0 ± 0.5	21
2,5-Dichloro-*p*-hydroquinone	+0.285	2.38	20
		3.2 ± 0.4	22
		2.30 ± 0.3	This work
2,3-Dicyano-*p*-hydroquinone	+0.510	2.2 ± 0.3	This work

$$2HO_2 \longrightarrow H_2O_2 + O_2 \quad (16)$$

than the decay of the conjugate base $\cdot O_2^-$. The rate constants for the one-electron reduction of $\cdot HO_2$ by various donors AH_2, reaction 17, are relatively low (see below).

$$\cdot HO_2 + AH_2 \longrightarrow H_2O_2 + \cdot AH \quad (17)$$

Consequently, using this fast-reaction technique experimental conditions could not be adjusted to determine the potential of the $\cdot HO_2/H_2O_2$ couple, since reaction 17 cannot compete with (16) at the relatively high concentrations of $\cdot HO_2$ (~8–12 μM) necessary for this work.

A different approach was used instead: at relatively very low steady-state concentrations of $\cdot HO_2$ radicals, as in ^{60}Co γ radiolysis, the yield of H_2O_2 should double whenever reaction 17 takes place with 100% efficiency. Table II gives the yields (G values) of hydrogen peroxide determined in oxygenated acid solutions of various hydroquinones and phenols. Included are results from the literature.[20-22]

TABLE III: Rate Constants of Electron Transfer Reactions Involving $\cdot O_2^-$, $\cdot HO_2$, and O_2 in Aqueous Solutions

System[a]	E^{01}, V[b]	k_{obsd}(electron transfer), M^{-1} sec^{-1}	Ref
	Reaction $\cdot O_2^- + A \rightleftharpoons O_2 + \cdot A^-$		
NADH	−0.325	$<<27$	25
Menaquinone	+0.002	Very low	26
Duroquinone	+0.068	5.0×10^6	26
1,4-Naphthaquinone-2-sulfonate	+0.118	6.6×10^8	13
2,5-Dimethylbenzoquinone	+0.176	3.6×10^8; 7.5×10^8	26,13
Cytochrome C	+0.270	1.1×10^5	34
p-Benzoquinone	+0.293	1.0×10^9	26,13
Tetranitromethane	+0.310	2.0×10^9	27
Diphenoquinone	+0.534	1.4×10^9	13
Br_2	+0.650	5.6×10^9	24
	Reaction $\cdot O_2^- + AH_2 \longrightarrow HO_2^- + \cdot AH$		
Methyl-*p*-hydroquinone	+0.233	1.7×10^7	c
p-Hydroquinone	+0.280	1.7×10^7	c
2,5-Dichloro-*p*-hydroquinone	+0.285	1.3×10^7	c
	Reaction $A^- + O_2 \rightleftharpoons A + \cdot O_2^-$		
(Acetophenone)$^-$	−1.29	2.3×10^9	28
(Thymine)$^-$		3.5×10^9	28
(Adenine)$^-$		3.5×10^9	28
(*N*-Methylmaleimide)$^-$		2.0×10^9	29
NAD·	−0.325	1.9×10^9	30
(Lipoate)$^-$		9.0×10^8	31
(9,10-Anthraquinone-2-sulfonate)$^-$	−0.225	4.6×10^8	32
(9,10-Anthraquinone-1-sulfonate)$^-$	−0.218	4.2×10^8	32
(9,10-Anthraquinone-2,6-disulfonate)$^-$	−0.184	5.0×10^8	33
(Vitamin K)$^-$	−0.06	2.0×10^8	26
Cytochrome b_5	~−0.06	~5.0×10^6	34
(Menaquinone)$^-$	+0.002	~5.0×10^6[e]	34
(Duroquinone)$^-$	+0.05	2.0×10^8	26
(2,5-Dimethyl-*p*-benzoquinone)$^-$	+0.176	$<<1.0 \times 10^7$	26
(*p*-Benzoquinone)$^-$	+0.293	$<<1.0 \times 10^7$	26
	Reaction[d] $\cdot HO_2 + A \rightleftharpoons O_2 + \cdot AH$		
Cytochrome C	+0.254	Unreactive	35
Tetranitromethane	+0.310	5.6×10^5	27
Br_2	+0.650	1.1×10^8	24

[a] Solution at near neutral pH, unless stated otherwise. [b] Redox potential of parent compounds at pH 7.0, 25°, from ref 19. [c] This work. [d] Acidic Solutions. pH 0.4 to 2.0. [e] This value is surprisingly low.

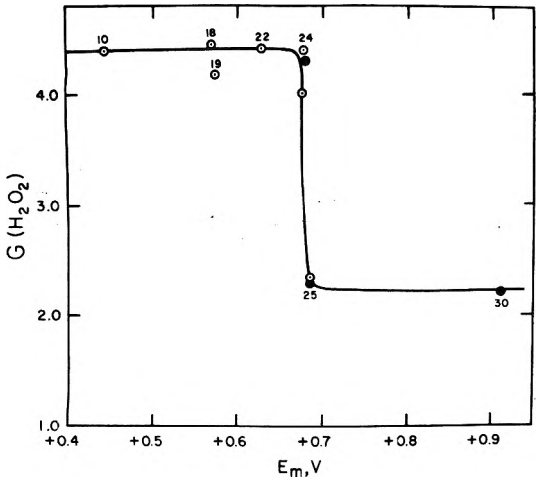

Figure 2. Dependence of $G(H_2O_2)$, produced from the ^{60}Co γ radiolysis of air-saturated aqueous solutions of various hydroquinones and phenols at pH ~0.4, upon the redox potential of the acceptors used. Open symbols are from ref 20–22, and closed symbols from this work.

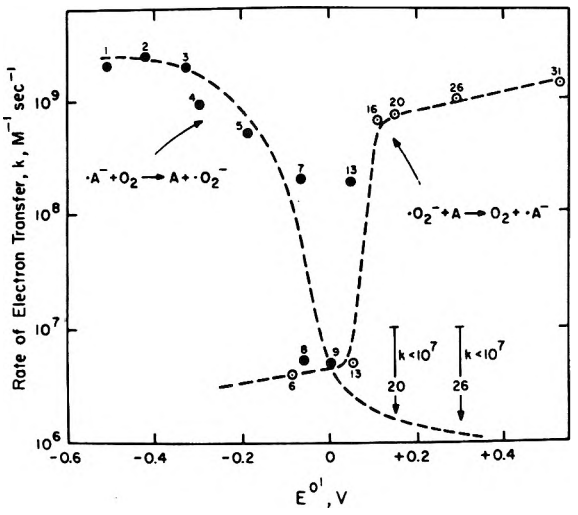

Figure 3. Dependence of the reaction rate constants of electron transfer processes involving O_2 and $\cdot O_2^-$ upon the redox potential of the acceptor or donor molecules. See Table III for details and references to literature values.

The $G(H_2O_2)$ yields were found to decrease with increase in the redox potential of the AH_2 donors. These results are presented in Figure 2. An abrupt change in the yields of H_2O_2 can be noticed and is interpreted as due to the inability of AH_2 donors to reduce $\cdot HO_2$ radicals *via* an electron transfer reaction 17.

Difficulties similar to those mentioned above for the determination of the potential of the $\cdot HO_2|H_2O_2$ couple are encountered for the $O_2|\cdot HO_2$ couple. Based on the pK_a = 4.85 for the $\cdot HO_2$ radical, reaction 1, one can calculate that the potential for the $O_2|\cdot HO_2$ will be ~+0.3 V higher than that of the $O_2|\cdot O_2^-$ couple. Thus a E_k^{01} value of ~+0.37 V may be expected for the $O_2|\cdot HO_2$ couple.

Discussion

The titration method described above to follow the one-electron transfer reactions of $\cdot O_2^-$ and $\cdot HO_2$ radicals with electron acceptor, or electron donor, compounds gives kinetic potentials for the redox couples which appear to be significant. While these potentials are not thermodynamic values, and are based on the known two-electron redox potentials of the compounds used, they do provide a scale for convenient comparison and prediction of the course of a chemical reaction.

Table III tabulates most of the known rate constants, k_{obsd}, for electron transfer processes of these species in aqueous solutions. Almost all these rates were determined previously[24-35] by various workers and using different techniques (including pulse radiolysis, flash photolysis, and esr).

The kinetic potential E_k^{01} = +0.07 V for the $O_2|\cdot O_2^-$ couple was determined above. Various calculated thermodynamic values of −0.59 V,[36] −0.36 V,[37] and −0.23 V[38] for the same redox couples were reported. These values cannot be compared with the E_k^{01} value since different basis for reference were used. It can be shown, however, that the E_k^{01} value for this couple is in reasonably good agreement with data in the literature on the reactions of $\cdot O_2^-$ and $\cdot HO_2$. The k_{obsd} values given in Table III for the reaction $\cdot O_2^- + A \rightleftharpoons O_2 + \cdot A^-$ are all (except for cytochrome C, where steric barriers may affect the electron transfer process) in good agreement with the E_k^{01} and E^{01} potentials of O_2 and of A, respectively. Thus $k_{obsd} \leq 5.6 \times 10^9\ M^{-1}\ sec^{-1}$ can be obtained. For and NADH, k_{obsd} is extremely slow as could have been predicted. It is clear that if one took the most positive thermodynamically calculated value for the $O_2|\cdot O_2^-$ couple, E^{01} = −0.23 V,[38] one could not explain the relatively low k_{obsd} values for menaquinone and duroquinone.

Similarly the k_{obsd} values for the reaction $\cdot A^- + O_2 \rightleftharpoons A + \cdot O_2^-$ given in Table III and plotted in Figure 3 are in fairly good agreement with the E_k^{01} value for the $O_2|\cdot O_2^-$ couple.

Much less information is available on the potential of the $O_2^-|H_2O_2$ couple. A thermodynamic value of +0.90 V has been calculated.[37] The E_k^{01} value for this couple ≥+0.36 V.

References and Notes

(1) Visiting scientist from the Radiation Chemistry Section, C.S.M.C.R.I., Bhavnagar, India.
(2) "Oxidases and Related Redox Systems," T. E. King, H. S. Mason, and M. Morrison, Ed., Wiley, New York, N.Y., 1965.
(3) "Biological Oxidations," T. P. Singer, Ed., Interscience, New York, N.Y., 1968.
(4) "Electron and Coupled Energy Transfer in Biological Systems," T. E. King and M. Klingerberg, Ed., Marcel Dekker, New York, N.Y., 1971.
(5) I. Fridovich, *Accounts Chem. Res.*, **5**, 321 (1972).
(6) D. Ballou, G. Palmer, and V. Massey, *Biochem. Biophys. Res. Commun.*, **36**, 898 (1969).
(7) D. Behar, G. Czapski, J. Rabani, L. M. Dorfman, and H. A. Schwarz, *J. Phys. Chem.*, **74**, 3209 (1970).
(8) M. Simic and E. Hayon, *J. Phys. Chem.* to be submitted for publication.
(9) B. H. J. Bielski and J. M. Gebicki, *Advan. Radiat. Chem.*, **2**, 177 (1970).
(10) G. Czapski, *Annu. Rev. Phys. Chem.*, **22**, 171 (1971).
(11) (a) P. S. Rao and E. Hayon, *J. Amer. Chem. Soc.*, **96**, 1287 (1974); (b) *ibid.*, in press.
(12) P. S. Rao and E. Hayon, *J. Amer. Chem. Soc.*, **96**, 1295 (1974).
(13) P. S. Rao and E. Hayon, *Biochem. Biophys. Res. Commun.*, **51**, 468 (1973).
(14) M. Simic, P. Neta, and E. Hayon, *J. Phys. Chem.*, **73**, 3794 (1969).
(15) J. P. Keene, E. D. Black, and E. Hayon, *Rev. Sci. Instrum.*, **40**, 1199 (1969).
(16) M. Anbar and P. Neta, *Int. J. Appl. Radiat. Isotopes*, **18**, 493 (1967).
(17) M. Simic and E. Hayon, *Biochem. Biophys. Res. Commun.*, **50**, 364 (1973).
(18) E. Hayon and M. Simic, *J. Amer. Chem. Soc.*, **95**, 6681 (1973).
(19) "Handbook of Biochemistry," Chemical Rubber Co., Cleveland, Ohio, 1970, p J-33; W. M. Clark, "Oxidation Reduction Potentials of Organic Systems," Williams and Wilkins, Baltimore, 1960; L. Meites "Polarographic Techniques," Interscience, New York, N.Y., 1967; I. M. Kolthoff and J. J. Lingane, "Polarography," Interscience, New York, N.Y., 1952; M. Brezina and P. Zuman, "Polarography," Interscience, New York, N.Y., 1958.

(20) B. H. J. Bielski and R. J. Becker, *J. Amer. Chem. Soc.*, **82,** 2164 (1960).
(21) T. J. Fellows and G. Hughes, *J. Chem. Soc., Perkins Trans. 1,* 1182 (1972).
(22) T. J. Fellows and G. Hughes, *Int. J. Radiat. Phys. Chem.*, **5,** 207 (1973).
(23) T. J. Sworski, *Radiat. Res.*, **4,** 483 (1956).
(24) H. C. Sutton and M. T. Downes, *J. Chem. Soc., Faraday Trans. 1,* **68,** 1498 (1972).
(25) E. J. Land and A. J. Swallow, *Biochem. Biophys. Acta,* **234,** 34 (1971).
(26) K. B. Patel and R. L. Willson, *J. Chem. Soc., Faraday Trans. 1,* **69,** 814 (1973).
(27) J. Rabani, W. A. Mulac, and M. S. Matheson, *J. Phys. Chem.*, **69,** 53 (1965).
(28) R. L. Willson, *Trans. Faraday Soc.*, **67,** 3008 (1971).
(29) E. Hayon and M. Simic, *Radiat. Res.*, **50, 464** (1972).
(30) R. L. Willson, *Chem. Commun.*, 1005 (1970).
(31) R. L. Willson, *Chem. Commun.*, 1425 (1970).
(32) B. E. Hulme, E. J. Land, and G. O. Phillips. *J. Chem. Soc., Faraday Trans. 1,* **68,** 1992 (1972).
(33) R. L. Willson, *Trans. Faraday Soc.*, **67,** 3020 (1971).
(34) T. Ohnishi, H. Yamazaki, T. Iyanagi, T. Nakamura, and T. Yamazski, *Biochim. Biophys. Acta,* **172,** 357 (1969).
(35) E. J. Land and A. J. Swallow, *Arch. Biochim. Biophys.*, **145,** 365 (1971).
(36) Reference 2, pp 20 and 34.
(37) L. E. Bennett, *Progr. Inorg. Chem.*, **18,** 1 (1973).
(38) J. H. Baxendale, M. D. Ward, and P. Wardman, *Trans. Faraday Soc.*, **67,** 2532 (1971).

Journal of Chemical and Engineering Data

JANUARY 1975, Vol. 20, No. 1

TABLE OF CONTENTS

■ Supplementary material for this paper is available separately, in photocopy or microfiche form. Ordering information is given in the paper.

Chemical Reaction Engineering—II

ADVANCES IN CHEMISTRY SERIES No. 133

A symposium co-sponsored by the American Chemical Society, the American Institute of Chemical Engineers, the Canadian Society for Chemical Engineering, and the European Federation of Chemical Engineering.

Here's an excellent source to bring you up-to-date on the continually changing state of the art in chemical reaction engineering. Fifty-one contributed papers concentrate on direct process applications and outline specific current processes and reaction types.

Subject areas include:

- novel reactor types; physical processes
- kinetics and mechanisms; heterogeneous catalytic reactors
- design models; optimal policies of operation; and more

698 pages (1974) Cloth bound $35.00. Postpaid in U.S. and Canada, plus 40 cents elsewhere.

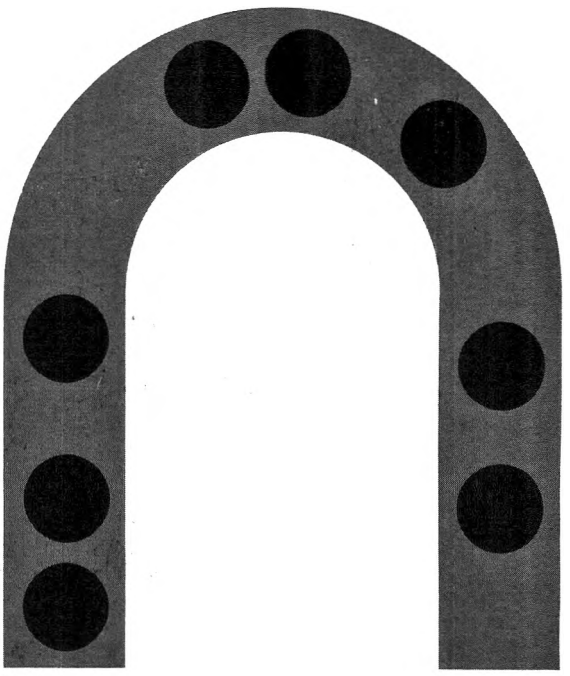

Other ACS books on chemical engineering include:

Annual Reviews of Industrial and Engineering Chemistry, Vol. 2

Fifteen reviews survey current work in industrial and engineering chemistry, focusing on new subject areas such as crystallization from melts, continuous crystallization from solution, chemical thermodynamics, and synthetic fibers. Ten topics are continued from Vol. 1. Over 5,600 references.
537 pages. Cloth. (1972) $19.95

Applied Kinetics and Chemical Reaction Engineering

Fifteen articles survey the application of kinetics to phenomena involved in a chemical conversion process and the synthesis of a descriptive, theoretical framework suitable for design, control, and optimization of a reaction. Topics include mixing and contacting, surface catalysis, photochemical reactions, oscillating reactions, turbulent heat transfer and others.
224 pages. Cloth. (1967) $7.50, plus 25¢ in Canada, PUAS, 40¢ foreign.

No. 121 Molecular Sieves

Fifty-five papers from the Third International Conference on Molecular Sieves report on scientific and industrial progress in five sections: structure, crystallization, ion exchange and modification, sorption, and catalysis.

No. 118 Chemical Engineering in Medicine

Seventeen papers focus on such topics as blood oxygenation, inert gas exchange, oxygen transport in the brain, pharmacokinetics, infant oxygenators, thermal control, erythropoiesis blood gas partial pressures, placental oxygen transfer, and placental glucose metabolism.
365 pages. Cloth. (1973) $16.75

No. 109 Chemical Reaction Engineering

Fixed and fluid bed reactors, polymerization kinetics and reactor design, optimization of reactor performance, catalysis in gas-solid surface reactions, two-phase and slurry reactors, industrial process kinetics, and transient operation.
685 pages. Cloth. (1972) $16.50

No. 105 Anaerobic Biological Treatment Processes

Nine papers survey the state of the art of this natural process for waste treatment, with three papers on methane fermentation, others on process control and design. Considers volatile acid formation, toxicity, synergism, antagonism, pH control, heavy metals, light metal cations.
196 pages. Cloth. (1971) $9.00

No. 89 Isotope Effects in Chemical Processes

Methods of separating isotopes and labeled molecules—chemical exchange, electromigration, photochemical processes, and distillation—are examined, along with factors that suit a process to isotope separation—single stage fractionation, exchange rate, and reflux.
278 pages. Cloth. (1969) $13.00

No. 80 Chemical Reactions in Electrical Discharges

A wide range of topics is covered in 37 papers by chemists, physicists, and engineers—treatments of decomposition and dissociation reactions, ion-molecule reactions, chemical syntheses, and chemical engineering aspects and physics of reactions in electrical discharges.
514 pages. Cloth. (1969) $15.00

Order from: **Special Issues Sales/ American Chemical Society**
1155 Sixteenth Street, N.W., Washington, D.C. 20036

PHYSICAL CHEMISTRY

An Advanced Treatise

edited by HENRY EYRING, DOUGLAS HENDERSON and WILHELM JOST

VOLUME XIA/MATHEMATICAL METHODS

edited by DOUGLAS HENDERSON

CONTENTS: R. J. JACOB, Linear Vector Spaces. E. W. GRUNDKE, Generalized Functions. H. J. SILVERSTONE, Complex Variable Theory. D. HENDERSON, Boundary-Value Problems. R. G. STANTON and W. D. HOSKINS, Numerical Analysis. A. T. AMOS, Group Theory. F. D. PEAT, Density Matrices. C. MAVROYANNIS, The Green's Function Method.

1975, 576 pp., $45.00/£21.60; subscription price: $38.25/£18.40

MOLECULAR COLLISION THEORY

by M. S. CHILD

A Volume in the THEORETICAL CHEMISTRY Series

This book introduces the basic concepts of molecular collision theory with two main objects in view. It is addressed to the experimentalist seeking a framework for the interpretation of his increasingly sophisticated results. The standard Born, distorted wave, sudden, impulse and exponential approximations are developed from a strictly quantum mechanical standpoint. At the same time the theoretician will find an account of the part classical, part quantum mechanical behavior of nature on a molecular scale. Chapters are included on the semi-classical interpretation of elastic scattering cross-sections, and on the general semi-classical and matrix approximation which promises to become increasingly important.

1974, 312 pp., $22.00/£8.50

ANNUAL REPORTS IN INORGANIC AND GENERAL SYNTHESIS—1973

Volume 2

edited by KURT NIEDENZU and HANS ZIMMER

CONTENTS: Preface. J. J. ALEXANDER, Main Group Hydrides, Alkali and Alkaline Earth Elements. L. MELCHER FRENZEL, Boron. B. H. FREELAND and D. G. TUCK, Aluminum, Gallium, Indium and Thallium. K. J. SHAH, Silicon. R. D. JOYNER, Germanium, Tin and Lead. P. A. S. SMITH, Nitrogen. H.-D. EBERT and E. LINDNER, Phosphorus. L. C. DUNCAN, Arsenic, Antimony and Bismuth. K. SEPPELT, Chalcogens. M. J. STEFFEL, Halogens and Pseudohalogens. K. SEPPELT, Noble Gases. K. S. MAZDIYASNI, Yttrium, Scandium, Lanthanides and Actinides. K. S. MAZDIYASNI, Titanium, Zirconium and Hafnium. F. W. MOORE and G. A. TSIGDINOS, Vanadium, Niobium, Tantalum. G. A. TSIGDINOS and F. W. MOORE, Chromium, Molybdenum and Tungsten. G. DAVIES, Manganese, Technetium and Rhenium. J. R. WASSON and H. J. STOKLOSA, Iron. F. R. MITCHELL, Cobalt and Nickel. B. T. HEATON, The Platinum Metals. Part I: Ruthenium, Osmium, Rhodium and Iridium. B. T. HEATON, The Platinum Metals. Part II: Palladium and Platinum. J. R. WASSON and D. K. JOHNSON, Copper. B. J. McCORMICK, Silver and Gold. J. B. SMART, Zinc, Cadmium and Mercury. J. C. FANNING and N. DATTA-GUPTA, Metalloporphyrin Synthesis. References.

1974, 329 pp., $13.50/£6.50

ADVANCES IN MAGNETIC RESONANCE, Volume 7

edited by JOHN S. WAUGH

CONTENTS: J. L. BJORKSTAM, NMR Studies of Collective Atomic Motion. D. KIVELSON and K. OGAN, Spin Relaxation Theory in Terms of Mori's Formalism. G. L. CLOSS, Chemically Induced Dynamic Nuclear Polarization. B. R. APPLEMAN and B. P. DAILEY, Magnetic Shielding and Susceptibility Anisotropies.

1974, 336 pp., $28.50/£13.70

SCIENCE AND TECHNOLOGY OF SURFACE COATING

(A NATO Advanced Study Institute on the Science and Technology of Surface Coating held at Imperial College, University of London, in April, 1972)

edited by BRIAN N. CHAPMAN and J. C. ANDERSON

Some of the topics covered in the forty-six contributions to this volume include: conduction and diffusion processes; product finishing with electrostatically sprayed powder coatings; the basic principles of anodization; diffusion coating metals in molten fluorides; the basic principles of chemical vapour deposition (CVD); chemical vapour deposition from an aerosol; the basic principles of wetting processes; the basic principles of evaporation; the basic principles of ion plating; and periodic structure of ultra-thin semiconductor films.

1974, 476 pp., $38.25/£14.80

PHASE TRANSITIONS AND CRITICAL PHENOMENA, Volume 3

edited by C. DOMB and M. S. GREEN

PARTIAL CONTENTS: Graph Theory and Embeddings. Computer Techniques. Linked Cluster Expansions. Asymptotic Analysis of Coefficients. Heisenberg Model. Ising Models. Expansion of X-Y Model. Ferroelectric Models.

1975, in preparation

Prices subject to change without notice.

ACADEMIC PRESS, INC.

A Subsidiary of Harcourt Brace Jovanovich, Publishers

111 Fifth Avenue, New York, N.Y. 10003

24-28 Oval Road, London NW1 7DX